NASA/ OHIO SPACE GRANT CONSORTIUM

2017-2018 ANNUAL STUDENT RESEARCH SYMPOSIUM PROCEEDINGS XXVI

March 23, 2018
Held at the Ohio Aerospace Institute
Cleveland, Ohio

Follow OSGC on:

TABLE OF CONTENTS

Click on any Student Name to be immediately linked to the first page of his/her report!

FOREWORD

The Ohio Space Grant Consortium (OSGC), a member of the NASA National Space Grant College and Fellowship Program, awards graduate fellowships and undergraduate scholarships to students working toward degrees in Science, Technology, Engineering and Mathematics (STEM) disciplines at OSGC-member universities. The awards are made to United States citizens, and the students are competitively selected. Since the inception of the program in 1989, over 1,215 undergraduate scholarships and 172 graduate fellowships have been awarded.

Matching funds are provided by the 25 member universities/community colleges, the Ohio Aerospace Institute (OAI), Choose Ohio First, the Nord Family Foundation, the Nordson Corporation Foundation, and private industry. Note that this year ~ $500,000 will be directed to scholarships and fellowships representing contributions from NASA, the Ohio Aerospace Institute, member universities, foundations, and industry.

By helping more students to graduate with STEM-related degrees, OSGC provides more qualified technical employees to industry. The research conducted for the Master's fellowship must be of interest to NASA. A prime aspect of the scholarship program is the undergraduate research project that the student performs under the mentorship of a faculty member. This research experience is effective in encouraging U. S. undergraduate students to attend graduate school in STEM. The Education scholarship recipients are required to attend a workshop conducted by NASA personnel where they are exposed to NASA educational materials and create a lesson plan for use in their future classrooms.

On Friday, March 23, 2018, all OSGC Scholars and Fellows reported on these projects at the Twenty Sixth Annual Student Research Symposium held at the Ohio Aerospace Institute in Cleveland, Ohio. In multiple sessions, Fellows and Senior Scholars offered 15-minute oral presentations on their research projects and fielded questions from an audience of their peers and faculty, and received written critiques from a panel of evaluators. Junior, Community College, and Education Scholars presented posters of their research and entertained questions from all attendees during the poster session. The University of Akron Lunabotics Team and their Robot, CHRISTEE, along with the Lorain County Community College Unmanned Aerial Systems (UAS) team, and Ohio Drone LLC also participated with a display. All students were awarded Certificates of Recognition for participating.

Research reports of students from the following schools are contained in this publication:

Affiliate Members

- The University of Akron
- Baldwin Wallace University
- Case Western Reserve University
- Cedarville University
- Central State University
- Cleveland State University
- University of Dayton
- Kent State University
- Marietta College
- Miami University
- Ohio Northern University
- The Ohio State University
- Ohio University
- University of Cincinnati
- The University of Toledo
- Wilberforce University
- Wright State University
- Youngstown State University

Community Colleges

- Cincinnati State Technical and Community College
- Columbus State Community College
- Cuyahoga Community College
- Lorain County Community College

MEMBER INSTITUTIONS

Affiliate Members	***Campus Representative***
• Baldwin Wallace University	James W. McCargar, Ph.D.
• Case Western Reserve University	Roger D. Quinn, Ph. D.
• Cedarville University	Robert Chasnov, Ph.D., P.E.
• Central State University	Augustus Morris, Jr., Ph.D., P.E.
• Cleveland State University	Ms. Rose Begalla, M.A.
• Kent State University	Joseph D. Ortiz, Ph.D.
• Marietta College	Prof. Craig Rabatin, P.E.
• Miami University	James Moller, Ph.D., P.E.
• Ohio Northern University	Jed E. Marquart, Ph.D., P.E.*
• The Ohio State University	Dr. Mo Samimy
• Ohio University	Dr. Shawn Ostermann
• The University of Akron	Dr. Craig C. Menzemer
• University of Cincinnati	Dr. Kelly Cohen
• University of Dayton	Dr. Robert J. Wilkens
• The University of Toledo	Dr. Lesley M. Berhan
• Wilberforce University	Jennifer N. Williams, Ph.D.
• Wright State University	Mitch Wolff, Ph.D.
• Youngstown State University	Hazel Marie, Ph.D., P.E.

Community Colleges	***Campus Representative***
• Cincinnati State Technical and Community College	Professor Abigail Yee
• Columbus State Community College	Professor Jeffery M. Woodson, M.S., I.E.
• Cuyahoga Community College	Dr. Lam F. Wong
• Lakeland Community College	Dr. Steven Oluic, USA (ret.)
• Lorain County Community College	Regan L. Silvestri, Ph.D.
• Owens Community College	Dean Glenn Rettig
• Sinclair Community College	Eric C. Dunn

NASA Glenn Research Center - Representatives

- Dr. M. David Kankam
- Ms. Susan M. Kohler
- Mr. Robert F. LaSalvia

Lead Institution	***Representative***
• Ohio Aerospace Institute	Ms. Ann O. Heyward

*Dr. Marquart also serves as Director of the Ohio Space Grant Consortium

ACKNOWLEDGMENTS

Thank you to all who helped with the OSGC's 26th Annual Research Symposium!

STEM Panel:
- Joshua Allen (NASA Glenn Research Center)
- Emilio Borges (NASA Glenn Research Center)
- Ashley Bowers (Facebook)
- Karin Bozak (NASA Glenn Research Center)
- Rob Charvat (GE Aviation and Ohio Drone LLC)
- Brian Tomko (NASA Glenn Research Center)

Campus Representatives – 4-Year Universities
- Dr. James W. McCargar, Baldwin Wallace University
- Dr. Roger Quinn, Case Western Reserve University
- Robert Chasnov, Ph.D., P.E., Cedarville University
- Augustus Morris, Jr., Ph.D., P.E., Central State University
- Ms. Rose Begalla, M.A., Cleveland State University
- Dr. Joseph D. Ortiz, Kent State University
- Professor Craig Rabatin, Marietta College
- James Moller, Ph.D., P.E., Miami University
- Jed E. Marquart, Ph.D., P.E., Ohio Northern University*
- Dr. Mo Samimy, The Ohio State University
- Dr. Shawn Ostermann, Ohio University
- Dr. Craig C. Menzemer, The University of Akron
- Dr. Kelly Cohen, University of Cincinnati
- Dr. Robert J. Wilkens, University of Dayton
- Dr. Lesley M. Berhan, The University of Toledo
- Jennifer N. Williams, Ph.D., Wilberforce University
- Mitch Wolff, Ph.D., Wright State University
- Hazel Marie, Ph.D., P.E., Youngstown State University

Campus Representatives - Community Colleges
- Professor Abigail Yee, Cincinnati State Technical and Community College
- Professor Jeffery M. Woodson, M.S., I.E., Columbus State Community College
- Dr. Lam F. Wong, Cuyahoga Community College
- Dr. Steven Oluic, USA (ret.), Lakeland Community College
- Regan L. Silvestri, Ph.D., Lorain County Community College
- Dean Glenn Rettig, Owens Community College
- Eric C. Dunn, Sinclair Community College

Special thanks go out to the following:
- Jeff Rolf and OAI for hosting the event
- Ohio Aerospace Institute staff whose assistance made the event a huge success!
- Jay N. Reynolds, Cleveland State University, for coordinating the Poster Session.
- Everyone who served as an evaluator
- NASA Glenn Research Center – Human Resources – Christina Koleno
- Industry Attendees
- Silver Service Catering (Scot and Mary Lynne)
- Sharon Mitchell Photography

*Dr. Marquart also serves as Director of the Ohio Space Grant Consortium

2018 OSGC STUDENT RESEARCH SYMPOSIUM

Hosted By: Ohio Aerospace Institute (OAI)
22800 Cedar Point Road • Cleveland, OH 44142
• (440) 962-3000
Friday, March 23, 2018

AGENDA

8:00 AM – 8:30 AM	Sign-In / Continental Breakfast / Student Portraits (30 minutes).....Lobby
8:35 AM – 8:40 AM	Welcome to OAI (5 minutes) ..... Forum (Lobby Level) *Jeff Rolf* President and Chief Executive Officer, Ohio Aerospace Institute
8:40 AM – 8:45 AM	Welcome and Introductions (5 minutes) *Jed E. Marquart* Director, Ohio Space Grant Consortium
8:45 AM – 8:50 AM	Symposium Logistics (5 minutes) *Laura A. Stacko* Program Manager, Ohio Space Grant Consortium
8:50 AM – 9:00 AM	Group Photograph (10 minutes) .....Lobby / Atrium Stairwell
9:00 AM – 11:00 AM	Student Oral Presentations – Senior Scholars and Fellows (120 minutes) •Group 1 ..... Forum (Lobby Level) •Group 2 .....Presidents' Room (Lower Level) •Group 3 .....Industry Room A (2nd Floor) •Group 4 ..... Industry Room B (2nd Floor)
11:00 AM – 12:15 PM	Various Displays (75 minutes) •Student Poster Presentations.....Lobby Junior, Community College, and Pre-Service Teacher (Education) Scholars •NASA and Industry Displays .....Lobby •Student Team Displays.....Atrium (Lower Level)
12:15 PM – 1:15 PM	Luncheon Buffet (60 minutes).....Atrium / Sunroom (Lower Level)
1:15 PM – 2:15 PM	Panel Discussion and Q&A (60 minutes)..... Forum (Lobby Level) *"Launching a STEM Career"*

Panel Members:

- ⋆Joshua E. Allen, NASA Glenn Research Center
- ⋆Emilio J. Borges, NASA Glenn Research Center
- ⋆Ashley S. Bowers, Facebook
- ⋆Karin E. Bozak, NASA Glenn Research Center
- ⋆Robert C. Charvat, Ohio Drone LLC
- ⋆Brian J. Tomko, NASA Glenn Research Center

2:15 PM – 2:30 PM	Presentation of Best Poster Awards (15 minutes) .....Forum
2:30 PM	Symposium Adjourns

STUDENT ORAL PRESENTATIONS
9:00 AM to 11:00 AM (120 minutes)

Group 1 – Mechanical Engineering / Manufacturing Engineering **FORUM (AUDITORIUM – LOBBY LEVEL)** **Evaluators: Sreeramesh Kalluri, Steve K. Lilley, and Mrityunjay (Jay) Singh**	
9:00	Yonry R. Zhu, Senior, Mechanical Engineering, Ohio University ***Evaluation of Decay Functions for Vector Field Based Obstacle Avoidance***
9:15	Kayla M. Pariser, Senior, Mechanical Engineering, University of Dayton ***Reducing Passive Muscle Force: A Process for Patient Specific Muscle Parameter Calibration in RTSA Patients***
9:30	Alex J. Mazursky, Senior, Mechanical Engineering, Miami University ***Experimental Evaluation of a Miniature Haptic Actuator based on Electrorheological Fluid***
9:45	Ryan C. Lucas, Senior, Mechanical Engineering, Ohio University ***Quadrotor Flight Simulation with Disturbance Estimation Feedback***
10:00	Kristen N. Fulmer, Senior, Mechanical Engineering, Cleveland State University ***Electric Propulsion for Commercial Aircrafts***
10:15	Andrea L. Felicelli, Senior, Mechanical Engineering, The University of Akron ***DLP Stereolithography Using Vat-Free Photopolymerization***
10:30	Katie S. Cooperrider, Senior, Mechanical Engineering, Ohio Northern University ***Human Limitations on Gravitational Assists: A Study of the Impacts of Human Involvement on Space Travel***
10:45	Michael C. Curtice, Senior, Manufacturing Engineering, Central State University ***Automated All-Sky Acquisition Project (AAAP)***

Group 2 – Aerospace Engineering / Applied Mathematics / Electrical Engineering / Mechanical Engineering **PRESIDENTS' ROOM (LOWER LEVEL)** **Evaluators: Daniel G. Gerges, Michael King, and Jen-Ching Tsao**	
9:00	Nicole L. Whiting, Senior, Aerospace Engineering, The Ohio State University ***Dynamic Stall Control Over a Rotorcraft Airfoil Using NS-DBD Plasma Actuators***
9:15	Liberty M. Shockley, Senior, Aerospace Engineering, University of Cincinnati ***Development of Small UAV Engine Capabilities at High-Altitudes***
9:30	Alexander Margetis, Senior, Applied Mathematics, Kent State University ***Beltrami Flows***
9:45	DeGrafth A. Palmore, Senior, Electrical Engineering, The University of Akron ***Triangulation Using Antennas in the Near-Field***
10:00	Daniel D. Musci, Senior, Electrical Engineering, Ohio Northern University ***Raspberry Pi Drone***
10:15	Jodi C. Turk, Masters 1, Mechanical Engineering, Cleveland State University ***Particle Imaging Velocimetry Analysis of Wake Induced by Real Whiskers***
10:30	Collin E. Mikol, Masters 1, Mechanical Engineering, The Ohio State University ***Design, Modeling, and Experimental Testing of a Variable Stiffness Structure for Shape Morphing***

STUDENT ORAL PRESENTATIONS (Continued)
9:00 AM to 11:00 AM (120 minutes)

Group 3 – Chemical Engineering / Biology / Petroleum Engineering / Aerospace Engineering INDUSTRY ROOM A (SECOND FLOOR) Evaluators: Ann O. Heyward, Paul Penko, and Thomas P'Simer	
9:00	Uchechukwu N. Obiako, Senior, Chemical Engineering, Cleveland State University ***Low-Temperature Catalytic Gasification of Particulate Waste for In-Situ Resource Utilization***
9:15	Colin W. McConnell, Senior, Chemical Engineering, University of Cincinnati ***Carbon Nanotube-copper Composite Sheet for EMI Shielding of Aerospace Structures***
9:30	James D. Harding, Senior, Chemical Engineering, Youngstown State University ***Fracture Property Testing of 3D Printed, Carbon Fiber Reinforced ABS***
9:45	Daniel J. Stank, Senior, Biology, Cedarville University ***Elucidating the Pathway by Which miR-146a Leads to Upregulation in Phagocytosis***
10:00	Tayla R. Brooks, Senior, Biology, Baldwin Wallace University ***Investigating the Role of Pseudomonas Quinolone Signal Molecule in P.A Associated Keratitis***
10:15	Charles E. Drennen, Jr., Senior, Petroleum Engineering, Marietta College ***Testing a Novel Minerology Crossplot Hypothesis***
10:30	Nathaniel L. Richards, Masters 1, Aerospace Engineering, University of Cincinnati ***Enhanced Concussion Recovery Prognosis with Deep Neural Networks: Proof-of-Concept for Decision Support***

Group 4 – Geology / Physics / Astrophysics / Computer Engineering / Computer Science INDUSTRY ROOM B (SECOND FLOOR) Evaluators: Raquel L. Redhouse	
9:00	Hannah L. Schlaerth, Senior, Geology, Kent State University ***Remote Sensing of Water Quality Parameters Influencing Coral Reef Health, U.S. Virgin Islands***
9:15	Sarah C. Rouse, Senior, Geology, Cedarville University ***Characterization of Sand Grains of the Tensleep Sandstone (Pennsylvanian-Permian), Wyoming, USA***
9:30	Kyle S. Pellegrin, Senior, Physics, Baldwin Wallace University ***Validation of Variable Star Photometry Utilizing the Burrell Telescope***
9:45	Matthew A. Mircovich, Senior, Physics, University of Dayton ***Loss Characterization of Magnesium Doped Lithium Niobate***
10:00	Heidi E. Kuchta, Senior, Astrophysics, The University of Toledo ***An Optical, Near-IR, and X-ray Study of the Orion South Cluster***
10:15	Benjamin D. Shaffer, Senior, Computer Engineering, Miami University ***An Isolated DC-DC Converter with Bidirectional Current for Interfacing the Voltage Busses of the Dragon Capsule and ISS***
10:30	Maxime Maisonnet, Senior, Computer Science, Wilberforce University ***Biometric Authentication Techniques: A Survey***
10:45	Alexandrea C. Oliver, Senior, Computer Science, Wright State University ***Usability Assessment for Caregiver Behavior Analysis Using Gaming Technology***

STUDENT POSTER PRESENTATIONS
LOBBY (MAIN FLOOR)
11:00 AM to 12:15 PM (75 minutes)

Dr. Jay N. Reynolds, Coordinator of Poster Session

Junior Science, Technology, Engineering, and Mathematics (STEM) Scholarship Recipients **Evaluators: Tadas Bartkus, Liangyu Chen, Sreeramesh Kalluri, and Andrew H. Work**
Michaela M. Crouch, Mechanical Engineering, Cedarville University ***Evaluation of Fretting Corrosion Wear in Metal-on-Metal Hip Implants Subjected to Impaction and Cyclical Loading***
Rachel E. Evans, Mechanical Engineering, Wright State University ***The Effect of Scan Strategy on Porosity in Additive Manufacturing***
Lynnae S. Frisco, Manufacturing Engineering, Central State University ***Heated Clothing***
Brittney A. N. Gibbs, Biology, Wilberforce University ***Effects of Cellular Phone Radiation on the Male Reproductive System***
Clarissa A. Goldsmith, Mechanical Engineering, Case Western Reserve University ***Cyber Physical Farming Robot for Organic Farm Weed Control***
Mina G. Kamel, Computer Science, Cleveland State University ***Robotic Mouse in Maze***
Joel R. Kavaras, Mathematics, Baldwin Wallace University ***Mathematical Modeling of Beech Leaf Disease Spread***
DerekAllen L. Krieg, Petroleum Engineering, Marietta College ***Electric Generation Potential in the Upstream Oil & Gas Sector***
DeOnte M. Layton, Mechanical Engineering, Youngstown State University ***Reduction of Tractor-Trailer Base Drag by a Corrugated Boattail***
Matthew N. McCannon, Aeronautical and Astronautical Engineering, The Ohio State University ***Control of Dynamic Stall Over an Airfoil Using NS-DBD Plasma Actuators***
Asa E. E. Palmer, Mechanical Engineering, University of Dayton ***Effect of Curved Boundary Layer Fences on Aerodynamic Efficiency***
Kylon J. Payne, Manufacturing Engineering, Central State University ***Heated Clothing***
David B. Prigg, Mechanical Engineering, Case Western Reserve University ***Digital Analysis of Moths for Micro Aerial Vehicles***
Ann M. Rumsey, Manufacturing Engineering/Engineering Management, Miami University ***Micromilling of Glass***
Reannah N. Rymarz, Petroleum Engineering, Marietta College ***Investigating Storage Systems for Alternative Sources of Energy***
Anthony O. Smoktonowicz, Senior, Electrical Engineering Technology, The University of Toledo ***Flexible Wing Technology for Drone Applications***
Kyle W. Strahm, Mechanical Engineering, Ohio Northern University ***Verification of Ideal Gas Law***
Robert P. Thoerner, Senior, Biomedical Engineering, The University of Akron ***Development and Design of a Cellular 3D Printed Loading Device***
Matthias S. Weisfeld, Mechanical/Aerospace Engineering, Case Western Reserve University ***Manduca Sexta Flying Wing Micro-Air Vehicle***
Austin M. Wessels, Aerospace Engineering, University of Cincinnati ***Variable Pitch Quadcopter Flight Control***
Robert R. Wilson, Senior, Aerospace Engineering, Kent State University ***Subsonic Wind Tunnel Development***

STUDENT POSTER PRESENTATIONS (Continued)

LOBBY (MAIN FLOOR)
11:00 AM to 12:15 PM (75 minutes)

Sophomore Community College STEM Scholarship Recipients **Evaluators: Christopher Hocevar and Stewart J. Leib**
Fiovi E. Agbodjan, Electro-Mechanical Engineering Technology, Columbus State Community College ***Innovative Technologies Using in the Treatment of WEEE (Waste Electric and Electronic Equipment)***
Ola J. Ali, Pre-Engineering/Civil Engineering, Cuyahoga Community College ***Cleveland Radioactive Waste***
Debin B. Brady, Programming and Development, Cuyahoga Community College ***Internet Censorship and Freedom of Speech***
John D. Bukovac, Mechatronics Technology – Micro Electromechanical Systems (MEMS), Lorain County Community College ***Flexible Wearable Transmissive Pulse Oximeter Sensor***
Hanin M. Hamid, Pre-Engineering, Cuyahoga Community College ***Tetrachloroethylene in Dry Cleaning***
Evan W. Kolodey, Pre-Engineering, Lorain County Community College ***Identifying Potential Contaminates in a Water Supply***
Christian E. Lambiase, Mechanical Engineering Technology, Columbus State Community College ***Comparison of Changes in Strength, Toughness, and Hardness of Steel After Heat Treatment***
Ryan A. Reffner, Chemistry, Lorain County Community College ***Unprecedented Whiskey Flavors Created by a Novel Accelerated Pressure Aging Process***
Zachary D. Reser, Mechanical Engineering Technologies, Cincinnati State Technical and Community College ***Custom Modification of Mini Excavators***
Katherine M. Rucker, Construction Management, Columbus State Community College ***Augmented Reality in Construction Coordination***
Isis Simone Tubbs, Pre-Engineering, Cincinnati State Technical and Community College ***Exploring Transverse Myelitis***

STUDENT POSTER PRESENTATIONS (Continued)

LOBBY (MAIN FLOOR)
11:00 AM to 12:15 PM (75 minutes)

Pre-Service Teacher (Education) Scholarship Recipients **Evaluators: Mary Brown, Valerie Hale, Irina P'Simer, and Kim Tanger**
Shantelle M. Binfet, Senior, Early Childhood Education, Wright State University ***Food's Next Great Frontier***
Hayley R. Crider, Junior, Early Childhood Education, Wright State University ***Life on Mars***
Jacob T. Dunwiddie, Senior, Early Childhood Education, Kent State University ***Responsive S.T.E.M. Teaching Utilizing the 5E Inquiry Cycles***
Alexandra A. Flanigan, Post Bacc., Adolescent to Young Adult (AYA), Integrated Science, Cleveland State University ***Studying Snow and Ice Changes***
Abigail M. Fuhrmann, Senior, Middle Childhood Education, Mathematics and Science, The Ohio State University ***Solar System Exploration***
Keilee L. Guthrie, Junior, Early Childhood Education, Ohio University ***Does My Hero Eat Like an Astronaut? What Astronauts Eat to Stay Healthy and Fit***
Elizabeth K. Han, Senior, Middle Childhood Education, Mathematics and Science, The Ohio State University ***Moon Movements***
Kaleb A. Irey, Sophomore, Adolescent to Young Adult (AYA), Mathematics, Cedarville University ***Measurements of Great Proportions***
DeVante M. Jackson, Junior, Adolescent to Young Adult (AYA), Mathematics, Central State University ***How Do Space Heroes Stay Alive?***
Kenton C. D. Jarvis, Junior, General Engineering/Adolescent to Young Adult (AYA), Mathematics, Ohio Northern University ***Newtons Ride***
Brittany A. Layden, Senior, Adolescent to Young Adult (AYA), Science, The University of Toledo ***The Science of Snowflakes***
Meghan G. Mulligan, Sophomore, Adolescent to Young Adult (AYA), Life Science/Chemistry, Miami University ***Coral Reefs: "Canaries" of the Sea***
Kristen E. Pierce, Post Bacc., Middle Childhood Education, Mathematics, The Ohio State University ***Incorporating STEM into ELA: Humans on Mars?***
Kaycie R. Riley, Junior, Adolescent to Young Adult (AYA), Mathematics, Miami University ***Building a Better Model: The Solar System***
Rachel E. Sauder, Senior, Adolescent to Young Adult (AYA), Integrated Science, Ohio Northern University ***Space Plants: Growing Peas as NASA Scientists***
Matthew W. Walker, Sophomore, Adolescent to Young Adult (AYA), Mathematics/Engineering, Ohio Northern University ***Water Filtration***

STUDENT TEAMS
ATRIUM (OUTSIDE PRESIDENT'S ROOM/LOWER LEVEL)
11:00 AM to 12:15 (75 minutes)

Case Western Reserve University Unmanned Aircraft Systems (UAS) Team
Professor Marlin Linger

The University of Akron (UA) NASA Robotics Mining Competition Team
Team Members: Seth Carpenter Sean Collins Kaylin Cozzens Dana Cressman Erika Nosal ***Advisor:*** Dr. Seungdeog Choi

Ohio Drone LLC
Team Members: Rob Charvat Emilio Borges James Hillegas

Ohio Space Grant Consortium

26th Annual OSGC Student Research Symposium

Friday, March 23, 2018
Ohio Aerospace Institute
Cleveland, Ohio

Welcome Session

Jeff Rolf, former President and CEO of the Ohio Aerospace Institute, bids everyone good morning and commends the Ohio Space Grant and its students for all the good work they're doing.

OSGC Director, Dr. Jed Marquart, initiates a round of applause for all of the OSGC's scholars and fellows.

Senior and Fellow Presentations

Tayla Brooks (Baldwin Wallace University) discusses ”Investigating the Role of Pseudomonas quinolone molecule in Pseudomonas aeruginosa Associated Bacterial Keratitis.”

Alex Mazursky (Miami University) presents his findings on “Experimental Evaluation of a Miniature Haptic Actuator based on Electrorheological Fluid.”

James Harding (Youngstown State University) elaborates on “Fracture Testing of 3D Printed, Carbon Fiber Reinforced ABS.”

Andrea Felicelli (The University of Akron) details her research on “Digital Light Processing Stereolithography Using Vat-Free Photopolymerization.”

Michael Curtice (Central State University) explains “Automated All-Sky Acquisition Project (AAAP).”

Uchechukwu Obiako’s research on “Catalytic Gasification of Waste Materials” could be a solution for waste management in Space.

Senior and Fellow Presentations

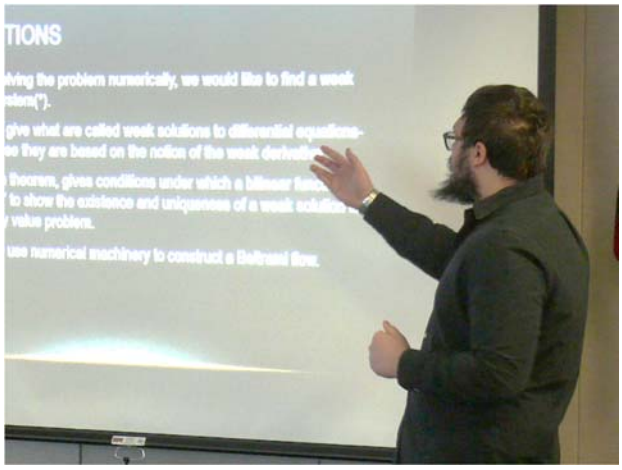

Alexander Margetis (Kent State University) explains the nature of "Beltrami Flows."

Alexandrea Oliver (Wright State University) presents "Usability Assessment for Caregiver Behavior Analysis Using Gaming Technology."

Charles Drennen (Marietta College) describes "Testing a Novel Minerology Crossplot Hypothesis."

Katie Cooperrider (Ohio Northern University) on "Human Limitations on Gravitational Assists: A Study of the Impacts of Human Involvement on Space Travel."

Heidi Kuchta (The University of Toledo) shows "An Optical, Near-IR, and X-ray Study of the Orion South Cluster."

Ryan Lucas (Ohio University) shares his research on "Quadrotor Flight Simulation with Disturbance Estimation Feedback."

Senior and Fellow Presentations

DeGrafth Palmore (The University of Akron) digs in on ” Triangulation Using Antennas in the Near-Field.”

Collin Mikol’s (The Ohio State University) shares his research on “Design, Modeling, and Experimental Testing of a Variable Stiffness Structure for Shape Morphing” and captured the audience’s attention.

Kayla Pariser (University of Dayton) discusses “Reducing Passive Muscle Force: A Process for Patient Specific Muscle Parameter Calibration in RTSA Patients.”

Yonry Zhu (Ohio University) delves into “Evaluation of Decay Functions for Vector Field Based Obstacle Avoidance.”

Student Teams

The University of Akron
Lunabotics Team
(from left to right):

Kaylin Cozzens,
Seth Carpenter,
Dana Cressman,
C.H.R.I.S.T.E.E.
The Robot,
and
Erika Nosal

Pioneers on the frontier of UAS (Unmanned Aerial Systems) technology
(from left to right):

Rob Charvat (former Scholar and Fellow) of GE Aviation and Ohio Drone LLC and Marlin Linger who heads a Statewide drone education program funded by the OSGC.

NASA Glenn HR

Christina Koleno
NASA Glenn Research Center Human Resources

Poster Session

Shantelle Binfet (Wright State University) explains her research poster: "Food's Next Great Frontier" with Jed Marquart.

Senior Central State University Michael Curtice listens to fellow Juniors, Kylon Payne and Lynnae Frisco, and their project on "Heated Clothing."

Andrew Work (OAI) hears about Mina Kamel's (Cleveland State University) research on the "Robotic Mouse In Maze."

Anthony Smoktonowicz (The University of Toledo) awaiting evaluation of his poster on "Flexible Wing Technology Applied to Drone Technology."

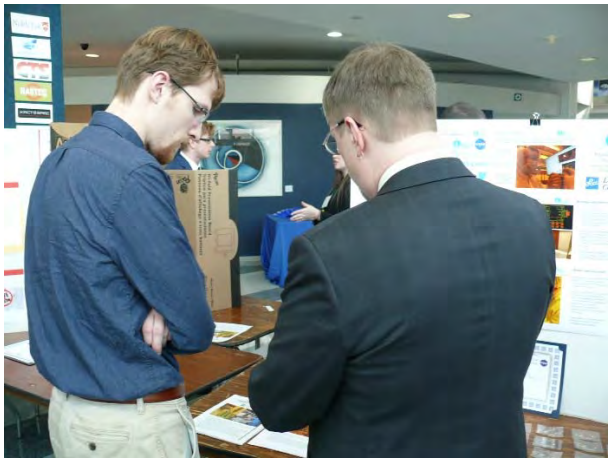

John Bukovac (Lorain County Community College) (right) explains his "Flexible Wearable Transmissive Pulse Oximeter Sensor" to Colin McConnell (University of Cincinnati) (left).

Cuyahoga Community College students, Ola Ali and Debin Brady, in front of Ola's research poster titled: "Cleveland Radioactive Waste: An Environmental Concern"

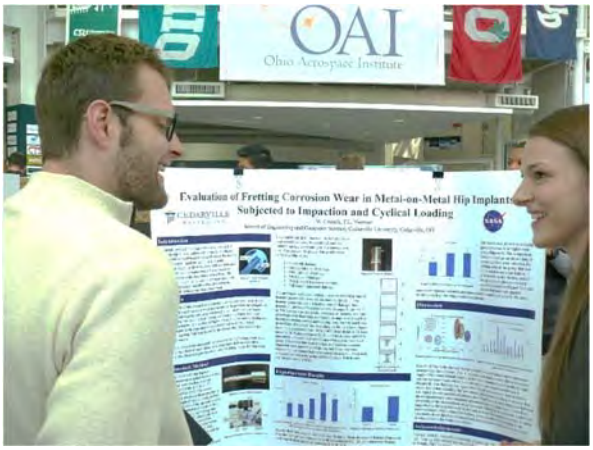

Michaela Crouch (Cedarville University) discusses her research on "Evaluation of Fretting Corrosion Wear in Metal-on-Metal Hip Implants Subjected to Physiological Loading" with Tadas Bartkus (OAI)

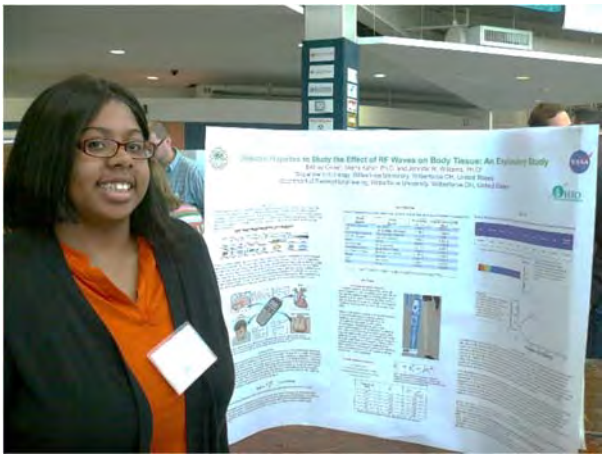

Brittney Gibbs (Wilberforce University) showcasing her research poster: "Effects of Cellular Phone Radiation on the Male Reproductive System"

Representing Lorain County Community College (left to right): Johnny Vanderford, Dr. Celestia Lau, Evan Kolodey, Ryan Reffner, and John Bukovac.

Clarissa Goldsmith (Case Western Reserve University) shares her research poster on "Cyber Physical Farming Robot for Organic Farm Weed Control" with Jeff Rolf.

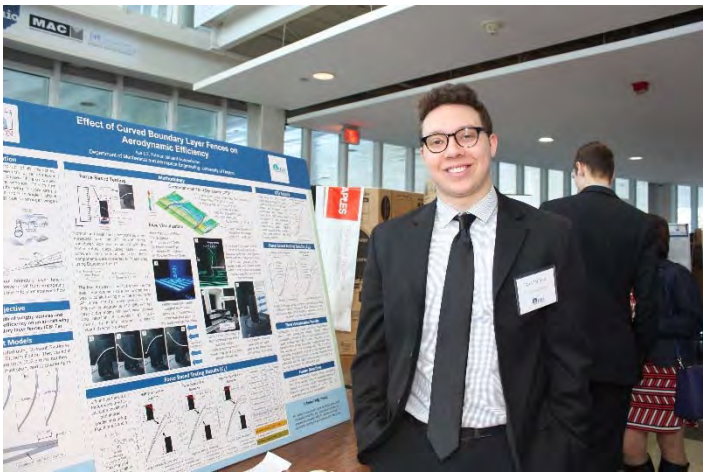

Asa Palmer (University of Dayton) and his poster on "Effect of Curved Boundary Layer Fences on Aerodynamic Efficiency."

From left to right: Central State Campus Representative Augustus Morris, Jr., Jennifer Williams, Wilberforce University Campus Representative, students Brittney Gibbs, Maxime Maisonnet, and his Advisor, Rakia Zammouri

Launching A STEM (Science, Technology, Engineering, and Math) Career

Last year's Symposium saw the introduction of a panel on "Launching a STEM Career" comprised of former OSGC Scholars and Fellows. This replaced a keynote speaker and was well received. So naturally the only thing to do this year was bring it back!

This year's STEM Panel members (from left to right): Ashley Bowers (Facebook), Brian Tomko (NASA Glenn Research Center); Rob Charvat (GE Aviation and Ohio Drone LLC); Emilio Borges (NASA Glenn Research Center and Ohio Drove LLC); Karin Bozak (NASA Glenn Research Center); and Joshua Allen (NASA Glenn Research Center).

Poster Competition Winners

The winners of the Poster Session were presented with a gift card and Certificate of Recognition by OSGC Director, Dr. Jed E. Marquart.

Featured from left to right with Dr. Marquart are:

- Brittany Layden (The University of Toledo), “Best Education Poster”
- Zachary Reser (Cincinnati State Technical and Community College), “Best Community College Poster”
- Asa Palmer (University of Dayton), “Best STEM Poster”

Innovative Technologies Used in the Treatment of WEEE
(Waste Electrical and Electronic Equipment)

Student Researcher: Fiovi E. Agbodjan

Advisor: Professor Jeffery M. Woodson, M.S., I.E.

Columbus State Community College
Electro-Mechanical Engineering Technology Program

Abstract
This research will present the most recent technologies in North America for the treatment of some WEEE (cathode ray tubes) in order to recycle their materials. This study will emphasize on the industrialization of processes of dismantling, calibration and sorting of the components of the apparatuses. In particular, it shows that optical sorting, technologies of plastics separation, and automatic sorting of glasses from cathode ray tubes are now industrialized in the countries with strong lawful requirements. Guide its decisions supporting research and development initiatives for WEEE recycling technologies; those intended to improve the recycling performance of materials for the selective treatment of hazardous components and substances.

Project Objectives
The flow of WEEE grows rapidly: the complexity of the elements that compose them, the dangerousness or the toxicity of certain contained substances and the impact on the environment via the exploitation of the raw materials in their composition fully justify a specific waste management which results from these devices once they are used. In addition, this waste represents an interesting source of secondary raw materials.

Have the main technical indicators characterizing the innovative processes available or the facilities exploiting these processes: typologies of incoming flows and fractions of separated materials, hourly and annual capacities, strong and weak points or perfectible points, levels or perspectives of industrialization, mapping of their developments.

Methodology Used
This study was conducted on the basis of three main areas of investigation: A specific documentary research on recycling technologies for WEEE as well as on processes for sorting and separating materials in general (mechanical, physicochemical or optical chemical solutions); Surveys of equipment suppliers (separation, sorting); Investigations and visits to industrialize.

Results Obtained
The cathode ray tube is the inner part of the screen, consisting of an electron gun and a glass tube inside which is a metal mask. They come from the disassembly of screens (televisions and monitors), which is done manually, then are treated specifically. The cathode ray tube is composed of two qualities of glass: - the slab which represents approximately 2/3 of the weight of the tube and which contains barium - the cone which represents approximately 1/3 of the weight of the tube and which contains 20% of lead Cathode ray tube imaging technology today characterizes almost all end-of-life screens; the "cathode-ray tube" component can represent up to 60% of the weight of the screens. The recycling of the cathode ray tube glasses requires the extraction of the luminescent powders fixed on the part of the slab of the tube. In all cases of closed-loop glass recycling and in most of those considered open-loop, the separation between the barium glasses of the slab part and the glasses with high lead content of the

cone is another imperative. Two technological models presented below that meet these requirements emerge from this study: - a treatment system based on the cutting of the tube into two glass qualities (slab and cone) after dismantling and then the preparation of the glass (wet or dry washing), (wet and granulometric preparation) for their recycling; a treatment method based on the grinding of the entire tube, its preparation (dry or wet washing and granulometric preparation) and the mechanized separation by optical.

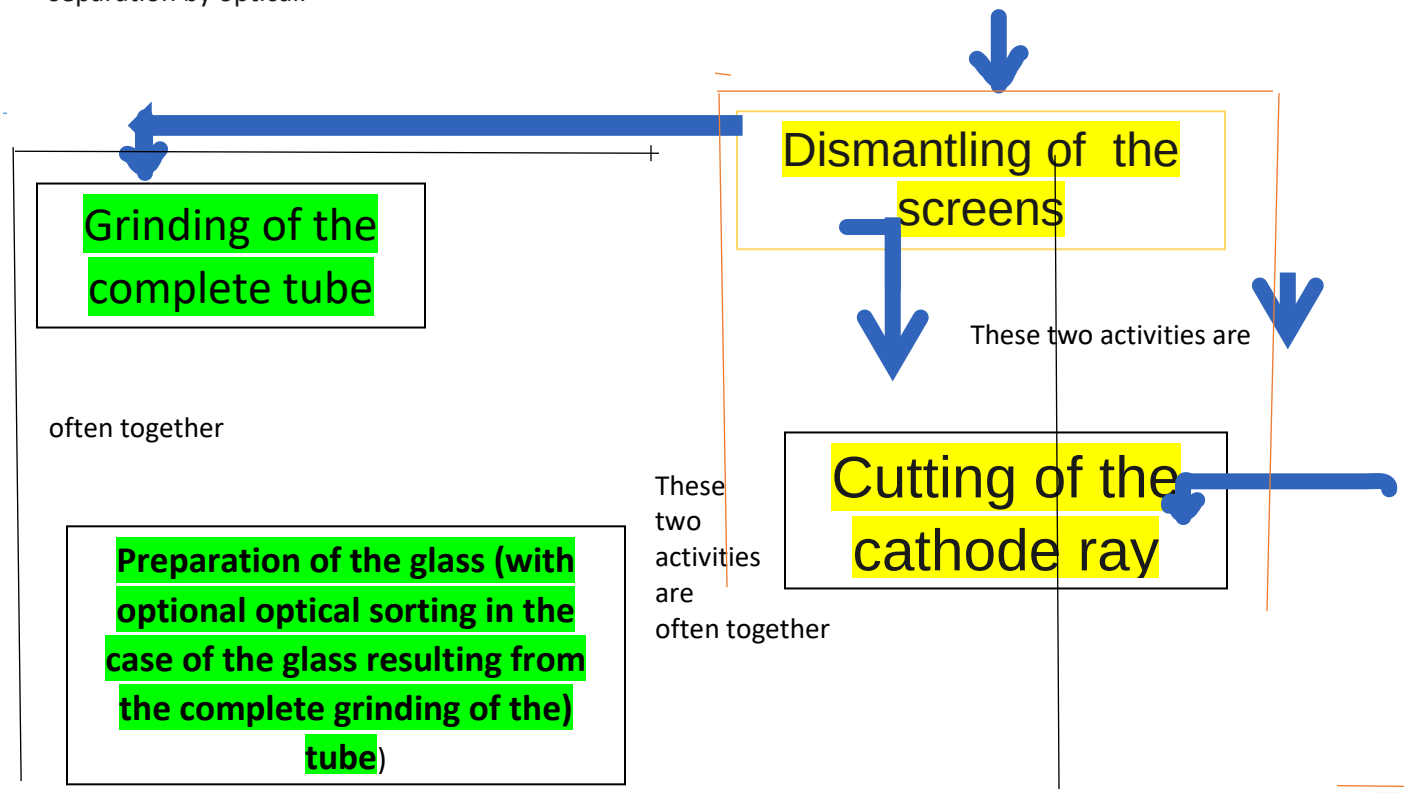

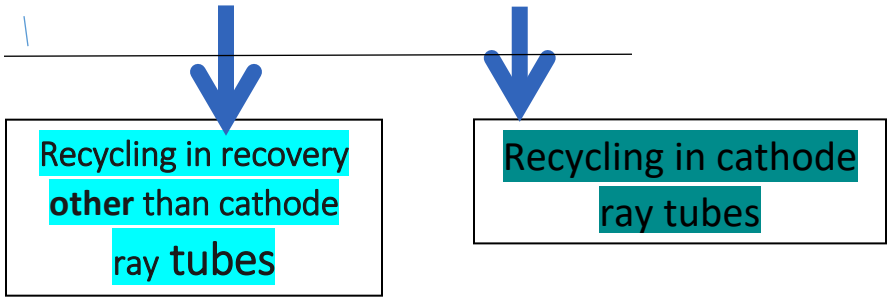

References

1. http://www.bhs-sonthofen.de, July, 2007.
2. www.mrtsystem.com/home; www.mewa-recycling.de, August, 2008.
3. EERA : « Towards sustainable WEEE recycling », January 2007.
4. Gary and Mark, plant managers at Rumpke Recycling.

Cleveland Radioactive Waste: An Environmental Concern

Student Researcher: Ola J. Ali

Advisor: Professor Christopher Huhnke

Cuyahoga Community College
Engineering/ Engineering Technology

The United States is considered as a first world country. This meant that we are far more developed industrially. Sacrifices come along with these developments. Our land, water, and air are sacrificed. They are usually the first ones affected by industrial wastes leaks resulting in contamination and pollution. If we think about it, war is also an industry where weapons are made to be used or sold. The US is one of the top countries that produce weapons since history. Cleveland, in particular, has a forgotten past that still haunts the present today. During World War II, Harshaw Chemical Co. of Cleveland Ohio located at 1000 Harvard Avenue, was part of the Manhattan Project which uses process uranium to make fuel for Nuclear weapons ("Harshaw Chemical Co."). The production duration was from 1942 to 1955 and decontamination was done until late 1960 but radiological surveys made on 1976 till 1979 and again on 1984 had identified widespread contamination ("Harshaw Chemical Co."). This research will make a brief analysis on the extent of the radioactive contamination of in Cleveland Ohio, particularly by the Harshaw Chemical Co. Is the contamination still prevalent as of today?

Light, warm, and dry, is what sandy soil are known for. Also, sandy soil is more likely to be acidic and it is known for being low in nutrients. According to research gate, 60 percent of uranium formed in the sandy soil. Due to this formation of relatively high soluble Uranium, carbonate complexes after liming of carbonate-rich, uranium- contaminated soils, the mobility of Uranium in these soils increased and the underlying ground water was polluted ("reasrchgate").

The type of uranium used for nuclear weapons is the uranium-235 ("Uranium-235"). Its radioactive isotope has a half-life of 703, 800, 000 years ("Uranium-235"). It is only around 76 years from 1942 since Harshaw Chemical Co. had first operated. This would basically mean that whatever radioactive isotope left in the soil in Harvard Avenue due to their activities in World War II have not been gone. This can be proven when the US Army Corps of Engineers have collected and analyzed samples in one part of the area for FUSRAP or Formerly Utilized Sites Remedial Action Program, related contaminants on August 2015 ("Cuyahoga Riverbank"). Their analysis identified the following contaminants: isotopic thorium (Th-228, Th-230, Th-232), isotopic radium (Ra-226) and isotopic uranium (U-234, U-235, U-238), ("Cuyahoga Riverbank"). Aside from this, the soil and groundwater of the site also contained volatile organic compounds, semi-volatile organic compounds, and metals are also present that are above acceptable levels ("Hazardous Waste"). BASF SE Corporation now owns 25 acres of this site when they have purchased it in 2006 ("Hazardous Waste"). 11 acres of the site, on the other hand, is owned by Chevron ("Harshaw Chemical Co."). BASF was issued an administrative order by the EPA to have a corrective action on their site and currently, the cleanup status is under investigative phase ("Hazardous Waste"). Chevron, on the other hand, is also working to clean up the site together with the US Army Corps of Engineers and other regulatory agencies ("Harshaw Chemical Co.").

Our past, present, and future are connected. Whatever happens in the past may have an effect in our present which in turn would also affect our future. This is what happened in the Harvard Avenue. The past activities have greatly affected our present due to the contamination it had cost. It would greatly

affect our future if this contamination problem is not resolved or efforts to clean up will not be successful at our present time. Deducting the 76 years, it would affect us for 703, 799, 924 years to be exact. This paper recommends delving further into the effects of each contaminant identified to the environment and health of people exposed to them.

Works Cited

1. "Cuyahoga Riverbank Inspection and Soil Sampling Harshaw Chemical Company FUSRAP Site." 24 August 2015. *US Army Corps of Engineers- Buffalo District.* www.lrb.usace.army.mil/Portals/45/docs/FUSRAP/Harshaw/harshaw-riverbanksampling-2016-04.pdf
2. "Harshaw Chemical Co., Waste Lands, America's Forgotten Nuclear Legacy." *The Wall Street Journal*, Dow Jones & Company, Inc. 2013, projects.wsj.com/waste-lands/site/193-harshaw-chemical-co/
3. "Hazardous Waste Cleanup – BASF Corporation-Cleveland Ohio." *United States Environmental Protection Agency,* EPA.gov. www.epa.gov/hwcorrectiveactionsites/hazardous-waste-cleanup-basf-corporation-cleveland-ohio
4. "Uranium-235." *Chemistry Learner*. www.chemistrylearner.com/uranium-235.html
5. "Sandy Soil." *Researchgate*. https://www.researchgate.net/figure/Percentage-of-Uranium-forms-in-the-sandy-soil-as-affected-by-200-mg-kg-treatment_fig2_258567612
6. "Soil Types." *Boughton*. https://www.boughton.co.uk/products/topsoils/soil-types/

Food's Next Great Frontier

Student Researcher: Shantelle M. Binfet

Advisor: Dr. Romena Holbert

Wright State University
College of Education and Human Services

Abstract
This multi-day unit called, "Food's Next Great Frontier," explores principles of space food and nutrition and includes NASA materials. Students will learn the differences between eating food on Earth and in space through a blind taste test of food on Earth versus food taken to space. Students will be prompted as to why they think the space food looked different than the food they eat on Earth. Students will also watch NASA videos of astronauts eating food in space and learn why it must be freeze dried or dehydrated due to storage space and lack of gravity. Then, they will participate in an activity where the students will create their own "space pudding" to help students visualize the rehydration process that space food goes through. The unit will be wrapped up by having students draw a picture of the kind of food they would want NASA to make for them if they were going on a space mission and explain why.

Lesson
Throughout this lesson segment, the driving question will be: What are the differences between eating on Earth and in space? The first lesson would begin by giving each student a "menu" with the food items only listed by number and table so that students can explore the different samples of food on their own and decide which ones they like best. Each table will have one food found on Earth and that same food with how it would appear in space. As a class, we will then total up the different foods students enjoyed from each table to see which ones our class likes the most and create a graph. This will lead into a discussion where students share their thoughts and observations of the different foods they tasted and the importance of food for living things. It will be revealed that the food they may have found to be "different" at each table was food that astronauts eat in space! Students will be asked why they think the space food looked different from the food found on Earth and what other foods they think astronauts eat in space. Students will be informed that NASA tries exceptionally hard to prepare foods for astronauts that they would eat in their homes on Earth as well as eat a balanced diet. However, storage and the environment in space can sometimes alter how astronauts eat.

The next lesson in the series focuses on what gravity is and the effect it has on food on Earth as well as when it is lessened in space. Students will talk about what they had for dinner the night before and if it was difficult to eat. They will also think about one of the biggest problems astronauts may have while eating in space: lack of gravity. They will then watch videos that NASA posted on astronauts eating in space to give them a visual representation. We will then explore the process food must go through before it can leave for space. Students will create their own "space" pudding to give them a hands-on experience of how food is re-hydrated once an astronaut wants to eat it in space. They will "rehydrate" instant pudding mix in a Ziploc bag. Lastly, students will draw a picture of what kind of food they would want NASA to make for them if they were going on a space mission and write why in a journal entry.

Objectives
- Students will understand the basic needs of living things.
- Students will be able to explain the differences between eating on Earth and in space.

Alignment
Grade One Life Science: Focuses on the physical needs of living things.

Underlying Theory
This lesson uses Gardner's Multiple Intelligences theory as its underlying approach to learning. Students are given various opportunities for visual, bodily kinesthetic, spatial, auditory, and linguistic learning. It is important that a lesson appeals to as many intelligences as possible, as well as incorporates multimodal learning so that students are given an equal opportunity to learn content. Students learn in a multitude of ways, so it makes the most sense to have lessons that fit their needs best.

Student Engagement
This introductory activity is a very hands-on approach and encourages student exploration of the content. Students are actively involved in discussions throughout the learning segments. Students will also be making personal connections with how and what astronauts eat in space to the food they eat on a daily basis.

Resources
In the first learning experience, students will be provided with a blank "menu" for their blind taste test where they will check off which sampled foods they enjoyed the most. Foods such as astronaut ice cream, ice cream, freeze-dried strawberries, fresh strawberries, etc., will be provided for students to taste. Throughout the second learning experience, videos of NASA astronauts eating in space will be shown to the students and how their food is made as a visual representation. Students will then be provided with a Ziploc bag, instant pudding mix, milk, and a straw to make their "space pudding." Lastly, students will be provided a paper and drawing materials to create a picture of what kind of food they would want NASA to make them if they were traveling to space as an astronaut.

Results
Anticipated results of this lesson would be that students would be highly engaged in this hands-on experience. Students would be most interested in opportunities to participate in activities throughout that they can express their creativity and actively explore the content, such as in the blind taste test in the first learning experience.

Assessment
Students will be assessed informally and formally throughout this lesson segment. The teacher will informally assess students' understanding of the content during class and individual discussions as well as throughout the various activities. Students will also be informally assessed on their responses to the driving question throughout the learning experiences: What are the differences between eating on Earth and in space? As a wrap up to the learning segment, students will be formally assessed on their picture and journal entry response to: What kind of food they would want NASA to make for them if they were going on a space mission and why?

Conclusion
Overall, this lesson allows students to explore and learn about what astronauts' nutrition is like in space. I anticipate that students would really enjoy this hands-on approach to learning and exploring content. Students would also be able to personally connect astronaut nutrition to their own lives through comparisons, making it relevant to their everyday lives.

Internet Censorship and Freedom of Speech

Student Researcher: Debin B. Brady

Advisor: Kathleen Tamerlano

Cuyahoga Community College
Information Technology Programming and Development

Abstract
In 1776 the United States Constitution was first drafted. Within the First Amendment it is written that: "Congress shall make no law prohibiting the free exercise thereof; or abridging the freedom of speech". Over the past semi centennial there have been countless disputes regarding freedom of speech. In more recent times Freedom of Speech disputes have been targeted towards Internet Censorship. This has created much controversy, many believe that censoring the internet violates our freedom of speech. Should the government be allowed to decide what content is blocked on the internet from its citizens? According to the American Library Association, censorship is the suppression of ideas and information that certain persons find objectionable or dangerous. However, if the First Amendment says that we have the right to choose, here is where the controversy lies.

Freedom of speech is not absolute. There are already laws in place that forbid certain types of speech such as: fraudulent advertisements, child pornography, and job ads that discriminate on the basis of race just to name a few. Most would agree that the three subjects mentioned above are offensive and should be censored. Can internet censorship really be considered a violation of our freedom of speech when it protects a person from being a victim of fraud, protects a child from unwillingly being victimized by an adult, or prevents any human from having to experience prejudice just because the color of their skin is different?

Project Objective
My objective is to research if our freedom of speech is violated by internet censorship, by focusing on the various benefits and disadvantages that will stem from implementing additional Internet Censorship laws within the United States.

Methodology Used
I used various internet resources to research this topic. These resources included research articles, non-profit organization and government websites, and blogs. I obtained more detailed information on the First Amendment and its meaning, the types of information the government wants to censor, and statistical data that represents Americans thoughts on internet censorship. Graphs were used to assess the most popular types of subjects that are censored on the internet.

Another important piece of internet censorship is knowing the methods used to censor internet content. Internet censoring comes in many facets. Some individuals use self-censorship. This is due to moral, religious, or business beliefs and/or standards. Many countries have implemented internet censorship with various degrees. There are numerous methods used to obtain the result of blocking internet content. A few of the methods used are: Internet Protocol (IP) address blocking – websites are blocked, not allowing users to view, URL filtering – searches for keywords in the URL string, and Network Disconnection – turning off machines by removing cables or cutting off all routers. There are also non-technical censorship methods that are used. A few examples of these are: Letters sent to publishers/authors to block access to specific site content, Bribes – sent to publishers/authors to

withdraw certain material, and Confiscation – equipment can be taken or destroyed for displaying unlawful content.

Results Obtained

Results from the information gathered will show whether or not people feel their freedom of speech is being violated by the creation of Internet Censorship laws. On the other hand, the results can also enlighten people, showing them that having some internet censorship laws in place can serve as a protection. These results also have future potential of being used to petition against some of the internet censorship laws, if many agree that the laws are in violation of the First Amendment – freedom of speech.

References

1. Intellectual Freedom and Censorship Q & A:

http://www.ala.org/advocacy/intfreedom/censorship/faq#ifpoint3

2. Internet Censorship and Freedom of Speech, Leatherman (1999, December 19):

http://www.szasz.com/undergraduate/leathermanpaper.html

3. Internet Censorship

http://wikipedia.org/wiki/Internet_censorship.org

Investigating the Role of Pseudomonas quinolone molecule in Pseudomonas aeruginosa Associated Bacterial Keratitis

Student Researcher: Tayla R. Brooks

Advisor: Michael E. Kovach

Baldwin Wallace University
Department of Biology and Geology

Abstract
Nearly 30 million individuals in the U.S wear contact lenses. Of those people, 40-90% of them do not properly clean their contact lenses, which can cause bacterial keratitis, a serious eye infection caused by *Pseudomonas aeruginosa*. The mechanism by which the bacterium *Pseudomonas aeruginosa* is able to successfully colonize the eye has not been extensively studied; therefore, current medical treatments are limited. The purpose of this study is to find out how Quorum Sensing plays a role in the colonization of *Pseudomonas aeruginosa* in Bacteria Keratitis. This will allow for the development of better treatment option for individuals with bacterial keratitis. Thin layer chromatography analysis, fluorometer assay, time interval culture assay was performed. These assays allow for verification that the *PqsC* mutant lacks the ability to make the pseudomonas quinolone signal (PQS) system, and allow us to see what stage of growth the organism is at during a certain period of time. Each of the assays confirm that the PQS mutant was still producing the Pseudomonas quinolone signaling molecule. It was also determined that the clinical strain produces the most amount of PQS, and the parent strain produces no PQS. Lastly it was found that strains were growing at different rates and present in different phases of growth.

Introduction
Nearly 30 million individuals in the U.S wear contact lenses. Of those people, 40-90% of contact wearers do not properly clean contact lenses, which can cause bacterial keratitis a serious eye infection caused by *Pseudomonas aeruginosa*. *P. aeruginosa* is a Gram negative opportunistic pathogen, meaning it takes advantage of an opportunity that is not normally available such as an individual that is immunocompromised. This organism's ability to colonize the eye is not well understood, specifically its pathogenicity. The process of bacterial keratitis depends on interaction between the bacterium and its host as well as the virulence factors produced by the microbe. The mechanism by which this bacterium is able to be successful in reference to colonization has not been extensively studied; therefore, the current medical treatments are limited. These treatments consist of multiple antibiotics that are used simultaneously with frequent dosing and which must be introduced rapidly following the onset of symptoms in order to minimize corneal damage. [1]. Such treatments are not always successful, and with the increase in contact lens wearers as well as the increase in bacteria that are able to cause bacterial Keratitis, these bacterial mechanisms must be studied in order to be able to treat patients. [2,3]

In a study by Sewell et.al, the proteomic profiles of a clinical isolate of *Pseudomonas aeruginosa (P. aeruginosa)* obtained from an infected cornea of a contact lens wearer and the laboratory *strain P. aeruginosa* ATCC 10145 were compared [6]. This study found that there was a significant variation in the level of Pseudomonas specific proteins. Some of the proteins detected at higher levels in the clinical strain of *P. aeruginosa* were proteins known to be virulence factors [6]. These results confirm that the keratitis-associated P. aeruginosa strain is pathogenic and expresses a higher number of virulence

factors compared to the laboratory strain ATCC 10145. The identification of these protein will allow for the development of new strategies to combat *P. aeruginosa*. Among those proteins found, members of the quinolone signaling (PQS) system PqsB, C, and D were also detected in the clinical strain but not in the ATCC 10145 strain [6].Under stressful conditions, the quinolone signaling system appears to play a role in Quorum sensing [4]. Quorum sensing is a system of stimuli and response correlated to population density. Quorum sensing (QS) enables bacteria to restrict the expression of specific genes to the high cell densities at which the resulting phenotypes will be most beneficial. This system controls the rhl quorum-sensing system [5] that controls the cell density. The latter controls the secretion of several virulence factors, suggesting that the PQS system could be regulating the secretion of virulence factors in keratitis. In this paper we investigate the role quorum sensing in the colonization method of *Pseudomonas aeruginosa* through running a series of assay. Which could potentially allow for better treatment options.

Methodology

Strain Information

Wild-type strain of MPA01 and its transposon mutant PA0998-1 (*PQSc* mutant) was obtain from Dr. Rachida Bouhenni at Summa Health Akron, Ohio. A clinical strain from a patients cornea effected with bacterial keratitis was also obtain from Summa Health Akron, Ohio. All strains were grown at 37˚C on a roller drum.

Thin Layer Chromatography

Overnight cultures were grown at different time points (24,48,72 hours) and PQS was extracted using acidified ethyl acetate. The extracts from each strain were spotted onto a TLC plate. The solvent consisted of a 95:5 ration of dichloromethane and methanol. The solvent was allowed to run for 5 minutes or until the solvent front ran 75% up the plate. The results were visualized using UV light and photographed.

Cell Growth Assay

Cultures grown at different time points in minimal media with Iron. 1 ml of the culture was ran through a spectrophotometer to measure cell density of each strain.

Fluorometer Assay

Cultures were grown in minimal media for 24, 48, and 72 hours. PQS was extracted from strains using acidified ethyl acetate. The Organic phase was stored at -20˚ C until it could be analyzed using fluorography. The relative concentrations of PQS present in the extracts was determined using a fluorometer at 340 nm excitation and by comparing the emissions at 450 nanometers.

Results

PQS production seen in pqsC mutant strain

In order to study the role of PQS is colonization a mutant containing the inability to produce the molecule was obtain. This mutant was a transposon insert so further verification analysis was conducted. In this study the mutant showed to still produce PQS as seen in figure 1. And figure 3. This production of PQS seen raised further question and further analysis of the strain. When analyzing the fluorometer reading it was that PQS production was visible at a small amount during the 48 hour mark (figure 3). It was also hypothesized that the fluorescent band that was seen in figure 1 could potentially be a precursor molecule being shown. Both figures suggest that PQS production could potentially be present.

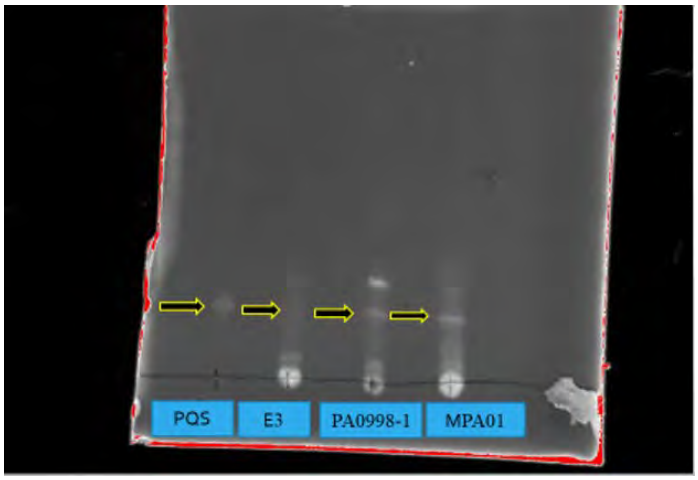

Figure 1. Extract of *Pseudomonas* strains spotted onto TLC plate. Lab synthesized PQS was used as reference to see if PQS molecule was present in the other samples. All strains produced PQS molecule.

Cultures grown in 1xmme with Iron grow at different rates

It was noticed that cultures appeared to have a significant difference n turbidity suggesting that the strain were growing at different rates during incubation periods. This becomes problematic when trying to eliminate other variables from changing the results. After doing experimentation and testing cultures using the spectrophotometer, it was found that culture have difference in turbidity, suggesting that each culture is at a different growth cycle.

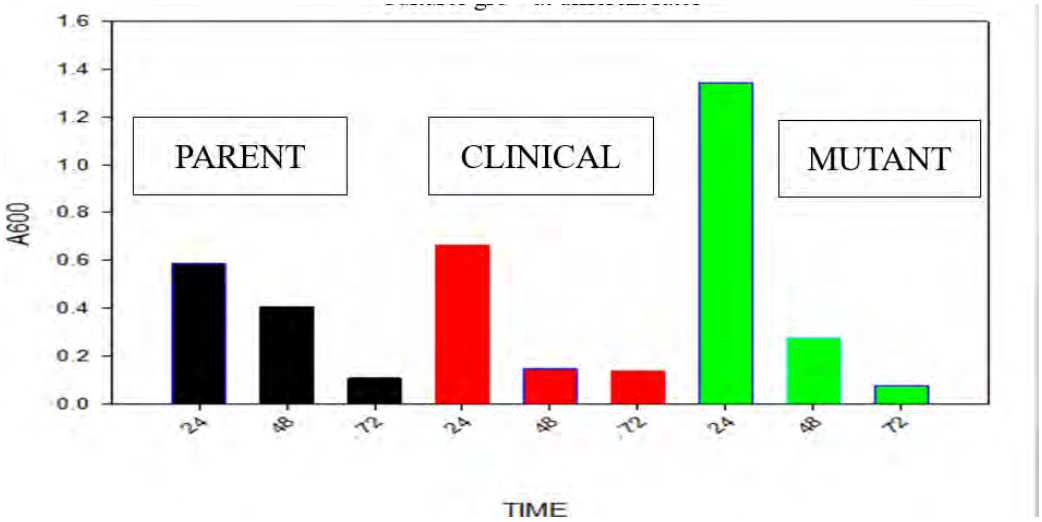

Figure 2. *Pseudomonas* strain were grown in 1x MME w/ iron at 37° C for specific time points (24,48, and 72 hrs). The absorbance at 600 was determined for each culture to determine the amount of cell growth. Results showed that there is a reduction in cell number over time.

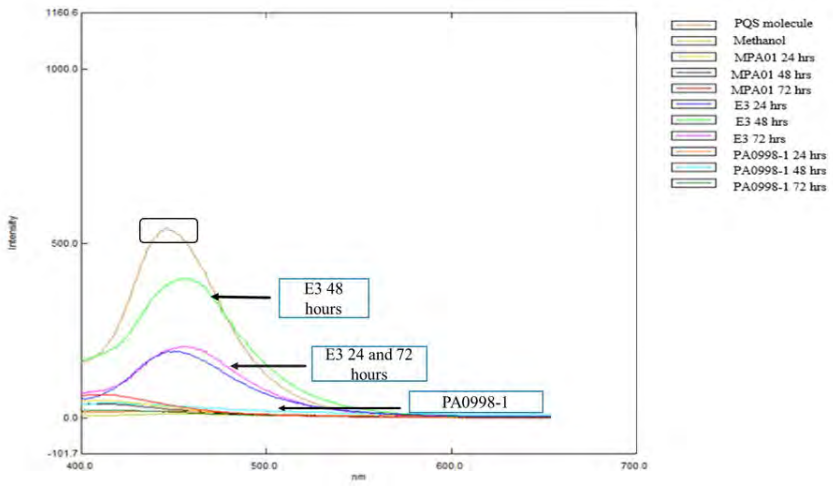

Figure 3. Extractions visualized using fluorometer producing PQS. *Pseudomonas* strains were grown in 1x MME w/iron for 24,48, and 72 hrs. PQS extraction was done on each culture and extracts were stored at -20˚ C for future analysis. PQS fluoresces at 450 nm when excited at 340 nm Extracts from each strain were analyzed using a fluorometer to determine the relative concentration of PQS present in each strain of *Pseudomonas*. Results showed *pqsC* mutant strain produced PQS at 48 hour mark. Suggestion that the PQS system is not blocked in the mutant strain.

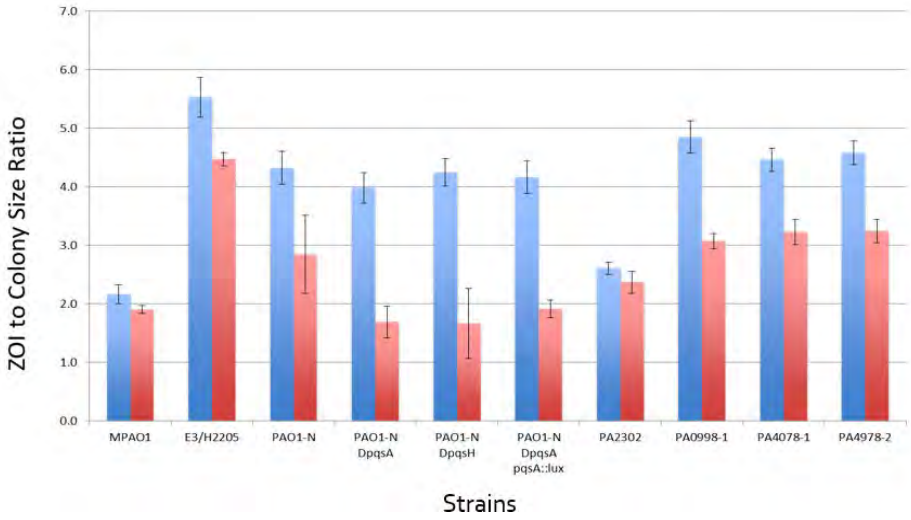

Figure 4. Pseudomonas strains were grown in 1X MME w/ succinate + Fe O/N at 37C. One microliter of this culture was spotted on to a 1X MME w/ succinate + Fe agar plate and incubated O/N at 37C. Plates were UV inactivated in five different sets for 20 minutes each. Results read at 22.5 hours of incubation with top agarose layer. N= 5 for each strain per each condition. Methionine and glucose added to agar overlay. Blue bars = without methionine, Red bars = with methionine.

Conclusion

TLC analysis confirmed the production of PQS by all of the *Pseudomonas* strains tested. The *pqsC* mutant should lack the ability to produce PQS. If the mutant still produces PQS further analysis on the role of PQS in colonization will be complicated. To determine the role being played, a mutant without the PQS must be produced. It was also seen in the analysis of the fluorometer reading that PQS is being produce at a low amount. These finding are inconsistent with other research done using the *pqsC* mutant.

The A600 data suggest that each strain is growing at different rates. These different growth rates could potentially have an effect on the results, since PQS is thought to be a molecule involved in quorum sensing a cell density dependent signaling system.

Based on the data received we can conclude that PQS is being produced by the PQS mutant. Limiting experimentation to determine its role in bacterial keratitis. Further analysis of the mutant's strains needs to be conducted.

Further research should consist of doing a biosensor assay and eventually creating a line of mutant strains in the clinical strain that was able to cause the infection. Mutants in this strain will further help with the evaluation of the PQS molecule, and potentially help with the enhancement of new treatment options for the infection.

Flexible Wearable Transmissive Pulse Oximeter Sensor

Student Researcher: John Bukovac

Advisor: Johnny Vanderford

Lorain County Community College
Microelectomechanical Systems

Abstract

Pulse oximetry is a non-invasive, continuous measurement of blood oxygenation, using light and photocells to measure the oxygen percentage and pulse rate of patients. This saves lives by speeding up the process of measuring blood gas in patients, which in-turn lowers the death rate from hypoxemia significantly. This is especially the case for infants who are at a higher risk of hypoxemia, in particular immediately after birth. There are many methods of which to apply pulse oximetry to a biomedical device, one of the most popular being flexible electronic technology otherwise known as wearable devices. Flexible electronics is the use of pliable plastic substrates to build circuits using materials such as polyimide, PEEK, or Mylar plastic on which electronic components are attached to complete the designed circuit. The use of printable inks, thick film pastes, MEMS devices, and flexible substrates will be used to manufacture miniaturized flexible circuits. The process of design, assembly, and testing of the flexible pulse oximeter will be described in detail in this report.

Project Objective

The Purpose of this project was to develop and fabricate a low cost flexible pulse oximeter that can be used as a wearable device to monitor the pulse rate and oxygen levels of premature and newborn babies to help prevent hypoxemia as well as detail the processes, materials, and equipment used to manufacture this device.

Circuit Description

This circuit uses a photo-transducer to quantify the percentage of light of a specific wavelength (Red and InfraRed (IR)) that is being blocked by red blood cells. An LED emits light with this wavelength (680 nm for Red and 940 nm for IR) which oxygenated blood cells block/absorb. When a finger or any other part of the body is placed over the LED, the light from the LED is partially blocked by the blood that is flowing through the skin. The remaining light from the LED is absorbed by the photo-transducer and the sensor signal fluctuates as the blood is pumped from the heart, simulating the pulse. The sensor also can determine the percentage of oxygen in the blood of the patient by determining how much of the light is being blocked by the blood in the skin. A Texas Instruments LM358 Operational Amplifier (OpAmp) was used in conjunction with both passive capacitors and resistors to both filter out electronic noise (such as frequencies above 50 Hz) as well as amplify the relatively small-amplitude signal being output from the photonic sensor. This circuit was built using surface mount technology in order to reduce the size and overall form-factor of the circuit.

Fabrication Process

The fabrication process was performed using a screen printer and a screen in the Lorain County Community College Center for Microelectronic Sensor Fabrication and Hybrid Board Assembly, a 2000 sqft class 10,000 cleanroom with average temperature of 19 °C and 20% RH%. After layout was drawn

on EasyEDS, a Printed Circuit Board (PCB) layout program, a photoplot of the artwork was created and used to make a screen using UV light photolithographic processing. The screen provided by Utz used 325 mesh stainless steel with 1.1 mil thick mesh weaving and 20 mil thick emulsion. Once the screen was made it was loaded onto an AMI Presco 435 screen printer for transferring the artwork of the layout to a 7 mil thick Mylar substrate using electrically conductive paste. The screen printing processes are similar to hybrid thick film processing with a squeegee speed of 5 mm/second, a snapoff height of 30 mils, and a squeegee pressure of 3. The conductive paste used to create this layout artwork is Ferro Corp (formally Electro Science Laboratories (ESL)) 1901-S silver conductive polymer paste. The polymer within the paste creates a more elastic conductive trace and improves the amount of overall flexibility a flexible circuit has. The substrate was then placed into a convection curing oven and cured at 125 °C for 10 minutes before being transferred to a second convection curing oven and cured at 150 °C for 15 minutes. The curing schedule is critical to the overall flexibility of the substrate and the adhesive properties of the paste to the substrate. Next the printed and cured artwork was prepared for the application of the individual surface mount electronic parts of the circuit by applying the 1901-S conductive paste using a Westbond 7200 CR-79 semi-automatic pick and place system. This equipment utilizes both epoxy dispensing and a vacuum pick up tip for picking up individual components and placing them on the pads with dispensed epoxy. The substrate was then placed into the curing oven for the same curing schedule provided above to adhere the SMT parts to the substrate. The circuit was tested at three volts with the application of the patients' finger to the photonic sensor and LED.

Results

A flexible circuit was successfully designed, fabricated, and at a total material cost of $3.50 per Mylar substrate at low volume unit pricing. Testing of the circuit functionality depends greatly on the pressure at which the patent applies to the circuit in addition to the amount of current passing through the LED for emitting light. Further research indicates that skin complexion also causes additional variance although early testing of this had mixed results. Processability of polymer based conductive adhesives has advantages and disadvantages when compared to traditional rigid PCB processing. The primary advantages are both the ability to form a custom built flexible substrate in comparison to traditional FR4 fiberglass and the minimum resolution of printing, with 50 micron features possible. The disadvantage is the limited processing time between cycles of printing. The polymer catalyst mixed into the paste cures at room temperature and requires rapid printing cycles to keep the printed polymer paste from curing in the open screen mesh. Compare this to traditional hybrid thick film screen printing in which glass frit filled cermet pastes have work-life greater than several hours before noticeable changes occur. Cleanup of the polymer paste also requires additional materials beyond solvents for specifically breaking up the polymer crosslinks in the paste. These disadvantages are outweighed by the concept that this process could be made into a flexible PCB capable of being manufactured at high-volume capacities.

Acknowledgements

The author formally acknowledges NASA for the community college grant award.

The author also acknowledges Prof. Johnny Vanderford and Jared Dumont for advice in design and manufacturing of this project.

Human Limitations on Gravitational Assists: A Study of the Impacts of Human Involvement on Space Travel

Student Researcher: Katie S. Cooperrider

Advisor: Dr. Jed E. Marquart, P. E.

Ohio Northern University
College of Engineering

Abstract

Through the course of this paper, the impacts of the physical limitations of humans on space travel will be explored. Observing the physics of gravitational assists and the gravitational forces associated with them, the researcher will quantitatively define these impacts. The study performed is entirely mathematical, with no physical models being made. The research will be comprised of gravitational assists around the moon, Earth and Mars. Using previously defined equations for the physics associated in this study, the researcher will determine how quickly an unmanned space craft could reach a determined destination without the limitations of human passengers. Following this calculation for each of the three planetary bodies, comparisons will be made between these values and the furthest traveled distance of a manned spacecraft. From here, conclusions will be drawn as to how severely, if at all, human presence is hindering overall space travel.

Nomenclature

μ = Gravitational Parameter
M = Mass of Planet
G = Gravitational Constant
a = Semi-major axis of an orbit
AU = Astronomical Unit of length
$dist_O$ = Planet's average distance to Sun
V_{craft} = Velocity of the Spacecraft
r = Spacecraft's distance from a planet's center
V_∞ = Hyperbolic Excess Velocity
V_{esc} = Velocity required to escape a planetary body's orbit
δ = Turning angle
e = Eccentricity of orbit
β = Flight path angle
$r_{P/O}$ = Radius at Perigee relative to planetary body (e.g. Planet O)
$V_{initial_O}$ = Velocity of spacecraft at beginning of gravitational assist
$V_{exit_{O/S}}$ = Spacecraft exit velocity from orbit of planetary body relative to the Sun
$V_{O/S}$ = Velocity of planetary body relative to the Sun
$r_{P,O}$ = Radius at perigee of a respective planetary body
$V_{craft,P}$ = Velocity of spacecraft at perigee
$F_{grav,normal_O}$ = Force of gravity normally experienced on a body due to gravity of the planet
$mass_{craft}$ = Mass of the spacecraft, represents manned and unmanned
$grav_O$ = Gravitational force of a planet (i.e. 9.81 m/s^2 = Earth)
a_{craft_O} = Centripetal acceleration of the spacecraft around a planetary body

$F_{grav_{craft,O}}$ = Force of gravity experienced between the spacecraft and the planet
$G_{force,O}$ = Gravitational forces (g-forces) experienced by spacecraft
/S = Relative to the Sun
/M = Relative to the Moon
/E = Relative to Earth
/MA = Relative to Mars

Introduction

Prior to the discovery of gravitational assists for spacecraft propulsion, much space travel was governed by the principle of Newton's Third Law of Motion. Following this principle, scientists and engineers of the time, primarily the 1930s, found through their research that space travel was severely limited. Though fuel could be used to propel the spacecraft further into space, the amount necessary proved nearly impossible to integrate into the technology at the time. Holding massive amounts of fuel would significantly increase the weight of the craft, thus creating a paradox between weight and fuel. Moving further into the 20th century, more time, energy and money was put into solving this seemingly unsolvable problem. Decades carried on, with the possibility of further space exploration appearing to be an impossibility. It was not until 1961 when Dr. Michael Minovitch discovered gravity propelled space travel that the vast unknown came into the grasp of our world [1].

Gravitational assists are complicated mathematical problems that can be difficult to grasp even if you are in the mindset of a physicist. The entire system consists of a conservation of energy, so it can be a challenge to understand how speed can be gained but not lost upon departure from the planet. Therefore, it is important to view the system from a different point of reference than solely the spacecraft and the planetary body being orbited. Though it is crucial to perform the calculations between these two bodies, it is equally as important to look at the system from the point of view of a third celestial body, in this case the sun. The velocities of interest in this experiment only have value because their speed is being calculated relative to the sun, otherwise there would be no change in velocity from beginning to end of the assist. This is because in the view of the planet and craft, the craft does speed up but it will slow down by the same amount when exiting the planetary orbit. When looking from the perspective of the Sun, the spacecraft and the planetary body are both changing directions in their orbits, creating a difference between the incoming and outgoing velocities of the craft that was not present in the more zoomed-in view of the system. Though this does not entirely explain the complexities of the orbital mechanic of gravitational assists, it does make this method valuable to space travel [2].

An excellent example of the use of gravitational assists is found when looking at the journey of the Voyager 2 as it made its way through the outer planets all the way to Neptune. This spacecraft was able to perform gravitational assists after launching from Earth in August 1977 to reach Neptune only 12 years later. From Earth, its path included assists from Jupiter, Saturn and Uranus, which was only made possible due to a planetary alignment that occurs every 175 years [2]. This great distance traveled and fast speed of travel would not have been possible without the discovery of gravitational assists. The spacecraft would not have been able to carry enough fuel to make it to these outer planets without severely impacting the weight of the craft and making more fuel necessary for travel. Gravitational assists made this and other major space expeditions, such as Voyager 1, possible, which has greatly increased the knowledge we have about the universe and how much of it we have been able to explore.

Problem Description

As was stated previously, the main objective of the presented research was to determine how gravitational force limits of humans can impede upon space travel, if at all, in terms of gravitational assists. Human beings can only withstand high gravitational forces for a few seconds, i.e. 3-4 g's for brief sections of a rollercoaster, without blacking out or dying. Even pilots who are trained to withstand higher gravitational forces and wear special suits inflight can only experience 9 g's for less than a second without devastating results [3]. Since there is an increase in gravitational force as a spacecraft slingshots around a celestial body, the researcher wanted to investigate these forces and correlate them to the acceleration and speed of the craft. Knowing that the acceleration would have to be minimal enough to prevent gravitational damages to the passengers' bodies, it was assumed that the rate and distance of travel would be hindered accordingly.

Since humans were determined to be the limiting factor in this research, the researcher chose to calculate how quickly a manned spacecraft could reach a predetermined location, in this case Neptune, under these limited conditions. The same calculations would then be performed using an unmanned spacecraft free of human limitations. These calculations will be expanded upon in the 'Mathematical Modeling' section of this paper. Once these computations were performed for gravitational assists around the moon, Earth, and Mars, the researcher would then determine how much space travel was being hindered in terms of spacecraft speed. This hindrance would come from the minimization of acceleration during the gravitational assists in order to prevent bodily damage. In order to define these human impacts quantitatively, the researcher had to expand the problem definition to encompass all of the intricacies of space travel. This included establishing which assumptions needed to be made for the mathematical model, as well as addressing the experimental system's necessity of a hyperbolic orbit. In order for a spacecraft to be able to perform a gravitational assist, it must enter a hyperbolic orbit around the chosen body that is also moving relative to the craft's destination. Discovered equations for this type of orbit that were used in previous studies were employed in this research. Having determined all components of the problem being presented, the researcher was able to begin creating the mathematical model for the experiment.

Mathematical Modeling

To begin the calculations, the researcher first had to make several assumptions to simplify the mathematics to the point of solvability:

- The spacecraft will maintain a constant velocity from the end of the gravitational assist to the destination planet Neptune.
- The fastest velocity in the system is determined to occur either at the perigee or at the exit of the hyperbolic orbit. For this reason, only these two areas will be investigated in the mathematical experiment.
- The sun is at the center of the system and acts as a tertiary body that the entire system moves relative to.
- The mass of the spacecraft is taken to be 9000 pounds [16] when unmanned, which is based on the unmanned Mars Rover.
- The mass of the spacecraft when manned with a full crew is assumed to be 10000 pounds. This accounts for four astronauts at the maximum allowable weight limits, 180 pounds [17], along with the weight of extra gear required for their survival. The amount of astronauts was based off of the group size for sending astronauts to Mars through the Mars One program [18].

In order to begin calculations, several variables needed to be identified and solved for in each of the three cases: assists around the moon, the Earth and Mars. For simplification, the planets will be represented by a stand-in, Planet O. The first step in the process was to solve for the gravitational parameter, μ_O, for the planet [4] (see Equation 1).

$$\mu_O = G * M_O \tag{1}$$

Here, the gravitational constant, G, has a value of $6.673*10^{-11}$ Nm^2/kg^2. The value of the mass of each planet, M_O, varies and is in the units of kilograms. Also needed was the value of the semi-major axis of each planet's orbit. This was found using the standard astronomical unit, AU, which has a value of 149,597,870.7 kilometers [6], as well as the planet's average distance from the sun.

$$a_O = AU * dist_o \tag{2}$$

Having these two values for each case, it was then possible to develop the equation to find the velocity of the spacecraft at any point in the hyperbolic orbit of the gravitational assist. This equation was developed below using the Vis-Viva Equation [7]:

$$V_{craft,O} = \sqrt{\frac{2\mu_O}{r_O} - \frac{\mu_O}{a_O}} \tag{3}$$

where the only unknown that needed to be solved for was the variable r_O. This represents the spacecraft's distance from the center of the planet at any specified point in its orbit. For the purpose of this experiment, this value was take to be the distance of the craft from the center of the celestial body when it was exiting the gravitational assist. This specification would allow for the exit velocity to be accurately calculated. From this speed, the hyperbolic excess velocity, V_∞, can be solved for (see Equation 4) [8].

$$V_{\infty_O} = \sqrt{V_{craft,O}^2 - V_{esc,O}^2} = V_{\infty_O}^- = V_{\infty_O}^+ \tag{4}$$

In this equation, the escape velocity $V_{esc,O}$ was a given value [5] for each planetary body. It should be noted that the calculated velocity will be equivalent to the incoming, $V_{\infty_O}^-$, and outgoing, $V_{\infty_O}^+$, hyperbolic excess velocities, as the spacecraft's energy remains constant. Another value that needed to be calculated for the research was the turning angle δ. This value was found using given values of orbital eccentricity, e, for each planetary body (see Equation 5).

$$\delta_O = 2sin^{-1}\left(\frac{1}{e_O}\right) \tag{5}$$

As was stated in the previous section, the spacecraft, whether manned or unmanned, needed to be in a hyperbolic orbit to perform the gravitational assist. Using the representative celestial body Planet O, the following visual is used to highlight the important phases and variables of the craft's path (see Figure 1). This model will be the basis for the orbits around the moon, the Earth and Mars.

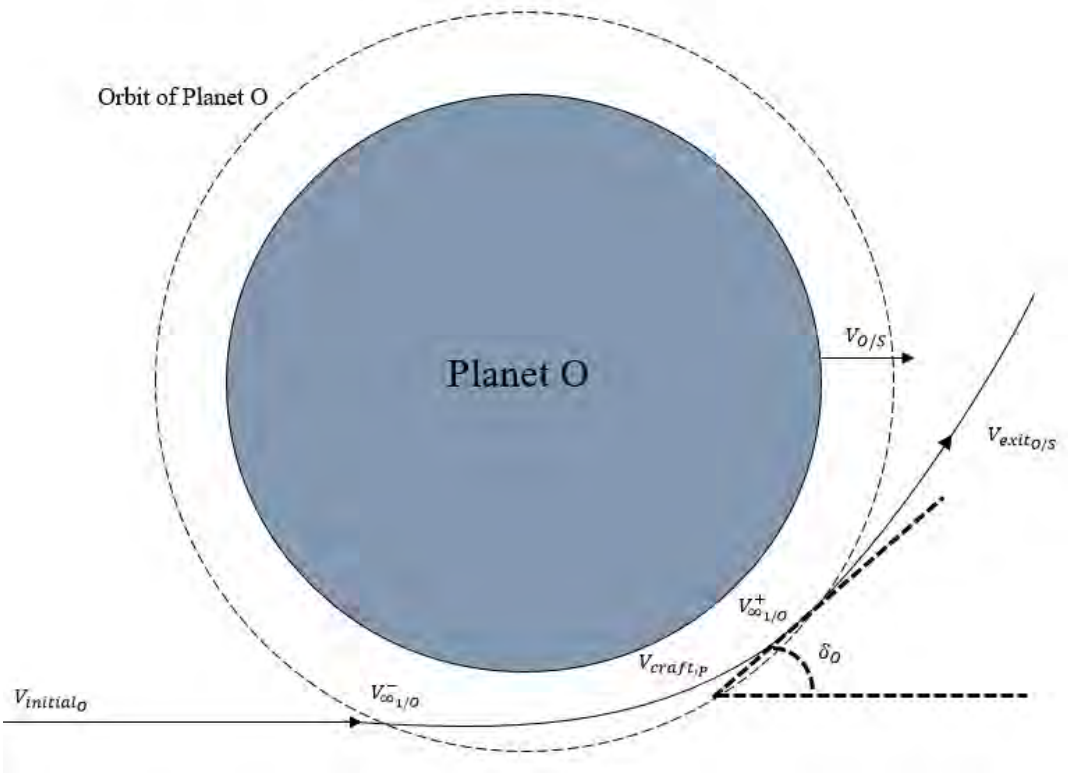

Figure 1. Hyperbolic Orbit of Spacecraft around Planet O

Using this model, several equations were generated that allowed for calculations of the velocities at the end of the gravitational assist and at the point of perigee [7]. Equations 6 and 7 are used to create the basis for the hyperbolic orbit of the assist. These solve for the flight path angle, β, and the exit velocity relative to the Sun, $V_{exit,O/S}$, respectively.

$$\beta_O = tan^{-1}\left[\frac{\sqrt{\frac{\mu_S}{a_O}} + V_{\infty_O}\sin\left(2sin^{-1}\left(\frac{1}{1+\frac{r_{P/O}\,V_{\infty_O}^2}{\mu_O}}\right)\right)}{V_{\infty_O}\cos\left(2sin^{-1}\left(\frac{1}{1+\frac{r_{P/O}V_{\infty_O}^2}{\mu_O}}\right)\right)}\right] \quad \textbf{(6)}$$

$$V_{exit,O/S} = tan^{-1}\left(\frac{V_{O/S} + V^{+}_{\infty_{1/O}} sin\delta_O}{V^{-}_{\infty_{1/O}} cos\delta_O}\right) \quad \textbf{(7)}$$

In Equation 6, the values of the hyperbolic excess velocity, the gravitational parameters of the Sun and Planet O, and the semi-major axis were solved for in the previously presented Equations 1, 2 and 4. The only remaining unknown needed to solve the flight path angle is the value of the radius at perigee relative to the celestial body. For the purposes of this study, this value will be equal to the given radius at perigee used in later calculations [10, 11, 12].

For the exit velocity to become solvable, in incoming and outgoing hyperbolic excess velocities, $V_{\infty_{1/O}}^{-}$ and $V_{\infty_{1/O}}^{+}$ respectively, as well as the planetary body's velocity relative to the sun, $V_{O/S}$, needed to be found. Solving for the latter involved a simple equation [7] using previously calculated values (see Equation 9).

$$V_{O/S} = \sqrt{\frac{\mu_S}{a_O}} \tag{9}$$

The calculation of the incoming and outgoing hyperbolic excess velocities would prove to be slightly more difficult. To begin, a vector representation of the velocities of the system based on Figure 1 was created to highlight the important velocities related to the exit speed (see Figure 2).

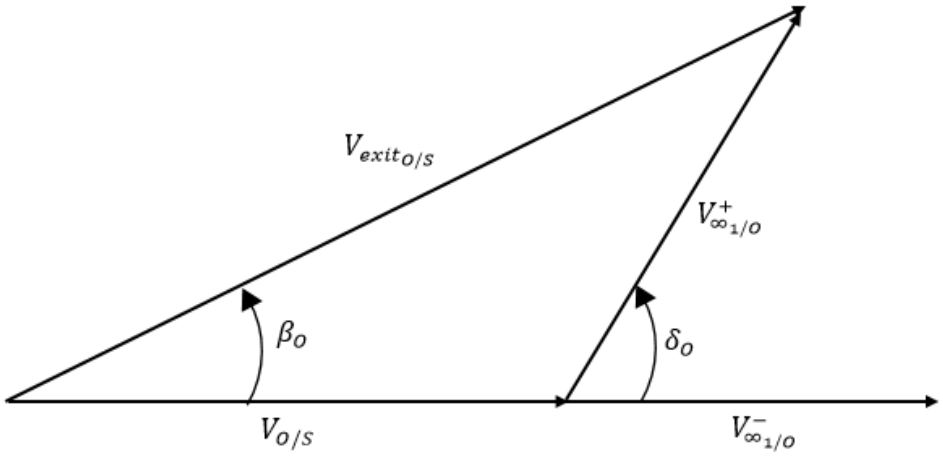

s

Figure 2. Vector Representation of System Velocities

Since the values of the turning angle and flight path angle were calculated in Equations 5 and 6, respectively, this allowed the researcher to use trigonometry to solve for the unknowns. Beginning with the hyperbolic excess velocities, a relation between incoming and outgoing was made using the turning angle (see Equation 10). Rearranging this to solve for outgoing excess velocity yielded Equation 11.

$$cos\delta_O = \frac{V_{\infty_{1/O}}^{-}}{V_{\infty_{1/O}}^{+}} \tag{10}$$

$$V_{\infty_{1/O}}^{+} = \frac{V_{\infty_{1/O}}^{-}}{cos\delta_O} \tag{11}$$

In order to solve for each of these values mathematically, we first need to look at the hyperbolic velocities' relation to the initial velocity of the system. Noted as such in Figure 1, the initial velocity begins the path of the hyperbolic orbit. Equation 12 represents the calculation of this value:

$$V_{initial_O} = V_{O/S} + V_{\infty_{1/O}}^{-} \tag{12}$$

where both the initial velocity and the incoming hyperbolic velocities are unknowns. For the purposes of the research, the initial velocity was chosen to be altered by the researcher to allow for various calculations of the system. As the initial velocity will be a determined number, the incoming hyperbolic

velocity will be able to be solved for. Looking back at Equation 11, it is also now possible to calculate the value of the outgoing hyperbolic velocity, thus solving all unknowns in the equation for exit velocity (Equation 7).

The researcher had now found a solution for one of the two velocities in the system that was being investigated. As was stated in the assumptions, the highest velocity encountered in the gravitational assist was believed to be either at the perigee or at the exit of the planetary body's orbit. From this, the researcher decided to calculate only these two values of velocity and compare them to the initial velocity for acceleratory purposes. Having solved for one of these in the previous steps, the next task was to create a calculation for the velocity at perigee. This proved to be fairly simple, as the equation was found in other studies of similar purpose [7]. This equation is, in fact, a rewrite of Equation 4 presented earlier in this paper. Solving for the velocity of the craft rather than the hyperbolic excess velocity yields this equation (see Equation 13).

$$V_{craft,O} = \sqrt{V_{\infty_O}^2 + V_{esc,O}^2} \tag{13}$$

Although the value of the escape velocity was given for its previous use, in order to solve for velocity at perigee, $V_{craft,P}$, it needed to be calculated. Employing Equation 14 [9], the value of radius of perigee $r_{P.O}$, here a given average value [10, 11, 12], is used for the spacecraft's distance from the celestial body's center. It was also necessary to recalculate the value of the hyperbolic excess velocity, as the previously computed value depended upon the distance of the spacecraft at the exit of the assist. Shown in Equation 15, the excess velocity of the hyperbolic orbit was found using the gravitational parameter and semi-major axis of the planetary body. Substituting these into Equation 13 yields the final form of the calculation of this other desired velocity (see Equation 16).

$$V_{esc,O} = \sqrt{\frac{2\mu_O}{r_{P,O}}} \tag{14}$$

$$V_{\infty_O} = \sqrt{\frac{\mu_O}{a_O}} \tag{15}$$

$$V_{craft,P} = \sqrt{V_{\infty_O}^2 + V_{esc,O}^2} \tag{16}$$

Now that both velocities of interest were solved for, the next step in the research was to find the gravitational forces corresponding to these velocities. In order to do so, the normal gravitational force encountered by the manned or unmanned spacecraft needed to be calculated [13] (see Equation 17).

$$F_{grav,normal_O} = mass_{craft} * grav_O \tag{17}$$

In this equation, the $mass_{craft}$ corresponds to either the mass of the unmanned or the manned spacecraft. The variable $grav_o$ represents to the gravity of each planet, i.e. 9.81 m/s^2 for Earth [5]. Following this, the gravitational force between the planetary body and spacecraft needed to be calculated. The first step in finding this value in to calculate the centripetal acceleration of the craft. Since the velocity calculated at both the perigee and exit of the assist are assumed to be running tangential to the planet, their vector directions are changing as the craft moves around the planetary

body. As a result of this, a centripetal acceleration is experienced. This can be calculated using a ratio of the velocity of the craft and its distance from the center of the celestial body [14] (see Equation 18).

$$a_{craft_O} = \frac{V_{craft,O}^2}{r_O} \quad \textbf{(18)}$$

This equation will be employed both at the point of exit velocity and at perigee for the respective celestial body, with the velocity and distance of the craft being either that at exit velocity or at perigee. In order to calculated the gravitational force experienced on the craft due to acceleration, the principle of force equals mass times acceleration was employed (see Equation 19).

$$F_{grav_{craft,O}} = mass_{craft} * a_{craft_O} \quad \textbf{(19)}$$

From this point, the gravitational force experienced by the craft could be found using a ratio between the two forces [15] (see Equation 20).

$$G_{force,O} = \frac{F_{grav_{craft,O}}}{F_{grav,normal_O}} \quad \textbf{(20)}$$

The coding program Matlab was employed to calculate the values presented in the previous equations and the program Excel was used to interpret these values. The results from each of the three planetary models will be discussed further in the following sections.

Results and Discussion

For the researcher to be able to conclude on the impacts of human presence in spacecrafts, several iterations were run with variations of a few important variables. These included the distance of the spacecraft when it was exiting the gravitational assist and the initial speed of the craft when beginning the assist, which were determined to be the primary influential factors in the experiment. These iterations looked to see at which point the acceleration became too great for human safety to become realistic. In order to create a clear cut-off, this limit was taken to be 4 g's, as the trained astronauts would be conditioned to experience this impact for more time than the average human. For the unmanned spacecraft, the maximum allowable g's forces were taken to be 7 g's, as the materials are not as susceptible to gravitational impacts as the biology of humans, but they can still be impacted by them. The results of these calculations are found in Tables 1, 2 and 3 in the Appendix.

It should be noted that the tables do not include any information regarding the gravitational forces experienced at perigee. This omission was due to the low forces experienced at this point in the hyperbolic orbit. Although initially believed to be an area where the maximum gravitational forces may occur, calculations showed that at this location there was no more than $6.71*10^{-5}$ g's experienced by either the unmanned or manned craft. This low gravitational force is believed to be due to the low values of velocity at this location. For each calculation, the velocity at perigee was found to be between 0.1987 km/s and 0.02455 km/s, which equates to between 715.32 and 88.38 km/hr. Since the values of velocity and gravitational force were so low, the perigee was no longer a point of interest for the experiment. Knowing that the main focus of the experiment shifted to the velocity and g-forces calculated at the exit of the gravitational assist.

Though the initial velocity was believed to be crucial to the calculations when the research began, upon further investigation it was determined that this value had very little impact upon the final results. The researcher input an initial velocity of 10, 20 and 30 km/s for each of the three planetary systems while the distance of the craft from the center of the planet was held constant. For the calculations of the gravitational assist around the moon, the change in the exit velocity varied by no more than 0.00152% among the three initial velocity settings, while the change in the gravitational forces experienced between a 0.00137% and 0.00304% change. Results from the Earth and Mars calculations yielded similar results, with the exit velocity varying by no more than 0.03938% and 0.02782%, respectively, as the initial velocity was increased. The gravitational forces due to these velocities was also minimal, resulting in a 0.07874% change around the Earth and 0.05564% change around Mars. It should be noted that the manned and unmanned spacecraft calculations yield exactly the same values in each of the three planetary cases, and at each initial velocity. As this changes were very small, the initial velocity was concluded to be less of a factor in the calculations than was initially thought.

It was apparent, however, that the distance at which the exit from the gravitational assist took place did have an impact, though slight. Though there was absolutely no change on the exit velocity in any of the planetary cases with any initial velocity, the gravitational forces did see some changes. The distance of the craft from the center of the planet was tested at 95% and 105% of the radius of perigee for the respective celestial body. Each of the cases for both the unmanned and manned crafts experienced a 10.526% increase in gravitational forces experienced by the craft as the distance between the planet and craft was decreased. This was a significant increase in terms of gravitational forces present in the system, and solidified the major impact this distance had on the results of the experiment.

Looking at the Tables 1-3 in the Appendix, the researcher was able to observe the impacts on both exit velocity and gravitational forces for both the manned and unmanned spacecrafts. As was mentioned in previous explanations of distance and initial velocity results, the data for both the manned and unmanned crafts was exactly the same. This meant that there was no impact on these two variables as a result of humans being introduced to the system. It should also be noted that for the systems of the Earth and Mars, there was no higher than 0.002 and 0.005 gravitational forces experienced at any point, respectively, for either the manned or unmanned craft. This meant that there was no possible case for human impact upon space travel due to these forces, as unacceptable values would only be found if the system was pushed to extremes. There was, however, a restriction encountered in the calculations surrounding the gravitational assist around the moon. This limitation came from the gravitational forces experienced by the craft, as those calculated at 95% and 105% of the radius of perigee resulted in g-forces around 7 g's. Though this fell within the allowable range for the spacecraft, it was too large for that of the craft with humans present. Therefore, it was necessary to make alterations to the input variables to allow for safe travel. This was done by adjusting the most impactful variable, the distance of the craft from the celestial body's center. When this value was changed to 162% of the radius at perigee, it brought the g-forces experienced to just below 4 g's. It did not, however, impact the exit velocity in any way, meaning that the presence of humans in the craft has no impact on space travel in terms of speed. As there was no significant impacts on the speed, it was deemed unnecessary to calculate the time to reach Neptune from each of the gravitational assists, as it would only reiterate the results presented.

Conclusions

Though the research did not yield the results desired, there is still much to be learned from the results obtained. The most important lesson to be taken from this is the ability for the spacecraft to reach faster speeds during the gravitational assists without the need for concern for human passengers. It should

also be noted that the distance of the craft from the center of the planetary body plays a crucial part in the gravitational forces experienced during the assist, and should be treated as an important variable in future research endeavors. Alterations may be made to the experiment to yield more drastic results, such as increasing the initial velocity to unreasonable speeds to see the trend of change in velocities and gravitational forces.

Appendices

[1] Result Table – Moon Gravitational Assist

	Moon			
	Initial Velocity (km/s)	**Distance from center (km)**	**Exit Velocity (km/s)**	**G-Force at Exit Velocity**
Unmanned Craft	10	345135 (95% of r_p)	61.575899882	6.78137119405925
	10	381465 (105% of r_p)	61.575899882	6.13552631843456
	20	345135 (95% of r_p)	61.575431157	6.78126795295066
	20	381465 (105% of r_p)	61.575431157	6.1354329098125
	30	345135 (95% of r_p)	61.574962403	6.78116470599258
	30	381465 (105% of r_p)	61.574962403	6.13533949589804
Manned Craft	10	345135 (95% of r_p)	61.575899882	6.78137119405925
	10	381465 (105% of r_p)	61.575899882	6.13552631843456
	20	345135 (95% of r_p)	61.575431157	6.78126795295066
	20	381465 (105% of r_p)	61.575431157	6.1354329098125
	30	345135 (95% of r_p)	61.574962403	6.78116470599258
	30	381465 (105% of r_p)	61.574962403	6.13533949589804
Manned Craft	10	588546 (162% of r_p)	61.575899882	3.97673002120758
	20	588546 (162% of r_p)	61.575431157	3.97666947858217
	30	588546 (162% of r_p)	61.574962403	3.97660893252651

[2] Result Table – Earth Gravitational Assist

	Earth			
	Initial Velocity (km/s)	**Distance from center (km)**	**Exit Velocity (km/s)**	**G-Force at Exit Velocity**
Unmanned Craft	10	139735500 (95% of r_p)	57.500476179	0.002411943453468
	10	154444500 (105% of r_p)	57.500476179	0.002182234553138
	20	139735500 (95% of r_p)	57.489162620	0.002410994418567
	20	154444500 (105% of r_p)	57.489162620	0.002181375902513
	30	139735500 (95% of r_p)	57.477834435	0.002410044343848
	30	154444500 (105% of r_p)	57.477834435	0.002180516311100
	10	139735500 (95% of r_p)	57.500476179	0.002411943453468
	10	154444500 (105% of r_p)	57.500476179	0.002182234553138
	20	139735500 (95% of r_p)	57.489162620	0.002410994418567

Manned Craft	20	154444500 (105% of r_p)	57.489162620	0.002181375902513
	30	139735500 (95% of r_p)	57.477834435	0.002410044343848
	30	154444500 (105% of r_p)	57.477834435	0.002180516311100

[3] Result Table – Mars Gravitational Assist

	Mars			
	Initial Velocity (km/s)	**Distance from center (km)**	**Exit Velocity (km/s)**	**G-Force at Exit Velocity**
Unmanned Craft	10	196289000 (95% of r_p)	65.491175737	0.005889734288470
	10	216951000 (105% of r_p)	65.491175737	0.005328807213378
	20	196289000 (95% of r_p)	65.482072021	0.005888096976548
	20	216951000 (105% of r_p)	65.482072021	0.005327325835924
	30	196289000 (95% of r_p)	65.472954394	0.005886457390833
	30	216951000 (105% of r_p)	65.472954394	0.005325842401230
Manned Craft	10	196289000 (95% of r_p)	65.491175737	0.005889734288470
	10	216951000 (105% of r_p)	65.491175737	0.005328807213378
	20	196289000 (95% of r_p)	65.482072021	0.005888096976548
	20	216951000 (105% of r_p)	65.482072021	0.005327325835924
	30	196289000 (95% of r_p)	65.472954394	0.005886457390833
	30	216951000 (105% of r_p)	65.472954394	0.005325842401230

[4] Matlab Code:

```
format long

V_initial_moon = 10; %km/s
V_initial_earth = 10;
V_initial_mars = 10;

m_craft_u = 10000*(0.453592); %%kg
m_craft_m = 9000*(0.453592); %%kg

grav_moon = 1.62; %% m/s^2
grav_earth = 9.81; %% m/s^2
grav_mars = 3.71; %% m/s^2

G = 6.673*(10^-17); %%N*km^2/kg^2
M_moon = 0.073*(10^24); %%kg
M_earth = 5.9723*(10^24); %%kg
M_mars = 0.642*(10^24); %%kg

mu_moon = G*M_moon*(10^-3); %%km^3/s^2
mu_earth = G*M_earth*(10^-3); %%km^3/s^2
mu_mars = G*M_mars*(10^-3); %%km^3/s^2
mu_sun = 1.32712440042*(10^20)*(10^-3); %%km^3/s^2
```

```
AU = 1.496*(10^8); %%km

a_moon = 0.3844*(10^6); %%km
a_earth = 1*AU; %%km
a_mars = 1.524*AU; %%km

%% Calc for Velocity at Perigee
r_p_moon = 0.3633*(10^6); %%km
r_p_earth = 147.09*(10^6); %%km
r_p_mars = 206.62*(10^6); %%km

Vesc_moon_calc = sqrt((2*mu_moon)/r_p_moon);
Vesc_earth_calc = sqrt((2*mu_earth)/r_p_earth);
Vesc_mars_calc = sqrt((2*mu_mars)/r_p_mars);

Vinf_moon_calc = sqrt(mu_moon/a_moon);
Vinf_earth_calc = sqrt(mu_earth/a_earth);
Vinf_mars_calc = sqrt(mu_mars/a_mars);

V_p_moon = sqrt(((Vinf_moon_calc)^2)+((Vesc_moon_calc)^2));
V_p_earth = sqrt(((Vinf_earth_calc)^2)+((Vesc_earth_calc)^2));
V_p_mars = sqrt(((Vinf_mars_calc)^2)+((Vesc_mars_calc)^2));

e_moon = ((r_p_moon*(V_p_moon^2))/mu_moon)-1;
e_earth = ((r_p_earth*(V_p_earth^2))/mu_earth)-1;
e_mars = ((r_p_mars*(V_p_mars^2))/mu_mars)-1;

r_moon =  0.588546*(10^6); %% km
r_earth = 139.7355*(10^6);
r_mars = 216.951*(10^6);

%% Calc for velocity at exit of gravitational assist
Vcraft_moon = sqrt(((2*mu_moon)/r_moon)-(mu_moon/a_moon));  %%km/s
Vcraft_earth = sqrt(((2*mu_earth)/r_earth)-(mu_earth/a_earth)); %%km/s
Vcraft_mars = sqrt(((2*mu_mars)/r_mars)-(mu_mars/a_mars)); %%km/s

V_E_S = sqrt(mu_sun/a_earth); %%km/s
V_M_S = sqrt(mu_sun/a_moon); %%km/s
V_MA_S = sqrt(mu_sun/a_mars); %%km/s

Vesc_moon_g = 2.38; %%km/s
Vesc_earth_g = 11.186; %%km/s
Vesc_mars_g = 5.03; %%km/s

Vinf_moon = sqrt((Vcraft_moon^2)-(Vesc_moon_calc^2)); %%km/s
Vinf_earth = sqrt((Vcraft_earth^2)-(Vesc_earth_g^2)); %%km/s
Vinf_mars = sqrt((Vcraft_mars^2)-(Vesc_mars_g^2)); %%km/s
```

```
TurnA_moon = 2*asind(1/e_moon);
TurnA_earth = 2*asind(1/e_earth);
TurnA_mars = 2*asind(1/e_mars);

rp_moon = 0.7266*(10^6);
rp_earth = 294.18*(10^6);
rp_mars = 413.24*(10^6);

beta_moon =
atand(((sqrt(mu_sun/a_moon))+Vinf_moon*sind(2*asind(1/(1+((rp_moon*(Vinf_moon^2))/mu_moon))
)))/(Vinf_moon*cosd(2*asind(1/(1+((r_p_moon*(Vinf_moon^2))/mu_moon))))));
beta_earth =
atand(((sqrt(mu_sun/a_earth))+Vinf_earth*sind(2*asind(1/(1+((rp_earth*(Vinf_earth^2))/mu_earth)))))
/(Vinf_earth*cosd(2*asind(1/(1+((r_p_earth*(Vinf_earth^2))/mu_earth))))));
beta_mars =
atand(((sqrt(mu_sun/a_mars))+Vinf_mars*sind(2*asind(1/(1+((rp_mars*(Vinf_mars^2))/mu_mars)))))/(
Vinf_mars*cosd(2*asind(1/(1+((r_p_mars*(Vinf_mars^2))/mu_mars))))));

Vinf1_inc_moon = V_initial_moon - V_M_S;
Vinf1_inc_earth = V_initial_earth - V_E_S;
Vinf1_inc_mars = V_initial_mars - V_MA_S;

Vinf1_out_moon = Vinf1_inc_moon/cosd(TurnA_moon);
Vinf1_out_earth = Vinf1_inc_earth/cosd(TurnA_earth);
Vinf1_out_mars = Vinf1_inc_mars/cosd(TurnA_mars);

V_exit_moon = atand((V_M_S +
Vinf1_out_moon*sind(TurnA_moon))/(Vinf1_inc_moon*cosd(TurnA_moon)))
V_exit_earth = atand((V_E_S +
Vinf1_out_earth*sind(TurnA_earth))/(Vinf1_inc_earth*cosd(TurnA_earth)));
V_exit_mars = atand((V_MA_S +
Vinf1_out_mars*sind(TurnA_mars))/(Vinf1_inc_mars*cosd(TurnA_mars)));

%% Calc gravitational forces
F_grav_normal_moon_u = m_craft_u*grav_moon;
F_grav_normal_earth_u = m_craft_u*grav_earth;
F_grav_normal_mars_u = m_craft_u*grav_mars;
F_grav_normal_moon_m = m_craft_m*grav_moon;
F_grav_normal_earth_m = m_craft_m*grav_earth;
F_grav_normal_mars_m = m_craft_m*grav_mars;

%% Unmanned
a_craft_moon_exit = (V_exit_moon^2)/r_moon;
a_craft_earth_exit = (V_exit_earth^2)/r_earth;
a_craft_mars_exit = (V_exit_mars^2)/r_mars;

Fgrav_exit_moon_u = m_craft_u*a_craft_moon_exit;
Fgrav_exit_earth_u = m_craft_u*a_craft_earth_exit;
```

```
Fgrav_exit_mars_u = m_craft_u*a_craft_mars_exit;

a_craft_moon_perigee = (V_p_moon^2)/r_p_moon;
a_craft_earth_perigee = (V_p_earth^2)/r_p_earth;
a_craft_mars_perigee = (V_p_mars^2)/r_p_mars;

Fgrav_perigee_moon_u = m_craft_u*a_craft_moon_perigee;
Fgrav_perigee_earth_u = m_craft_u*a_craft_earth_perigee;
Fgrav_perigee_mars_u = m_craft_u*a_craft_mars_perigee;

Gforce_moon_u = (Fgrav_exit_moon_u/F_grav_normal_moon_u)*1000
Gforce_earth_u = (Fgrav_exit_earth_u/F_grav_normal_earth_u)*1000;
Gforce_mars_u = (Fgrav_exit_mars_u/F_grav_normal_mars_u)*1000;
Gforce_moon_u_p = (Fgrav_perigee_moon_u/F_grav_normal_moon_u)*1000;
Gforce_earth_u_p = (Fgrav_perigee_earth_u/F_grav_normal_earth_u)*1000;
Gforce_mars_u_p = (Fgrav_perigee_mars_u/F_grav_normal_mars_u)*1000;

%% Manned
Fgrav_exit_moon_m = m_craft_m*a_craft_moon_exit;
Fgrav_exit_earth_m = m_craft_m*a_craft_earth_exit;
Fgrav_exit_mars_m = m_craft_m*a_craft_mars_exit;

Fgrav_perigee_moon_m = m_craft_m*a_craft_moon_perigee;
Fgrav_perigee_earth_m = m_craft_m*a_craft_moon_perigee;
Fgrav_perigee_mars_m = m_craft_m*a_craft_moon_perigee;

Gforce_moon_m = (Fgrav_exit_moon_m/F_grav_normal_moon_m)*1000
Gforce_earth_m = (Fgrav_exit_earth_m/F_grav_normal_earth_m)*1000;
Gforce_mars_m = (Fgrav_exit_mars_m/F_grav_normal_mars_m)*1000;
Gforce_moon_m_p = (Fgrav_perigee_moon_m/F_grav_normal_moon_m)*1000;
Gforce_earth_m_p = (Fgrav_perigee_earth_m/F_grav_normal_earth_m)*1000;
Gforce_mars_m_p = (Fgrav_perigee_mars_m/F_grav_normal_mars_m)*1000;
```

References

1. “Gravity Assist.” *Gravity Assist*, Michael A. Minovitch, www.gravityassist.com/.
2. Shortt, David. “Gravity Assist.” *The Planetary Society*, 27 Sept. 2013, www.planetary.org/blogs/guest-blogs/2013/20130926-gravity-assist.html.
3. Elert, Glenn. “Acceleration That Would Kill a Human.” *Acceleration That Would Kill a Human - The Physics Factbook*, hypertextbook.com/facts/2004/YuriyRafailov.shtml.
4. “Standard Gravitational Parameter.” *Vaporia*, www.vaporia.com/astro/start/standardgravitationalparameter.html.
5. Williams, Dr. David R. “Planetary Fact Sheet - Metric.” *NASA*, NASA Goddard Space Flight Center, nssdc.gsfc.nasa.gov/planetary/factsheet/.
6. *Planet Tables*. www.astronomynotes.com/tables/tablesb.htm.
7. Reid, David B. “The Use of Gravity Assist Flybys in Plane Change Maneuvers.” *University of Colorado Boulder*, University of Colorado Boulder - Aerospace Engineering Science, 6 Dec. 2012, ccar.colorado.edu/asen5050/projects/projects_2012/reid/.
8. “Velocity of a Hyperbola.” *Clowder*, clowder.net/hop/TMI/HypVel.html.

9. [9] “Escape Velocity.” *Escape Velocity*, Hyperphysics, hyperphysics.phy-astr.gsu.edu/hbase/ vesc.html.
10. Williams, David R. “Moon Fact Sheet.” *NASA*, NASA, 3 July 2017, nssdc.gsfc.nasa.gov/ planetary/factsheet/moonfact.html.
11. Williams, David R. “Earth Fact Sheet.” *NASA*, NASA, 16 March 2017, nssdc.gsfc.nasa. gov/planetary/factsheet/earthfact.html.
12. Williams, David R. “Mars Fact Sheet.” *NASA*, NASA, 23 December 2016, nssdc.gsfc. nasa.gov/planetary/factsheet/marsfact.html.
13. Newton's Law of Universal Gravitation.” *The Physics Classroom*, www.physics classroom.com/class/circles/Lesson-3/Newton-s-Law-of-Universal-Gravitation.
14. “Centripetal and Centrifugal Force - Acceleration.” *The Engineering Toolbox*, www.engineeringtoolbox.com/centripetal-acceleration-d_1285.html.
15. “Calculation of the G-Force.” *Physics Stack Exchange*, 23 Nov. 2010, physics.stack exchange.com/questions/1227/calculation-of-the-g-force.
16. “Spacecraft - Mars Science Laboratory.” *NASA*, USA Government, mars.nasa.gov/msl/mission/spacecraft/.
17. [17] “Size of Apollo Era Astronauts.” *Space Stack Exchange*, space.stackexchange.com/ questions/2253/size-of-apollo-era-astronauts.
18. “Mars One Astronauts.” *Mars One*, www.mars-one.com/mission/mars-one-astronauts.
19. Hopper, Douglas J. *Interplanetary Flight Using the Planetary Gravity Assist Maneuver*. United States Airforce Institute of Technology, www.dept.aoe.vt.edu/~cdhall/courses/mech533/ Reports92b.pdf.
20. Erickson, Kristen, et al. “Basics of Space Flight.” NASA, NASA Science, solarsystem.nasa.gov/basics/.
21. “Gravitational Slingshot.” *Mathpages*, www.mathpages.com/home/kmath114/kmath114 .htm.
22. Van Allen, James A. “Gravitational Assist in Celestial Mechanics - A Tutorial.” *American Journal of Physics*, vol. 71, no. 448, Nov. 2002, aapt.scitation.org/doi/abs/10.1119/1.1539102.
23. Pitjeva, E. V. “Determination of the Value of the Heliocentric Gravitational Constant from Modern Observations of Planets and Spacecraft.” *Journal of Physical and Chemical Reference Data*, vol. 44, no. 3, May 2015. *AIP Journal of Physical and Chemical Reference Data*, aip.scitation.org/doi/10.1063/1.4921980.
24. “Solar System Exploration: In Depth.” *NASA*, NASA, 5 Dec. 2017, solarsystem.nasa.gov /moons/earths-moon/in-depth/.
25. Redd, Nola Taylor. “How Far Away Is Neptune?” *Space.com*, www.space.com/18923-neptune-distance.html.
26. “Distances Between the Planets of the Solar System.” *The Planets*, theplanets.org/ distances-between-planets/.

Life on Mars

Student Researcher: Hayley R. Crider

Advisor: Romena Holbert

Wright State University
Education Department

Abstract
My multi-day unit is called, "Life on Mars". In my educational project students will learn about life on Mars through a series of four lessons. The first lesson covers information on learning about life on Mars. Students will watch an educational video and then use information they learned in that video to make four-door foldable with facts about different things on Mars, such as water, weather, gravity, etc.

In the second lesson students will use their creative writing skills and knowledge from the previous lesson and write their own story about their day on Mars. This will be a fun and creative prompt that students will enjoy writing about. They will also draw a picture of their day to be displayed with their story.

The third lesson, students will begin to learn about rovers; how they work, but more specifically the rovers currently on Mars. They will watch a video where a man who actually drives the rovers for NASA talks about the process and all the things they can do. Students will brainstorm ideas about what tools rovers have. This will be useful for the next lesson.

After learning about the function of a rover, in the fourth lesson students will build their own rover.

Objectives: This series of lessons brings out the STEM qualities students need to practice. They will be problem solving and working together to create a rover out of a shoebox and other materials. They will also calculate the speed of their rovers going down a ramp on a worksheet attached to the lesson. Through these lessons they will practice their comprehension and creative writing skills.

The students will use research, data, guidelines, and resources to help them through this series of lessons resulting in constructing a functioning shoebox rover.

Evaluation of Fretting Corrosion Wear in Metal-on-Metal Hip Implants Subjected to Physiological Loading

Student Researcher: Michaela M. Crouch

Advisor: Dr. Timothy Norman

Cedarville University
Department of Engineering and Computer Science

Abstract
Fretting corrosion is a significant factor in the increased failure rates of metal-on-metal hip implants. These implants are composed of a metal femoral head and metal stem, the interface of which is where fretting corrosion occurs. When the implants are placed in the body, fretting wear is accelerated due to the corrosive environment.

This work builds on previous research that investigated the effect of taper-trunnion angular mismatch and surface roughness on fretting wear. In the previous studies, finite element analysis was completed to determine theoretical volumetric fretting wear, and electrochemical analysis was done while cyclically loading hip implant specimens. Electrochemical analysis was also done on specimens subjected to reimpaction and reloading. This project analyzes the wear on trunnion surfaces to validate previous experimental results.

Project Objectives
The overall goal of this research is to correlate fretting-corrosion wear from electrochemical experiments to wear measurements from analysis of trunnion surfaces. Previous investigations included electrochemical experiments that were performed to determine the effects of taper-trunnion angular mismatch and higher impaction loading on fretting corrosion. These experiments were performed under simulated physiological loading. The first objective of the current study was to determine a method for evaluating the visible fretting wear area on the specimens used in the previous experiments. Using this evaluation, the effects of the taper-trunnion angular mismatch and higher impaction loads and reloading on the fretting wear area were to be determined.

Methodology Used
The first of the two previous experiments consisted of twenty-five Ti-6Al-4V hip implant specimens. These specimens received an initial impaction of 450 lbs to join the femoral head and stem and were then cyclically tested between 0 and 450 lbs at 1 Hz at 17° according to ASTM 1875. The second experiment was performed on twelve of those specimens. Eight of the twelve received a second higher impaction of 991 lbs, and all twelve specimens were cyclically loaded again as in the first experiment. For both experiments, electrochemical analysis was performed. The voltage was monitored in real time as the specimens were being tested. The resulting voltage curve was integrated to produce "Fretting Level," which is a parameter that can be used to indicate the amount of fretting corrosion for a specimen.

To complete our first objective, the femoral stem-head assemblies were disassembled, and the trunnion surface was examined. The damage was then characterized by grades. The grades were defined as**:**

1 – No visible damage
2 – Thin partial line of damage
3 – Thin full line of damage
4 – Thick line of damage
5 – Partial length transverse damage
6 – Full length transverse damage

Sketches of these grades are shown in Figure 1 below. The specimens were also broken up into more general groups of damage (grades 2-6) or no visible damage (grade 1). The damage group was also broken up by type of damage: line damage, 1, (grades 2-4) and transverse damage, 2, (grades 5-6). The average damage grade, existence of damage, and type of damage were then compared based on angular mismatch of the taper-trunnion surface and loading. Angular mismatch was broken up into five categories depending on the location of taper-trunnion engagement: most distal (MD), least distal (LD), least proximal (LP), mid proximal (MiP), and most proximal (MP). Specimens that were only tested once were put in the L load group. Specimens that were retested and received a second impaction were put in the LH group, and those that were retested but not reimpacted, were categorized as LL. Statistical comparisons were done using ANOVA tests in JMP® with significance set at $p<0.05$.

Results Obtained

The results from the statistical comparisons show that angular mismatch significantly affects the type of damage (Figure 2), with line damage occurring in more distal contact (MD, LD) and transverse damage occurring in more proximal contact (LP, MiP, MP). This is because proximal contact allows for more toggle of the femoral head (taper) on the stem (trunnion) and results in more transverse fretting corrosion area. The results also show that reloading specimens results in higher wear grade (Figure 3). However, the comparison based on load group shows that the second impaction alone did not have a significant effect on fretting area (Figure 4). The inspection of the fretting area on the trunnion surface also supported the results of the electrochemical analysis performed in the previous studies. To get a better estimate of the volumetric fretting wear caused by the physiological loading of the specimens, three-dimensional inspection and analysis of the fretting areas on the trunnion surfaces needs to be completed.

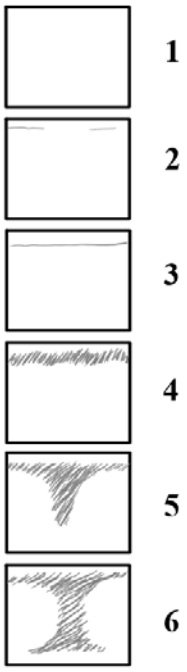

Figure 1. Sketches of Wear by Grade

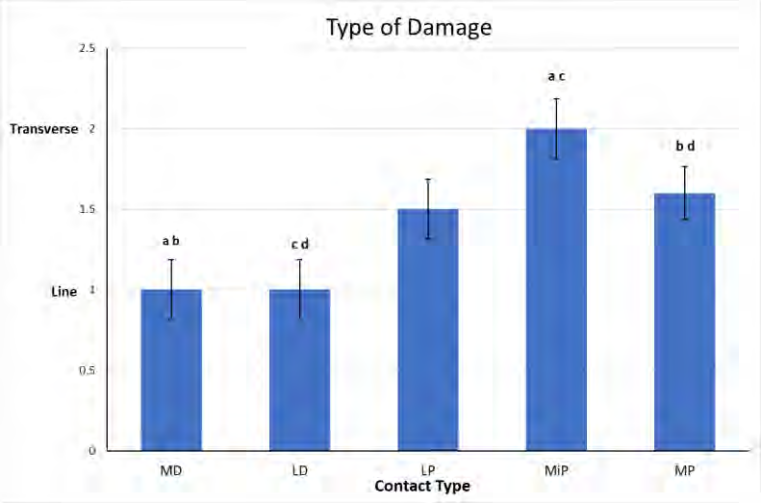

Figure 2. Angular mismatch's effect on type of damage (mean± SD). Significantly difference groups are indicated by the same letter.

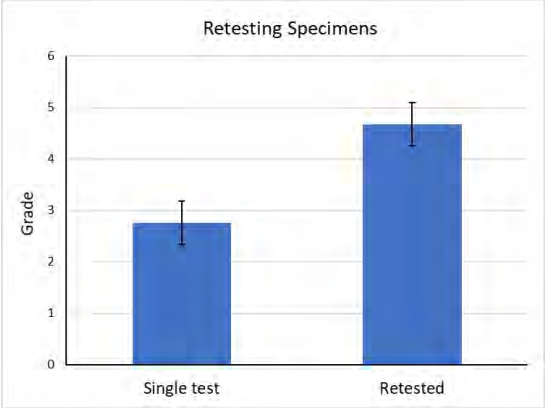

Figure 3. The effect of reloading on fretting area

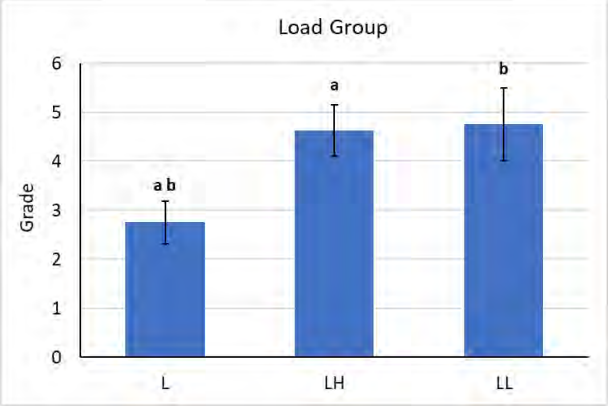

Figure 4. The effect of reimpaction on fretting area

Acknowledgments

J. Morin, BSME, Cedarville University, Cedarville, Ohio

T. K. Fehring, MD, OrthoCarolina, Charlotte, North Carolina

D. Erdahl, PhD, University of Dayton Research Laboratory, Dayton, Ohio

Automated All-Sky Acquisition Project (AAAP)

Student Researcher: Michael C. Curtice

Advisor: Mahmound Abdallah, Ph.D.

Central State University
Manufacturing Engineering

Abstract

The US Army Research Laboratory (ARL) seeks to provide a decisive edge for the land forces. One area ARL is focused on is Energy. Currently on the battlefield soldiers use diesel powered generators as a source of power. Manually transporting the fuel to the generators is dangerous. If you are a soldier in the convoy you are at high risk of being attacked by the enemy. To help reduce potential casualties, ARL is working on integrating renewable energy with non-renewable energy generators. These generators that the soldiers will use are mobile hybrid micro-grids. These generators have two means of producing power and have the ability to produce enough power for a forward operating base (FOB). ARL started a research project called Atmospheric Renewable Energy Case Study; to help with the advancement of creating the hybrid micro-grids. I have worked with ARL on the Atmospheric Renewable Energy Case Study #2. The purpose of the study was to study the atmospheric impact on the photovoltaic (PV) panel, take photo images of the sky and apply them for machine learning cloud assessment and to quantitatively describe the ARE2 PV power train.

The power and solar radiation data were recorded and documented daily. The data were plotted on a times series graph that showed the power and solar radiation for the previous day. With the graphs, the power generated by the power train can be observed and compared with the weather conditions of a certain day. Weather reports for the area were also documented daily with this information the cloud conditions can verify the decrease in power at certain parts of the day. The data collected was compared with data collected from the National Research Energy Laboratories. The results ARE2 obtained were confirmed to be reasonable. Images of the sky were manually taken every hour until the close of business using a simulated whole sky imager (s-WSI). The images were later be digitized and will be used for machine learning. The images corresponded with the weather summaries. With these sources of information, the power train output could be analyzed. When the power data graph would show a drop in the power output, the weather reports and images would prove the cloudy conditions.

Project Objectives/Methodology

The photo collection process can be improved by automating it. This way an individual will not need to conduct photo observations at certain points of the day. The next phase of this research, called the "Automated All-Sky Acquisition Project" (AAAP), will automate the process. A PV panel, batteries, charge controller load and simulated whole sky imager will be required. The PV panel will provide power. The batteries will store or discharge power and the load will absorb power. The charge controller will regulate the power between the three elements to provide even power distribution. The s-WSI will be attached to the PV panel and will be programmed to conduct photo observations at certain intervals from a 24-hour period.

Results

The panels and frame were fastened onto a trailer with wheels. This system is now mobile and can be position where desired.

Figure 1.1.

The maximum angle required for the panels is 43 degrees. The system was designed that the panels can rest on a flat plane when not being used. To power the actuator two 12 volt lead acid batteries will be utilized. Below Figure 1.2 shows the battery.

Figure 1.2.

Figure 1.3.

The hinge that connects the actuator to the frame was custom built at Central State University. The next step is to construct the sun tracking mechanism for the panels and interface an Arduino microcontroller with the actuator. The s-WSI images are flushed out from the sunlight. The settings for the exposure need to be changed within the camera to reduce the sunlight rays in the image. Then the clouds around the sun can be analyzed.

Figure 1.4.

References

1. Author: Gail Vaucher, Atmospheric Renewable Energy Research, Volume 1(“To BE or not to BE”). October 13, 2017.
2. Author: Gail Vaucher, Atmospheric Renewable Energy Research, Volume 2, Assessment Process for Solar-Powered Meteorological Applications. October 13, 2017.
3. Author: Gail Vaucher, Morris Berman and Jeffrey A. Smith, Atmospheric Renewable Energy Research, Volume 3, Solar-Power Microgrids and Atmospheric Influences. October 13, 2017.

Testing a Novel Minerology Crossplot Hypothesis

Student Researcher: Charles E. Drennen

Advisor: Professor Craig Rabatin

Marietta College
Department of Petroleum Engineering and Geology

Abstract
Within petroleum formation evaluation, graphs known as crossplots are used to show relationships between reservoir parameters and display different formation attributes. The effective porosity vs bulk density crossplot was developed by Professor Ben Ebenhack during his time working in the oil and gas industry. This crossplot provides a more definitive rock density for the formation; therefore, indicating a more accurate measure of formation mineralogy than is currently available through crossplot analysis. The effective porosity vs. bulk density crossplot is theoretical and does not exist in any industry literature. With current knowledge of the plot, it is not viable when the data is heavily skewed by clay, gas, or heavy mineral effects. We possess a large Fortran 77 program from Professor Ebenhack's industry work, and we believe this includes robust corrective formulas making the effective porosity vs. bulk density plot viable under all practical circumstances. Locating these formulas within the code will allow for the creation of a crossplot program featuring the theoretical crossplot in Microsoft Excel. Once fully realized, the effective porosity vs bulk density crossplot will add another tool for petroleum engineers and logging specialists to analyze petroleum-producing formations.

Project Objectives
The primary objective of this research project is to uncover the gas, clay, and heavy mineral corrections necessary to make effective porosity vs. bulk density crossplot an effective tool to analyze oil and gas reservoir rock mineralogy. We have collectively identified that there is a piece missing in the effective porosity vs bulk density crossplot, and the code was a tool used to look for the missing piece of that analysis. Currently, the effective porosity vs bulk density crossplot works only in data that is not heavily skewed by these effects. The general formula from for clay correction from Ransom is included in Figure 1. An example of a density neutron plot, where current industry corrections occur, appears in Figure 2, displaying corrections for gas and clay effects from Ransom. A subsequent objective was to create an Excel workbook showing that these corrections worked and providing evidence for the theoretical crossplot.

Methodology Used
It is believed by Professor Ebenhack that the corrections necessary to make the effective porosity vs bulk density crossplot (Figure 3) effective were contained in the volumes of a FORTRAN 77 program. The program allowed Ebenhack and his colleagues to manipulate and analyze crossplots during their time in the oil and gas industry. Ebenhack believes the formulas necessary to support his theoretical crossplot are within these thousands of lines of code. This program took Bob Ransom, the world's premier formation evaluation specialist, and a career programmer at their company 10 years to develop, and neither Ransom nor the programmer can locate or replicate where this missing piece. Previous attempts at proving this hypothesis by Aaron Kurtz involved replicating the functioning of the entire crossplot program from scratch, including the effective porosity vs bulk density feature. This is where the problem of a lack of proper corrections became apparent, as the theoretical crossplot did not work properly with heavily gas, clay, and heavy mineral-affected data. I chose to analyze the FORTRAN code directly, if past

efforts to replicate its functioning were not completely affirming of the hypothesis. I studied some basic FORTRAN 95 tutorials including *Introduction to Programming using FORTRAN 95* using a Silverfrost Plato compiler to familiarize myself with the language. This is acceptable for learning FORTRAN 77 as well, since the more recent version was added on to FORTRAN 77 and they function in a similar way. I also took time to develop a clear understanding of complex corrections and how they fit into generating the theoretical crossplot. I then read and annotated the code, seeking any keywords or variables related the density neutron, N vs gamma, or effective porosity vs bulk density crossplots, and also any mention of data corrections with clay, gas, or heavy minerals. After reading through all of the code, I reviewed my annotations looking for expressions where the data switched from original to corrected. I made note of these expressions and variables and conducted a second search of the code for anything that would lead to the corrections themselves. By finding these corrections, I planned to reverse engineer the code to complete the missing piece of crossplot.

Results Obtained

The conclusion of this project is negative: I did not find the necessary corrections or any corrective formulas within the given code. Mention of various corrections for density neutron and other plots were found, but these only included logic-based switches on which corrected data to use. The code did not feature the mathematics or any details of the corrections themselves. It is possible that printed versions of the code are missing or were never passed on. It is also possible that this version of the program was printed prior to the development of the effective porosity vs bulk density crossplot into the program. Because Professor Ebenhack is the sole owner of the remaining FORTRAN code from this program, it is not likely these corrections will be found within original program.

Significance and Interpretation of Results

The fact that these corrections were not found within the volumes of code does not discredit the effective porosity vs bulk density crossplot, but it does narrow down the options for proving its hypothesis. At this point, future researchers are not advised to continue analyzing the FORTRAN code unless they are coding experts. I recommend future research to explore the crossplot empirically with a working model. Perhaps using trial and error in experimenting with different corrections of a data for a pre-determined rock type would allow for development of more robust corrections. The potential usefulness of this crossplot is increasing as the petroleum industry shifts its focus to unconventional reservoirs such as the Marcellus shale. The mineralogy of unconventional reservoirs is complex and often less understood than conventional resources. The effective porosity vs bulk density crossplot could give operators a better understanding of the rock types within their reservoirs and how to produce them most effectively.

Figures/Charts

$$\Phi_{D\ clay\ corrected} = \Phi_D - (V_{clay})(\Phi_{D-wetclay})$$

$$\Phi_{N\ clay\ corrected} = \Phi_N - (V_{clay})(\Phi_{N-wetclay})$$

Figure 1. Known formula to clay-correct density neutron crossplot (Kurtz 16, from Ransom 254).

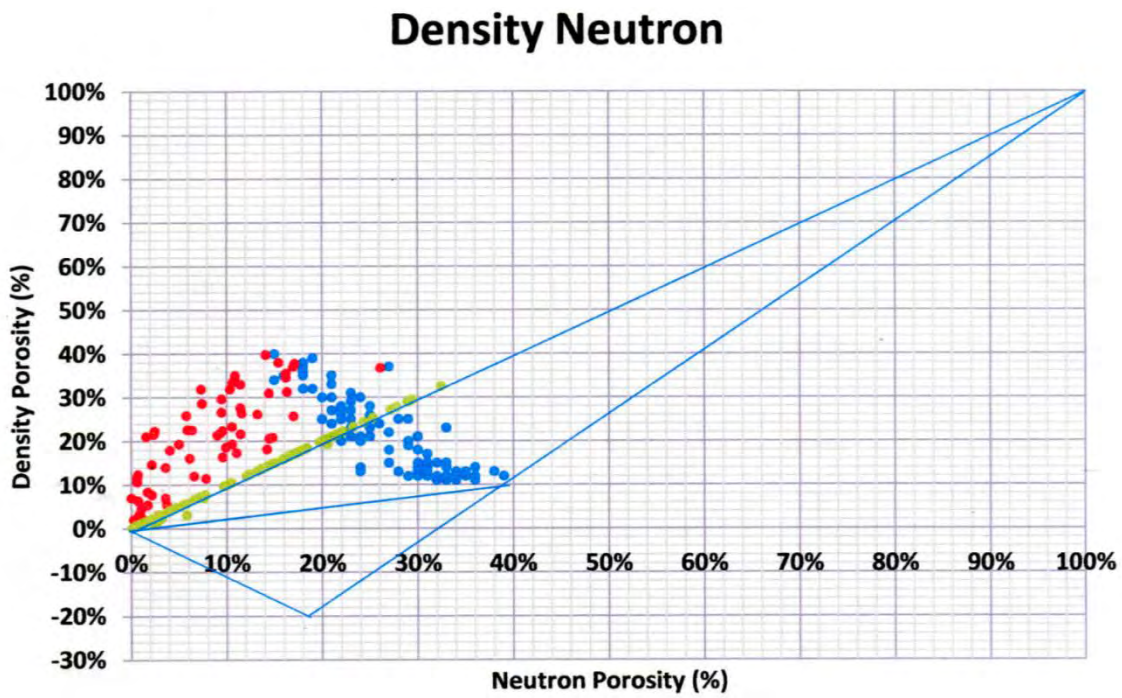

Figure 2. Density Neutron Crossplot with gas and clay corrections. Clay and gas corrected data is in green. Clay corrected data is in red. Original data is in blue. Some green data points below the clean sandstone line (uppermost diagonal) indicates the potential of heavy minerals that may require correction (Kurtz 19, from Ransom)

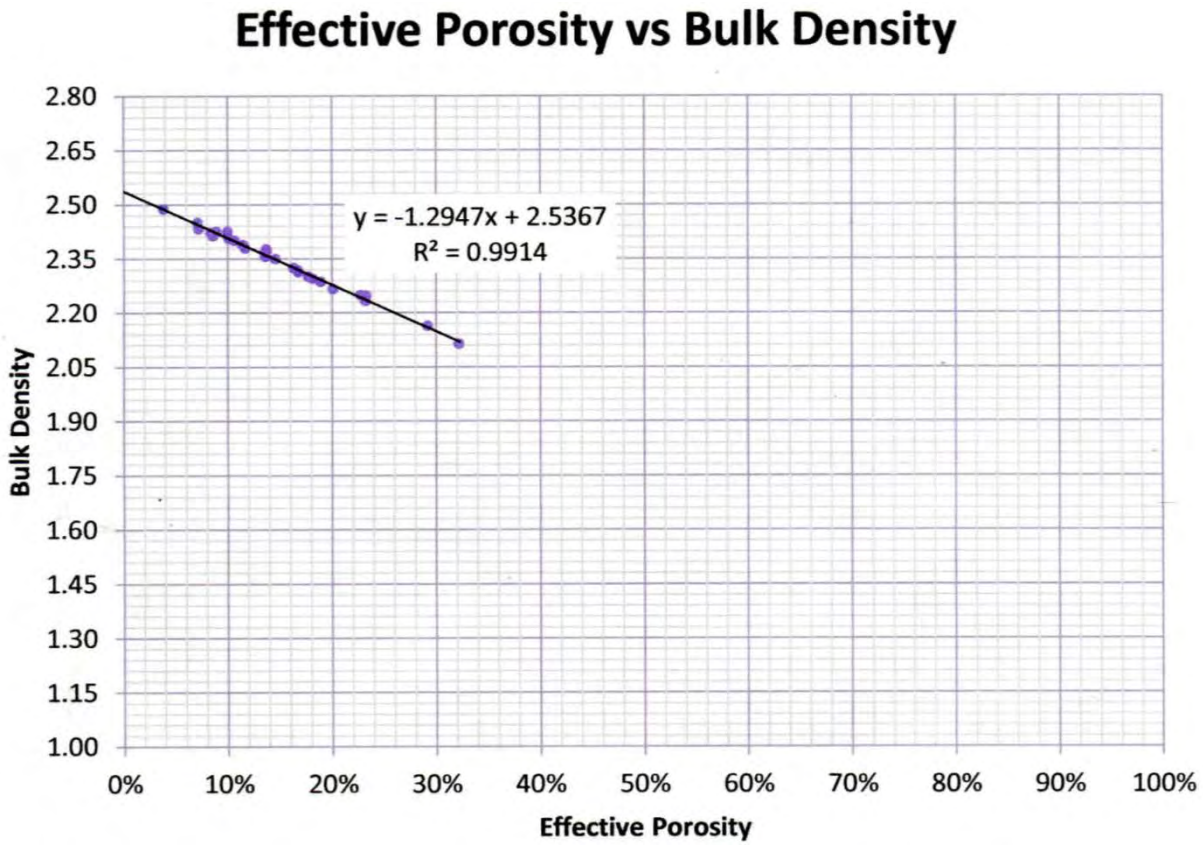

Figure 3. Effective Porosity vs Bulk Density crossplot. The actual bulk density of the reservoir rock is found by extrapolating the trendline through the plot data to the y-axis. The point of intersection is the bulk density, which is how rock types such as sandstone or dolomite are classified (Kurtz 21, from Ebenhack)

Acknowledgments and References

1. Ebenhack, Ben W.; Benedum Professor and Industry Partners Chair, Petroleum Engineering.
2. Kurtz, Aaron. “Determining Mineralogy from Traditional Well Log Data”. Marietta College: 2013. Print.
3. Ransom, Robert. *Practical Formation Evaluation*. John Wiley & Sons Inc., 1995. Print.

Responsive STEM Teaching Utilizing the 5E Inquiry Cycles

Student Researcher: Jacob T. Dunwiddie

Advisor: Dr. Bridget Mulvey

Kent State University
College of Education

Abstract
This project explores how early childhood educators can plan inquiry-based STEM lessons through the iterative and flexible use of the 5E learning cycle with Kindergarteners in a play-based curriculum. The science content emphasis was on physical science, force and motion in particular. Essential teacher actions involve learning about and building lessons around the interests of young children that foster accurate scientific inquiry and understanding.

As a field student and student teacher this school year, I oversaw the curriculum planning for the STEM area, with guidance from my mentor teachers. I documented children's actions and ideas over time through photos, anecdotal observations, and lessons guided by children's interests and experiences. My teaching investigated young children's evolving ideas and interests, responding with lessons that supported them. I seek to show how teachers can use play-based 5E learning cycles to facilitate natural, relevant STEM and STEAM (STEM plus Art) inquiries with young children.

Lesson
I want to highlight the responsive nature of teaching to the children's interest, so the lesson was developed after extensive observations of my students engaging with various materials and listening to their interests. One topic that was recurring was the creation of marble ramps.

Children would spend significant portions of their play in a space that offered the materials needed to create their ramps. I documented the children grappling with issues of force and motion. From this observation during play I planned provocations in this classroom space to have children think more scientifically about their marble ramps. This lesson is not one instance, but a long-term, sustained inquiry lesson. The lessons are from the beginning of November and still happening in my class.

Originally, the children were interested in force and motion, specifically how much force was needed to manipulate their marbles in specific ways. Then reflecting on my practice, I realized the children were actually interested in how their design process of the marble ramps effected the force and motion of the marbles. From this the STEM lesson focused on the engineering design process. As children went through the design process (defining problems, designing solutions, and optimizing solutions). The provocations served as a scaffold for children to define the problem, then through planning children drafted solution, and finally when they tested their ramps the optimized solutions by making edits.

This experience shows young children's innate ability to think scientifically and craving for challenging, real, and meaningful STEM work. Additionally, the context in which I was planning was play-based, while my teacher actions made the children feel like they were playing. This acceptance of my invitations to learning was made possible by the inquiry, and free nature of the 5E framework.

Objectives
Student will be able to…

1. …go through the engineering design process by defining problems, designing solutions, and optimizing solutions with materials
2. …explain how the position, motion, and force of an object is impacted by their engineering design decisions

Alignment
Ohio Department of Jobs and Family Services – Early Learning and Development and Standards (Kindergarten)>Cognition and General Knowledge>Science >With modeling and support, explores the position and motion of objects

Underlying Theory
The project is rooted in social constructivist teaching theory, specifically the work of John Dewey. Dewey believed that experiences should be meaningful and authentic to children. My entire series of lessons are based on the interest of children (marble ramps) and allowing the children to go through the engineering design process that real engineers use, making this experience meaningful to the children. Additionally, the 5E model for learning is within the pedagogical framework of John Dewey, even though he did not directly develop the framework. The 5E, play-based model, and the STEM work my students were engaged with was completed collaboratively. At its heart, social constructivism or social learning, is for children to co-construct knowledge with each other. If you were to observe my students in this work you would see them co- planning, talking about engineering solutions, and providing feedback to each other.

Resources
As mentioned, in my classroom this project was completed in a specific space. My classroom is an open space that is ever changing based on the children's interests. In the room, we have "spaces": Tool Area, Nature Table, Math Area, Writing Center, Art Studio, House, Story Table, Block Area, Library, and Meeting Space. These spaces were named by the children to showcase our values and inquires as a class. The dynamic spaces in our class allow for multiple modalities of learning. The entire project happening in Block Area. The children used the many blocks and small construction tools to design their marble ramps. To test their ramps I provided standard marbles, about 20. Lastly, I provided plan documents to help children design their plans on paper first then build it with the block. These materials were arranged in the space to be organized, but so children could also see what was offered. The idea is they could visualize a possible plan with the materials, plan it, test it, and revise their plans.

Results
Children, through several rounds of revisions and experience in the space, were able to successfully go through the engineering design process. However, this did not mean they always worked the way the children anticipated. Additionally, all children started to understand or fully understood that the position, motion, and force of an object is impacted by their engineering design decisions.

Assessment
I assessed the children in several ways. First, could they go through the engineering design process with minimal scaffolding or support from me. Second, were children able to tell me through one on one discussions how their designs work with the integration of academic language (force, design, motion). Third, were children's plans and designs matching up; I needed children to follow their plans and if they made changes, edit it on their document or get a new one.

Conclusion

The young, kindergarten children were able to go through a real engineering design process that fostered accurate scientific thinking about force and motion in a play-based context and using the 5E framework.

The Effect of Scan Strategy on Porosity in Additive Manufacturing

Student Researcher: Rachel E. Evans

Advisor: Dr. Joy Gockel

Wright State University
Department of Mechanical and Materials Engineering

Abstract
There are many factors to consider when manufacturing any type of product. One such consideration is the structural defects in the material that make up the desired product's composition, which can be very detrimental to its performance and efficiency. In additive manufacturing, structural defects can be caused by a number of factors; however, this project concentrates on porosity that is caused by the scanning pattern of the laser. A heat transfer solution code, along with two MATLAB codes, are used to investigate the effects of the different scanning strategies. This research project explores how the process of production may be revised to reduce material defects.

Project Objectives
Additive manufacturing, commonly known as 3-D printing, is the process of joining layers of material together to make a three-dimensional object. The laser powder bed fusion process refers to a subcategory of additive manufacturing. In this process, a laser beam creates a melt pool within a layer of powder material. This repeated layer-by-layer to create the three-dimensional object [1].

There are three types of porosity in the laser bed fusion process: keyholing, balling, and lack-of-fusion. This research project investigates lack-of-fusion porosity, which is a void in the material that is caused by locations that fail to reach the melting temperature.

Methodology Used
For this project, a MATLAB path code was generated in which the user inputs scan pattern parameters, such as scan width, speed, and hatch spacing. This path code then outputs a file that describes the path that the laser beam follows. This outputted path file is then entered into a heat transfer solution code that generates a number of points and their corresponding temperatures due to the power of the laser beam. Then, a MATLAB code was created to visualize where lack of fusion porosity occurred. This code uses the outputted information from the heat transfer code to produce a visual representation of the x-y coordinates and their temperatures. A flow chart of this process can be seen in Figure 1.

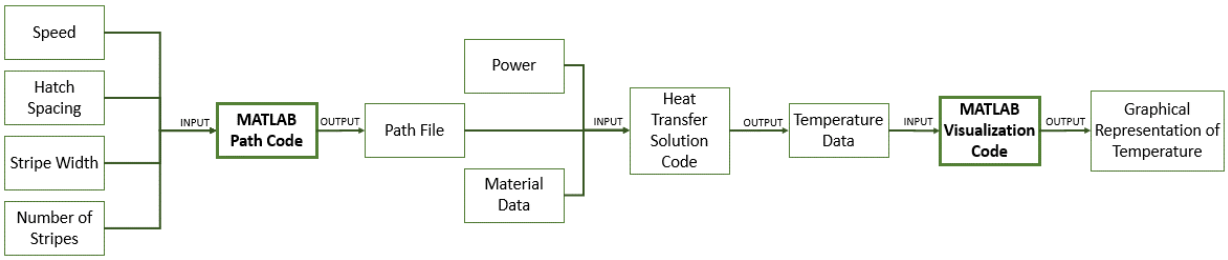

Figure 1. The procedure of this project.

Results Obtained

Two tests were used to investigate the effects of both speed and hatch spacing. In the first test, the project investigated the effect of speed by running the codes at various speeds and a single hatch (Figure 2). In the second test, the process was done again with 10 hatches to investigate the effects of hatch spacing (Figure 3). In each of these tests, the power that was used in the trials was 285 W and the material was Alloy 718, which has a liquidus temperature of 1610 K. The stripe width was also kept constant at 5 mm.

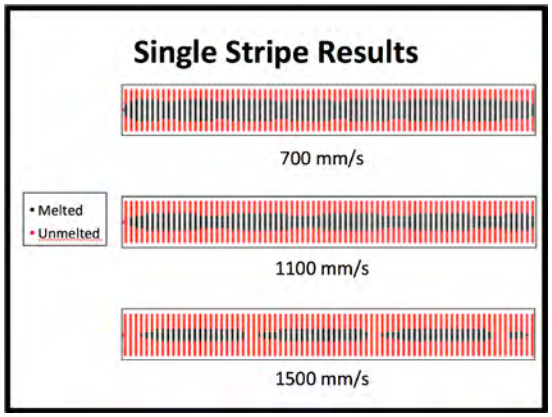

Figure 2. Results from single hatch test.

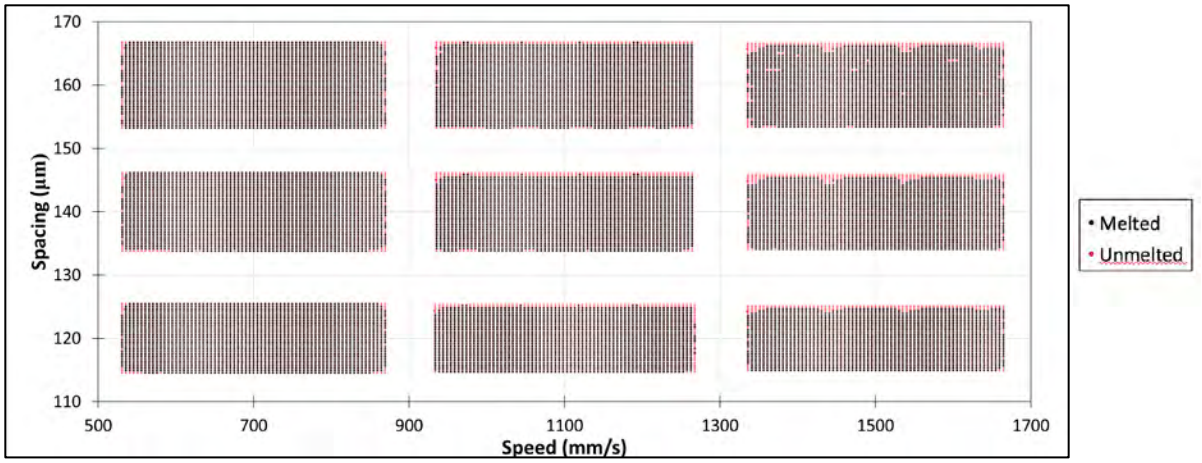

Figure 3. Results from multiple hatch test.

Interpretation of Results

After analyzing the graph of the temperatures at different speeds and hatch spacing, it can be concluded that higher speeds and larger hatch spacing lead to an increase in lack-of-fusion porosity. Also, it is observed that many of the pores occur around the side edges of the laser path, where the beam starts and stops to create the stripes. Therefore, it can also be concluded that many of the problem areas occur around the edges of the laser path.

Reference

1. Plotkowski, Alex et al. “Verification and Validation of a rapid heat transfer calculation methodology for transient melt pool solidification conditions in powder bed metal additive manufacturing.” (2017).

Digital Light Processing Stereolithography Using Vat-Free Photopolymerization

Student Researcher: Andrea L. Felicelli

Advisor: Dr. Jae-Won Choi

The University of Akron
Mechanical Engineering Department

Abstrac

Digital Light Processing Stereolithography is a form of additive manufacturing that traditionally uses a vat, or large container, to hold photopolymer resin that is cured by a high-resolution digital light projector to form structures. This technique has several limitations, including difficulty in producing structures with large horizontal areas, material waste, and lack of efficient use of photopolymer amounts compared to the structures formed. It's also limited by heightened risk of over curing and lack of depth control during the curing process. There is a possibility of replacing the vat used in the current technology with a "vat free" stacking mechanism using a liquid bridge, a common natural phenomenon generally formed between two solid bodies due to surface tension forces. This stacking mechanism can be implemented using two glass plates in between which a liquid bridge can be formed and maintained, and a 3D part can be cured within. The benefits of this approach include its simple configuration, material savings due to it being vat-free, and high-resolution layer formation.

Project Objectives

This research is based on previous work by an Akron PhD student on liquid bridge approach to microstereolithography (MSL). MSL has limitations when it comes to the fabrication process, many of which are increased by the traditional vat approach. Previously, a liquid bridge based microstereolithography was investigated as a means of improving the fabrication process of MSL. Our objective is to use this same liquid bridge phenomenon to develop a relatively low-cost digital light processing stereolithography system. This system will cure photopolymer material using 470nm wavelength light from a digital light projector within a liquid-bridge formed between upper and lower substrate plates, removing the need for a traditional vat.

Methodology Used

The printer being developed was designed around a predefined custom photopolymer resin that cures at 470 nm (natural light) wavelength. A digital light projector with a blue LED light source of appropriate wavelength was used to project a different white cross section for each layer of the print. This light should be able to completely cure the photopolymer layer within a 10 second time interval. For this application, a pico digital light projector was preferred due to its much shorter projecting distance. The projector was attached to the top of metal frame with a fixture, to project images down onto the transparent top substrate.

As for the vat-free design, a pump syringe filled with the photopolymer resin pumps a small amount through a hole in the bottom substrate onto the 1x1 inch print surface. Then, the z-axis moves the lower glass plate from its initial position touching the top substrate, a distance of 3mm max, to form the liquid bridge. The projector projects the 2D cross sectional image through the transparent PMP

glass top substrate, allowing the resin with the liquid bridge to cure where light is shone. The bottom substrate is attached to a linear guide that moves along our z-axis while powered by a Nema 23 stepper motor. The motor is programmed using Arduino Uno software and code.

The liquid bridge itself has some limitations. Experiments done with our resin show that the liquid bridge will rupture at 3mm height. There also is a problem with layer adhesion to the bottom substrate, which could cause problems during the printing process. To help deter this, a Teflon coated film is adhered to the top substrate.

Results Obtained

The system was built and is currently undergoing testing and troubleshooting for software and hardware. The main problem that has been faced has been seemingly insufficient light intensity from the projector. Ways to improve this, and material curing time, are being looked into. Another problem faced during prints, as mentioned previously, is the adhesion of the resin to the bottom substrate, causing the print to fail as more layers cannot be added. This is one disadvantage of the liquid bridge method relative to a traditional vat.

Figures/Charts

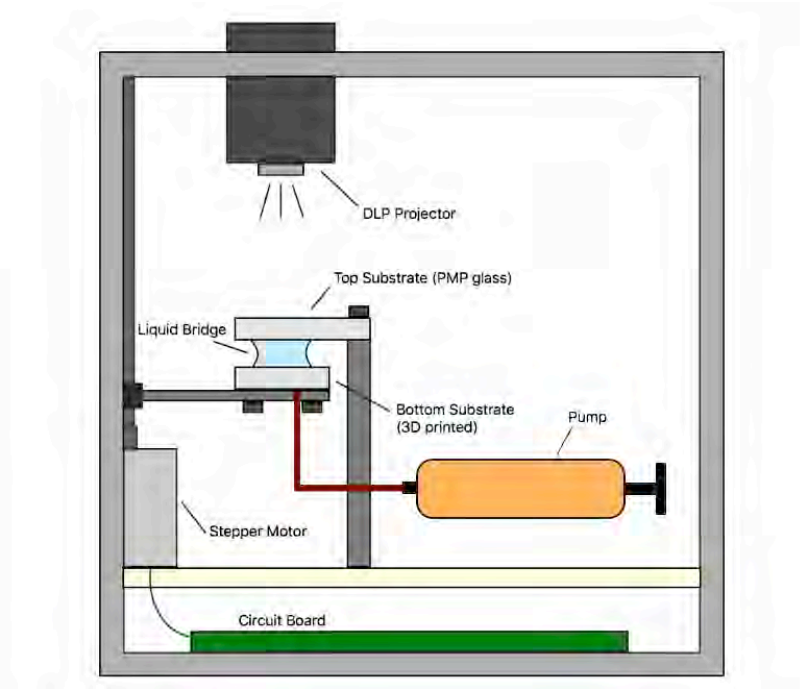

Acknowledgments and References

- Yanfeng L., (2016)“A Study On Liquid Bridge Based Microstereolithography (Lbmsl) System”, Doctoral Dissertation
- Yuan L., James E. S., (2016) “Capillary breakup of a liquid bridge: identifying regimes and transitions”, Journal of Fluid Mechanics, Volume 797

Studying Snow and Ice Changes

Student Researcher: Alexandra A. Flanigan

Advisor: Dr. Kristine Still

Cleveland State University
College of Education and Human Services

Abstract
This lesson will use data collected by NASA to compare snow and ice amounts over the span of ten years. Students will be collecting, plotting, and analyzing data to determine trends and patterns. They will access their data from the MY NASA DATA Live Access Server. By the end of the lesson, students will be able to understand how calculations can be performed on data expressed as maps, such as averaging or subtracting. They will also be able to observe changes in snow and ice over a 10-year period and draw conclusions about trends indicated by the observations. Students will work in teams and prepare a presentation that they could pitch to environmental policy makers in regard to global climate change.

Lesson Objectives
The primary purpose of the lesson is to explore how snow and ice cover have changed over ten year increments where the students live. The lesson is modified from a MY NASA DATA lesson titled "Studying Snow and Ice Changes". Students will need access to a computer with internet access. Students will be able to understand how calculations can be performed on data expressed as maps, such as averaging or subtracting and observe changes in snow and ice over a 10-year period and draw conclusions about trends indicated by the observations. The lesson begins with a formative assessment, although students are first told that they will be having a snowball fight. They will be asked to consider what their experiences with snow and ice over as far back as they can remember and write down their thoughts about snow and climate change on white computer paper. The students will then be told to crumple their papers and throw them around the room when they teacher yells, "snowball fight"! After they are engaged in the content of their lesson, they will learn how to access snow and ice cover data from MY NASA DATA. They must set their parameters to observe the Cryosphere and input the coordinates of their chosen location.

Methodology and Alignment Used
This lesson's underlying theories stem from a constructivist approach and incorporates collaboration and technology in order to engage students and promote deeper learning. Students are prompted to think about the climate they experience where they live and consider the changes that occurring over time. Working in teams to use technology and computation to manipulate data sets and drawing conclusions from data is a science and engineering practice that prompts critical thinking. Studying Snow and Ice changes with MY NASA DATA incorporates Ohio Standards for Learning (ES.3.3: Global Environmental Problems and Issues-Climate Change-Investigating climate change data) and Next Generation Science Standards (HS-ESS3-6: Use a computational representation to illustrate the relationships among Earth systems and how those relationships are being modified due to human activity).

Anticipated Results

The formative assessment used to at the beginning of the lesson is expected to spark prior knowledge and conversation climate change's effects on snow and ice. Once the students have gone through the process of collecting their data, they will compile it in an Excel file (Microsoft Excel or Google Sheets will work), and create graphs from their data. They will compare their graphs to the map of North America presented to them and draw conclusions about climate change from their data by answering the provided questions. This gives the students hands-on experience in using data for research.

To elaborate further, the teams of students will present their data to the class. They will create a creative presentation of their choice that highlights the effects of climate change as if the class was a room full of environmental policy makers. Students are also asked to be creative and make a poster to inspire important changes. This lesson fosters a sense of teamwork, creativity, and trying to come up with solutions for real world problems. Their presentations will be evaluated by their team as a whole, the class, and the teacher.

Resources

MY NASA DATA's Climate Change Lesson, "Studying Snow and Ice Changes".
https://mynasadata.larc.nasa.gov/lesson-plans/climate-change-lessons/?page_id=474?&passid=69

Solar System Exploration

Student Researcher: Abigail M. Fuhrmann

Advisors: Kim Zaccaro and Laura Lyght

The Ohio State University
Department of Education and Human Ecology

Abstract
The basis of this lesson plan revolves around teaching students about the planets for the first time, and allowing adequate time for students to learn on their own and also in a group. Students will work in a group to rotate through stations, with each station focusing on one planet, the sun, or comet (5.ESS.1). Within the stations, students are able to research and explore the planets through a variety of materials, where they will organize the information about the planet in a chart provided on a handout and specify which resource the information came from (RI.5.9), and then synthesize the information into a written summary (RI.5.9). The plan can be spread out for 3-10 days which allows the teacher to expand or condense the materials as needed. Students in the 5th grade science class where I am student teaching will be participating in the lesson and activity to create a model of the solar system.

Alignment to Grade Level State Standards

- 5.ESS.1 The solar system includes the sun and all celestial bodies that orbit the sun. Each planet in the solar system has unique characteristics.
- RI.5.7 Draw on information from multiple print or digital sources, demonstrating the ability to locate an answer to a question quickly or to solve a problem efficiently.
- RI.5.9 Integrate information from several texts on the same topic in order to write or speak about the subject knowledgeably.

Learning Objectives

- LO #1- Students will be able to explain the characteristics of a planet as it relates to distance from the Sun, size, composition, and movement. (Understand)
- LO #2- Students will be able to create a model of the solar system using facts from multiple print or digital sources. (Create)

Lesson
This lesson connects 5th grade Ohio Content Standards with NASA resources to provide a rich and engaging 21st-Century learning opportunity. The class will watch a short video clip from NASA for a general introduction to the planets orbiting the sun and their characteristics. After the digital engagement, students will complete a 3-2-1 with a class discussion following to check students' prior understanding. The students will be creating a model of the solar system using facts from multiple print or digital sources. The model will include paper, string, printed images of planets, and will be done in groups of 3-4 students. Content engagement will be through Solar System Stations that include print sources such as magazines, textbooks, non-fiction books, and digital engagement sources such as NASA video clips or websites on a Chromebook. Students will engage in student-led collaborative learning at each station and will improve their group work as well. If desired, gifted students can be station leaders and help guide students at that station.

During the stations the teacher will walk around and ask guiding questions, and make sure the tasks are being divided for students in the group. The station represents one celestial body, and at each station they must learn the name of the planet, distance away from the sun, size, composition, and orbit of the celestial body represented, using the resources. They will have a handout to guide and record their findings. After they have been through all 10 stations (8 planets, sun, 1 general comet), they will create the model of the solar system with

the string, images, and facts they collected at each station. The lesson can be split between 2-10 days, and conclude each day with a parking lot on the chalk board called “Sticky Conclusions” where each student puts a fact on a post-it-note and adds it to the drawing of the celestial bodies on the chalk board.

Materials/Resources

Each student needs the worksheet for use at each station, and a sticky note for the conclusion. Each station needs to be have a book about that celestial object represented at that station, science textbook, 2 Chromebooks open to a NASA video and NASA website about that celestial object, headphones, strings cut a particular length for each station (one per group), and images of the planets/sun/comet to color. Other materials include glue, tape, twist ties, construction paper, and also a video for the opening activity.

Theory and Methodology

This lesson allows students to control their learning through “student discovery” learning. Allowing students to see the learning that they are doing on their own and the discoveries they are making based on their interests and questions will open the door for students’ love towards science. Students are engaged in group work which allows them to ask questions towards each other, learn how to work cooperatively and also focus individually within the stations. Theory also says that groups of more than 4 students will prevent all student from engaging fully with each other and the content. While students are working, the educator is walking around talking to students and asking them engaging questions on all levels of Bloom’s Taxonomy. This allows educators to intentionally model the social interaction model of questioning, listening, reflecting and responding that scientist use in their exchanges with each other. The conclusion activity allows students to summarize what they learned that day and build on something from each day’s activities, along with show their thoughts to their peers. Teachers that incorporate a number of different teaching methods throughout a lesson ensure they will reach a large number of students.

Assessment

The assessments for this lesson began with seeing what students already knew from the video in the 3-2-1 opener after the introduction video as a pre-assessment (LO#1). Then students described the purpose of a model and how it could help us in the future (LO#2). The sticky conclusions for the end of each day allowed students to show what they learned during that day’s stations about the celestial objects and express this visually (LO #1, #2). Finally, the most important assessment is the handout where students wrote their research about each celestial object and the Solar System Model students created (LO #1, #2).

Results

Students began this lesson with very little knowledge pertaining to space, the solar system, planets and space exploration as shown in the 3-2-1 activity. Students were able to process why we were creating a model and expressed how it would help us as we continued to learn about the solar system. Students were able to explain the characteristics of a planet if they used their model they created. Some students were able to grasp the distances of the planets, and their size and composition, while others still struggled because they could not physically see them. All students were able to create a model of the solar system.

Conclusion

The lesson allowed students to learn the basic knowledge about the celestial objects in our solar system and how to use materials appropriately when researching this topic. After creating a model of the solar system, students could talk about the characteristics of the planets, sun and comets and became more engaged in the overall topic of space. The students enjoyed learning in groups and individually about the planets and crafting to create a model of the solar system.

Electric Propulsion for Commercial Aircrafts

Student Researcher: Kristen N. Fulmer

Advisor: Dr. Wei Zhang

Cleveland State University
Mechanical Engineering Department

Abstract
This concept development project investigates integrating and testing the hybrid propulsion system on commercial aircrafts and assist in the ongoing research of the propulsion team. No data will be provided since the scope of the project was done as assistance to proprietary information and such information is not the property of the author. Electric propulsion technology for manned flight capable of phasing out existing internal combustion engines will result in cleaner energy usage for aviation structures. This will take a projection of at least 15 years. Currently, electric propulsion systems use power from gas turbine engines to electrically operate fans that have been placed into the rudder of a commercial airplane. The electric system is operating from two additional motors which will provide power and feedback for occurrences of failure. My research is performed in conjunction with the exiting propulsion team at NASA Plum Brook Station in Sandusky, Ohio. Together we run testing on a full-size scale of the electrical system for the future STARC-ABL concept.

Project Objectives
The aircraft industry is continuing to integrate latest ideas into the skies, one such is making current operating aircrafts more fuel efficient using hybrid electric propulsion systems. Some major reasons for utilizing this technology are reduction in noise, pollution, low fuel costs, torque-speed characteristics, low vibration, and no altitude effects. All concerns for investors in the aviation market who may see potential losses in business. However, the major drawbacks with using electrical powered fans are they lack availability, high initial cost for integration into existing aircrafts, power comparations to the turbine engine are subpar, and endurance during normal expected flight operations. Modern electric motors have an efficiency rating of approximately 5-15 kW/kg. With a battery storage capacity that is about 5-10% of fuel. For an electric aircraft to be operable it must be efficient lightweight and slow flying. In order to fully improve electrical and mechanical properties of the aircraft a subscale was constructed, and repeatable testing has been conducted to understand ways in which the addition of the electrical system and energy storage units would operate without depriving the aircraft's on-board power source in case of failure.

Methodology
In order to make accurate comparisons between a STARC-ABL and the subscale model used in the NEAT facilities, a repeatable method of powering and testing the subscale model is needed. A crude diagram providing visual explanation to the setup of the hybrid propulsion system have been showed in Figure 1 and Figure 2. To ensure the method of powering and testing the units involved in the subscale STARC-ABL model were correct, the building chosen for the testing was fitted with the proper power unit and input power to be able to supply the necessary electricity. The building also required a wind tunnel that would simulate the intake air for the fan component. The building was previously used by NASA and was

restored for testing by NEAT. In order to place confidence in the experiment's subscale model the test's data had to match that of a full-scale aircraft.

Flight profile energy management tests are desired for the hybrid propulsion electrical system. The electrical test components were designed and previously tested by NEAT before installment into the subscale model. The loading position of the motors and storage units were positioned in a similar position that would be behind the cockpit of the plane. This carries much significance as for weight balance and energy distributions.

The flight profile energy management tests on the components were performed using various different electrical signals to the hybrid propulsion electrical system. Identification of key performance parameters for the propulsion system were appropriately simulated at ground tests and flight demonstrations using data software.

In addition to confidence being made in the subscale aircraft model understanding of the propulsion system's operating band had to be made. The propulsion power requirements had to support the loading of the aircraft and during ground conditions be reliable during cruise flight and climbing flight. The following simplified equation was used to calculate the propulsion power requirements at these flight conditions, respectively.

$$Cruise\ flight\ power = \frac{m_{total} * V_{airspeed} * g}{e_{prop} * \frac{L}{D}} = P_{L\,(\min)}$$

$$Climbing\ flight\ power = P_L + (V_{vertical} * M_{motor} * \frac{g}{e_{prop}} = P_{C(\max)}$$

m_{total} is the aircraft's mass, $V_{airspeed}$, is the measured air speed, g is the gravitational constant at atmospheric pressures, e_{prop}, is the efficiency of the propulsion system, and $\frac{L}{D}$, is the glide angle. $V_{vertical}$, is the vertical speed, m_{motor}, is the mass of the aircraft's motor including the additional weight of the propulsion system. All variables are in S.I. units.

The ratio between P_C, max power and P_L, minimum power determines the operating band. Note g is constant. The glide angle, $\frac{L}{D}$, is the ratio lift over drag. For the STARC-ABL it is approximately 15:1, as it is for any commercial aircraft.

This subscale model requires the presence of batteries and storage devices for the electrical system and this range of endurance was calculated to understand the limitations of currently available electric motors. The following equation was used to calculate the range and endurance of batteries.

$$Range = \frac{\frac{m_{batteries}}{m_{total}} * battery\ energy\ density * e_{prop} * e_{motor} * \frac{L}{D}}{g}$$

$$Endurance = \frac{Range}{airspeed}$$

$m_{batteries}$, is the mass of the batteries, e_{motor}, is the efficiency of the motors for the propulsion system and all previously denoted variables are the same demotion.

Different techniques of reliability between the components were tested. Fail safety testing techniques were put in place. Insulation of the electrical wiring were monitored and changed to material that proved more heat tolerable. The motors were installed in precise fabrication units for the ventilation and resistivity of the desired optimizable operation. Results produced when testing the propulsion system components varied little when compared to data from the aircraft's standard operation tests. Data results of the system are ongoing for the purpose of eliminating various performance parameters.

With confidence in testing, the next step in performance experiments has begun. This involves insolating component parameters that are optimizable for the operation of the propulsion system. This means research is to be performed on the specific sub components of the propulsion system; motors, generators, and fans. In addition, the energy storage capacity of the batteries will be tested. Hydrogen fuel cells, and high temperature superconducting motors are expected to reach power densities that will maintain the efficiency of the propulsion system's requirements.

Figures and Charts

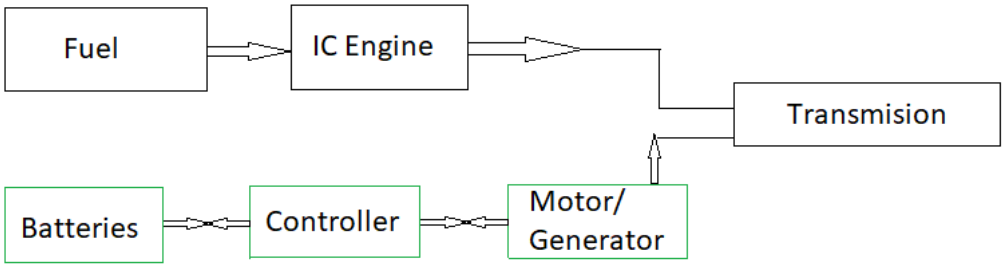

Figure 1. Schematic of hybrid propulsion system in parallel with aircraft turbine engines

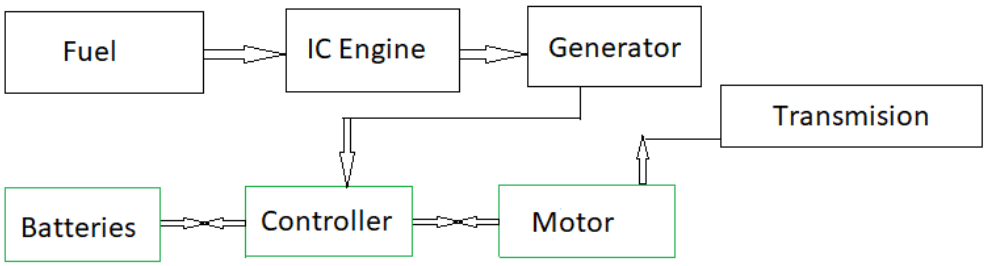

Figure 2. Schematic of hybrid propulsion system in series with aircraft turbine engines

These are very crude schematic diagrams. Figure 1 and Figure 2 show large simplifications to the overall necessary development of a hybrid propulsion system and is only used here to demonstrate the relationship the aircraft engine and electrical components will have. Electric motors are very high in power to weight ratio, meaning electric motors are efficient in converting energy, but energy storage devices, batteries, are required to feed them energy. Batteries have low energy densities and will need to position at optimizable position in the aircraft.

Significances

The tests performed showed the reliability and modifications are still to be made. NEAT is able to produce more precise data using the subscale model than before the operation of the facility. There is still work to be done in order to eliminate the errors within the signal deliveries and optimization between the motors and the propulsion system, but NEAT shows great promise in taking evaluation changes in test procedure and insolation of the components to make improvements in the reliability.

Areas which NEAT will continue to evaluate the development of powertrains for components. Insolating and understanding the operating band of motors, generators, and power electronics. Running the appropriate altitude and ground tests in wind tunnels and flight simulations, as well as being flexible to the possibility of viable concepts not previously tested.

Acknowledgments

The author of this paper would like to thank NEAT at Plum Brook for supplying access to the faculties and access to the NASA site to conduct this research. The author would like to thank Dr. Rodger Dyson, and Dr. Wei Zhang for their supervision and cooperation on the project.

References

1. NASA, NEAT facilities. NASA's Electric Aircraft TestBed. Plum Brook Station. Sandusky, Ohio
2. < https://www.nasa.gov/centers/glenn/about/fs01grc.html>

Cyber Physical Farming Robot for Organic Farm Weed Control

Student Researcher: Clarissa A. Goldsmith

Advisor: Dr. Roger D. Quinn

Case Western Reserve University
Mechanical and Aerospace Engineering

Abstract
For countless farmers, weeding poses a significant and laborious task throughout the growing season. The labor involved with manual weeding is prohibitively expensive to many, and those willing to provide such labor are becoming increasingly scarce. In addition, the cost of herbicides, the evolving chemical resistance of weeds, and environmental concerns necessitate an elimination of the use of chemicals. This lack of a cost-effective, environmentally friendly solution means that significant amounts of crops are lost to weeds each growing season. Robotics has recently begun to be applied to farming as an opportunity to reduce cost and labor and increase efficiency, particularly in the dull and laborious weeding process. An autonomous robot could be capable of extensive durations in fields for weeding and could adapt to changing operating conditions, which would overall greatly increase farm productivity. Legged robots in particular drastically decrease the amount of space required to traverse fields, can work in fields sooner after rainfall without creating ruts in the soil, and can change into a variety of configurations for confined or open spaces.

Project Objectives
This project involved the development of a prototype actuation package for the leg of a hexapod farming robot, known as Agrobot, for use in further development of a full scale robot design.
To compare to the traditional farming equipment or labor it would be replacing, the robot would need to weigh no more than 550 kg, have a maximum speed of 0.3 m/s, and have a ground clearance of 1 m. These overall weight and height requirements translate to a single leg weighing no more than 90 kg with the tallest joint at about 1.52 m. In addition, the overall design needed to minimize cost. This last requirement was left purposefully vague because no concrete and universal cost exists to use as a comparison. All of the primary requirements with the exception of ground clearance are directly affected by the method of actuation. Direct Current (DC) electric motors provide a cheap and easy to control method of actuation, so an initial objective was that the actuation be provided by DC motors.

Methodology
Using the height and weight criteria outlined previously, Agrobot's locomotion was simulated in Animatlab [1], neuromechanical simulation software used regularly in the Case Western BioRobotics lab, which output the positions, velocities, and torques at each joint during movement as shown in Figure 1b. The highest overall torque and speed values were then taken as the values to be designed for in all joints, for the sake of simplicity and additional safety. The speed and torque values were then used for component selection, with research beginning with DC electrical components and eventually moving to hydraulics and force transfer components such as linkages and gearboxes. Once component selection was narrowed down to a specific method of actuation, a preliminary 3D CAD model was developed to ensure the proposed actuation method adhered to the required range of motion while remaining within feasible actuator specifications and leg dimensions. Model development and component research were

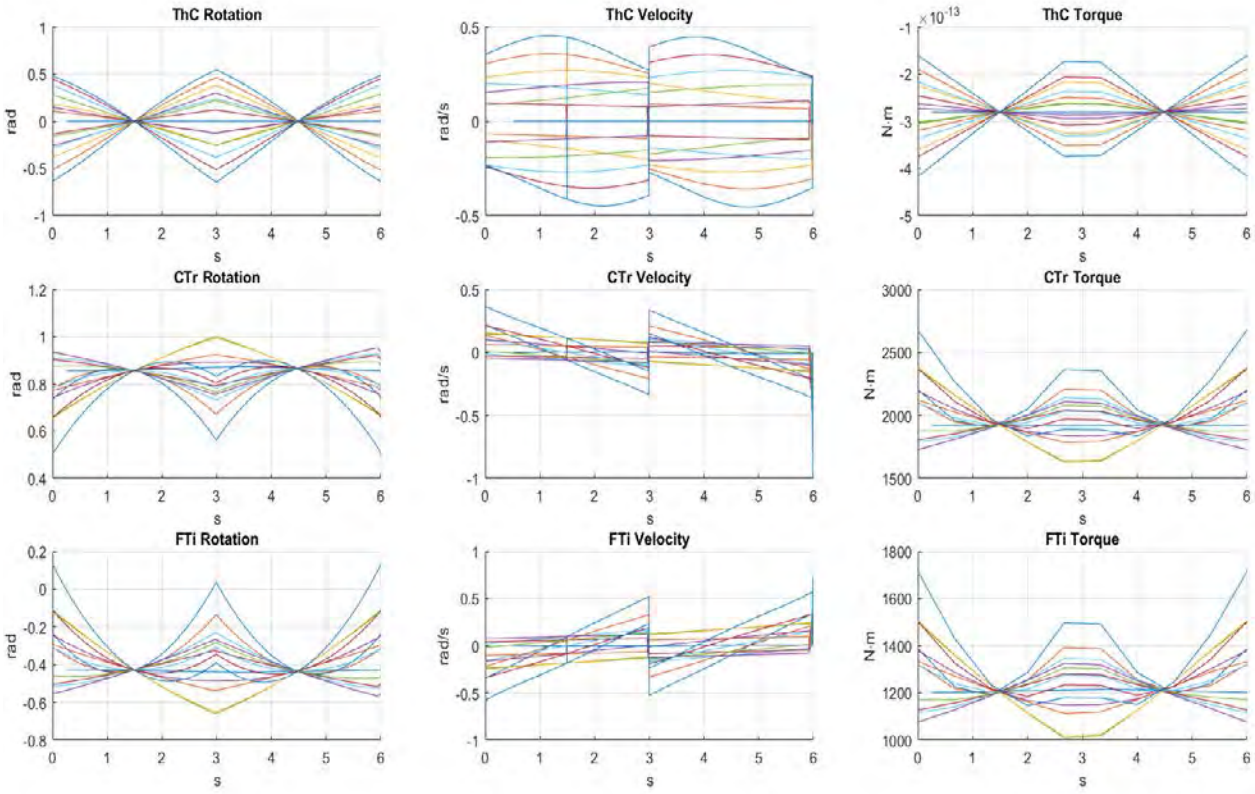

(a)

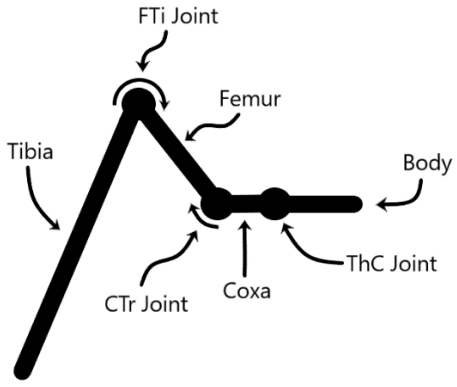

(b)

Figure 1. Kinematics of the AgroBot leg (a) One of the figures provided by the AnimatLab simulation detailing position, velocity, and torque of each joint while walking (b) Diagram of robotic leg with segment and joint definitions.

then performed iteratively to develop the overall design and select the remaining actuator specifications. These specifications achieved, the model was expanded to include full detailed components, including functional stand-ins of the actuators for use in simulation. FEA analysis was performed on the model to obtain factor of safety data and to allow for the inclusion of weight relief and other design simplifications.

Results

(a) (b)

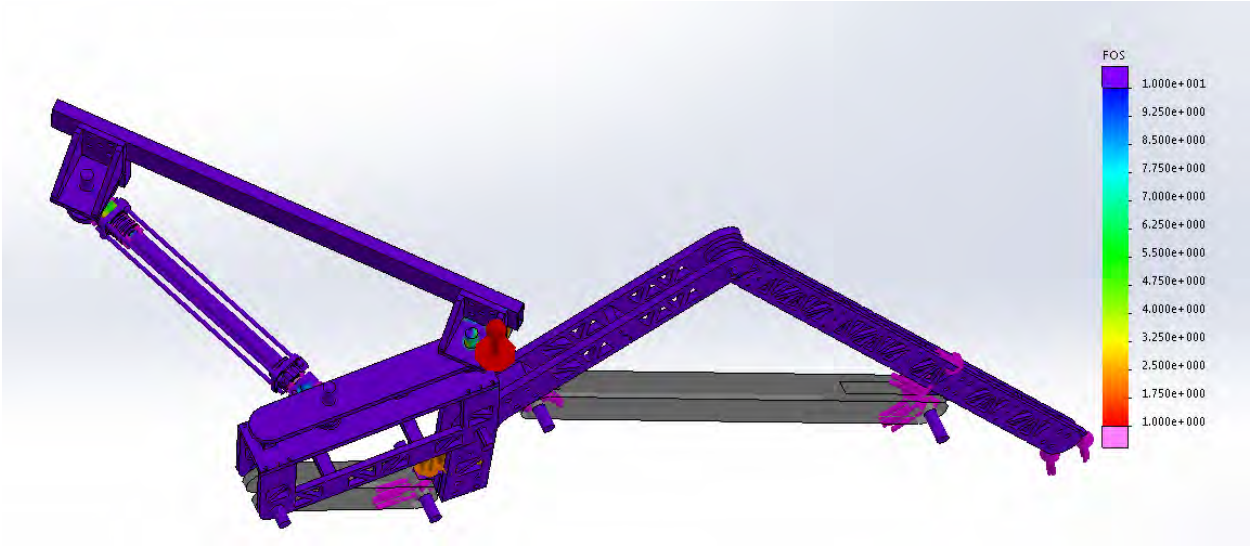

(c)

Figure 2. The current state of the AgroBot leg design. (a) Full render of the leg (b) Close-up of the "swivel bracket" portion of the leg (c) Full Factor of Safety Plot of the leg

The detailed design of the AgroBot leg can be seen in Figures 2a-b. The leg's tibia is around 1.44 m long, and the femur around 1 m. Most pieces of the assembly are made of 6061 T6 aluminum to minimize weight, with the exception of some parts of the femur and all shafts, for structural reasons. These pieces are instead made out of A36 steel for plates, and carbon steel for shafts. The entire assembly weighs around 72 kg, and can withstand all worst case scenario forces by a factor of 2. These forces correspond to the leg being prevented from moving while the actuators are powered, as well as supporting half of the weight of the robot. In many pieces of the leg, the factor of safety is closer to 10 or more, as shown in Figure 2c. Each joint in the leg is actuated by linear hydraulic actuators, also known as hydraulic cylinders. Early on in component selection research, it was determined that DC motors could not output the desired torque without some sort of additional gearing, and the required gearboxes were prohibitively expensive, ranging from $6000-$18000 per gearbox. Hydraulics were then chosen in lieu of electronics due to affordability and force capacity, despite the relative difficulty of control from electronics. The cylinders can produce up to 3000 Nm of torque at their designated joint at a rate of 2-3

RPM, relying on the fixtured offset from the joint to produce the desired torque, and weigh 15 kgs each. Each cylinder costs between $100-$200 apiece, depending on what size cylinder radius is preferred. This cost, combined with the estimated costs for other hydraulic components, adds to a total cost of $5,000 per leg, an incredibly affordable cost in comparison to DC motors.

Future Work

The Agrobot leg design is currently in the middling phases of the detail design. Some manner of foot needs to be designed to aid in maintaining purchase with the ground. Ideally, this would be a passively activated tarsal segment attached to the tibia, but could be as simple as making the end of the tibia pointed to indent into the ground. Further FEA analysis also needs to be conducted on the existing components to decrease the factor of safety from 10 to around 3 to 4, to further decrease the overall leg weight. Once the design is optimized in this manner, the components also need mounting points for hydraulic hose routing and electronic sensors. These additions might warrant additional modeling of the hydraulic hose routing. In regard to the hydraulics, the design requires further evaluation of the overall hydraulic circuit, including the final selection of valves, pumps, and power units. Once these tasks are completed, the leg could be released for manufacturing, after which a litany of tests would need to be performed to ensure the leg actuation works as intended and operates safely.

Reference

1. [1] D. M. Cofer, G. Cymbalyuk, J. Reid, Y. Zhu, Heitler W., and D. H. Edwards. "AnimatLab: A 3D Graphics Environment for Neuromechanical Simulations," Journal of Neuroscience Methods, vol. 187, pp. 280-8, 2010.

What Does an Astronaut Eat to Say Healthy and Fit?
Does My Hero That Eat Like An Astronaut?

Student Researcher: Keilee L. Guthrie

Advisor: Paige Klatt

Ohio University
Early Childhood Education

Abstract
This multi-day lesson will be an introductory lesson to students on the basic needs of living things with the focus being food and nutrient consumption to help them perform necessary tasks. Students will be given time to research what an astronaut eats prior to departure as well as while they are in space and compare that information to the research they have conducted on what their favorite superhero or person would eat in a day. Students will research how important working out and being physically fit is for their selected personnel as well as an astronaut. Students will learn the importance of food and nutrients for consumption to perform daily tasks as well as the importance of being fit to perform their job. Their research will be conducted by using approved literature and online sources and then they will create a way to share their information to the class.

Lesson
This lesson will be a multi-day lesson where each day will be broken down to focus on different aspects of the presentation as to not overwhelm students as well as give them the time to find correct and sufficient information.

The first lesson will focus on the astronauts and the teacher will have already done research to provide the students with food and physical fitness information so that all the students have the same information to work from. On this day, the teacher will introduce the basics needs of living things and how important food and being healthy is all living things. After discussing this information, the teacher will introduce the research project and plan for the week. Following this information, the teacher will use the Smartboard to discuss relevant information for the students to use as reference for their research project. Students will be given time to use their own laptops to research more information on astronauts that the student thinks will be necessary for their presentation.

The following day or two, the lesson will focus on who the student wants to conduct their own research on to compare an astronaut too. That can include, but not limited to, superheroes, athletes, or their best friend. They will be given time to research on their laptops with reliable sites such as NASA Kid's Club and others, and literature if they wish, to gain the information necessary. Students should be given ample amount of time to conduct their research which means an hour or more to help them feel confident in their information and this may spend to two days.

Students will be given time to complete their presentation while in school and they may wish to present the information in any fashion which can include PowerPoint, Google Slides, or a poster board among other ways. Students should be given ample amount of time but should be prepared to present at the end of the week after introducing the lesson.

Learning Objectives

The objective for this lesson is for my students to learn that all living things have basic needs that must be met to survive and perform daily tasks. My students will learn that those basic needs will vary among the living thing and can apply that information to the needs of other livings things as well as their basic needs. My students will learn that there are differences in every living thing on what is needed to survive, and that the environment can greatly affect those needs.

Ohio Academic Content Standards

This lesson can be modified to fit several age groups and align with multiple science standards. A few of the standards that are involved with this lesson include:

- Life Science: Physical and Behavioral Traits of Living Things & Basic Needs of Living Things (Grades K-1)
- Life Science: Interactions with Habitats (2nd Grade)

As far as technology standards go, the lesson correlates with the following Ohio's Learning **Standard for Technology:**

Strand	Description
Information & Communication (K-2, 3-5)	Topic 1: Identify and use appropriate digital learning tools and resources to accomplish a defined task.
Information & Communication (K-2, 3-5)	Topic 3: Use digital learning tools and resources to construct knowledge.

This lesson is designed to get students to be thinking about what needs individuals need to survive every day which includes food, fitness and health because needs vary among all individuals. This lesson is designed to engage students through fun learning options and choosing of their own learning modalities. This lesson is designed for children to be engaged through hands-on learning and individualized learning while using technology to help them understand their chosen individual.

Resources required

- Paper
- Pencils
- Markers
- Laptops

Assessment of Lesson

An informal assessment will used throughout the week that the students are spending time to research and work on their own projects. The creation of the project, in whatever format the student choose, will be the formal assessment of the whole project.

Critique and Conclusion of the Project

Overall, this will be a fun and engaging project that will allow students to use a variety of learning modalities as well as interdisciplinary project. If there is a greater allotment of time needed based of the grade level that would be suggested as not all students move at the same speed. However, this will be an activity that students will enjoy, and it is a great way to learn more about your students as you will learn more about their favorite hero or individual that they compared an astronaut, too.

Tetrachlorethylene in Dry Cleaning

Student Researcher: Hanin M. Hamid

Advisor: Christopher Huhnke

Cuyahoga Community College
Engineering Technology

Abstract

Dry cleaning is a cleaning process for clothing and textiles using a chemical solvent other than water, which is called Perchloroethylene or Tetrachlorenthylene. It commonly known as "PERC" in the industry. In 1925, the production of PERC occurred in the United State, but it was used for the first time as a dry cleaning in 1934. Today, it is considered to be the most widely used solvent because of its ability to dissolves greases, oils and waxes without affecting fabrics. Tetrachlorethylene is present in the air we breathe, the water we drink, soil, and less often in food. Furthermore, as any other volatile organic solvent, PERC can cause a serious health hazards if exposure is not properly controlled. What makes PERC such an effective solvent? How does it affect the environment and human's health? How can we control the hazards of using PERC? What is the proper way of disposal? Despite the hazords, PERC is highly beneficial in the dry-cleaning industry if it is handled correctly and disposed properly ("Perchloroethylene (PCE) Pollution," n.d.).

What is PERC?

PERC is a halogenated organic compound composed of two atoms of carbon and four atoms of chlorine (two chlorine atoms linked to each carbon). The two carbons are linked to each other by a double chemical bond. It is a colorless liquid with a sweetish smell which is not flammable under room temperature and pressure. It evaporates easily into air. When it's in the air, it can condense again and get into soil and water. It can also be washed out of the air with rain. PERC can also get into soil and water during waste disposal, or by leaking from underground storage tanks ("Perchloroethylene (PCE) Pollution," n.d.).

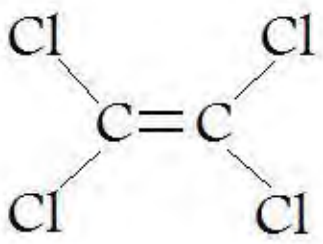

Figure 1. Chemical Formula of PERC

The Risks of PERC on Humans and the Environment

PERC is found in the air, drinking water, and soil. It can be detected in most people's blood as well as in breast milk. It was proven by multiple scientific and government agencies that PERC's most dangerous noncancerous toxicity is brain and nervous system damage. Therefore, they have set a safe exposure. PERC most likely enters the body from inhalation of vapors, and eventually causes multiple issues including, but not limited to the following:

- Dizziness, drowsiness and loss of coordination.
- Mild loss of memory, visual perception, and reaction time.
- Redness and blistering of the skin after prolonged dermal contact.

PERC is a reasonably anticipated carcinogen, which means that it was proven to cause tumors in mice and it has the potential to cause cancer in humans, such as lung, colon-rectum, Esophageal, and bladder cancer. In addition, PERC can be found in the air and is shown to be oxidized with a half-life of 96 days. It can also be found on the subsurface, and underground water due to the disposal and leaking issues that will contaminate water bodies and surrounding areas and spread contamination to anything that it reaches ("Tetracholorethylene (Perchloroethylene)," 2014).

Regulation of PERC Use

Multiple government agencies regulate Tetrachlorthylene levels and exposure to ensure human and environmental safety. The Occupational Safety and Health Administration (OSHA), which is responsible for health and safety regulations in the workplace, limits workplace exposure to Tetrachlorethylene in the air to 100 parts per million (ppm) during an average 8-hour work day and a maximum of 300 ppm over any-five minutes period (OSHA, 2005).

The EPA limits the concentrations of Tetrachlorethylene in drinking water to 0.005 mg/L or 5 parts per billion (ppb), with an ultimate goal of 0 ppb. Indeed, the US Food and Drug Administration (FDA) has set a limit of 5 ppb in bottled water (" Perchloroethylene," 2000).

Proper Disposal of PERC

Prior to all the regulations and the rules that was set to the amount of safe exposure to PERC, dry cleaners used to dump off the remaining waste into the nearest area as it was helping tree growth without realizing the extent of health hazards that it was causing to soil and people. Therefore, government and health and safety agencies have regulated the process of disposing PERC by containing hazardous material to a licensed, permitted waste treatment, storage, and disposal facility (TSDF) assuring that containerization process is done accurately and no material is leaking through ("Perchloroethylene (PCE) Pollution," n.d.).

References

1. OSHA. (2005). Reducing Worker Exposure to Perchloroethylene (PERC) in Dry Cleaning. Retrieved March 22, 2018, from https://www.osha.gov/dsg/guidance/perc.html
2. Perchloroethylene (PCE) Pollution. (n.d.). Retrieved March 22, 2018, from https://www.environmentalpollutioncenters.org/perchloroethylene/
3. Tetrachloroethylene. (2000, January). Retrieved March 22, 2018, from https://www.epa.gov/sites/production/files/2016-09/documents/tetrachloroethylene.pdf
4. Tetrachlorethylene (Perchloroethylene). (2014, January 6). Retrieved March 22, 2018, from https://www.cancer.org/cancer/cancer-causes/tetrachlorethylene-perchloroethylene.html

Moon Movements

Student Researcher: Elizabeth K. Han

Advisor: Dave Andereck

The Ohio State University
College of Education and Human Ecology

Abstract
Students will learn about moon phases and their relationship with positions of Sun, Earth, and Moon through an inquiry-based lesson. In groups, students will work with various-sized balls that represent Sun, Earth, and Moon to act out position and movement of each body. Students, applying and building on prior understanding of the behavior of light, will arrive at the fact that the half of the moon's surface that faces the sun is the portion that reflects light and is visible to our eyes. Students who represent the moon will color half of their ball black to represent that half which is not reflecting sunlight therefore not visible from Earth. Then, students who represent the earth can share what they observe of the moon—the different moon phases based on position of Sun, Earth, and Moon. This activity for understanding why the moon appears to us in different phases will lead into the activity of sketching phases, and finally, creating a moon phase model out of Oreo cookies.

Project Objectives
Students will investigate the positions of the sun, moon and Earth to detect and test the reasons why the moon and sun appear to change position in the sky and the phases of the moon.

Objectives are aligned with the following 5th grade science standard:
Most of the cycles and patterns of motion between the Earth and sun are predictable.

Methodology to be Used
This 5th grade science lesson plan, based on NASA Space Place's "The Moon's Phases in Oreos" activity, is intended for two fifty-minute class periods. Rooted in inquiry-based learning, the amount of information that the instructor "tells" students is limited. Rather, the teacher's role is to facilitate student learning through asking probing questions. Students are encouraged to use available materials to model the sun, moon, and Earth, make observations, answer guiding questions, and build their own understanding of the effects of position on the phases of the moon.

Materials
Handout, cardboard box, clay balls, string, tape, flashlight, ping pong balls, sharpie markers, Oreo cookies, plastic spoons

Lesson Plan
In groups of three to four, students acquire a cardboard box, clay balls, string, tape, and a flashlight. Using these materials, they represent the Earth and moon with differently-sized balls of clay, hanging in the cardboard box. Students take turns shining the flashlight at the Earth and moon clay balls to observe the patterns of shadow and light on the spheres. They are hands-on with the sun-earth-moon model, taking special note of the appearance of the moon from the Earth, while answering guiding questions on a handout. From this activity, students walk away with an understanding that the sun always illuminates half of the moon's surface (except for when the moon enters the Earth's shadow). This understanding is

assessed at the end of this activity, when students are asked to color in a ping pong ball to represent the portion of the moon which is never reached by sunlight. If they successfully color half the ping pong ball, students move on to the next activity, and if not, they are re-directed to the model of clay spheres for another round of observations.

Next, students stand and act out the roles of sun, moon, and Earth. The sun student represents the group's source of light. The moon student holds the half-shaded ping pong ball with respect to the sun, so that the unshaded half faces the light source. As the moon student orbits around the Earth student, the Earth student makes observations about the appearance of the ping pong ball moon, and sketches the various moon phases. Students switch roles until each make observations and sketches. They discuss and compare their results until they reach an agreement on a sketch. After reaching a consensus, students have their picture approved by the instructor.

After moon phase pictures have been approved, each group receives plastic spoons and four Oreo cookies to carve out their moon phases. The "Moon Phase and Libration, 2018" recording taken by NASA's Lunar Reconnaissance Orbiter can play on the classroom's screen as students are carving their moon phases. The learning segment is wrapped up with a whole class discussion of findings and consuming the Oreo cookie moons.

Expected Results

Main Ideas

One of the key concepts that students are to realize through the first group activity is that sunlight reaches and illuminates up to one half of a spherical body—that is, the Earth or moon. No matter where the moon is, the sun illuminates the half of its surface which faces the sun (an exception is when the moon is within the Earth's shadow).

One of the key concepts learned through the second activity—acting out the sun, Earth, and moon—is that the moon's appearance looks different from the Earth, based on the position of each of the three bodies. The illuminated portion of the moon is always the half facing the sun, and this does not change throughout the moon's orbit around the Earth. However, the shape of the visible portion of the moon from the Earth's perspective does indeed change as the moon orbits around the Earth. Students observe and sketch 8 moon phases. (At the 5th grade level, observational differences in moon phases are the emphases, not the names of phases).

Accommodations and Modifications

Extension questions for enrichment may include observing and discussing lunar and/or solar eclipses.

An accommodation for struggling students may include observing and sketching 4 moon phases.

Possible Misconceptions

The moon is a light source. Students need to know that the moon does not produce its own light. The moon is visible from the Earth because it reflects light from the sun.

The sun illuminates all of the moon. Students may "see" the entire moon-sphere during the first experiment. Light sources other than the flashlights being used need to be limited during the first experiment so that students can observe that the flashlight illuminates half of the moon-sphere and that other visibility on the spheres are just scattered light from other sources in the room.

The entire moon is always visible from the Earth. During the second activity, the moon student must hold the shaded ping pong ball accurately, with the "lit" half facing the sun. The Earth student should

only be noting the “lit” portion of the ping pong ball, since the moon does not produce light and its only visibility is the portion that reflects sunlight.

References

1. NASA Space Place. (2014). *The Moon’s Phases in Oreos*. Retrieved from https://spaceplace.nasa.gov/oreo-moon/en/
2. NASA’s Scientific Visualization Studio. (2017). *Moon Phase and Libration, 2018.* Retrieved from https://moon.nasa.gov/resources/154/?category=videos

Fracture Testing of 3D Printed, Carbon Fiber Reinforced ABS

Student Researcher: James D. Harding

Advisor: Dr. Pedro Cortes

Youngstown State University
Chemical Engineering Department

Abstract
Additive manufacturing has found useful application in a number of modern industries including: the automotive industry, aerospace industry, and the biomedical industry. Fused deposition modeling (FDM) is a popular method of production for thermoplastic parts. However, production via FDM often constrains the material's mechanical properties when compared to other manufacturing methods. One proposed method of fixing this property deficit is the addition of reinforcements such as short carbon fibers.

The research conducted investigated the fracturing properties of 3D printed Acrylonitrile Butadiene Styrene (ABS) that has been reinforced with short carbon fibers. Initially, production parameters for the prints were established. Then, tensile and flexural test were carried out experimentally with parts produced via that method. Determinations were also made regarding material properties at low and high velocity impacts.

Project Objectives
The overall objective of determining the fracturing properties of 3D printed, carbon fiber reinforced ABS can be simplified into several objective statements.

1) Determine a methodology for producing consistent, high quality 3D prints utilizing carbon fiber reinforced ABS filament.
2) Preform tensile and flexural tests on prints to obtain the related properties.
3) Investigate the behavior of 3D printed, carbon fiber reinforced ABS impact plates when subjected to high and low velocity impacts

Methodology
The 3D printing was done on a Maker Bot 2X. In order to establish a reliable method for production of 3D prints a system of trial and error was started at the standard conditions for regular ABS. Upon establishing an effective extrusion temperature and head size, print speed and plate level were examined.

Upon achieving the production of high quality prints, parts were created for testing the tensile strength of the printed material. Utilizing a Universal Instron Machine and Blue Hill 3 software, the samples were slowly pulled apart at a rate of 2mm/min and raw testing data was obtained. The tensile strength of the material was calculated using this raw data and the following equations:

$$\sigma = \frac{F}{A}$$

$$e = \frac{\Delta L}{\Delta Lo}$$

Where σ, is the stress, F, the applied force, A, the cross-sectional area, e, the engineering strain, ΔL, the elongation, and ΔLo, the original length of the testing sample. Table 1 shows the data obtained from each sample.

The flexural test was done in a similar manner to the tensile test. Parts in the shape of a rectangle were produced and placed on a Universal Instron Machine. The machine was outfitted for standard 3 point bending testing and the loading rate was set at 2 mm/min. Raw data was recorded and obtained via the Blue Hill 3 software and the sample stress/strain was calculated using the following equations:

$$\sigma = \frac{3FL}{2bd^2}$$
$$e = 6\Delta L \frac{d}{Lo^2}$$

Where F, is the load acting on the sample, b, the width of the sample, d, the thickness of the sample, L, the length of the span, and ΔL the elongation. Table 2 shows the data obtained from each sample tested.

For the low velocity impact testing, square plates of four inches in width and 4 inches in length were printed and placed at the bottom of a free fall impact tower. The tower is equipped with a polycarbonate impactor weighing 4.04 Kg that was dropped from 10 inches, 15 inches, and 20 inches above the impact plate. The force of the impact is calculated via the potential energy equation:

$$E = m*g*h$$

Where E is the low velocity impact energy, m, the mass of the impactor, h, the height at which the impactor was dropped and g, the gravitational constant. Table 3 shows calculated energy of each impact.

For high velocity impact testing, the test plates used were identical to the ones utilized in the low impact testing. The sample was secured in container at the end of a gas gun barrel. The gun would build up various amounts of pressure by siphoning nitrogen gas from a nearby tank and expel it to launch the impactor at the sample. The velocity of the impactor was measured by a chronograph that was attached to the system. The gun's sabot catcher would stop the sabot and only allow its payload, a small ball bearing of weight 0.002 Kg, to make contact with the sample. The energy of the impact was calculated with the following equation:

$$E = \tfrac{1}{2}\, mv^2$$

Where m is the mass of the projectile, v is the velocity at which the projectile travels, and E is the final impact energy. Table 4 shows the calculated energy of each impact

Results Obtained

It was discovered that the following conditions be met to produce high quality 3D printed, carbon fiber reinforce, ABS parts. Extrusion temperature should be set at 235°C, bed temperature should be set at 110°C, the head size should be approximately 1 mm in diameter, and the print could be performed at 40 mm/s or less.

The tensile tests revealed an average maximum stress of 34.2772564 MPa and an average maximum strain of 0.053416273. The flexural test data suggested an average breaking stress of 74.86523413 MPa and an average breaking strain of 0.021371493. During the low velocity impact testing the test plates were able to withstand the 10 inch drop, 10.0666296 J, with only a minor indentation the size of a golf ball dimple. The plates completely failed to stop the weight at the 15 inch, 15.0999444 J, drop height. It is worth noting that while the plate was completely pierced, similarly to the 20 inch drop, the impact bar did not completely push through and became lodged in the material. This suggests that the 15 inch impact was near the 7.5 mm thick plate's perforation limit. During the high velocity impact testing, the 7.5mm plates were able to withstand 4.7 J of force, but were completely perforated when exposed a force of 7.8 J. The necessary amount of energy to pierce such a plate is somewhere in that range.

Figures and Tables

Table 1. Tensile Testing Data of 3D Printed, Carbon Fiber Reinforced ABS Parts

Sample	Applied Force (N)	Width (in)	Thickness (in)	Cross Sectional Area (in^2)	Cross Sectional Area (m^2)	Stress (Pa)	Length (mm)	Elongation (mm)	Strain
1	305.82675	0.309	0.0415	0.0128235	8.27321E-06	**36965914.97**	25.4	1.39342	**0.054859**
2	245.67238	0.2846667	0.041	0.011671333	7.52988E-06	**32626345.23**	25.4	1.33015	**0.052368**
3	241.08246	0.2676667	0.042	0.011242	7.25289E-06	**33239509.02**	25.4	1.34675	**0.053022**

Table 2. Flexural Test Data of 3D Printed, Carbon Fiber Reinforced ABS Parts

Sample	Load (N)	Width (mm)	Thickness (mm)	Span (mm)	Stress (Pa)	Elongation (mm)	Strain
1	174.0052	15.63333333	4.806666667	100	**72262650.48**	6.84341	**0.019736**
2	198.9353	15.63333333	4.86	100	**80812582.52**	7.45339	**0.021734**
3	193.8378	15.63	5.10	100	**71520469.39**	7.4	**0.022644**

Table 3. Low Velocity Impact Testing Data of 3D Printed, Carbon Fiber Reinforced ABS Plates

Sample	Thickness (mm)	Height (in)	Height (m)	Mass (Kg)	Gravitational Constant (m/s^2)	Potential Energy (J)	Break through?
1	7.676666667	10	0.254	4.04	9.81	**10.0666296**	**No**
2	7.446666667	20	0.508	4.04	9.81	**20.1332592**	**Yes**
3	7.476666667	15	0.381	4.04	9.81	**15.0999444**	**Yes *Barely**

Table 4. High Velocity Impact Testing Data of 3D Printed, Carbon Fiber Reinforced ABS Plates

Sample	Mass (kg)	Velocity (ft/s)	Velocity (m/s)	Energy of Impact (J)	Break Through?
1	0.002	352	107.2896	**11.51105827**	**Yes**
2	0.002	225	68.58	**4.7032164**	**No**
3	0.002	290	88.392	**7.813145664**	**Yes**

Three samples were chosen for each experiment sample size in an attempt to balance the time available for fabrication of necessary parts and minimizing the likelihood of errors/outliers.

Acknowledgments
The author of this paper would like to thank Dr. Pedro Cortes for his continuous support and instruction in proper data collection over the course of this project. The author would also like to thank Jay Wargacki for providing the author access to both his lab and his experience with 3D printers. Finally, the author would like to extend their thanks to Manush Ravi Prime and the gentleman of the machining lab for sharing their knowledge and equipment.

Measurements of Great Proportions

Student Researcher: Kaleb A. Irey

Advisor: Dr. Robert Chasnov

Cedarville University
Department of Science and Mathematics, and Education

Abstract
This lesson explores similar shapes, proportions associated with them, and their use in the real world. The lesson will begin with a brief review of what similar shapes are, then moves into groupwork where groups will first use a model to find the diameter of the moon, then they will receive an experiment model that is useful to estimate the diameter of the sun, which they will assess. Then, students will discuss possibilities to get better results if they ran the experiments again.

Lesson
This lesson will span two or three classes. The beginning stages of the lesson are found in NASA's "Diameter of the Moon" lesson. After quickly reviewing what makes shapes similar with the whole class, emphasizing the congruent angles and proportional size, I explain the model to the right, used to calculate the moon's diameter, indicating where and why there are similar triangles involved.

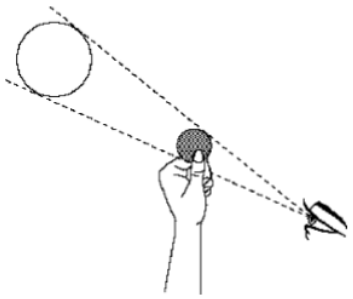

From this, we will derive the proportion used in the experiment. Students will then have a chance to go outside to use the experiment and find the moon's diameter. Students who did so successfully and satisfactorily will then be given instructions to measure the diameter of the sun using an index card and a punched hole. They must first indicate where a similar shape lies and what proportion will be used in the experiment, with some help from the teacher. Then the students will execute the sun experiment to find its diameter.

Once both experiments are finished, the students will be given the true diameters of the moon and sun, then will have time to finish the lesson by discussing what factors may have caused greater error during their experiments. They will be encouraged to seek ways to better their results in the future, such as greater precision, more trials, etc.

Objectives

- To form a greater understanding of similar shapes and the proportions associated with them.
- To help students identify similar shapes in real life rather than on a white board.

Alignment

- Ohio's Geometry—Similarity, Right Triangles, and Trigonometry Standard 5
- Ohio's Geometry—Modeling with Geometry Standard 1
- Ohio's Algebra—Creating Equations Standard 1

Theory
This lesson is more teacher-centered due to the lectures, review, and teacher approval necessary. I find this teaching style more attractive since students may otherwise feel they are taking shots in the dark. However, the lesson becomes progressively less about what the teacher says and more about what the students think, indicating that the teacher is not the giver of correct answers, but that students may think critically themselves and constructively criticize their own work to arrive at good answers.

Student Involvement

Students will be out of their seats and measuring huge distances related to the sun and moon, so it is to be expected students are more involved during this lesson than if they simply sat as the teacher used a white board to teach about similar figures and proportions. They will also be provided with more of an open-ended question than what a homework sheet would normally give, causing them to think deeper about the model rather than recite answers they have learned from pattern recognition.

Materials
Each group will require a cardboard disc with diameter around 2 cm, and a stake or window sill the disc can be placed on to cover the moon to perform the first experiment. They also each require an index card, a hole punch, a meter stick, a centimeter ruler, and a piece of paper to mark for the second experiment. None of these materials would be difficult to obtain and may be found in a science classroom already.

Experiment Layout
For the moon experiment, students will first lay the cardboard disc exactly covering the moon from their point of view. They will then recognize and solve a proportion using the diameter of the cardboard disc, the distance to the moon, and the distance from their eye to the disc, finding the diameter of the moon.

For the sun experiment, students will punch a hole into their index card and hold it as perpendicular to the sun's light as possible. They will position a sheet of paper about 1 meter away, then trace the sun's image as best they can. They will then create and solve a proportion using the diameter of the image, the distance to the sun, and the distance from the punched hole to the image to find the sun's diameter.

Assessment
Students will be loosely assessed as the teacher discusses the sun experiment's setup with them. The students will also turn in diagrams of both experiments that will indicate what measurements are used in the proportions. Furthermore, they ought to submit the work they did to set up and solve a proportion for the respective diameters. The last thing required of them will be a few sentences summarizing whether they thought their calculation to be relatively good compared to the true diameters of the moon and sun, as well as some quick ideas of what may produce better results if they were given these experiments to perform again. They will also be encouraged to submit other ways to use proportions or similar figures to measure things otherwise difficult.

Conclusion
It is assumed students may have drawbacks when it comes to finding the similar figures within the experiments, since the idea is so abstract and foreign. Yet, the teacher interaction ought to help the students start to understand how to identify similar figures in real life situations. Otherwise, it is good practice for solving proportions, measuring precisely, and running experiments that use mathematical concepts to model our universe.

How Do Space Heroes Stay Alive?

Student Researcher: DeVante M. Jackson

Advisor: Dr. Rajeev Swami

Central State University
College of Education

Abstract
In this Morning Activity, we will be tackling space food and nutrition. With each student being different, this lesson will be interactive, informational, and adaptive. It will consist of a basic introduction, open floor discussion, hands-on activity, and social awareness activity. These will all be approached in a unique manner. We will also be breaking down space food and nutrition in two different ways. First scientifically and then mathematically. This will increase the lessons chances of being effective. For example; in-order to speak in the open floor discussion, the student must first try a piece of dried fruit. Playing with the sense will hopefully serve as a catalyst to many ideas or talking points. There will also be 3 energizers in your back pocket to keep the scholars involved

Objective
The scholars will design their own protein bar with organic materials and dry it out using an oven of some sort

Science Standards:
- Senses
- Matter, energy, and organization in living systems
- Personal Health

Math Standards:
- Computation
- Measurement
- Reasoning
- Observing
- Communicating

Materials
Variety of dried fruit, soft sweet potatoes, hemp seeds, rice, almonds, nutmeg, honey, blender, oven, pans, and knife

Energizers

These energizers are used to keep the scholars involved. When they seem to become disengaged or tired, pull one of these of your back pocket to change the mood.

Space Chairs (Musical Chairs)
- Gets the scholars up and out of their chairs
- Must use a take-off simulation to start the music
- Use music that the scholars enjoy

Shooting Stars

- Call out different things to challenge the scholars' observation and listening skills. If the said "things" apply then those students must switch chairs. For example, "I need all my supernovas wearing red shows to burst!"

Guess the Dried Item

- One student must pick and taste a piece of dried fruit. With the others not knowing, they must act out or describe the item. Make sure to include vegetables, jerky, and a variety of dried fruits to lighten the mood.

First, start the activity with a video of monkeys in space. This will make the scholars interested because it's something different. Second, Show a short video on space travel and its necessities.

Discussion Questions

1. Who is your favorite super hero and why?
2. What do you think you favorite super hero eats to stay alive?
3. What do you eat to stay alive and why?

Activity instructions (Give every 3 students a different piece of dehydrated or dried food)

1. Place all items used for the protein bar on the same table and a general information/ history sheet on dehydrated foods.
2. Separate the groups by what fruit they ate
3. Each group should have a 1 Astronaut (President and or speaker), 2nd Astronaut (gets supplies from the table), and a 3rd Astronaut (records data)
4. Each group must have a plan with reasoning as to why they want the items they chose
5. Once the game plan has been told to you, allow the 2nd Astronaut to get the wanted items from the "Launch Pad"
6. Instructor must visit each station with the blender to assist the scholars in mixing their material. The 3rd Astronaut must work with the group on proportioning and translate that to the instructor.
7. Once all groups have finished the blending portion, spread the mixes and allow the bars to dry out all day on law heat.
8. As the mixed are being dried, the 1st Astronaut much create a sales pitch that includes a quote from a famous astronaut, and it must be named after a spaceship or space center. The pitches will be given the next day, as the class tries everyone's bar.
9. Be sure to make your own bar prior to this activity and allow for them to taste it.

Conclusion

Allow for the presidents to speak on their bar and compare it to other protein bars today. Revisit the discussion questions and then ask each group to respond as a collective to the following questions.

1. Would your favorite super hero eat your bar? Why or why not?
2. What reason did you guys choose the items you did?
3. Would you feed this to a space monkey?

Investigation of Sensors for Monitoring Corrosion on Suspension Bridge Main Cables

Student Researcher: Tyrone Jacobs, Jr.

Advisor: Dr. Douglas K. Nims, Ph.D., P.E.

The University of Toledo
Department of Electrical Engineering and Computer Science

Abstract
The Anthony Wayne Trail Bridge (AWB) is a suspension bridge that spans over Maumee River in Toledo, Ohio. It was constructed in 1931 and since then, there have been many rehabilitation projects done on the bridge. There has been a report that revealed severe corrosion and wire breaks on the insides of the main cables, in which those cables were given a status of "poor". This report led the Ohio Department of Transportation (ODOT) to consider installation of a dehumidification system on the bridge. Main cable corrosion of suspension bridges is becoming a wide-spread problem, especially overseas. Wires of the bridge main cables are now wrapped with strands and therefore, corrosion is hidden in visual inspections. New efforts have been worked towards to prevent corrosion of the wiring, like a dehumidification system. This system will blow dry air into the cabling and exhaust humid air from it. This will allow me to study the relationship between relative humidity and the corrosion rate of the cabling.

Project Objectives
The primary objective of my research is garner a better understanding of dehumidification systems and checking the functionality of this system before it would be installed onto the Anthony Wayne Bridge (AWB). First, I wanted to study dehumidification systems and its application on suspension bridges. Secondly, I wanted to gain an understanding of acoustic and linear polarization resistance corrosion sensors and how they help me monitor and record data. Lastly, I wanted to simulate 2 (two) tests by creating an environmental chamber that would simulate the real-life conditions that the wiring would go through.

Methodology Used
The first step in beginning this process is to setup a makeshift system as to where we put a dehumidification system into actual practice to see how we can the relative humidity levels inside of the cable wrapping, and then, evaluating our results. My first step was to help design the environmental chamber used to simulation the conditions a cable from the Anthony Wayne Trail Bridge would be under. Once the dehumidification system is built, I moved onto the first test. This test is one that will allow me to use a humidification system on the cables and will let me further understand the relationship between relative humidity and corrosion rates. I increased the relative humidity amounts to a certain extreme and noticed that the dehumidification system started to reduce humidity levels.

The data acquisition system that I used recorded and graphed the data (which I will show later in the "Results" section). This step was repeated at least 60 – 80 times over 1-minute intervals. With each minute that passed, I documented where the humidity level was. As you will see later, the results will show you that the humidity level cannot go below 40%, nor can it go above 80%.

After this test is over, I conducted a second test. With this test, I was able to set a lower and upper limit of humidity level that was controlled. The “lower limit” humidity is where when reached, the dehumidifier will turn of. The “upper limit” humidity level is where it will turn on. The dehumidification system was turned off and the environmental chamber was subject to humid air for an hour, or more, to allow the humidity level to rise. This is what I previously mentioned where I explained that I had to watch the humidity level rise over 1-minute intervals, and monitoring the exact level of humidity at each minute. The objective of this second test is to set limits and to not let the humidity pass those extremes, or limits, to start the process of corrosion.

Results Obtained

Which you will see in the Figures/Charts section, the results of our tests showed us the correlation between relative humidity and corrosion, and how when the cables are under a certain condition, what could potentially happen to them.

Significance and Interpretation of Results

The “preliminary test” that I conducted showed me the relationship between relative humidity and corrosion rates. As the relative humidity hit a certain level, the corrosion rate would start to grow. Also, when the relative humidity hit its maximum, the corrosion rate’s maximum was around the same area as well. A second test was also conducted to check the feasibility of keeping relative humidity in a certain level in which no corrosion occurs. The lower and upper limits of relative humidity were defined by the controller. The figures under “Final Test Results” show that the relative humidity level cannot pass a level of 50%, and this is where corrosion stops growing.

Figures/Charts

The figures below show the relationship between humidity and the dehumidification system over a certain period (typically an hour to an hour and twenty minutes). You can see the real-time results through the monitored and recorded data points.

Preliminary Test Results

As you can see in Figure 1, the humidity level reached 80% after 39 minutes, and then dropped to 64 and lower after 40 minutes. As you can also see below, the corrosion rate peaked at about 2.00E-5 g/cm2/year at 75 minutes.

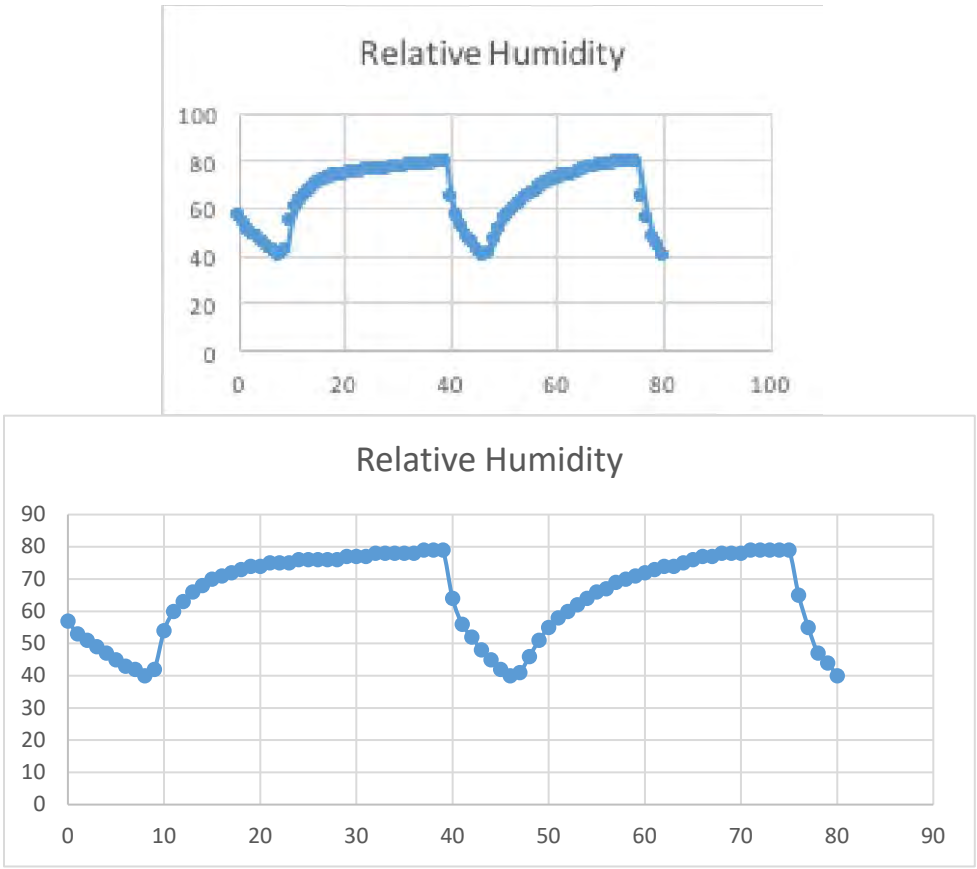

Figure 1.

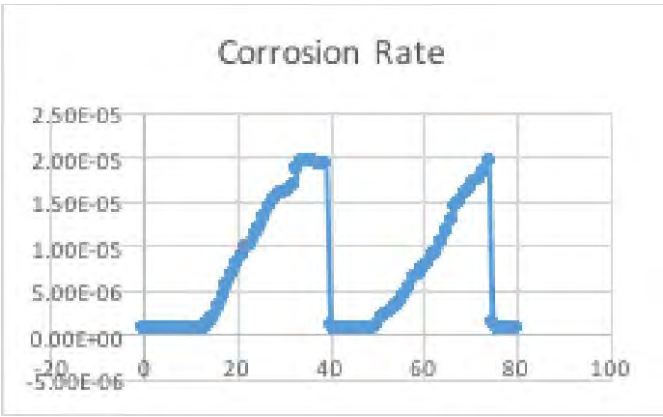

Figure 2.

Once the dehumidifier and injection fan started to generate dry air, the relative humidity began to fall and the corrosion rate dropped significantly. From this test, I was able to conclude that the dehumidification system worked as I thought it would and that there would be no occurrence of corrosion beyond 60%.

Final Test Results

For this test, the chamber was subject to humid air a period of time to allow the humidity level to rise and to let the corrosion to start growing. As seen below in Figure 3, when the relative humidity went beyond 60%, the corrosion rate started to rise (you can see this in Figure 4). In minute 10, you can see the relative humidity level reach its maximum of 80%, as well as the corrosion rate hitting its maximum of about 5.00E-06 g/cm2/year.

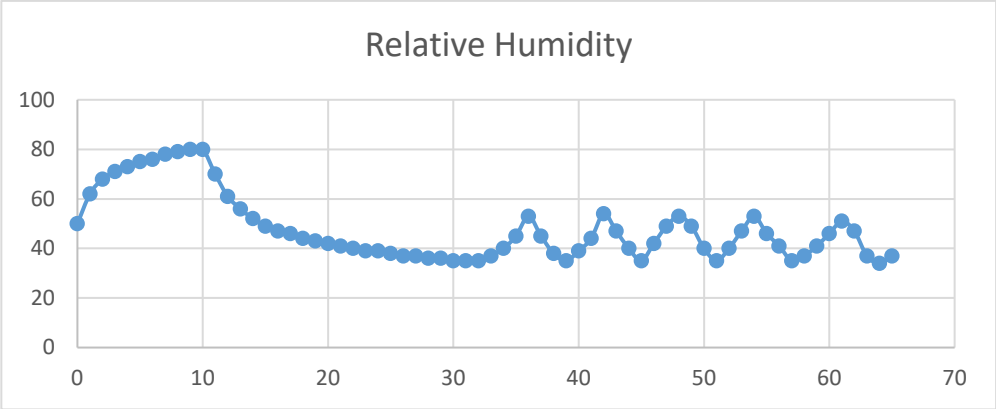

Figure 3.

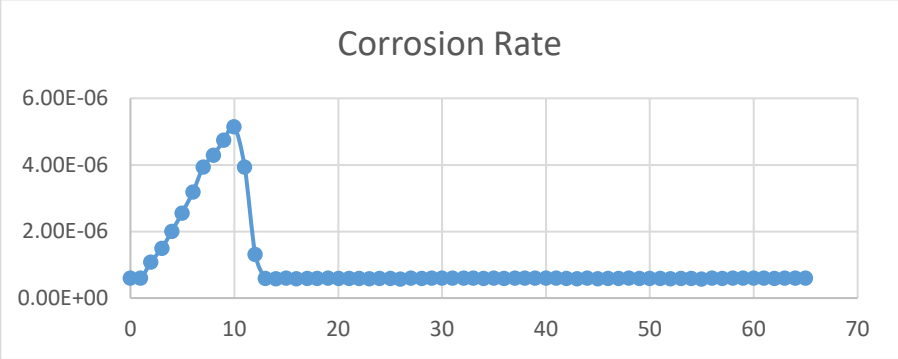

Figure 4.

Acknowledgments

I first would like to thank my advisor, Dr. Douglas Nims, Ph.D., P.E., for guiding me through my research for these last 5-6 months. Secondly, I would like to thank a student pursuing his Master's in Civil Engineering, Abdullah Haroon, for taking time out of his busy schedule to meet with me and check in on my progress. I would also like to give thanks to my National Society of Black Engineers UT Chapter Advisor, Dr. Lesley Berhan, for believing in me and helping me secure a research opportunity. Finally, I would like to give thanks to the Ohio Space Grant Consortium, NASA, and other organizations who made this all possible. Thank you.

References

1. Bloomstine, Matthew L., and Ove Sørensen. 2006. "Prevention of Main Cable Corrosion by Dehumidification." *5th International Cable Supported Bridge Operators' Conference,* New York.
2. Bloomstine, Matthew. 2011. "Main Cable Corrosion Protection by Dehumidification Experience Optimization and New Development." *6th New York Bridge Conference.* 39-54.
3. Burgess & Niple, Inc. 2008. *Physical condition report of bridge no. LUC-2-1862.* Toledo: Ohio DOT, District 2.Modjeski and Masters, Inc. 2013. *The Anthony Wayne Bridge over the Maumee River: 2013 Cable Strength Evaluation Report for the Ohio DOT.* Prepared for ARCADIS.

Newton's Ride

Student Teacher: Kenton C. D. Jarvis

Advisor: Dr. Todd France

Ohio Northern University
Engineering Education and Computer Science

Abstract
Students discover the wondrous world of motion starting with Newton' three laws of motion. Students then practice their understanding of the three laws by displaying their interpretation of Newton's three Laws of Motion with Newton cars. Students are then introduced to working with kinematic equations that will allow them to estimate the force their weight produces based on the distance and instantaneous acceleration of their car.

Project Objectives
By the end of the lesson students will be able to define Newton's three Laws of Motion. After defining the law students can then display the law using a Newton's car. When students are asked what Newton's first law of motion is, the response should be "An object at rest stays at rest or an object in motion stays in motion, unless acted upon by an outside force." Students should be able to give similar responses for Newton's second and third laws of motion. After modeling the motion of a Newton's car students will then use the kinematic equations to predict the motion of the car.

Methodology Used
The methodology behind this lesson is using both verbal communication and kinesthetic learning to explore Newton's three Laws of Motion. The teacher defines Newton's Laws and then guides student exploration through examples and a hands-on activity. The activity is using Newton's cars to display the three laws of motion. The Newton car uses predetermined weights to propel the car. When the weight is propelled in one direction the car is propelled with an equal and opposite force. Students can then measure the weight and the distance of the car and predict how far the car will go with using the kinematic equations.

Results Obtained
If tested in a classroom setting the desired results would be to:

1. Have a challenging but engaging activity to encourage students to pursue a STEAM field.
2. Define Newton's three Laws of Motion
3. Provide examples of Newton's three Laws of motion.
4. Have an understanding of how to manipulate the kinematic equations to find distance, velocity, and acceleration.

References

1. YouTube. (2018). Newton's Laws Of Motion (1): The Law Of Inertia. [online] Available at: https://www.youtube.com/watch?v=Q0Wz5P0JdeU [Accessed 22 Mar. 2018].
2. YouTube. (2018). *Space Station Boost Proves Newton's Laws - All 3 of Them!* [online] Available at: https://www.youtube.com/watch?v=d1iO-yDp_nA [Accessed 22 Mar. 2018].
3. YouTube. (2018). *Newton's Laws Of Motion (2): Force, Mass And Acceleration*. [online] Available at: https://www.youtube.com/watch?v=WzvhuQ5RWJE [Accessed 22 Mar. 2018].
4. YouTube. (2018). *Newton's 3rd Law experiment on International Space Station*. [online] Available at: https://www.youtube.com/watch?v=cVSvatgXRBk [Accessed 22 Mar. 2018].
5. Swift.sonoma.edu. (2018). [online] Available at: http://swift.sonoma.edu/education/newton/newton_1/nlawpost106epo.pdf [Accessed 22 Mar. 2018].
6. Swift.sonoma.edu. (2018). [online] Available at: http://swift.sonoma.edu/education/newton/newton_2/nlawpost206epo.pdf [Accessed 22 Mar. 2018].
7. Swift.sonoma.edu. (2018). [online] Available at: http://swift.sonoma.edu/education/newton/newton_3/nlawpost306epo.pdf [Accessed 22 Mar. 2018].

Robotic Mouse in Maze

Student Researcher: Mina G. Kamel

Advisor: Rose Begalla

Cleveland State University
Computer Science

Abstract

With the recent demand of our service members to perform operations in both urban and underground environments, there has become a large need for robots displaying different forms of artificial intelligence. One such example of AI is with a machine being able to navigate through an area by itself, able to retain both where it has been, and where it must go to return back to its original location. A real-world example of this is in dealing with underground caves. In this type of operational environment, current robotic assets require the use of radio frequency transmissions, dealing with an operator having a remote with which he can drive the robot through a tunnel and monitor its location via a video camera mounted upon the top of the robot. Due to the environment in a cave and the limitations of RF capabilities, the operator has to maintain a fairly close distance to the robot itself. In doing so, the operator is still vulnerable to many dangers such as explosions or cave-ins. With the use of an AI type robot, we will be able to navigate through dangerous situations while keeping a safe distance.

Project Objectives

The objective is to design and build a Micro Mouse that can maneuver its way through a maze in the quickest amount of time as possible. The drive system, the control system, and an array of sensors are the main systems that work together to help the Micro Mouse maneuver through a maze [8]. The mouse must be able to navigate through any type of maze using speed sensors, wall detectors and an artificial intelligence that stores its previously traveled path. The mouse is to be completely autonomous and the length and width of the mouse may not exceed 6 inches by 6 inches. Once the Micro Mouse begins to travel through the maze it is essential that it is able to detect how close it is to the walls, when it is stuck at a dead end, and it must also keep its previous locations stored in memory. Overall, the main objective is to complete a maze in the shortest amount of time without damaging the maze walls [1].

Methodology Used

The objective of the Micro Mouse is to autonomously navigate through a given maze, which is to be determined upon run time, in the shortest amount of time possible while internally keeping track of its previous locations to ensure that it does not follow a previously attempted course. Since the Micro Mouse is to be fully autonomous, no user interaction is authorized, with the exception of the user turning the robot on and off. In order to complete this task, the Micro Mouse robot is equipped with wall sensors (4x), stepper motors (2x), and two internal variables monitoring the location and direction of movement. The entire robot is fed from a 12V DC re-chargeable power source. Level-0 functionality is illustrated in Figure 4.1, with a summarized description of such functionality in Table 4.1.

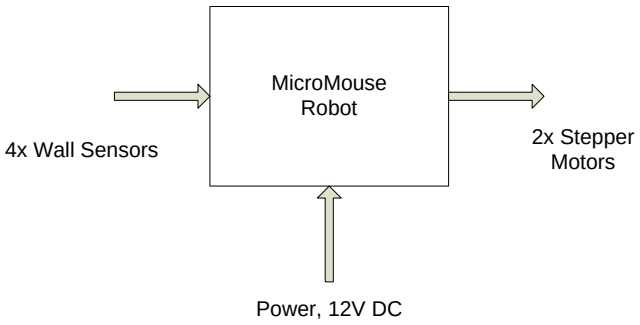

Figure 1. Level-0 functionality for Micro Mouse.

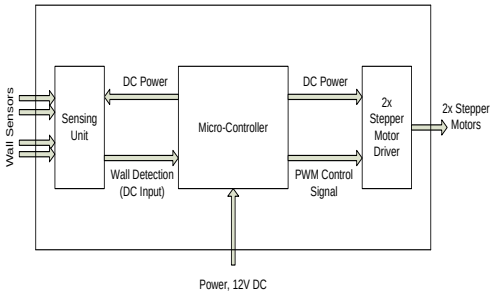

Figure 2. Level-1 design for Micro Mouse.

Status/Results Obtained

The AI technology currently behind driverless cars, Watson-assisted medical diagnosing, and US military drones will gradually become available for general use in the foreseeable future. It is crucial that carefully constructed legal frameworks are in place before this happens, so as to realize the potential of these technologies in ways that safely minimize any risks of a negative overall development. I believe that my application is for a good purpose and at the end it will convey better and bigger applications. At the end, the experiment resulted as success. It took time to compile the code to the mice in order to bypass the high-wall and figure out an alternative way. After it slowly made it, I was able to adjust the speed and it became more efficient. What made it much easier was that I used more coding lines that helped me for debugging after.

References

1. Harrison, Pete. "Micromouse Information Centre Maze Solving." Micromouse Information Centre. 17 Nov 2007. 29 Mar 2009 <http://micromouse.cannock.ac.uk/index.htm>.
2. "Micromouse Info." Micromouse Competition. University of California - Davis. 4 Feb 2009 <http://www.ece.ucdavis.edu/umouse/home/>.
3. Tantos, Andras. "H-bridge secrets part 1." 2007. The H-Storm Web. 29 Mar 2009 <http://www.modularcircuits.com/h-bridge_secrets1.htm>.

Mathematical Modeling of Beech Leaf Disease Spread

Student Researcher: Joel R. Kavaras

Advisor: Dr. Aaron Montgomery

Baldwin Wallace University
Department of Mathematics

Abstract

Beech Leaf Disease (BLD), after first appearing in Lake County in 2012, now affects American beech (*Fagus grandifolia*) populations across northeast Ohio, Pennsylvania, southwest New York, and parts of West Virginia and Ontario. The disease attacks the leaves and buds, causing striping and banding followed by shriveling, discoloration, and eventually reduced leaf and bud production. So far, a causal agent remains unknown, while tree mortality (especially in saplings) and the thinning of canopies in larger trees across affected areas make the disease a growing concern each year.[1] To mathematically model the spread of the disease, we used data collected from 2010-2017 on 154 beech-containing plots of land within Cleveland Metroparks to construct a table that marked each plot as either having at least one infected tree in a given year or not, and to construct an array that stored the distance between each pair of plots. We then used MATLAB software to construct a model that created a likelihood function with five parameters that weighted ambient risk of infection against risk of infection from nearby sampled trees. Using the method of maximum likelihood estimation, we found the values of those parameters that best fit the observed data to achieve preliminary results. Particularly, the values we obtained showed that the ambient risk of infection decreased significantly after the first year the infection appeared in the sampled plots. This suggests that an initial infection event may have occurred in the first year the disease appeared on park land, and then from that point forward it spread primarily via infected trees within the park system.

Project Objectives

This research project is focused on creating the first mathematical model of BLD spread data by mapping the diseased trees graphically to analyze the spread across Cleveland Metroparks land over time. Working with data provided by Cleveland Metroparks researchers and using the tools of statistics and graph theory as a framework, there is potential to identify patterns in the data revealing how the disease spreads, with this first model addressing the role of distance between beech trees in affecting the probability of spread.

Methodology Used

The data for this research was shared with us by Cleveland Metroparks Natural Resources Division, and included data collected from 2010-2017 as part of the park's Plant Community Assessment Program.[3] The data we received was specific to beech trees on 300 twice-sampled plots and included the coordinates for each plot, the number of beech trees greater than one meter tall present in each plot, and whether those trees were infected with BLD or not. We curated the data by first using Microsoft Excel to create an array of distances between each pair of the 154 beech-containing plots, which took the form of a symmetrical 154x154 matrix. In addition to this distance array, we also used Excel to create a table of the plots, the year of their second sample, and the infection status of those plots. Using MATLAB software, we coded a basic Susceptible-Infected (SI) model that assessed each plot from year to

year for the three years during which BLD was present on park land. The probability of a given plot transitioning from "susceptible" to "infected" was evaluated using the following formula:

$$\alpha + \sum \beta e^{-\gamma \cdot d(p_i, p_j)}$$

Where α is an ambient infection risk subject to change from year to year, β and γ are scaling parameters that do not change from year to year, and $d(p_i, p_j)$ is the distance between the plots. The sum is taken over all beech-containing plots in the data. This model was used to determine a likelihood function for the infection status of each plot, then, using the method of maximum likelihood estimation, we found the values of the parameters that maximize the likelihood function given the observed data.

Results

The maximum likelihood estimators (MLEs) we obtained were:

$\alpha_1 = 0.2$ $\beta = 0.08$
$\alpha_2 = 0$ $\gamma = 0.7$
$\alpha_3 = 0$

with each α pertaining to a given year after the disease was present in the plots sampled.

Significance and Interpretation of Results

First, it must be noted that these estimates are preliminary and coarse. Nonetheless, the MLEs produced by this model are noteworthy, especially regarding the α parameters. Particularly, the α_2 and α_3 parameters, which represent the ambient probability of infection in years two and three after the disease appeared in the sample, are significantly less than α_1, which likewise represents the ambient risk of infection after the first year the disease appeared. This suggests that there may have been an initial infection event when BLD first appeared in the sample, and then afterward the infection primarily spread between trees within the sample that had become infected.

Acknowledgments

We thank Cleveland Metroparks Natural Resources Division for providing us with the data used to construct our model and we thank Dr. Constance E. Hausman of Cleveland Metroparks for her guidance and consultation on this project. We thank Dr. Kathryn Flinn (Baldwin Wallace University) for her consultation on the biological aspects of this research.

References

1. Pogacnik, John & Macy, Tom. (2016). Forest Health Pest Alert: Beech Leaf Disease. Ohio Department of Natural Resources Division of Forestry.
2. Williams, A. B. (1936). *The composition and dynamics of a beech maple climax community*. Cleveland, OH: Cleveland Museum of Natural History.
3. E. Hausman, Constance & Robison, Terry & J. Mack Jr, John. (2011). Using the generalized random tessellation (GRTS) survey design for monitoring and assessment of terrestrial plant communities at local, regional and ecoregional scales.

Identifying Possible Contaminants in a Water Supply

Student Researcher: Evan W. Kolodey

Advisor: Dr. Celestia Lau

Lorain County Community College
Division of Mathematics and Science

Abstract

A multi-building facility has drinking fountains spread throughout that are used by its occupants on a daily basis. However, most of the people seeking hydration choose bottled water over the tap water because of the metallic taste in most of the fountains. Within my research, I plan on investigating the pH of the water, chloride ion abundance, calcium ion abundance, conductivity, as well as levels of metal contamination usually associated with metallic taste in water (Cu, Pb, Mn, and Zn.) I will be using the school's atomic absorption spectrometer to measure the levels of chemical elements utilizing the absorption of optical radiation by these free atoms in their gaseous state, as well as Vernier lab equipment. I hope to discover trends of certain pH / metal contamination in specific areas to help the facility narrow down the source(s) of the water problem.

Background and Approach

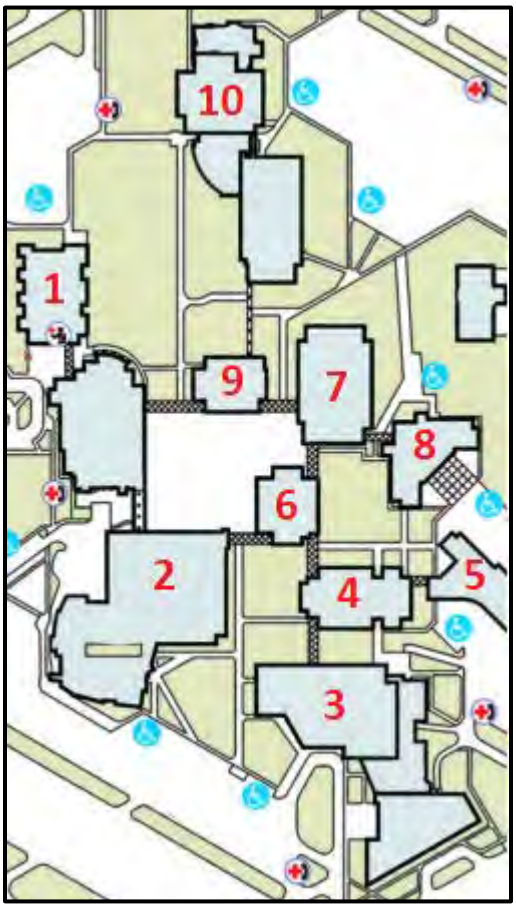

Figure 1. Map of Facility

A conductivity test would determine if any contaminants are salts, or electrolytes, as a good first test. Chloride Ion concentrations greater than 250 mg/L can give rise to detectable taste in water[1] so amounts greater than that would be an indicator of an excess chloride contamination. pH stands for "potential of hydrogen," referring to the amount of hydrogen found in a substance (in this case, water). pH is measured on a scale that runs from 0 to 14. Seven is neutral, meaning there is a balance between acid and alkalinity. A measurement below 7 means acid is present and a measurement above 7 is basic.

The U.S. Environmental Protection Agency (EPA) does not regulate the pH level in drinking water. However, the EPA recommends that public water systems maintain pH levels of between 6.5 and 8.5. Water with a low pH is acidic, naturally soft and corrosive. Acidic water can leach metals from pipes and fixtures, such as copper, lead and zinc. It can also damage metal pipes and cause aesthetic problems, such as a metallic or sour taste and blue-green stains in sinks and drains. Water with a low pH may contain metals in addition to the before-mentioned copper, lead and zinc.[2]

Calcium Ions are measured by what is called "water hardness." Hardness is caused by compounds of calcium and magnesium, and by a variety of other metals. General guidelines for classification of water by the United States Geological Survey are:

0 to 60 mg/L as soft
61 to 120 mg/L as moderately hard
121 to 180 mg/L as hard
180+ mg/L as very hard [3]

When a possible contamination was first noticed, a metallic taste was present in the water in building #1 and building #6. I devised a plan to obtain the piping blueprints of the facility, test the water at buildings on terminal points of the piping, then work with that data to conduct further tests to pinpoint and identify a contamination. With the above information, I narrowed the possible problems to test for down to, in order:

1. pH imbalance
2. An electrolyte contamination
3. Metal contamination, which would result from metals leeching into the water from piping and oxidation.

The plan for 10 samples was put into place, the first part of the experiment would be to clean the bottles and let them soak in Distilled/De-Ionized water (DI water). Next would be to test the water for contaminants in the bottle, as well as ensuring the accuracy of the equipment being used.
Part Two of the experiment would be to collect the water around campus in the same bottles and then test those bottles individually.

Part Three of this experiment is the use of the Atomic Absorption Spectrometer to identify specific metal contaminants.

Materials
(10) 250 mL Glass bottles
Vernier LabPro with compatible laptop
Vernier Conductivity Probe
Vernier Chloride Ion-Selective Electrode
Vernier Calcium Ion-Selective Electrode
Vernier pH Probe

Procedure
Part One – Testing the Collection Bottles and Equipment
1. Clean all 10 bottles with lab glass soap
2. Thoroughly rinsing each bottle three times with DI water
3. Fill all three bottles with DI water, seal the cap, and let set for 120 hours
(This time was chosen arbitrarily because of the time between scheduled lab times)
4. Prepare and calibrate all four Vernier probes for accurate use.
5. Open Bottle, test and record the pH of the water, chloride ion abundance, calcium ion abundance, and conductivity.
6. Repeat Step 5 for all samples.

Part Two – Testing the Water
1. Empty DI water at select fountain in select building, and immediately rinse three times with the fountain water, filling and sealing the bottle on the fourth fill.
2. Repeat step 1 for each bottle.
3. Repeat Steps 4-6 from Part One

Part Three – Atomic Absorption Spectrometer
1. Create elemental calibration standard solutions for AA Machine
2. Dilute water samples with Nitric Acid to remove any metals attached to the walls of the glass bottle.
3. Calibrate AAS
4. Test and record the results from the samples.

Data and Data Analysis

Distilled Water Calibration				
Sample #	Conductivity (µS/cm)	Chloride Ions (mg/L)	pH	Calcium Ions (mg/L)
1	0.00	0.00	8.78	0.00
2	0.00	0.03	8.63	0.00
3	0.00	0.00	8.41	0.33
4	0.00	0.01	8.18	0.14
5	0.00	0.08	8.14	0.04
6	0.00	0.01	7.89	0.35
7	0.00	0.01	7.85	0.18
8	0.00	0.07	7.91	0.04
9	0.00	0.00	7.94	0.00
10	0.00	0.03	7.87	0.00

Figure 2. DI Water Test Results

Facility Water Test				
Sample #	Conductivity (µS/cm)	Chloride Ions (mg/L)	pH	Calcium Ions (mg/L)
1	0.67	7.58	6.71	47.9
2	0.63	6.65	6.87	60.2
3	0.63	8.09	6.93	70.3
4	0.61	4.46	6.99	72.5
5	0.61	3.67	6.99	66.8
6	0.64	5.52	7.05	65.1
7	0.61	5.44	7.08	57.5
8	0.63	6.46	6.86	58.4
9	0.63	2.90	6.99	54.1
10	0.64	2.27	7.06	54.8

Figure 3. Collected Water Sample Tests

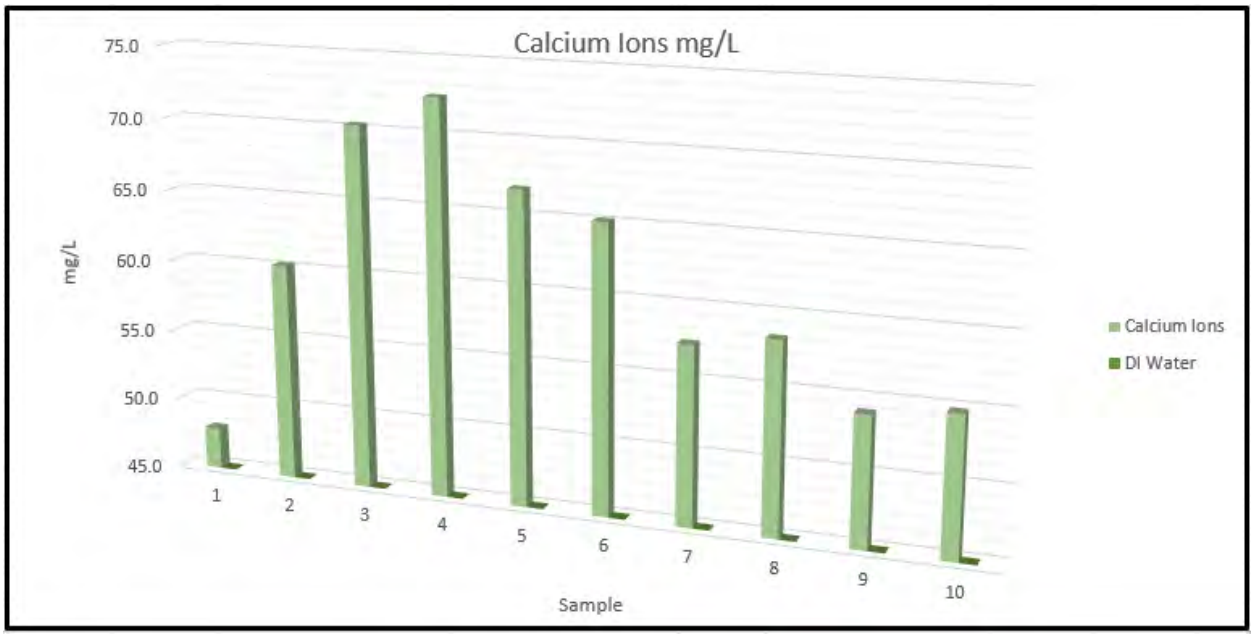

Figure 4. Facility Water Hardness Test Results

Difference Between DI Water and Sample				
Sample #	Conductivity (µS/cm)	Chloride Ions (mg/L)	pH	Calcium Ions (mg/L)
1	0.67	7.58	-2.07	47.90
2	0.63	6.62	-1.76	60.20
3	0.63	8.09	-1.48	69.97
4	0.61	4.45	-1.19	72.36
5	0.61	3.59	-1.15	66.76
6	0.64	5.51	-0.84	64.75
7	0.61	5.43	-0.77	57.32
8	0.63	6.39	-1.05	58.36
9	0.63	2.90	-0.95	54.10
10	0.64	2.24	-0.81	54.80
AVG	**0.63**	**5.28**	**-1.21**	**60.65**

Figure 5. Difference between collected facility samples and DI Water. Color represents deviation from the average in each category.

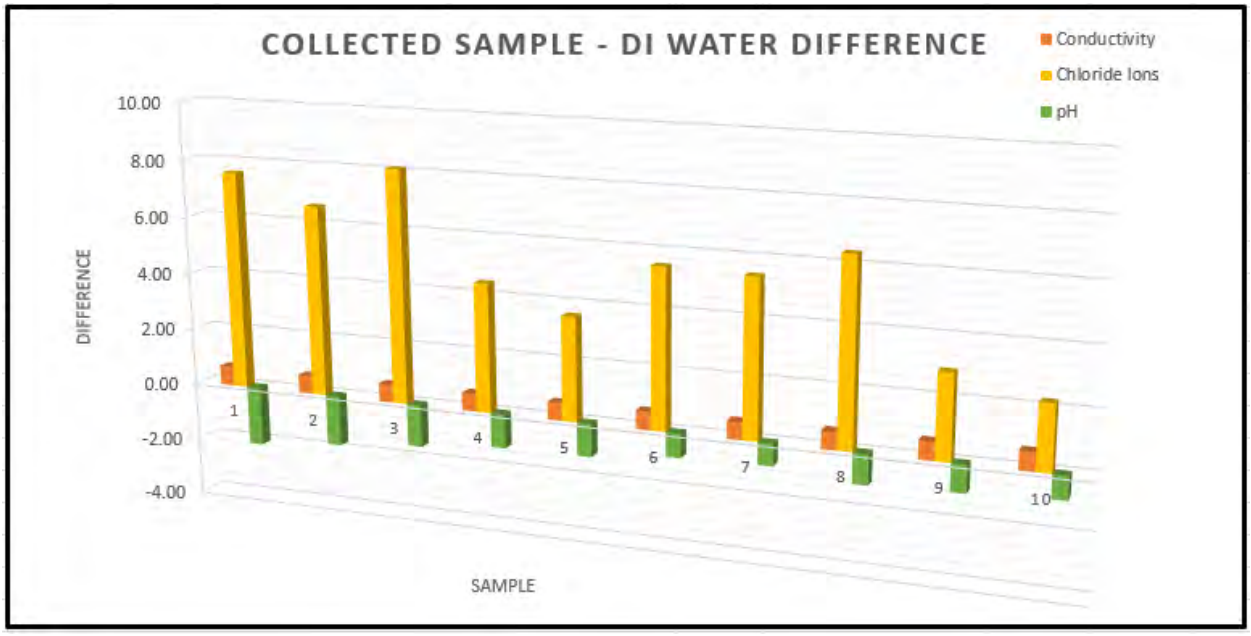

Figure 6. Difference data from Figure 5 visualized in graph form.

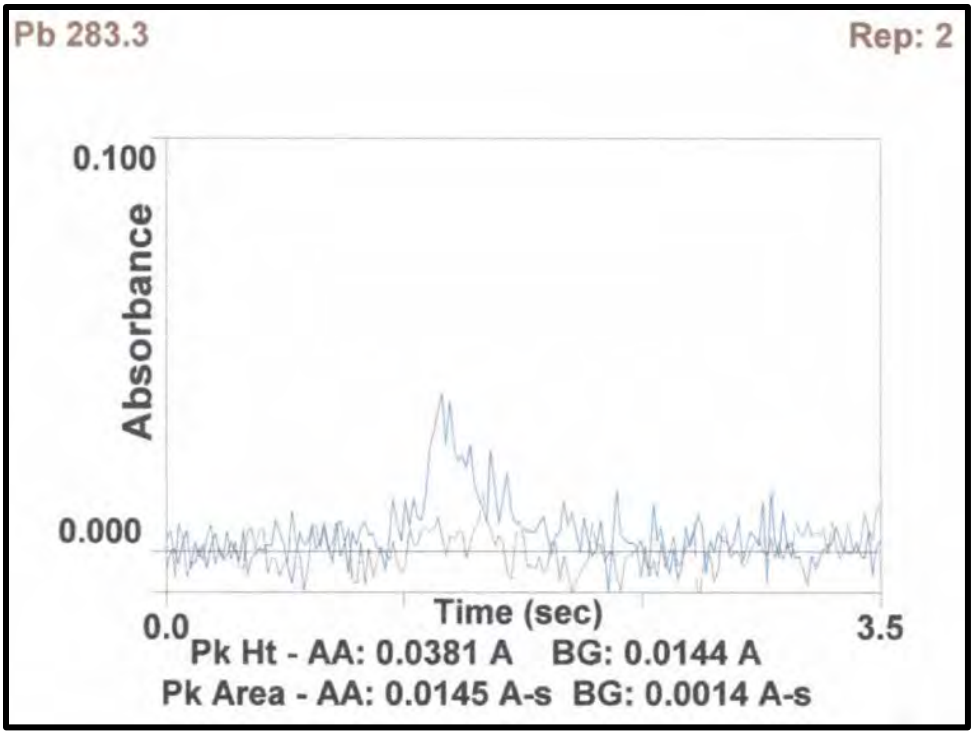

Figure 7. Results from Atomic Absorption Spectrometer

Conclusion

From the data provided in the experiments conducted on the facility water compared to DI Water, we cannot accurately determine that there are no metal contaminants in the water. What we can determine, with the certainty associated with Vernier lab equipment, is that the water quality at the facility does not step outside of the limits and recommendations established by the EPA, USGS, and the water department in the categories of Conductivity, Chloride Ion concentration, pH, and Calcium Ion concentrations. There is an interesting trend to be noted that building #1 has the lowest pH (6.71), highest conductivity, and the softest water; following the impact of low pH water mentioned in the Background and Approach section of this report. Although this pH level is an extreme compared to the rest of the samples, it is still within the recommended range by the EPA of 6.5-8.5.

In addition to the pH, another note about the data is that the water throughout the facility is considered "soft" according to the USGS, except for buildings #3-6 which are considered Moderately hard. Although there are no adverse health effects of hard water, it's interesting to note that the water is harder in the Southeast quadrant of the facility, and softest in the northwestern most buildings.

The pH difference between the DI water and the facility tap water is to be expected since the process for making DI water releases the carbon dioxide from the tap water, which would result in more basic water.

More information could be determined from this Independent Research Project if the blueprints of the facility could be obtained and if the Atomic Absorption Spectrometer (AA Machine) would have been operational. However, the security risk of releasing the water pipeline blueprints of the facility was determined by Plant Services to be too high for this kind of study conducted by a college student. In addition, although the AA Machine was set up and considered operational two weeks before this report,

the lab is still waiting for someone from PerkinElmer to visit and demonstrate the safe and effective use of the machine. Oberlin College offered their AA Machine the day this report was due, so I was only able to test for Pb. The results from the test place the levels of lead in the water to be well below what is considered safe by the EPA.

If I were to conduct these tests again, I would keep in mind that properly calibrating a Vernier probe can take more time than recommended by the Vernier handbook. In the case of the Chloride Ion ISE, after following handbook procedures of warming up the probe and calibrating it, a trend was noticed in the collected data of the DI water test of fewer and fewer Chloride ions. When the test was ran again, the downward trend continued until almost no Chloride ions were detected. I determined this was a result of the contamination of the buffer solution still present on the probe from calibration. After this discovery, careful consideration was given to thoroughly cleaning each probe after the calibration. All of this being considered, it was more efficient to conduct one test at a time on the samples rather than setting up all four probes and running four tests at a time.

References

1. World Health Organization, “Guidelines for drinking-water quality, 2nd ed. Vol. 2” (1996) http://www.who.int/water_sanitation_health/dwq/chloride.pdf (accessed 8 February 2018) Page 3, Para 4.
2. Water Systems Council, “pH in Drinking Water” (2007) https://www.watersystemscouncil.org/download/wellcare_information_sheets/potential_groundwater_contaminant_information_sheets/9709284pH_Update_September_2007.pdf (accessed 8 Feb 2018) Page 1.
3. USGS, “Water Hardness” (2016) https://water.usgs.gov/edu/hardness.html (accessed 8 Feb 2018) Para 4.

Electric Generation Potential in the Upstream and Midstream Oil and Gas Industry

Student Researcher: Derek L. Krieg

Advisor: Craig Rabatin

Marietta College
Edwy R. Brown Department of Petroleum Engineering and Geology

Abstract
With our world becoming evermore so dependent on electricity and energy, why not take advantage of every opportunity we have to produce electricity with existing systems? In 2015, the United States produced over 27 trillion cubic feet of natural gas (EIA). Likewise, the U.S. output about 8.8 million barrels of oil PER DAY in the same year (EIA). With such staggering production volumes, I wanted to research the potential for electricity to be produced just by the mere production and transportation of the hydrocarbons. My research showed there to be multiple ways to produce electricity in such manner, but the question then became "which options are feasible?"

Project Objectives
The purpose of this study was to discover missed opportunities to generate electricity along the path from production to end-use of hydrocarbons.

Methodology Used
The foundation to conduct this study is my experience with conventional and unconventional oil & gas production, multiple internships in the upstream sector, as well as my college courses on energy systems engineering. Furthermore, I discussed some of my thoughts with industry professionals in their respective areas.

Results Obtained
Opportunities within the upstream sector of the industry include thermoelectric generation, in-line turbine electric generation, natural gas combustion electric generation, renewable electric generation through wind turbines and solar panels, as well as Pavegen electric generating tiles. Of these options, most would only even perhaps be economical at a very large scale – one that is not attainable on a vast majority of production sites. However, I believe the strongest contender in the upstream sector would be to generate electricity from gas that would otherwise be flared. Fluenta.com estimates about 5 TCF (trillion cubic feet) is flared globally on an annual basis. This, with very rough estimating, could produce about 250,000 MW based on averages of EIA data.

Opportunities within the midstream sector of the industry are very similar with the exception of the combustion potential (as this would destroy their business of transporting the gas - they are the middle men). Midstream facilities would be able to take advantage of pressure and temperature differences even better than upstream, so the potential for in-line turbine and thermoelectric generation is greater.

Processing facilities would be a great place for those to be implemented, as the economics would be better and the efficiency would be greater.

Although many options exist to generate electricity by the production and transportation of hydrocarbons, they must be plausible and thus, there are many deciding factors. Namely, economics, efficiency, net generation, end use of electricity generated, durability, ease of use and installation, likelihood of damage, among others, will all be considerations to be made regarding the proposed generation system.

Perhaps the most economical, large-scale possibility would be to burn the gas in a natural gas combustion turbine. Obviously the electricity output would be magnitudes larger and might even help the wells to produce better (since they wouldn't have to produce into a high-pressured pipeline). Since a lot of the natural gas produced goes to natural-gas-fired power plants anyways, this setup essentially would take out all the middlemen. The economics of this option need studied much further, but one way to likely make it more economical would be to produce the electricity and send it to a central location where it would be transformed and sent into the grid. I believe selling the electricity to the grid will be the biggest expense and obstacle. Also, more professional electricians would need hired into the upstream companies, as there are few of these professionals that are currently employed with the upstream industry.

Indeed, multiple methods exist to produce electricity in the upstream and midstream oil and gas sector. Many of them take advantage of pressure differences and/or temperature differences along the flow path. However, most of them will not likely be economical to implement. Many of the methods would be fairly complex to install, require trained technicians to keep them maintained, and would produce minimal electricity. It would be likely that the company installing them would never make money back on their investment. I believe the most promising of the generation potentials are the ones that involve turbines and/or combustion. I believe the best opportunity would be to use a natural gas fired generator to create electricity from gas that would have otherwise been flared.

Acknowledgments and References

1. *U.S. Dry Natural Gas Production (Million Cubic Feet)*, www.eia.gov/dnav/ng/hist/n9070us2A.htm
2. *U.S. Field Production of Crude Oil (Thousand Barrels per Day),* www.eia.gov/dnav/pet/hist/LeafHandler.ashx?n=pet&s=mcrfpus2&f=a
3. "Do We Know How Much Gas Is Flared Globally?" *Fluenta*, 27 Oct. 2016, www.fluenta.com/news/know-much-gas-flared-globally/

An Optical, Near-IR, and X-ray Study of the Orion South Cluster

Student Researcher: Heidi E. Kuchta

Advisor: Dr. S. Thomas Megeath

The University of Toledo
Department of Physics and Astronomy

Abstract
We present a study of the Orion South Young Cluster (OSC), a cluster at southern edge of the Orion A molecular cloud and at a distance of 428 parsecs. We combine Discovery Channel Telescope i-band (0.8 microns) imaging, Kitt Peak National Observatory, KPNO, 4-meter H (1.6 micron) and Ks (2.1 micron)-band data, Spitzer Space Telescope 3.6-24 micron data, and XMM satellite X-ray data. The X-ray data detects young stars with active coronae while the Spitzer data can be used to identify dusty circumstellar disk around the young stars. We use these data to identify the member stars of this cluster. We find that only six out of the 40 X-ray sources have circumstellar disks implying a disk fraction of 15%. In contrast, about 50% of the X-ray emitting stars in the 2 Myr old Orion Nebula Cluster (ONC) have disks (this cluster is on the other end of the Orion A molecular cloud). The low disk fraction suggests that Orion South is older than the Orion A cluster, with an age of 4-5 Myr. To examine the ages independently, we construct an HR diagram for OSC using our photometry and existing spectra from the literature. Strangely, a comparison of these data with theoretical pre-main sequence tracks shows a cluster with an age similar to that of the ONC. Future work will focus on understanding this discrepancy as well as obtaining spectra for the faint members of the cluster with the Near Infrared High Throughput Spectrograph (NIHTS) spectrograph.

Project Objectives
The Orion A molecular cloud is the most active star forming cloud within 500 pc of the sun. This region is good for studying star formation because it's within close proximity which makes it easier to detect young stars and resolve dense groups and clusters of stars. I am hoping to understand how the Orion Nebular cloud and the Orion South cloud are related. I am trying to determine the star forming history of the Orion A cloud to better understand the physical processes that initiate and control star formation. Of particular interest is where star formation began in this cloud; whether it started everywhere along the 50 pc cloud at the same time, whether it started with the Orion Nebula Cluster, or whether is started on the opposite side of the cloud at the Orion South Cloud.

Most stars form in clusters, this allows us a snapshot of many stars that formed at about the same time and learn more about their properties. Most work on clusters in Orion A has focused on ONC, a massive (1500 stars) young (2 Myr) cluster at the northern end of the cloud. My project focusses on a much smaller region, the Orion South cluster. The goals of this project are to identify the members of this cluster, find the number of members, and determine the age of the cluster.

Methodology Used
Through The University of Toledo's partnership with the Discovery Channel Telescope, I had the opportunity to collect the i-band data that is used in this project. The raw data was then reduced with the standard procedure for CCD cameras: biases were subtracted from the raw images, and the resulting images were then divided by flat fields to take out the pixel to pixel gain variations. These reduced data were analyzed with the IDL program Photvis to identify the stars in the image and measure

their brightness. The resulting photometry were combined with the data from other telescopes to find all the stars in the region.

Using Discovery Channel Telescope i-band (0.8 microns) imaging, Kitt Peak National Observatory, KPNO, 4-meter H (1.6 micron) and Ks (2.1 micron)-band data, Spitzer Space Telescope 3.6-24 micron data, and XMM satellite X-ray data, I compiled a list of all the stars visible in our region of study. I then set parameters to identify subsets of sources in the list such as those with infrared excess indicative of young stars. The x-ray sources without disks, protostars, and the disk sources are shown in Figure 1. The indicators of youth that I used are red colors and infrared excesses indicative of protostars with dusty envelopes, infrared excesses indicative of a pre-main sequence star with a dusty disks (< 5 Myr), and/or stars with strong X-ray emission suggestive of young stars with active coronae.

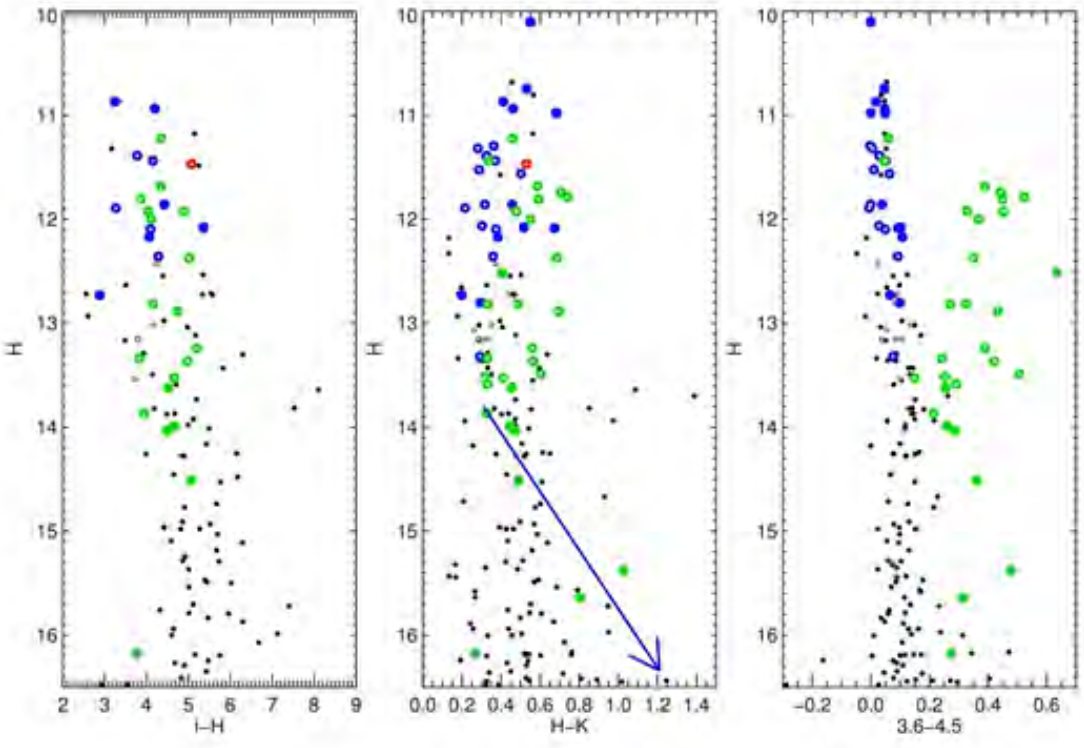

Figure 1. Color magnitude diagrams created from the combined data. Protostars in are marked red, X-ray identified young stars without disks in blue, stars with disks in green, points with a white center have spectra from Hsu et al. (2012). The blue arrow in the center plot represents the hydrogen burning limit for a 1-million-year-old population. Sources below the arrow are potential brown dwarfs or background stars.

The Hertzsprung-Russell diagram in Figure 2 used spectral types from Hsu et al. (2012), and bolometric corrections, intrinsic colors, and effective temperatures for each spectral type from Pecaut et al (2013). I compared the sources in H-band from KPNO to 2 Micron All Sky Survey (2MASS) and applied the bolometric corrections to determine the luminosities. There are some sources that are not clearly members of the cluster, either foreground or background stars. The majority of the cluster member candidates indicate an age of 2 million years. This is comparable to the ONC. I will update this figure once the NIHTS data is reduced and the spectral types of these sources is determined.

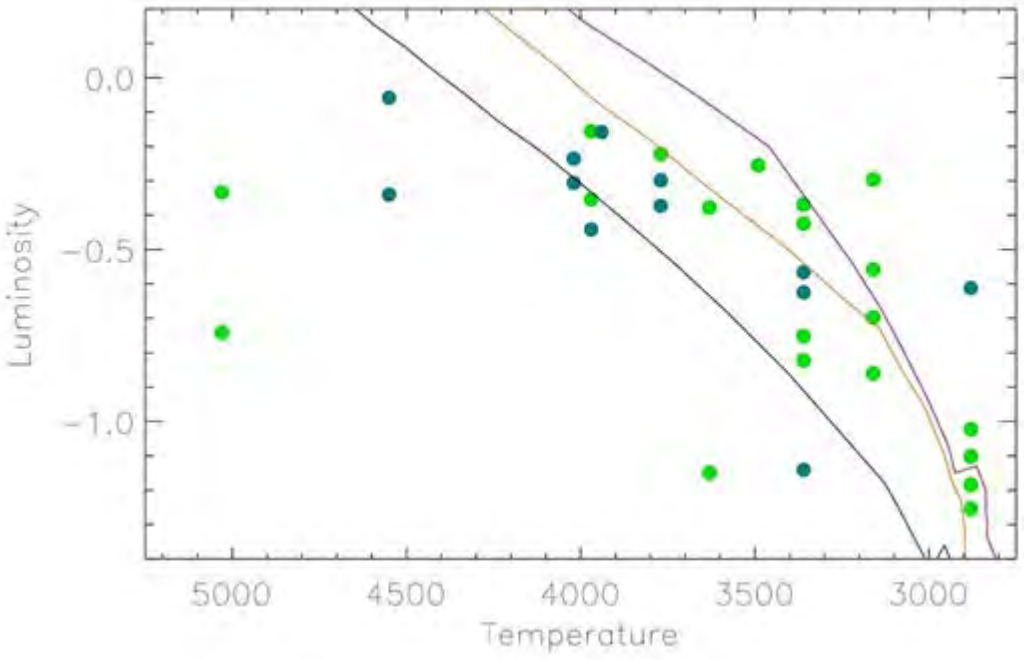

Figure 2. HR diagram of Orion south cluster. The green dots are the sources with disk, the blue are the young stars without disks identified with the X-rays. The temperatures were determined using the Spectra from Hsu et al. (2012). Isochrones from the pre-main sequence model of Baraffe et al. (2015) are shown, from top to bottom they are the 0.5, 1 and 3 Million-year tracks.

Results Obtained

We completed the full survey of this region. 65 members were found out of 532 stars. In the list of candidates there are 29 pre-main sequence stars with disks, 6 of which have x-ray detections, 2 protostars, and 34 young stars with x-ray emission that no longer have their disks. The data indicates that the cluster is about 2 million years old and has about 65 members. The HR diagram in Figure 2 shows the members which have spectral types in literature. Although as seen in Figure 2 there are outliers that do not follow the age tracks with the others. These could be foreground or background stars. The next step in this project is to add cool, low mass sources to the HR diagram to increase the accuracy.

I use the subsets of data to identify the member stars of the Orion South cluster. I found that only 6 out of the 40 x-ray sources have circumstellar disks implying a disk fraction of 15%. In contrast, about 50% of the x-ray emitting stars in the ONC have disks (Megeath et al. 2012). The disk fraction suggests and age of about 4-5 million years old. This Uncertainties of the age could be high due to an insufficient sample of x-ray sources for comparison. The x-ray sources without disks and the disk sources are shown in Figure 1.

The disk fraction indicates an age of approximately 4 to 5 million years, while the HR diagram indicates an age of about 2 million years. More work will need to go into better determination of the age. Potential low mass to sub stellar objects have been found and will be targets of upcoming spectroscopic observations.

Significance and Interpretation of Results

A major problem with the results I have so far is the discrepancy in ages found for the Orion South Cluster. This could be caused by multiple different issues and needs to be studied further. One possible issue is that there is an insufficient x-ray sample size for accurate comparison. Another possibility is that the OSC is closer than we took into consideration. The distance can be checked and fixed if needed with data from GAIA. I will also improve the age calculation by adding more stars to the HR diagram.

The brown dwarf and very low mass star candidates were selected as objects that had disks and were on or near the hydrogen burning limit. The blue line in Figure 1 shows the hydrogen burning limit and the green without white centers near the limit, brighter than 15^{th} magnitude, will be targets for observation in our upcoming Discovery Channel Telescope run with the Near Infrared High Throughput Spectrograph. During the first set of observations with NIHTS, I observed three of my targets. The spectra will be reduced and analyzed when the observations are finished.

This is the first combined x-ray and IR-excess census of this cluster. With this, we are able to identify more of the young stars. From this improved list of young stars, the approximate age can be determined with more certainty.

References

1. Baraffe, I., Homeier, D., Allard, F., & Chabrier, G. (2015). New evolutionary models for pre-main sequence and main sequence low-mass stars down to the hydrogen-burning limit. Astronomy and Astrophysics, 577, A42.
2. Hsu, W.-H., Hartmann, L., Allen, L., Hernández, J., Megeath, S. T., Mosby, G., et al. (2012). The Low-mass Stellar Population in L1641: Evidence for Environmental Dependence of the Stellar Initial Mass Function. The Astrophysical Journal, 752(1), 59.
3. Megeath, S. T., Gutermuth, R., Muzerolle, J., Kryukova, E., Flaherty, K., Hora, J. L., et al. (2012). The Spitzer Space Telescope Survey of the Orion A and B Molecular Clouds. I. A Census of Dusty Young Stellar Objects and a Study of Their Mid-infrared Variability. The Astronomical Journal, 144(6), 192.
4. Pecaut, M. J., & Mamajek, E. E. (2013). Intrinsic Colors, Temperatures, and Bolometric Corrections of Pre-main-sequence Stars. The Astrophysical Journal Supplement, 208(1), 9.

Comparison of Changes in Strength, Toughness, and Hardness of Steel After Heat Treatment

Student Researcher: Christian Lambiase

Advisor: Professor Adele Wright

Columbus State Community College
Engineering and Transport Technology

Abstract
The goal of this study is to observe and document the physical changes in steel as it undergoes different types of heat treatment and to then compare the results. This study will strive to identify the physical changes in the size and shape of steel grain after different heat treatments and will utilize Rockwell Hardness tests, Charpy Impact tests, and tension tests to quantify the differences in hardness, toughness, and strength of the steel.

Materials and Methods

Materials

- 8620 steel round rods, cold finish, annealed measuring ¾ inch diameter. The steel was ordered from MSC Industrial Direct, part #: 70872023.
- Plasti Dip® multi-purpose rubber coating, which was purchased from ACE Hardware, SKU #: 7581511603.

Fabrication and Test Equipment

- MAZAK Quick-Turn Smart 100S CNC lathe
- BridgePort Knee Mill
- Clausing Colchester engine lathe
- Speedy-Melt E-16 H furnace
- Allied High Tech M-Prep 3 polisher
- Tinius Olsen tensile tester
- American Machine and Metal Charpy impact tester
- Wilson model 5JR Rockwell Hardness testing machine
- Olympus Tokyo PME inverted microscope with a Hitachi KP-D20B camera

Sample Fabrication

Tension test samples were turned on a MAZAK Quick-Turn Smart 100S CNC lathe to a diameter of 0.502 inch and a length of 3.5 inches between the tapers of the threads. Charpy samples were machined on a BridgePort Knee Mill to the dimensions 0.394 x 0.394 x 2.2 inches with a 0.079 inch deep 45^{o} v-notch at the center of the 2.2 inch length. The Nital etch samples were cut on a Clausing Colchester engine lathe to a machine finish flat surface and were left with a ¾ inch diameter.

Heat Treating

Heat treatment was performed in a Speedy-Melt E-16 furnace. For AISI 8620 steel, the heat treatment temperature range for normalizing is between 1652^{o}F and 1697^{o}F (1.). For hardening, the heat treatment temperature range is between 1500^{o}F (2.) and 1598^{o}F (1.) for non-carburizing hardening. The quenching media for hardening is typically water or oil (2.). The tempering temperature range for non-carburized hardened AISI 8620 ranges between 400^{o}F to 1300^{o}F.

For this study Normalized and Hardened samples were heated to 1575^{o}F. This temperature was within the acceptable range for hardening AISI 8620 steel, but was 75^{o}F below the minimum threshold for normalizing. Normalizing at the subcritical temperature was due in part to a misinterpretation of the temperature range for the heat treatment specifications presented in the dataset. The normalized samples were allowed to air cool after the heat treatment. The hardened samples were water quenched and tempered in a home gas oven at 400^{o}F for two hours.

Testing Performed

To demonstrate the changes in mechanical properties, samples were fabricated from ¾ inch diameter AISI 8620 steel. The samples were then divided equally into three groups. One sample group was to be left untreated as a control sample. Another sample group was to be hardened by heating them to 1575^{o}F, quenching them in still water, and then tempering them in a 400^{o}F convection oven for two hours. The last sample group was to be normalized by heating them to 1575^{o}F and then allowing them to cool in still air. Each sample group consisted of three tensile test specimen, one specimen for Nital etching, and one specimen for Charpy impact and Rockwell Hardness testing.

Tension test samples were placed into a Tinius Olsen tensile tester and then a load was applied until the sample ruptured. From this test a load/strain graph of the elastic region was made, the ultimate load was recorded, and change in axial length was measured. From this, the % elongation, yield strength (σ_y), ultimate strength (σ_u), and Young's modulus (E) was calculated.

Charpy impact test samples were placed into an American Machine and Metal Charpy impact tester so their notch toughness could be measured. Following the Charpy impact test, the samples were gathered up for a hardness test. A Wilson model 5JR Rockwell Hardness testing machine was used for measuring hardness and was set to measure on the Rockwell C scale. Each of the Charpy samples had their hardness measured five times so that a mean hardness could be calculated.

The Nital etch samples were dipped into a multi-purpose rubber coating and then polished on an Allied High Tech M-Prep 3 polisher using the following grades of abrasives: 120 grit, 240 grit, 400 grit, 600 grit, 1200 grit, and 1µm polycrystalline diamond suspension. Samples were etched using a 10% Nital solution and then viewed on an Olympus Tokyo PME inverted microscope so their grain structure could be observed.

Terminology

Elasticity – The ability of a material to resist permanent deformation when placed under stress and return to its original dimensions when the stress has been relieved.
Ductility – Describes the amount of deformation a material exhibits when under tensile load.
Plasticity – The ability of a material to retain permanent deformations without breaking.
Brittleness – Describes the ability of a material to break without undergoing deformation when placed under stress, opposite of plasticity.
Toughness – The ability of a material to plastically deform without breaking when absorbing energy.
Yield Strength – The stress point at which a material will cease elastic deformation and begin plastic deformation.
Ultimate Strength – The stress point at which a material will be able to withstand the greatest load.
Hardness – The ability of a material to resist surface damage such as a scratch or indentation.
Young's Modulus – The linear relationship between stress and strain during elastic deformation.

Heat Treatments (3.)

Normalizing – To homogenize and produce a uniform structure in alloy steels by heating above the transformation range and cooling in air.

Hardening – The process of increasing the hardness of a ferrous alloy by austenitizing (heating above the transformation range) and quenching.

Tempering – The process of relieving stress in steels that are hardened by quenching for the purpose of toughening them and reducing brittleness.

Results and Analysis

Data Summary

Table 1. Data table summarizing the results of all tests

Material	Tension					Charpy	Rockwell
	Initial Diameter (in)	Elongation %	Yield Strength (KSI)	Ultimate Strength (KSI)	Young's Modulus (KSI)	Notch Toughness (in-lb)	Hardness HRC
Control 2	0.501		93.8	112	28181		
Control Mean	0.501		93.8	112	28181	954	17
Normalized 1	0.502	23.1	55.6	102	25262		
Normalized 2	0.503	21.4	55.4	102	21567		
Normalized 3	0.502	23.8	60.6	103	25262		
Normalized Mean	0.502	22.8	57.2	102	23901	528	16.2
Hardened 1	0.502	12.1	195	227	31578		
Hardened 2	0.504		163	226	29485		
Hardened 3	0.503	10.1	196	227	27958		
Hardened Mean	0.503	11.1	185	227	29661	750	41.4

Tension Testing

As seen in Image 1, all samples that underwent Tension testing exhibited ductile failure, as seen by the textbook cup and cone fracture.

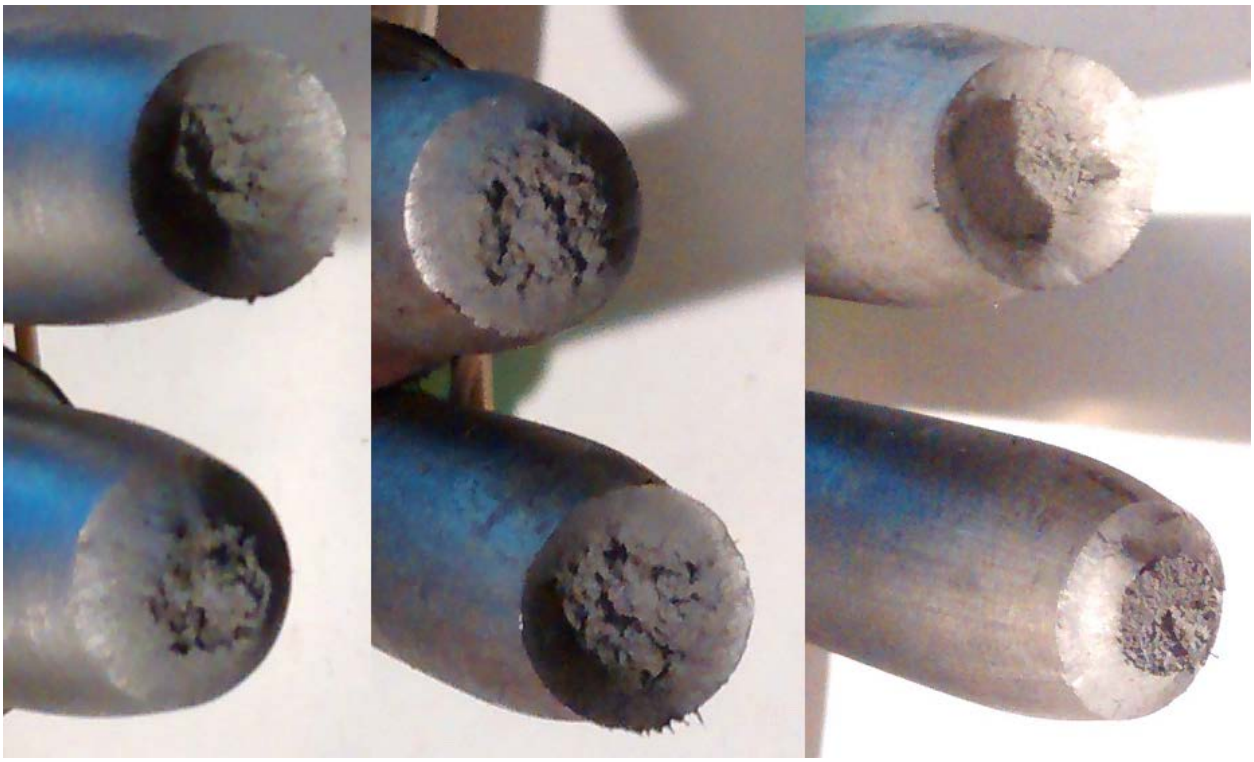

Image 1. Tension test samples. From left to right: Control, Normalized, and Hardened

Graph 1 compares the ultimate strength and yield strength of all the test samples. The data points within each sample group shows fairly consistent results. The group with the highest ultimate strength and yield strength was the Hardened samples, the sample group with the lowest ultimate strength and yield strength belong to the Normalized samples. Even though the difference between the ultimate strengths of the Control sample and Normalized samples are close, the difference in yield strength was much greater in the Control sample. Due to technical error in test setup and graphing, samples Control 1 and Control 3 have been excluded from this dataset.

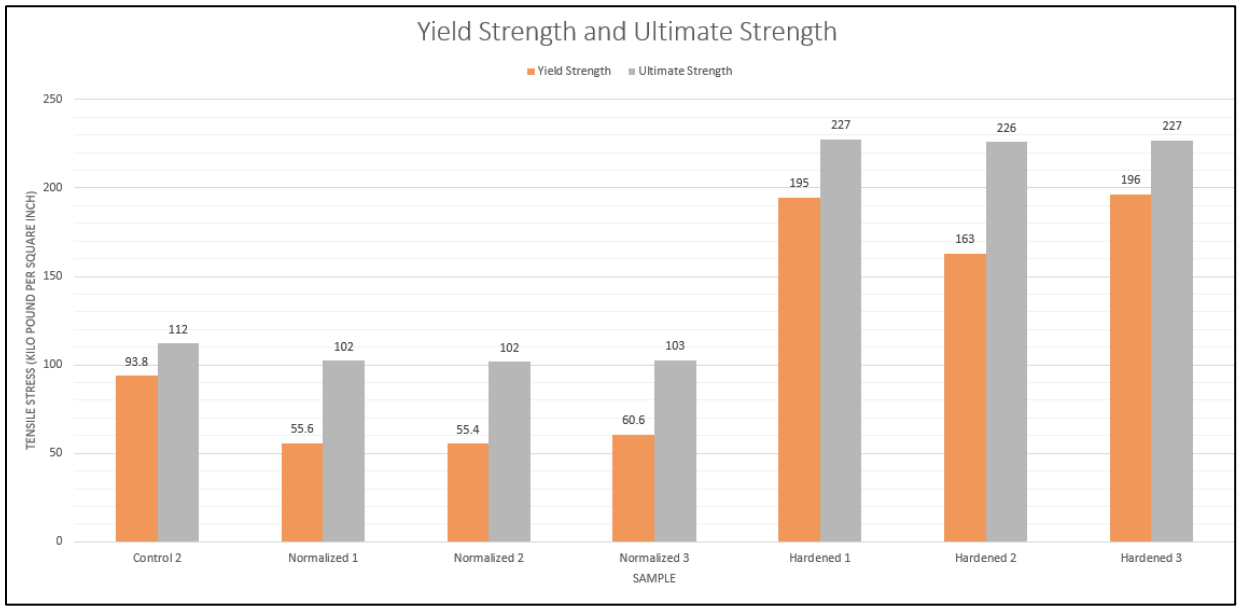

Graph 1. Tension test results showing yield strength and ultimate strength

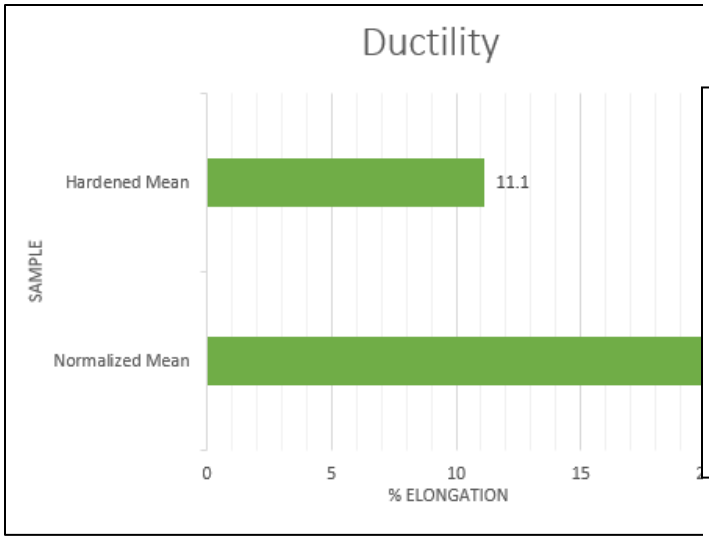

Graph 2 depicts the mean ductility of the Hardened and Normalized sample groups. Under load, the Hardened sample group elongated only half as far as the Normalized sample group. Samples Control 1, Control 2, Control 3, and Hardened 2 have been excluded from this dataset due to ruptures occurring outside the measure area.

Graph 2. Tension test results showing average ductility for Hardened and Normalized sample groups

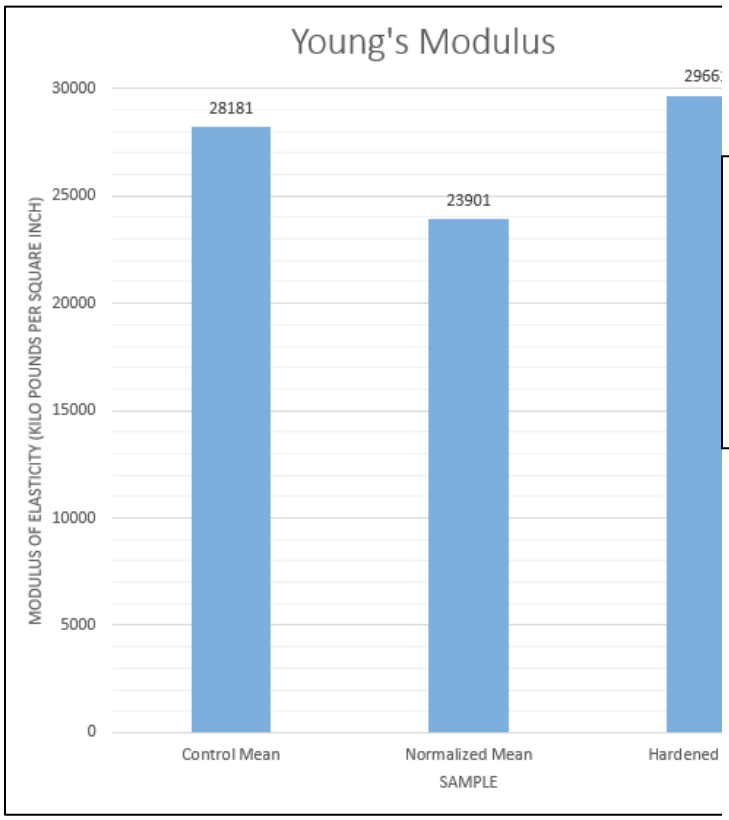

Graph 3 compares the mean elasticity of the sample groups. The Normalized sample group requires the least amount of energy to undergo the same proportional amount of elastic deformation as the Hardened and Control sample groups.

Graph 3. Tension test results showing the average modulus of elasticity for all sample groups

Charpy Impact Testing

The Control sample clearly suffered an almost pure ductile failure, as evidenced by the great amount of plastic deformation at the fracture site. The Control sample did not fully fracture into two separate pieces during the Charpy test, but were separated after the test. The Normalized appears to have suffered a mostly brittle failure, as indicated by the mostly smooth fracture, but likely started as a ductile failure before transitioning into a brittle failure. The Hardened sample appears to have suffered

a very ductile failure as it fractured at an angle approaching 45°. However it is perplexing that the fracture traveled inward giving the appearance of a cone and arrowhead.

Image 2. Charpy test samples. From left to right: Control, Normalized, and Hardened

In the Charpy impact test the Hardened sample required 750 inch-pounds of torque the shear. The Normalized sample required the least amount of torque to shear the sample at 528 inch-pounds. The Control sample required the greatest amount of torque to shear at 954 inch-pounds.

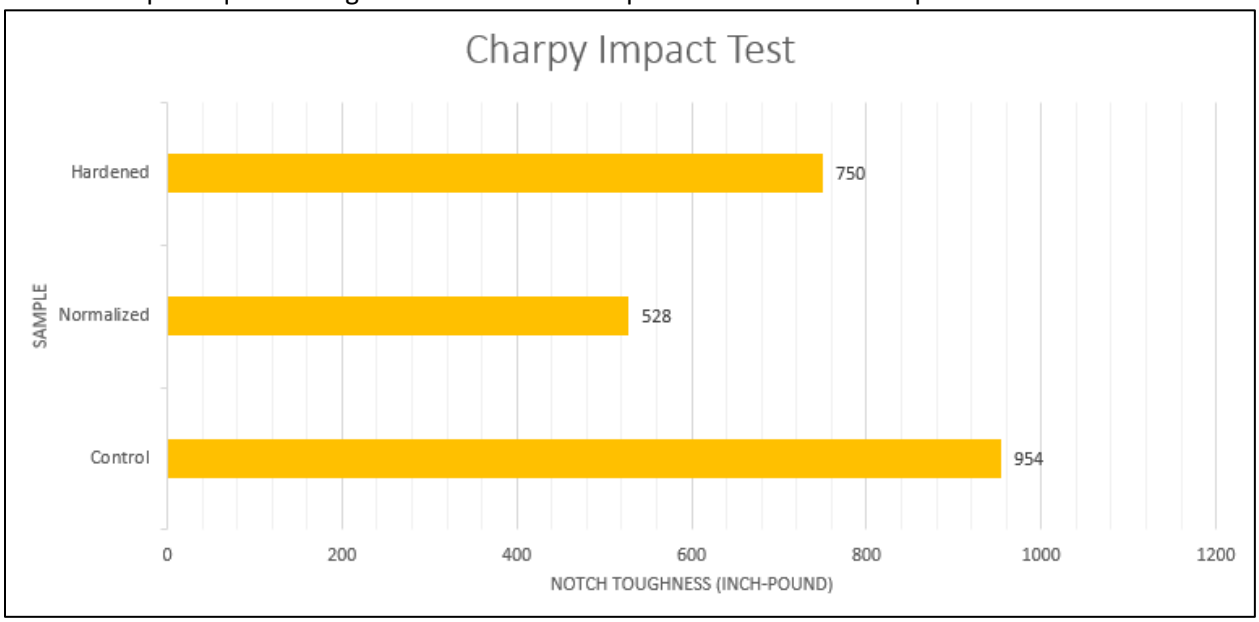

Graph 4. Charpy impact test results for all sample groups

Rockwell Hardness Testing

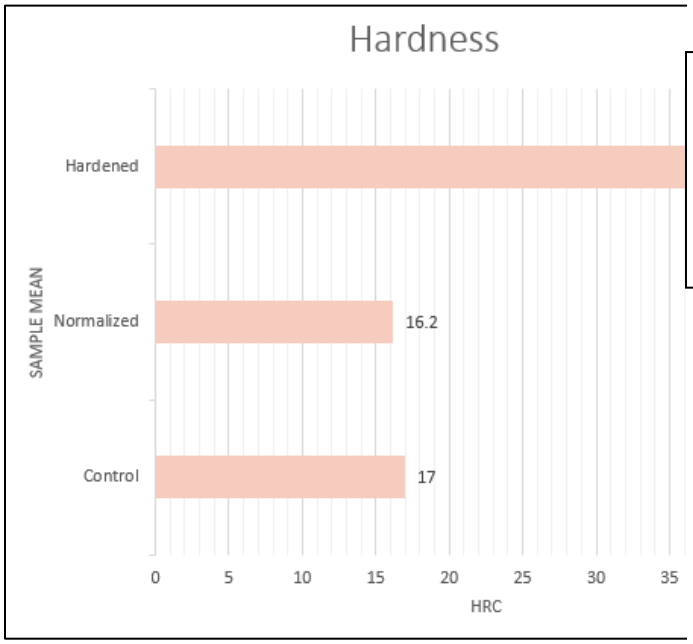

The Hardened sample had the greatest average hardness of 41.1, the Normalized sample had the lowest average hardness at 16.2, followed closely by the Control sample at 17.

Graph 5. Average hardness on the Rockwell C scale for all sample groups

Nital Etch and Microscopic Examination

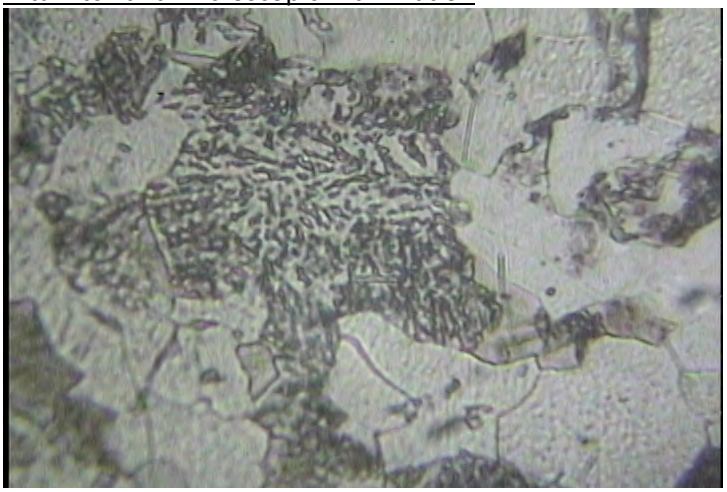

Image 3 is a microscopic view of the Control sample and displays a large grain of pearlite in the center, surrounded by fairly large grains of ferrite. The coarse grains of ferrite and pearlite are a good indication that the Control sample has retained the annealing that it received when it was made.

Image 3. Microscopic view of Control sample's grain structure

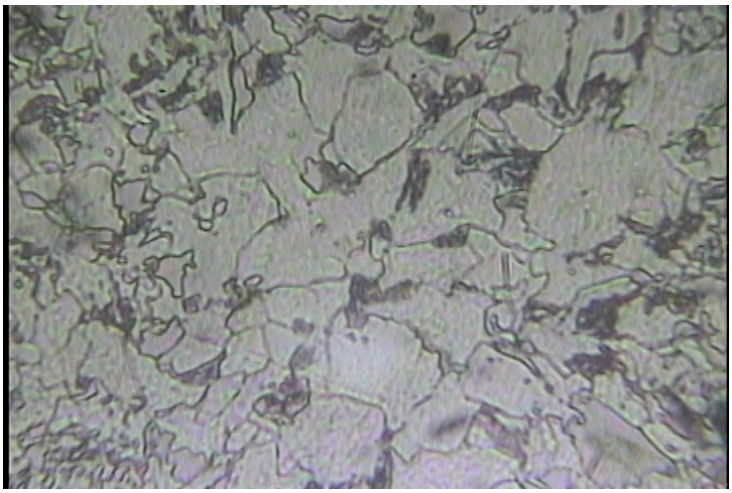

Image 4. Microscopic view of Normalized sample's grain structure

Image 4 is a microscopic view of the Normalized sample and displays many grains of ferrite of varying size with pockets of pearlite tucked in the grain boundaries. The ferrite is less coarse than in the Control sample and the pearlite grains are much smaller, which is a good indication that the sample was normalized.

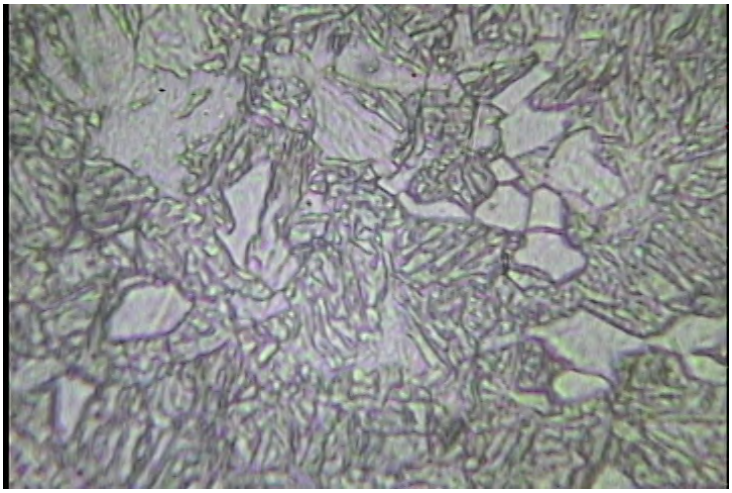

Image 5. Microscopic view of Hardened sample's grain structure

Image 5 is a microscopic view of the Hardened sample and displays some ferrite grains surrounded by a large quantity of tempered martensite. The presence of martensite is a sure indication that the sample was hardened. Since the normally long needle like grains of martensite are shorter and less needle like, it can be assume that the sample was tempered.

Images 3, 4, and 5 were captured using the same magnification and have not been cropped.

Comparison with Known Values

Data for the material properties for hardened 8620 steel, so all comparisons will be between the Normalized mean and the material properties data that was reference from the *Metals Handbook* (4.)

Tensile Strength

Graph 6 shows that the ultimate strength for the Normalized mean is greater than the reference by 11.1% and the yield strength for the Normalized mean is greater than the reference by 10.4%.

Graph 6. Comparing Normalized Mean with known Normalized values of ultimate strength and yield strength (4.)

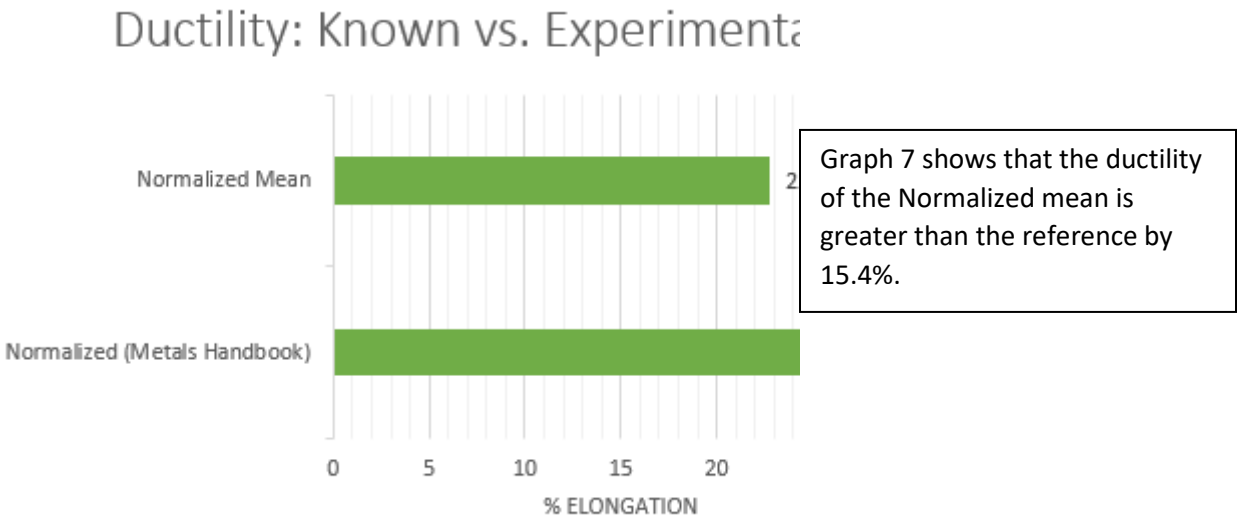

Graph 7 shows that the ductility of the Normalized mean is greater than the reference by 15.4%.

Graph 7. Comparing Normalized Mean with known Normalized ductility (4.)

Hardness

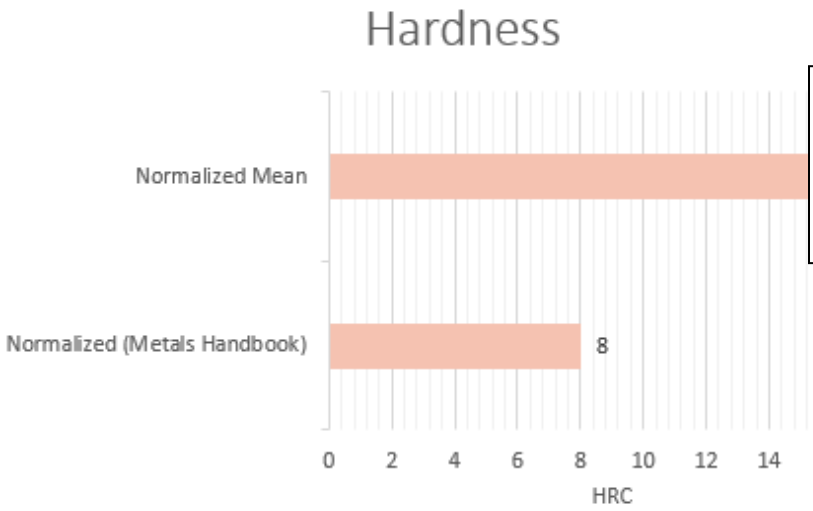

Graph 8 shows that the Normalized mean has more than twice the hardness than that of the reference.

Graph 8. Comparing Normalized Mean with known Normalized hardness (4.), converted from Brinell

From the comparisons the Normalized samples produced in this experiment were greater than what is referenced in the *Metals Handbook.*

Equations

Young's Modulus $E = \frac{\Delta\sigma}{\Delta\varepsilon}$

Ultimate Strength $\sigma_U = \frac{P_U}{A}$

Yield Strength $\sigma_Y = \frac{P_Y}{A}$

Ductility $\%\, Elongation = \frac{L_f - L_o}{L_o} * 100$

References

1. "Case Hardening Steel - AISI 8620." *S & T Stainless*, S&T Stainless Ltd., 10 Jan. 2014, stainless.steelandtube.co.nz/wp-content/uploads/2014/06/CaseHardeningSteelAISI8620.pdf.
2. "8620 Cold Roll Steel." *Speedy Metals Information for 8620 Cold Roll Steel*, Speedy Metals LLC, www.speedymetals.com/information/Material39.html.
3. Bruce, R. Gregg. *Modern Materials and Manufacturing Processes*. Pearson Education, 2010, Hardening, pp. 461, Normalize, pp. 465., Temper, pp. 469.
4. Davis, J. R. *Metals Handbook*. CRC Press, 1998.

Acknowledgments

- Professor Adele Wright for providing advice and guidance for this study
- Professor Shane Bendele and Danny Byas for assistance with fabricating test samples
- Nathan Gjerstad for going above and beyond
- Erik Aagard for encouraging me to do more than I thought possible

The Science of Snowflakes

Student Researcher: Brittany A. Layden

Advisor: Dr. Mark Templin

The University of Toledo
Judith Herb College of Education

Abstract

In this data analysis activity, students use satellite data to explore the relationship between the amount of water vapor and the temperature of clouds, as well as snowflake shapes and cloud temperature.

In the lesson, students will learn what snowflakes are, how they form, and how they are affected when variables, such as temperature and moisture, change. The purpose of the lesson is for students to use satellite data (provided by NASA) to explore how the amount of water vapor and the temperature of clouds, affects snowflake shapes.

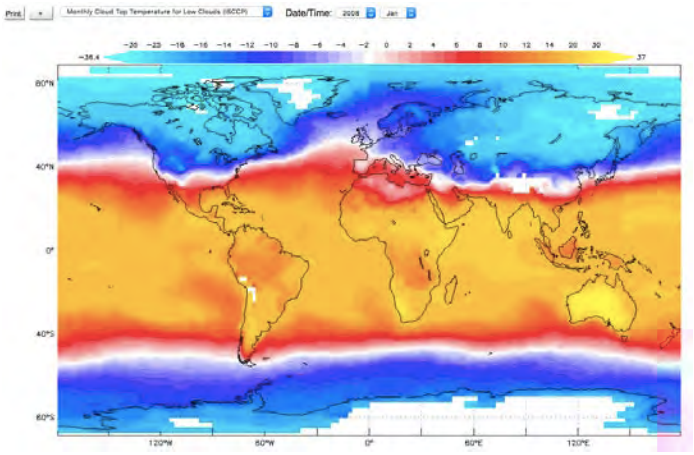

Source: 1 MY NASA DATA Live Access Server

Figure 1. Cloud Temperature (January 2008)

Lesson

The basis of this lesson comes from NASA's lesson plan, "MT NASA DATA: Cold, Clouds and Snowflakes". With each topic the students will brainstorm about a series of questions relating to snowflakes, complete an activity based off those questions, then have the opportunity to demonstrate what they learned. For example, the lesson begins with asking the students what snowflakes are and how they form. They will then explore the water cycle and discover how snowflakes form and what they are made of. To finish, the students will analyze data from graphs provided by NASA that displayed cloud top temperature and precipitation on a global scale for a given year and use that knowledge to create their prediction of what a snowflake would look like on a given date in a specific area of the world. They will use all this information to understand the role that diverse variables play in our planet's climate system.

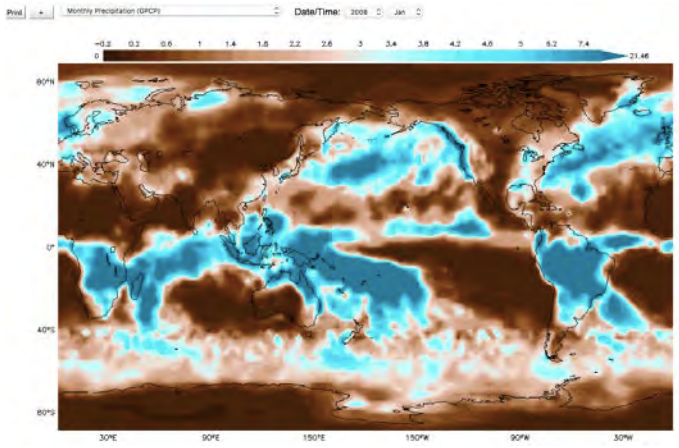

Source: 2 MY NASA DATA Live Access Server

Figure 2. Precipitation (January 2008)

Objectives

Students will: 1) Analyze NASA satellite data to create graphs, 2) Draw conclusions from maps and graphs, 3) Make predictions of on outcome based of given evidence and data, 4) Determine the latitude and longitude from a map location, and 5) Appreciate the beauty and complexity of a snowflake.

Standards

Next Generation Science Standards: Middle School Grades

1) MS-ESS2-1 Earth's Systems: Develop a model to describe the cycling of Earth's materials and the flow of energy that drives this process. 2) MS-ESS2-4 Earth's Systems: Develop a model to describe the cycling of water through Earth's systems driven by energy from the sun and the force of gravity. 3) MS-ESS3-5 Earth and Human Activity: Ask questions to clarify evidence of the factors that have caused the rise in global temperatures over the past century. 4) MS-ETS1-1 Engineering Design: Define the criteria and constraints of a design problem with sufficient precision to ensure a successful solution, taking into account relevant scientific principles and potential impacts on people and the natural environment that may limit possible solutions.

Underlying Theory

At this point in my life I find myself agreeing with the Progressive Philosophical Perspective of Education, which focuses on learning through one's environment. I believe that one learns best through experience. Like they say, *experience is the best teacher*. At times, it is important to use a teacher-based lecture so that students have a basic understanding of the material, however, the students will *remember* experiences in a more concrete way. When I look back at previous classes I have taken, I remember activities, labs, and group projects I completed. This is why I am such a strong believer in student-focused classrooms that involve group work, collaboration, and activities. I hope to successfully mesh these ideas in my classroom through this lesson.

Resources

Students will be provided with: 1) Snow Crystal Data Sheet, 2) NASA Data Reference Sheet, 3) Chrome Book, 4) White computer paper, and 5) Scissors.

Results

In performing this investigation, we can infer that cloud temperature, which varies within a cloud, affects the crystal shape of snowflakes. For instance, large, dendritic flakes grow best at temperatures of -10 to -12 degrees Celsius, while plates grow at warmer and colder conditions. If the flake passes through dry air, it may sublimate. If other ice crystals are present, they may aggregate onto the crystal. If liquid water is present, it may accrete. All these processes can alter snowflakes shapes.

Assessment

Students completed a data sheet that prompted them to use graphs that showed could temperature and precipitation in January 2008. They had to use latitude and longitude, along with the data given to predict what a snowflake might look like in a given area during January of 2008.

Conclusion

The students found that temperature and humidity are variables that greatly affect the shape of a snowflake. Students found that snowflakes will from into column shapes when temperatures go well below freezing and there is not much humidity in the air. Through investigation, they concluded that snowflakes are most complex and beautiful (dendrite shape) when the temperature is just before freezing (between 10 and 0 degrees Fahrenheit) and when precipitation or humidity is high.

Quadrotor Flight Simulation with Disturbance Estimation Feedback

Student Researcher: Ryan C. Lucas

Advisors: Robert L. Williams II, Ph.D., Jay Wilhelm, Ph.D.

Ohio University
Mechanical Engineering

Abstract

One of the drawbacks with the majority of haptic interfaces is that they lack mobility, meaning that the user is unable to move around with the interface. The long term goal of this research revolves around using a Quadrotor as a mobile haptic interface. The user would grab a handle that is attached to the base of the quadrotor, and the Quadrotor would present the user with varying resistance depending on its global position.

However, the majority of haptic systems used today are inherently stable due to them being non mobile (ie robotic arms). The disadvantage of using a drone as a haptic interface is that they become unstable when subjected to external disturbances, particularly when subjected to contact disturbances.

The short term goal of this research is to create a quadrotor flight simulation platform that can be used to demonstrate the effectiveness of different controllers at rejecting disturbances. A model of the Crazyflie 2.0 Quadrotor is made using the Simulink platform and compared to an analogous hardware setup. Three different flight scenarios are compared using the hardware setup and the simulation. The results from the simulation and experiment are compared both quantitatively and qualitatively, and a new control method is implemented using the simulation platform.

Table 1. List of symbolic parameters and their meaning (not all parameters are used in this report)

name	meaning
CG	quadcopter center of gravity
g	acceleration due to gravity
m	quadcopter mass
$\mathbf{I}_G$	quadcopter mass moment of inertia tensor about CG
$\mathbf{f}_i$	vector thrust force of motor i
$\mathbf{r}_i$	position vector from CG to the motor i axis
τ_i	torque of motor i
T	total thrust in the direction of the {1} frame Z axis
$\varphi = \{\psi \quad \theta \quad \phi\}$	Z-Y-X yaw-pitch-roll Euler angles
$\dot{\varphi} = \{\dot{\psi} \quad \dot{\theta} \quad \dot{\phi}\}$	Z-Y-X Euler angle rates
$\ddot{\varphi} = \{\ddot{\psi} \quad \ddot{\theta} \quad \ddot{\phi}\}$	Z-Y-X Euler angle accelerations
${}^0\omega_1 = \{\omega_x \quad \omega_y \quad \omega_z\}^T$	absolute angular velocity of {1} w.r.t. {0}
${}^0\alpha_1 = \{\alpha_x \quad \alpha_y \quad \alpha_z\}^T$	absolute angular acceleration of {1} w.r.t. {0}
$\dot{\theta}_i$	angular speed of motor i
$\ddot{\theta}_i$	angular acceleration of motor i
${}^0\mathbf{P}_1$	position vector from {0} to {1} origins
P	contact point of application for external force
C_L	lift coefficient
C_D	drag coefficient
$\mathbf{F}_E$	external force applied on the environment by the quadcopter
$\mathbf{M}_E$	external moment applied on the environment by the quadcopter
$\mathbf{r}_E$	moment arm position vector from CG to P

Quadrotor Position Kinematics

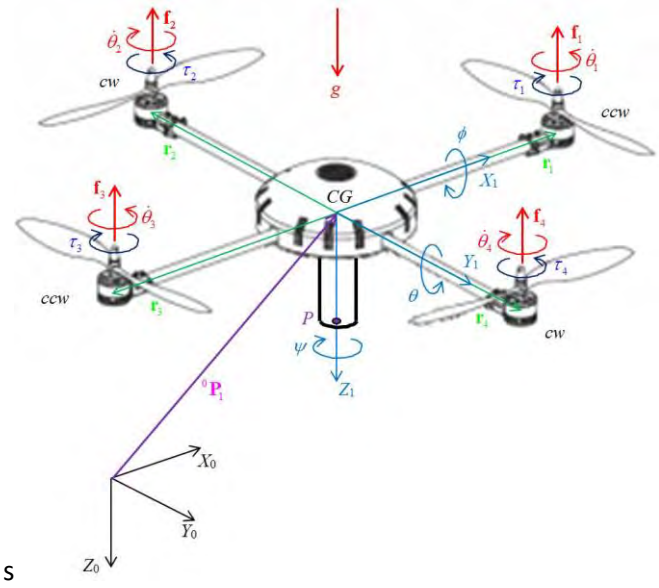

S

Figure1. Kinematic diagram of quadrotor.

Position vectors fixed in the moving frame {1} are:

$${}^1\mathbf{r}_1=\begin{Bmatrix} r\\0\\0\end{Bmatrix} \qquad {}^1\mathbf{r}_2=\begin{Bmatrix} 0\\-r\\0\end{Bmatrix} \qquad {}^1\mathbf{r}_3=\begin{Bmatrix} -r\\0\\0\end{Bmatrix} \qquad {}^1\mathbf{r}_4=\begin{Bmatrix} 0\\r\\0\end{Bmatrix}$$

$${}^1\left\{{}^{CG}\mathbf{P}_P\right\}=\begin{Bmatrix} p_x\\p_y\\p_z\end{Bmatrix} \qquad \left({}^1\left\{{}^{CG}\mathbf{P}_P\right\}=\begin{Bmatrix} 0\\0\\p\end{Bmatrix} \text{ is shown.}\right)$$

The Cartesian translational position, velocity, and acceleration vectors, with respect to the inertial frame, respectively are:

$${}^0\mathbf{P}_1=\begin{Bmatrix} x\\y\\z\end{Bmatrix} \qquad {}^0\dot{\mathbf{V}}_1=\begin{Bmatrix} \dot{x}\\\dot{y}\\\dot{z}\end{Bmatrix} \qquad {}^0\ddot{\mathbf{A}}_1=\begin{Bmatrix} \ddot{x}\\\ddot{y}\\\ddot{z}\end{Bmatrix}$$

The 3D angular convention used is the yaw-pitch-roll, Z-Y-X (Ψ-θ-Φ) Euler angles (see the above diagram):

$$\{\varphi\}=\begin{Bmatrix} \psi\\\theta\\\phi\end{Bmatrix}$$

Euler angle convention involves a series of three rotations about the moving (body) axes {1}. The set of Euler angles is NOT a vector (for large angle motions). The *Z-Y-X* Euler angles convention leads to the following orthonormal rotation matrix which gives the orientation of the moving frame {1} relative to the inertial frame {0}.

$$\left[{}^{0}_{1}\mathbf{R}\right]=\begin{bmatrix} c\psi c\theta & -s\psi c\phi + c\psi s\theta s\phi & s\psi s\phi + c\psi s\theta c\phi \\ s\psi c\theta & c\psi c\phi + s\psi s\theta s\phi & -c\psi s\phi + s\psi s\theta c\phi \\ -s\theta & c\theta s\phi & c\theta c\phi \end{bmatrix}$$

where the following abbreviations were used, for each of the three Euler angles:

$$c\alpha = \cos\alpha$$

$$s\alpha = \sin\alpha$$

The 4x4 homogeneous transformation matrix description of the quadcopter pose (position and orientation) is:

$$\left[{}^{0}_{1}\mathbf{T}\right]=\begin{bmatrix} \left[{}^{0}_{1}\mathbf{R}\right] & \left\{{}^{0}\mathbf{P}_{1}\right\} \\ 0 \quad 0 \quad 0 & 1 \end{bmatrix}$$

Quadrotor Dynamics

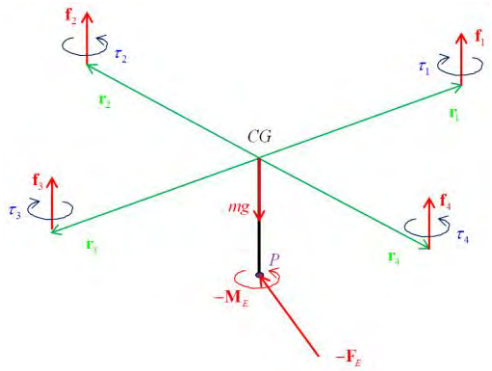

Figure 2. Free body diagram of Quadrotor with external forces and moments applied

Translational Dynamics

The wrench applied to the environment by the quadcopter at point *P*, in the coordinates of the moving frame {1}, is:

$${}^{1}\mathbf{W}_{E} = {}^{1}\begin{Bmatrix} \mathbf{F}_{E} \\ \mathbf{M}_{E} \end{Bmatrix} = \begin{Bmatrix} f_x \\ f_y \\ f_z \\ m_x \\ m_y \\ m_z \end{Bmatrix}$$

The individual thrust force magnitude for each motor is proportional to the square of its angular velocity. The constant of proportionality is the propeller lift coefficient *CL*.

$$f_i(t) = C_L \dot{\theta}_i^2(t)$$

This thrust is upward in the direction of the rotor axis, for all four motors/propellers:

$$ {}^{1}\mathbf{f}_i(t) = \begin{Bmatrix} 0 \\ 0 \\ C_L\dot{\theta}_i^2(t) \end{Bmatrix} $$

$$ {}^{0}\mathbf{f}_i(t) = {}^{0}_{1}\mathbf{R}\,{}^{1}\mathbf{f}_i(t) = \begin{Bmatrix} s\psi s\phi + c\psi s\theta c\phi \\ -c\psi s\phi + s\psi s\theta c\phi \\ c\theta c\phi \end{Bmatrix} C_L\dot{\theta}_i^2(t) $$

The expanded form of the translational equations of motion is:

$$ \begin{Bmatrix} s\psi s\phi + c\psi s\theta c\phi \\ -c\psi s\phi + s\psi s\theta c\phi \\ c\theta c\phi \end{Bmatrix} T + \begin{Bmatrix} 0 \\ 0 \\ -mg \end{Bmatrix} - \begin{Bmatrix} {}^{0}f_x \\ {}^{0}f_y \\ {}^{0}f_z \end{Bmatrix} = m \begin{Bmatrix} \ddot{x} \\ \ddot{y} \\ \ddot{z} \end{Bmatrix} $$

where *T* is the total thrust in the moving frame:

$$ T = C_L \sum_{i=1}^{4} \dot{\theta}_i^2 $$

and the force $\mathbf{F_E}$ applied to the environment by the quadcopter is expressed in {0} coordinates. It can be given in {0} coordinates directly or transformed from {1} coordinates as follows:

$$ {}^{0}\mathbf{F}_E = {}^{0}_{1}\mathbf{R}\,{}^{1}\mathbf{F}_E $$

$$ \begin{Bmatrix} {}^{0}f_x \\ {}^{0}f_y \\ {}^{0}f_z \end{Bmatrix} = \left[{}^{0}_{1}\mathbf{R} \right] \begin{Bmatrix} {}^{1}f_x \\ {}^{1}f_y \\ {}^{1}f_z \end{Bmatrix} $$

Rotational Dynamics

The rotor angular velocity and acceleration create a torque about the rotation axis for each motor *i* shaft:

$$ \tau_i(t) = I_P\ddot{\theta}_i(t) + C_D\dot{\theta}_i^2(t) $$

The rotor forces and torques create the torque vector about the moving frame axes as follows:

$$ {}^{1}\{\boldsymbol{\tau}_1\} = \begin{Bmatrix} \tau_{X_1} \\ \tau_{Y_1} \\ \tau_{Z_1} \end{Bmatrix} = \begin{Bmatrix} r(f_2 - f_4) \\ r(f_1 - f_3) \\ \sum_{i=1}^{4} \tau_i \end{Bmatrix} = \begin{Bmatrix} rC_L(\dot{\theta}_2^2 - \dot{\theta}_4^2) \\ rC_L(\dot{\theta}_1^2 - \dot{\theta}_3^2) \\ \sum_{i=1}^{4} \tau_i \end{Bmatrix} $$

From Euler's Rotational Dynamics Law, the external torque must be equal to the sum of the inertial torque , the centripetal forces torque, and the gyroscopic forces torque:

$$ \{\boldsymbol{\tau}_1\} - \{\mathbf{M}_E\} - \{\mathbf{r}_E\} \times \{\mathbf{F}_E\} = [\mathbf{I}_G]\{\boldsymbol{\alpha}\} + \{\boldsymbol{\omega}\} \times [\mathbf{I}_G]\{\boldsymbol{\omega}\} + \{\boldsymbol{\tau}_{GIR}\} $$

If we assume the quadcopter is symmetric about its *CG* and the body axes {1} are principal axes, then the mass moment of inertia tensor is not only symmetric and positive-definite, but is also diagonal:

$$[\mathbf{I}_G]=\begin{bmatrix} I_{xx} & 0 & 0 \\ 0 & I_{yy} & 0 \\ 0 & 0 & I_{zz} \end{bmatrix}$$

It is convenient to express the rotational dynamics equation in the coordinates (basis) of the moving frame {1}, since that is where, the centripetal forces torque, and the gyroscopic forces torque are already expressed:

$$\{\boldsymbol{\tau}_1\}-\{\mathbf{M}_E\}-\{{}^{CG}\mathbf{P}_P\}\times\{\mathbf{F}_E\}=[\mathbf{I}_G]\{\boldsymbol{\alpha}\}+\{\boldsymbol{\omega}\}\times[\mathbf{I}_G]\{\boldsymbol{\omega}\}+\{\boldsymbol{\tau}_{GYR}\}$$

However, if we consider centripetal and gyroscopic moments to be negligible, the dynamics equations can be expressed as:

$$\{\boldsymbol{\tau}_1\}-\{\mathbf{M}_E\}-\{{}^{CG}\mathbf{P}_P\}\times\{\mathbf{F}_E\}=[\mathbf{I}_G]\{\boldsymbol{\alpha}\}$$

So the expanded form of the rotational dynamics equations can be written as:

$$\begin{Bmatrix} \tau_{X_1} \\ \tau_{Y_1} \\ \tau_{Z_1} \end{Bmatrix}-\begin{Bmatrix} {}^1m_x \\ {}^1m_y \\ {}^1m_z \end{Bmatrix}-\begin{Bmatrix} 0 \\ 0 \\ p \end{Bmatrix}\times\begin{Bmatrix} {}^1f_x \\ {}^1f_y \\ {}^1f_z \end{Bmatrix}=\begin{bmatrix} I_{xx} & 0 & 0 \\ 0 & I_{yy} & 0 \\ 0 & 0 & I_{zz} \end{bmatrix}\begin{Bmatrix} \alpha_x \\ \alpha_y \\ \alpha_z \end{Bmatrix}$$

Existing Flight Control Architecture

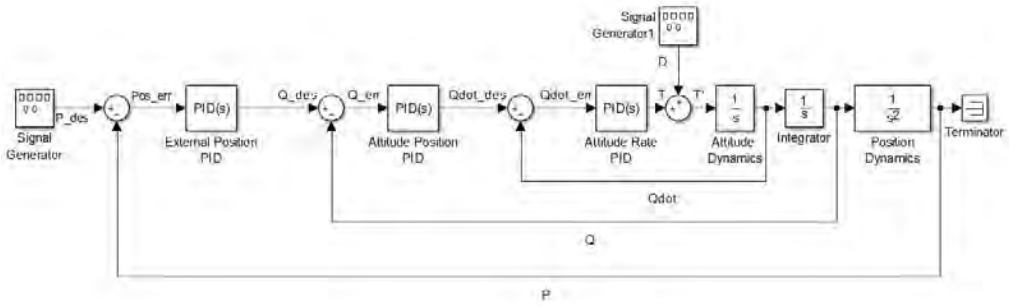

Figure 3. Existing flight controller architecture for crazyflie 2.0 setup

Shown above in Figure 3 is a linearized single degree of freedom block diagram of the Crazyflie 2.0 attitude control architecture integrated with motion capture position feedback. The coefficients for mass and moment of inertia values are NOT shown in this diagram.

The system has a total of three PID controllers. The first PID controller is an external Cartesian position controller that takes feedback from the Vicon motion capture system. The two remaining PID controllers are hardcoded into the Crazyflie Firmware. The inner controller stabilizes the attitude rate, and the outer control loop commands the quadrotors attitude position. The attitude dynamics transfer function relates thrust to velocity, and the position dynamics transfer function relates attitude to XY force due to thrust.

Table 3. Flight Controller Parameters

P_des	Desired XY Position		**Position Controller Gains**	X PID	Y PID	Z PID
Pos_err	XY Position Error		Kp (proportional)	29	29	45
P	XYZ Position		Ki (integral)	2.5	2.5	120
Q_des	Desired Attitude		Kd (derivative)	15	15	45
Q_err	Attitude Error		**Attitude Position Controller Gains**	Roll PID	Pitch PID	Yaw PID
Q	Attitude		Kp (proportional)	6	6	6
Qdot_des	Desired Attitude Rate		Ki (integral)	3	3	1
Qdot_err	Attitude Rate Error		Kd (derivative)	0	0	0.35
Qdot	Attitude Rate		**Attitude Rate Controller Gains**	Roll Rate PID	Pitch Rate PID	Yaw Rate PID
D	Disturbance		Kp (proportional)	250	250	120
T	Thrust Input		Ki (integral)	500	500	16.7
T'	Thrust + Disturbance		Kd (derivative)	2.5	2.5	0

Simulink Model

The Crazyflie flight simulator is a nonlinear model developed using the Simulink platform with the Aerospace toolbox. The duration of each simulation run is 100 seconds, and the simulation time step size is 0.001 seconds with an automatically selected numerical solver.

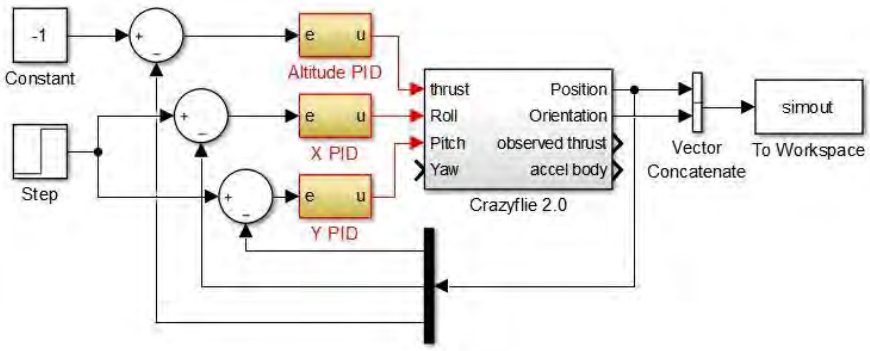

Figure 4. Top level diagram of crazyflie 2.0 flight simulator

The first level of the simulator consists of the external position PID controllers, and a custom made Crazyflie block. This simulator is entirely custom made excluding the six DOF aerospace block. The position and orientation results of the simulation are then sent to a matlab script that animates the flight scenario.

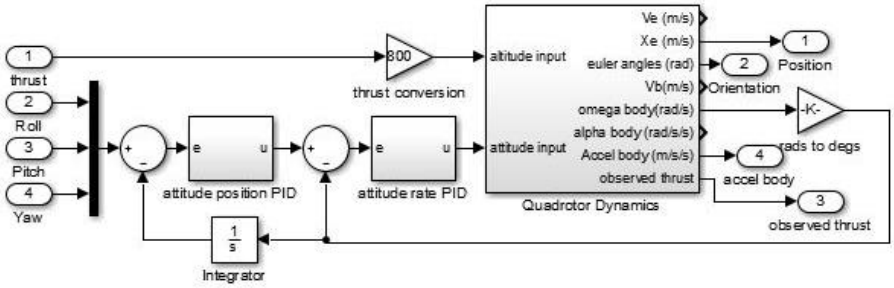

Figure 5. Diagram of crazyflie 2.0 internal flight controller

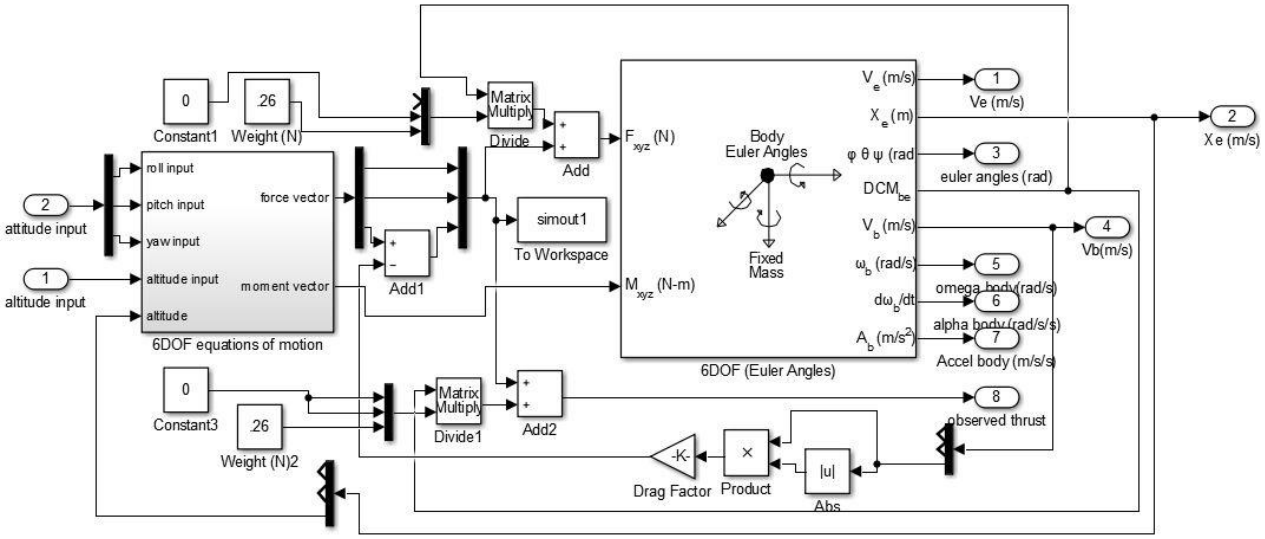

Figure 6. Diagram of crazyflie 2.0 dynamics

The second layer of the simulation consists of the Crazyflie's internal attitude rate and position controllers, and a quadrotor dynamics block. The dynamics block receives an attitude vector and a thrust input, then outputs the position and orientation of the quadrotor over time. The attitude rate is converted from radians per seconds to degrees per second before being fed back into the controllers. The quadrotor dynamics block consists of two primary blocks: an equation of motion block, and the 6DOF block from the Aerospace toolbox. The equations of motion block will take in the roll pitch yaw and altitude commands, and convert them into three dimensional forces and moments. The forces and moments are then sent to the 6DOF block where they are used to generate the motion of the quadrotor. Drag forces are also taken into account. The quadrotor is assumed to be an infinitely thin disk with the same diameter as the Crazyflie. However, incorporating aerodynamic drag had no noticeable effect on the systems dynamics.

Table 2. Numerical values for Crazyflie 2.0

m (mass)	m = 0.27 g
Principle Moments of inertia (Ixx, Iyy Izz)	Ixx =2.4E-5 kg*m^2 Iyy =2.4E-5 kg*m^2 Izz =3.2E-5 kg*m^2 NOTE:small variations have little effect
D (diameter)	9.2 cm

(see Landry in references)

Shown in Table 2 above are the key numerical parameters of the Crazyflie 2.0 (Landry et al.)

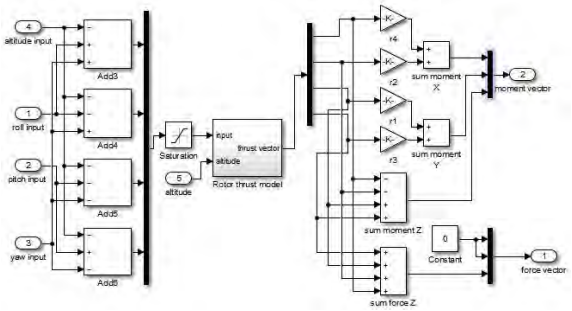

Figure 7. Diagram of quadrotor 6DOF equations of motion

The "equations of motion block" is almost entirely standard math operations. The only non-standard blocks being used are the custom rotor thrust model and the control input saturation block. NOTE: no consideration has been made regarding the yawing moments from the rotors.

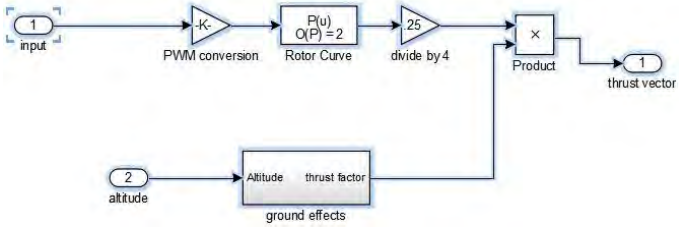

Figure 8. Diagram of rotor thrust model

The final level of the simulation is the rotor thrust model. The rotor model takes the PWM input from the controllers, and determines the rotor thrust via a second order fit from experimental data (Tobias et al.).

Hardware Setup

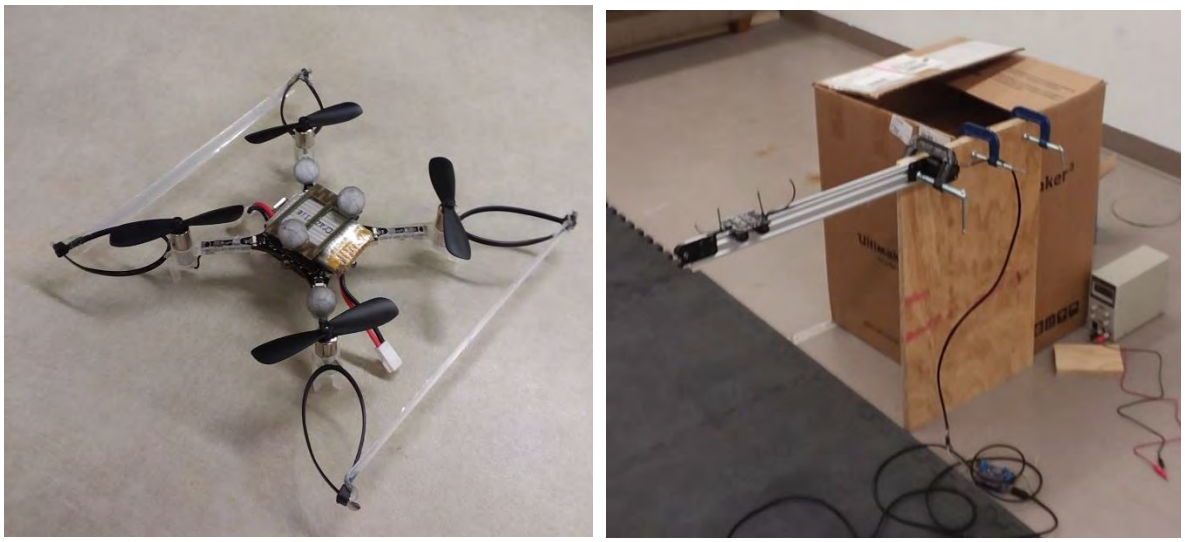

Figure 9. Crazyflie 2.0 quadrotor used for test flights (left), linear actuator setup for collecting disturbance response data (right)

The hardware used in this experiment consisted of the following items:

- **Crazyflie 2.0:** The crazyflie as seen in fig#9 was used for all of the test flights.
- **Vicon Motion Capture System:** The Vicon Motion capture system is used to collect position data of the Crazyflie, and also provide position feedback control.
- **Nema 17 V-slot Linear Actuator Kit:** The belt driven stepper motor Linear Actuator as seen in fig#9 was used to disturb the Crazyflie by hitting it with a light wooden rod.
- **Tekpower TP3005E DC Power Supply 30V 5A:** This power supply was used to power the Arduino motor controller and the Nema 17 stepper motor.
- **Arduino Uno w/ Adafruit MotorShield V2.3:** An Arduino Uno with an Adafruit motorshield was used to control the stepper motor.
- **Dowel rod:** Attached to the s linear actuator mount to disturb the Crazyflie.

Experimental Methods

Three different experiments were performed in order to test the accuracy of the quadrotor flight simulator. For each of the experiments the Crazyflie would start at a predefined origin, and its Cartesian position with respect to that origin would be recorded during the flight.

The first experiment was to have the Crazyflie 2.0 start at the origin (0,0,0) and fly to a point one meter directly above the origin (0,0,1). The position of the crazyflie would be recorded until it reached a steady state, and then it would slowly decrease in altitude until it landed on the origin.
For the second experiment the crazyflie started at the origin (0,0,0), then took off to a point one meter directly above the origin (0,0,1). The crazyflie would wait for fifteen seconds until it reached a steady state, then it would fly to a point in the XY direction (0.5,0.5,1). The crazyflie would wait for fifteen seconds until it reached a steady state, then moved back to the point directly above the origin (0,0,1).

The crazyflie would then slowly return to the origin (0,0,0).

For the final experiment the crazy flie would take off to a height (0,0,Z), then it would fly to a point (0,Y,Z) where it would hover in front of a small wooden post attached to a linear actuator. The crazyflie would reach a steady state then the linear actuator would extend and retract, giving the drone an impulse disturbance in the process.

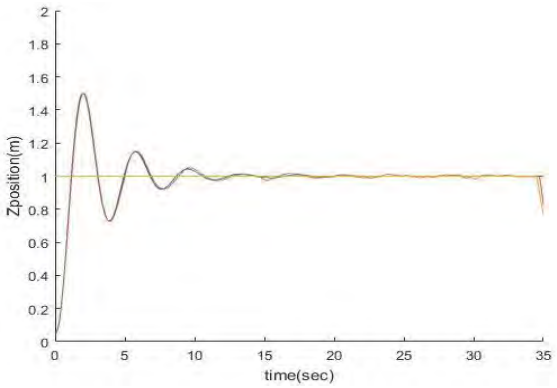

Figure 10. Comparison of the simulator altitude response (blue), actual altitude response (red), and desired altitude (yellow).

Of all of the results obtained, the altitude controller results are the cleanest fit. When plotted over top of each other the experimental results and the simulation results agree almost perfectly. Although it is hard to see, the plot actually has a red line and a blue line. This is most likely because this is the simplest controller in the whole simulation, being that it is only a single PID controller with no nested controllers. Unfortunately, this controller is not the most important when considering system stability.

Table 4. Comparison of simulation and experiment altitude response parameters

Data set	Rise Time (seconds)	Percent Overshoot(%)	Settling Time < 2% (seconds)
Simulator	1.16	57	11.70
Experiment	1.19	57	12.10
Percent Difference	2.55	0	2.93

Table 5. Comparison of simulator and experiment altitude peak/valley times

Simulator Peak/Valley Times	Experiment Peak/Valley Times	Percent difference	total difference
2	2.05	2.47	0.05
3.88	3.92	1.02	0.04
5.76	5.80	0.69	0.04
7.63	7.89	3.35	0.26
9.51	9.60	0.94	0.09
11.38	11.71	2.85	0.33

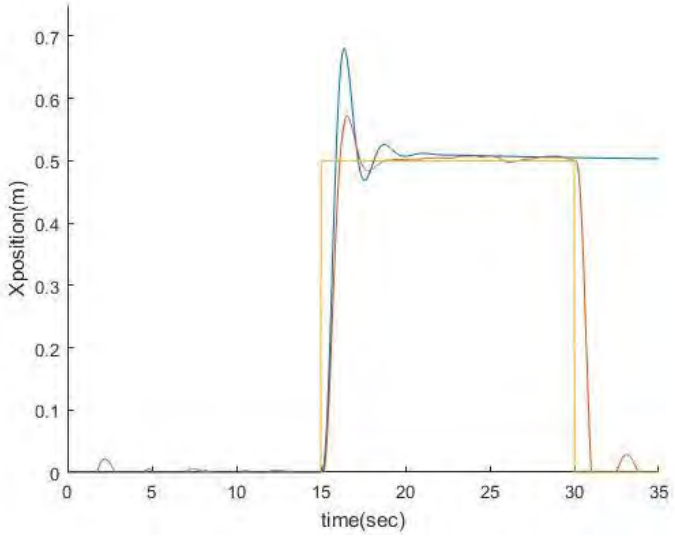

Figure 11: Comparison of the simulator X direction translational response (blue), actual response (red), and desired position (yellow).

When comparing the simulator translational response with the experimental data it is clear that the plots do not overlap as seamlessly as the altitude controller. Most notably, the simulation has significantly more overshoot than the actual response. However the peaks and valleys of both data sets align reasonably well.

Table 6. Comparison of simulation and experiment translational response parameters

Data set	Rise Time (seconds)	Percent Overshoot(%)	Settling Time < 2% (seconds)
Simulator	.89	35.9	6.8
Experiment	1.13	14.4	3.21
Percent difference	23.7	85.48	71.7

Table 7. Comparison of simulator and experiment translational peak/valley times

Simulator Peak/Valley Times	Experiment Peak/Valley Times	Percent Difference	Total Difference
16.38	16.55	1.0	0.17
17.59	17.81	1.2	0.22

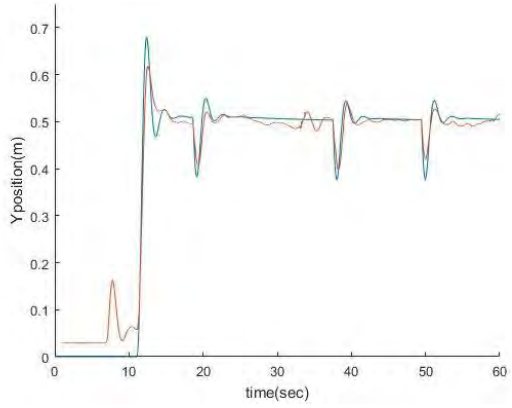

Figure 12. Simulator disturbance response (blue), and actual disturbance response (red).
Since the whole purpose of this simulation is to create feedback control methods for disturbance rejection, the most important set of data is from the impulse disturbance. Because no feasibly way to accurately determine impulse magnitude was developed, only the shape of impulse response can be analyzed with any degree of certainty. When the simulation response is scaled to roughly the same size as the experimental data, the frequencies match considerably well. Although the simulator gives no information on the magnitude of the response, it can still be used to compare the effects of different methods for rejecting disturbances.

Table 8. List of times between peaks and valleys of experimental disturbance response

Impulse	Peak 1 to 2 time	Peak 2 to 3 time
1	1.20	1.06
2	1.19	1.4
3	1.25	1.27
4 (plot not shown)	1.29	1.19
5 (plot not shown)	1.39	0.72
Average	**1.26**	**1.128**
Simulation results	**1.21**	**1.19**
Percent difference	**4%**	**5%**

Disturbance Estimator Implementation

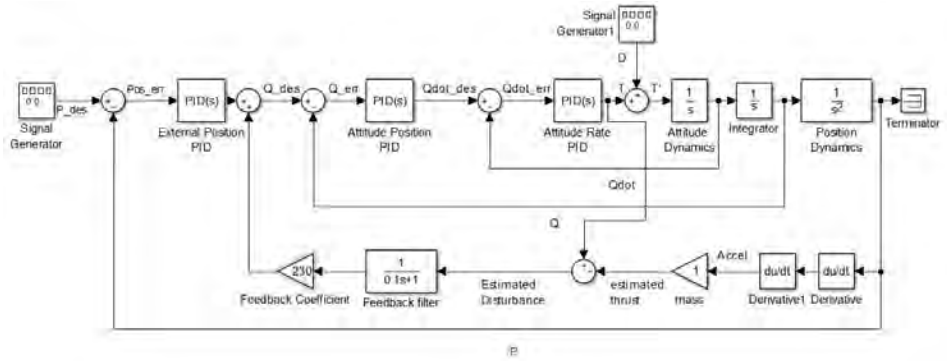

Figure 13. Simplified block iagram of quadrotor attitude control with disturbance estimator feedback

Shown above in Fig#13 is a picture of the previously presented control architecture with a disturbance estimator added and fed back into the external position controller input. The disturbance estimator will observe the acceleration of the quadrotor and calculate the inertial forces via inverse dynamics. The estimator then looks at the difference between the estimated forces and the controller input forces to determine the disturbance magnitude. The estimated disturbance is then filtered and added back into the position controller input. This will provide a greater response when the system is subjected to a disturbance without affecting the controllability of the system.

Table 9. Feedback filter coefficients

Filter Gain(feedback coefficient K)	230
Derivative Coefficient (A)	0.1
Proportional Coefficient(B)	1

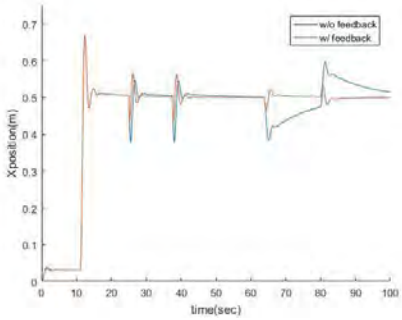

Figure14. Comparison of simulation disturbance response with disturbance estimator feedback (red) and without disturbance estimator feedback (blue)

Shown above is a plot of the simulation response to two impulse disturbances and a step disturbance. To quantify the magnitude of the disturbances the distance between the maximum and minimum peaks for each response is measured. For both the impulse and step disturbances the maximum displacement is reduced for the case with the disturbance estimator. In the case of the step response the steady state error is drastically reduced.

When considering the use of quadrotors as haptic interfaces, the use of a disturbance estimator could potentially improve the quadrotors ability to reject disturbances while providing reaction forces to the user. However, further research must be done to determine the effects of the disturbance estimator on the systems stability margins.

Table 10. Comparison of impulse and step disturbance responses with and without estimator feedback

Disturbance Type	Peak to peak distance w/ feedback	Peak to Peak Distance w/o feedback	Percent decrease with feedback
Impulse	0.1259	0.1678	24.97
Step	0.0551	0.1183	114.7

Conclusions

Based on the comparison between the simulation and experimental results in this research, this model seems sufficiently accurate to act as a qualitative aid in system design. The true effectiveness of this model cannot be evaluated until it is used to design and implement a real life controller. However, based on the results from the simulator, the use of an acceleration based disturbance estimator for feedback can help reduce the effect of both impulse and step disturbances. In particular, the observer's ability to reject the effect of step disturbances without affecting the controllability of the system could be very useful for turning quadrotors into haptic interfaces. However, the true effectiveness of the estimator and the accuracy of the simulation cannot be fully verified until the controller has been implemented on the actual hardware system.

Future Work

Further research in this area would require further refinement of the simulation by creating a more accurate model of the Crazyflie 2.0 attitude position and attitude rate controllers. Once the model's response to X and Y waypoint commands better matches the data being collected, further experiment should be performed to compare the stability margins of the simulation to the hardware systems stability margins. Finally after the model has been sufficiently refined, the disturbance observer should be implemented in the crazyflie 2.0 firmware. Finally, the performance results of the controller should be compared to the predicted results of the simulation.

References

1. Landry, Benoit. Planning and Control for Quadrotor Flight through Cluttered Environments. (39) MIT Department of Electrical Engineering and Computer Science , 2014.
2. Jung, Seul. Tomizuka, Masayoshi. Attitude control of a quad-rotor system using an acceleration-based disturbance observer:An empirical approach. IEEE/ASME International Conference on Advanced Intelligent Mechatronics, 2012.
3. *https://github.com/bitcraze/crazyflie-firmware*
4. Tobias. "Measuring propeller RPM: Part 3." Bitcraze, November 02, 2015. Bitcraze. March 20, 2018.

Beltrami Flows

Student Researcher: Alexander Margetis

Advisor: Dr. Benjamin Jaye

Kent State University
Department of Mathematical Sciences

Abstract
A Beltrami flow in R^3 is an incompressible (divergence free) vector field that is everywhere parallel to its curl. These flows arise naturally in many physical problems. In astrophysics and in plasma fusion Beltrami fields are known as force-free fields. They describe the equilibrium of perfectly conducting pressure-less plasma in the presence of a strong magnetic field. In fluid mechanics, Beltrami flows arise as steady states of the 3D Euler equations. Numerical evidence [PYOSL] suggests that in certain regimes turbulent flows organize into a coherent hierarchy of weakly interacting superimposed approximate Beltrami flows.

Given the importance of Beltrami fields, there are several approaches to proving existence of solutions, for instance [LA] use the calculus of variations, and [BA] use fixed point arguments. In this thesis we instead use a Hilbert space approach through the Lax-Milgram lemma.

The quantitative behavior of Beltrami fields is still an active research topic of mathematicians and is not well understood. For several recent contributions, see for instance [CC, EP, N].

Project Objectives
The main focus of this work will be to develop a thorough mathematical analysis of Beltrami flows. Methods for the construction of Beltrami flows. It will be shown that this can be done relatively explicitly via classical separation of variables methods in the case when one is solving the equation in a ball. In general domains, we shall construct Beltrami flows as a solution of certain variational problems in the calculus of variations. In this work, variable Beltrami coefficient α will be considered, building upon prior work by Laurence and Avellanda (1991) (which made rigorous a prior result of Woltjer (1958)) in the case when α is a constant. To carry this out, we shall first find a weak solution to of the boundary value problem in the modern framework of Sobolev spaces (see Evans 2010), and then appeal to Elliptic regularity theory to show that the flows constructed are infinitely differentiable.

The second component of the project will analyze the structure of Beltrami flows. These structure theorems will be applied to draw conclusions about the physical problems modelled by Beltrami flows. Along the way, alternative approaches will be given to recent Liouville type theorems (Nadirashvili 2014) characterizing Beltrami flows of finite energy.

Methodology
Our goal is to find a weak solution to the Beltrami flow, for a smooth function $\boldsymbol{\lambda(x)}$ in $\boldsymbol{\Omega}$ and a boundary function $\mathbf{g}$ on $\boldsymbol{\partial\Omega}$.

$$(1.1) \qquad \begin{cases} \nabla \times \mathbf{B} = \lambda(x)\mathbf{B} \text{ in } \Omega \\ \nabla \cdot \mathbf{B} = 0 \text{ in } \Omega \\ \mathbf{B} \cdot \mathbf{n} = g \text{ on } \partial\Omega \end{cases}$$

The project heavily uses the theory of **Sobolev Spaces**. These spaces are built on the notion of the weak derivative. We recall the classical integration by parts formula for an open set Ω with a smooth boundary: If f and g are continuously differentiable functions in Ω (we shall write $C^1(\Omega)$ for the collection of such functions), then

$$(1) \quad \int_\Omega \frac{\partial f}{\partial x_j} g dx = -\int_\Omega f \frac{\partial g}{\partial x_j} dx + \int_{\partial\Omega} f g n_i dS,$$

where $\boldsymbol{n} = (\boldsymbol{n_1}, \boldsymbol{n_2}, \boldsymbol{n_3})$ is the outward unit normal to **Ω**. We say that an integrable function **f** has a weak derivative function $D_j f \; if \; D_j f$ is an integrable function, and for any $C^1(\Omega)$ function **g** with **g = 0** on **∂Ω**,

$$\int_\Omega (D_j f) g dx = -\int_\Omega f \frac{\partial g}{\partial x_j} dx.$$

Essentially, this says that we do not require f to have a classical derivative, but there should be some function for which integration by parts still holds. By moving away from the classical, or strong, derivative we are able in this project to prove some quite powerful theorems about the existence of solutions to elliptic equations. We set $H^1(\Omega) = \{f: \Omega \to R^3 \; such \; that \; \int_\Omega |f|^2 + |\nabla f|^2 dx < \infty\}$, where $\nabla f = (D_1 f, D_2 f, D_3 f)$ is the weak gradiant of f. In our problem, we shall make use of two slightly less standard Sobolev spaces associated to vector fields, namely

$$H^1_n(\Omega) = \{\mathbf{B} : \Omega \to \mathbb{R}^3 : \int_\Omega \mathbf{B} \cdot \nabla f dx = -\int_\Omega (\nabla \cdot \mathbf{B}) f dx \text{ for every } f \in H^1(\Omega)\}$$

This means "$\mathbf{B} \cdot \mathbf{n} = 0$ on $\partial\Omega$".

$$H^1_{\tan}(\Omega) = \{\mathbf{B} : \Omega \to \mathbb{R}^3 : \int_\Omega \mathbf{B} \cdot \nabla \times \mathbf{F} dx = -\int_\Omega (\nabla \times \mathbf{B}) \cdot \mathbf{F} dx \text{ for every } \mathbf{F} \in H^1(\Omega)\}.$$

This means "$\mathbf{B} \times \mathbf{n} = 0$ on $\partial\Omega$".

Here $\nabla \times \boldsymbol{B} = (D_2 B_3 - D_3 B_2, D_3 B_1 - D_1 B_3, D_1 B_2 - D_2 B_1)$ is the weak curl. The Lax–Milgram theorem gives conditions under which a bilinear function can be "inverted" to show the existence and uniqueness of a weak solution to a given boundary value problem.

Results Obtained

The main result obtained in the project is the following theorem: If Ω is a smooth bounded domain, $\iint_{\partial\Omega} g \; dS = 0$, and the function $\lambda(x)$ is pointwise small enough depending on the geometry of $\partial\Omega$ then there exists $\boldsymbol{B}$ in $H^1(\Omega)$ such that $\boldsymbol{B} - g$ belongs to $H^1_n(\Omega)$ and $\boldsymbol{B}$ solves (1.1), meaning that $\int_\Omega (\nabla \times \boldsymbol{B}) f dx = \int_\Omega (\lambda \boldsymbol{B}) f dx \; and \; \int_\Omega (\nabla \cdot \boldsymbol{B}) f dx = 0$ for every $f \in H^1(\Omega)$.

The smallness assumption on the function $\lambda(x)$ comes from verifying that the bilinear form associated to the operator function $\nabla \times \boldsymbol{B} - \lambda \boldsymbol{B}$ satisfies a positive definiteness assumption called Ellipticity. More precisely, we need the function $\lambda(x)$ to be smaller than some constants appearing in inequalities called Sobolev or Poincare inequalities, which are a family of inequalities that compare the integral of a function to the integral of its weak gradient, provided that the function has zero boundary value in some sense.

Future Work

We aim develop finite element methods to approximate Beltrami flows. Finite element methods work by splitting the domain into small bits "a triangulation". We wrote a finite element code for solving the Poisson equation in a general polygonal domain using piecewise linear finite elements.

Dirichlet:
$\Omega = [0,1] \times [-1/2, 1/2]$

$$\begin{cases} \Delta u = -2\pi^2 \sin(\pi x)\cos(\pi y) \text{ in } \Omega \\ u = 0 \text{ on } \partial\Omega \end{cases}$$

Solution $u(x,y) = \sin \pi x \cos \pi y$

Neumann:
$\Omega = \{x^2 + y^2 \leq 1\}$

$$\begin{cases} \Delta u = 1 \\ \frac{\partial u}{\partial n} = 1/2 \text{ on } \partial\Omega \end{cases}$$

Solution $u(x,y) = (x^2 + y^2 - 1)/4$

.

The finite element approximations yield following graphs, which show good approximations to the actual solutions. The left hand graph is the Dirichlet problem, and the right hand graph is the Neumann problem.

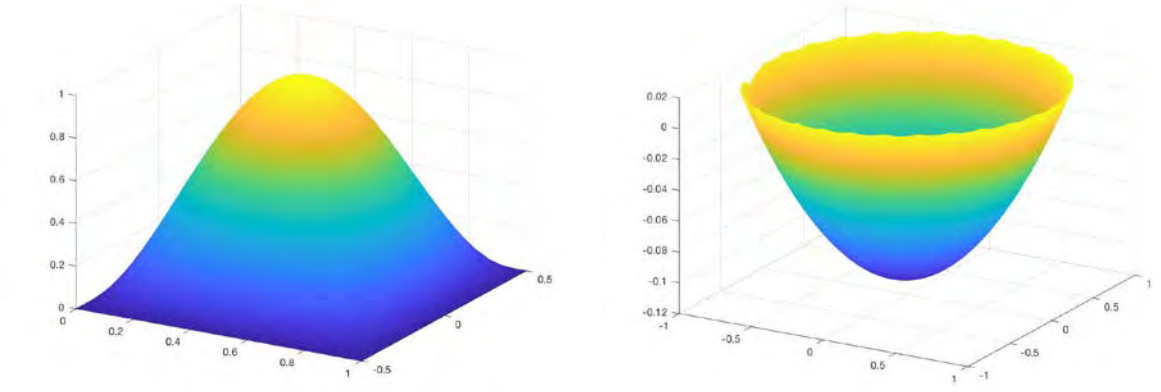

We intend to adapt the code to be able to model Beltrami flows with given boundary data.

Significance and Interpretation of Results

Beltrami flows arise in several areas of physics. One problem in which they occur naturally is in modeling the magnetic field of the sun. It is not yet possible to take accurate measurements of the magnetic field of the sun in the corona; measurements are instead taken in the photosphere, which is much cooler. A natural issue, therefore, is to reconstruct a Beltrami field in a domain from measurements on the boundary. Mathematically, this can be expressed as solving the problem the boundary value problem (1.1).

References

1. L. C. Evans, Partial Differential Equations, 2nd Edition, AMS Graduate Studies in Mathematics, 2010.
2. Laurence and Avellanda, On Woltjer's variational principle for force-free fields, J. Math. Phys. 1991.
3. N. Nadirashvili, Liouville theorem for Beltrami flow, to appear in Geometric and Functional Analysis.
4. [PYOSL] Pelz, Yakhot, Orszag, Shtilman, Levich, Velocity--vorticity patterns in turbulent flow. Phys. Rev. Lett. 1986.
5. L. Woltjer, A theorem on force-free fields, PNAS 1958.

Experimental Evaluation of a Miniature Haptic Actuator based on Electrorheological Fluid

Student Researcher: Alex J. Mazursky

Advisor: Dr. Jeong-Hoi Koo

Miami University
Department of Mechanical and Manufacturing Engineering

Abstract
Haptic feedback is desired for numerous applications including simulators, teleoperations, entertainment and more. While many devices today feature vibrotactile feedback, most do not provide kinesthetic feedback. To address the need for both vibrotactile and kinesthetic feedback, this study investigates the use of electrorheological (ER) fluids for their tunable viscosity under electrical stimulation. A prototype device containing ER fluid was designed and fabricated. The device operates based on pressure-driven flow of the fluid between charged plates due to user interaction with the touch contact surface. The prototype was tested using a dynamic mechanical analyzer to measure the actuator's resistive force with respect to indentation depth for a range of applied voltages and frequencies. The results indicate that increasing the applied voltage causes an increase in the force produced by the actuator. Varying the supplied signal over a range of voltages and frequencies can convey a range of force and vibrational feedback. This range is sufficient to transmit distinct haptic sensations to human operators and demonstrates the design's capability to transmit remote or virtual touch feedback conditions.

Introduction
In recent years, the rising implementation of haptic technology has transformed how we interact with electronic devices and digital information. Haptic technology conveys information to the user through touch sensations, offering a more engaging and realistic user experience. In addition to visual and auditory sensations, being able to touch, feel and manipulate objects in an environment, whether real or virtual, offers a greater sense of immersion in that environment.[1] Previous studies have shown that enhancing user immersion through haptic feedback results in improved user performance of typical tasks on devices.[2,3] The benefits of integrating haptic feedback have been realized across a wide range of applications, including medical training simulators, teleoperation and entertainment.[4-6]

For a device to provide complete haptic feedback, it must be capable of producing both tactile and kinesthetic sensations. Kinesthetic feedback is felt in one's joint and muscle nerves and provides information about position and movement. Tactile feedback consists of the sensations felt at the surface of one's skin and just underneath it. When sensing an object, humans may rub it to feel its texture and roughness (tactile sensation) and press it to feel its resistance and elasticity (kinesthetic sensation). Therefore, both sensations must be present to completely observe an object through touch.[1]

Though many devices today incorporate vibrotactile feedback, most neglect to integrate kinesthetic feedback due to size constraints. Many of the kinesthetic devices proposed in current research are based upon alternating current/direct current (AC/DC) motors to create force feedback sensations.[7-9] Despite developments toward AC/DC motor-based kinesthetic actuators, they cannot be easily implemented into small-scale devices, such as mobile handhelds, due to their size and power requirements. Additionally, active-controlled motors tend to have instability problems, which can be a significant roadblock for certain applications.[10,11]

To address this issue, researchers have proposed 'smart materials' to actuate the haptic sensations instead of traditional motors. Smart materials are designed to have variable properties dependent upon external stimuli, such as temperature, stress, magnetic or electric fields and more. Jansen *et al.* utilized a pouch containing magnetorheological (MR) fluid and an electromagnet array to produce haptic sensations over the pouch's flexible surface, deemed the "Mudpad."[12] The electromagnet array controlled the smart fluid's viscosity, and therefore, the kinesthetic and vibrotactile feedback observed when interacting with the "Mudpad." However, reducing the size of the "Mudpad" design for use in handheld applications may prove difficult due to its electromagnet coils. Beyond "Mudpad", Yang *et al*. (2010) introduced a miniature tunable stiffness display based on MR fluids, validating the feasibility of using MR fluid in smaller kinesthetic devices.[13] In a subsequent study, Yang *et al.* (2012) applied MR fluid in a miniature (10 x 10 x 12 mm) haptic button capable of producing a wide range of kinesthetic and vibrotactile feedback.[14] However, basing an actuator around MR fluid requires complex circuitry and manufacturing.

Analogous to MR fluid, electrorheological (ER) fluid's viscosity is reversibly tunable in response to electric fields.[15] Similarly, ER fluid features response times in the order of milliseconds, low power consumption and has few issues with stability.[16-18] Though MR fluid is capable of producing a larger range of yield stresses, ER fluid may prove advantageous in some haptic applications due to simple electrical control design, as only two electrodes are needed compared to a "bulky" solenoid coil for MR devices. With a miniature design in mind, it is also possible to improve upon the device fabrication.

Project Objectives

The goal of this paper is to fabricate an ER fluid-based actuator and validate its ability to convey both tactile and kinesthetic sensations. The actuator contains ER fluid, which provides the variable resistive force to the button's kinesthetic interface. By supplying voltage signals to electric field plates housed within the actuator, the device's force feedback is controlled. Introducing a frequency into the applied voltage results in oscillations in the kinesthetic response to produce a vibrotactile response. Therefore, the proposed ER fluid-based device is capable of producing haptic feedback.

Methodology

Working Principle and Design Considerations

Figure 1 depicts the cross-section and working principle of the proposed haptic actuator. The body of the actuator is cylindrical and contains two concentric electrodes separated by a small gap. The internal volume of the body is filled completely with ER fluid and is sealed within the body by a nonconductive, silicone rubber layer. The seal doubles as the elastic contact interface of the haptic actuator. By indenting the membrane interface, ER fluid is pushed through the gap between the electrodes and up into a reciprocating reservoir to compensate for the change in volume. Therefore, the device operates based on pressure-driven flow mode. When the pressure on the contact surface is removed, the fluid flows back from the reservoir and the device returns to its initial state.

When a voltage is supplied to the plates, the ER fluid in the gap forms a network of fibers along the field lines. The resultant change in viscosity produces a yield stress due to flow mode in relation to the voltage input and contributes to the kinesthetic force experienced by the user when indenting the membrane. Therefore, the total force feedback felt by the user can be represented by the relation:

$$F_{total} = F_{0V} + F_{ER} \quad (1)$$

where F_{total}: total force (N); F_{0V}: resistive force in off state; F_{ER}: force due to the ER effect. By providing an alternating signal to the electrodes, the viscosity of the fluid fluctuates in response and provides a time-dependent force to the user indicative of vibrational feedback.

Fabrication of the Actuator

The schematic view of the haptic actuator is shown in Figure 2. The two-piece, plastic housing contains the concentric electrode rings and ER fluid. The lower and upper electrodes are attached to the negative and positive halves of the housing, respectively, and are separated by a fixed, 1 mm gap. Conductive leads connect to the electrodes and are fed out through the side of the device to receive input voltage signals. The two halves of the housing are sealed by a groove fit. The actuator's volume is then filled with ER fluid and a thin silicone rubber membrane is placed over the top half of the device. The membrane is compressed against the upper surface of the positive housing by tightening the cover with nylon screws. The membrane therefore doubles as a seal and the actuator's contact surface. The assembled device measures 42 mm in diameter and 14.5 mm thick.

Experimental Evaluation

To evaluate the haptic performance of the device prototype, mechanical analysis was conducted using a dynamic mechanical analyzer (RSA3, TA Instruments), as seen in Figure 3. This experimentation measured the total resistive force with respect to indentation depth over the button's stroke of up to 1 mm. The performance was evaluated under different input voltage and frequency conditions using a tool similar in size to a human finger. This testing was performed with giant ER fluid inside the device, which produces greater yield stresses than conventional fluid.[19]

Results Obtained

Kinesthetic Response

Figure 4a shows the variation of the measured resistive force with respect to the pressed depth (varied from 0 mm to 1 mm) and the applied voltage across the 1 mm electrode gap (0 V/mm, 1 kV/mm, 2 kV/mm, and 3 kV/mm) at a pressing velocity of 1 mm/s. As shown in the figure, the resistive force increases as the input voltage and the pressed depth increase. The off-state resistive force at the maximum depth was measured to be about 1.4 N, and the maximum resistive force produced was found to be about 2.3 N with 3 kV supplied. It should be noted that a thin layer of air is trapped inside the device during assembly, causing an inevitable, small gap between the contact surface and fluid. Hence, when the actuator is indented at small depths, the stiffness of the membrane alone contributes to the total force. At larger strokes, the force due to the ER effect is present.

Tactile Response

Under direct current, the actuator operates kinesthetically, as no oscillations are produced in the response. To demonstrate a vibrotactile response, sinusoidal and square wave functions were applied at maximum voltage (3 kV/mm) and 3 Hz frequencies and the force vs. depth responses were observed, shown below in Figures 4b and 4c. From the resultant plots, it is evident that the actuator conveys vibrational feedback when excited with a harmonic voltage. The square waveform resulted in lesser amplitudes of vibration than the sinusoidal waveform due to its instantaneous nature. As a consequence of the fluctuating signal, greater amplitudes of vibration corresponded to reduced force at maximum depth. It should also be noted that the observed frequency is twice that of the applied frequency due to the absolute behavior of the resistive force.

Significance of Results

This article has proposed a new miniature haptic actuator based on ER fluids. An elastic contact surface was used to drive fluid between fixed electrodes to produce a range of kinesthetic and vibrotactile feedbacks. After constructing a prototype actuator, the device's behavior was characterized experimentally with a dynamic mechanical analyzer under different input voltages and frequencies. The results demonstrate that the resistive force increases as the indented depth and the input voltage increase. Additionally, the device is capable of producing vibrational feedback. Hence, this study validated that the proposed ER fluid–based haptic device can be used to provide haptic feedback in button-type applications. This work has potential to be implemented in a larger haptic display that can convey localized touch feedback over a continuous surface by using an array of electrodes.

Figures

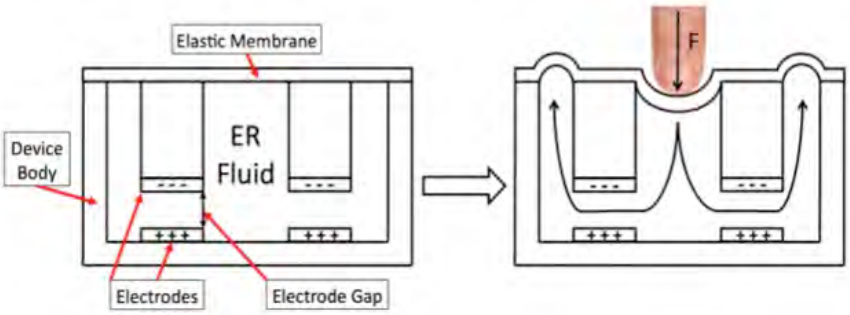

Figure 1. Diagram of the actuator's design features, flow mode under pressure and simple volume change compensation.

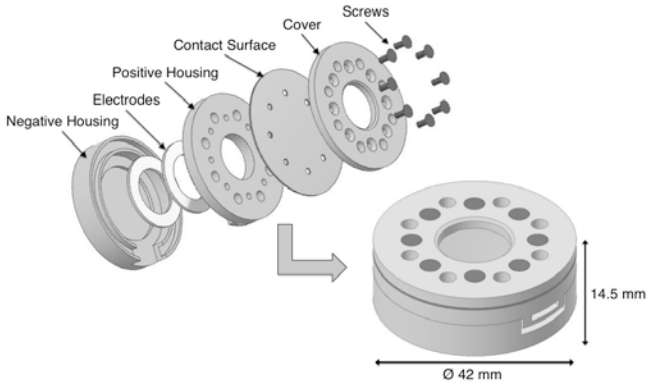

Figure 2. Schematic view of the proposed haptic button.

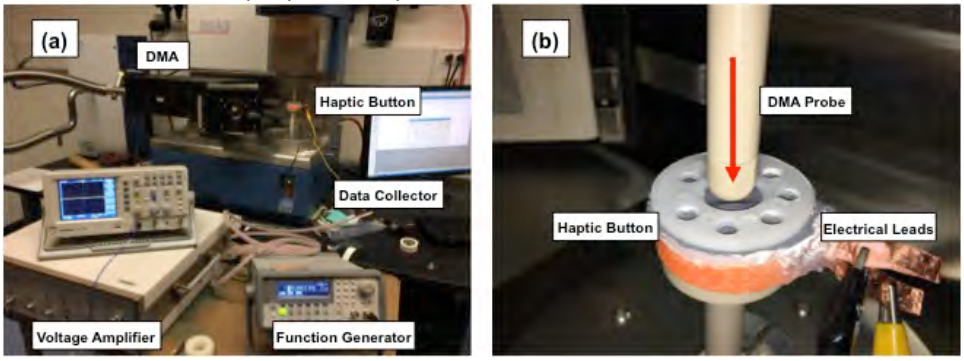

Figure 3. (a) Experimental setup to measure the generated force of the haptic button with respect to applied voltage and indentation depth and **(b)** a closer inspection of the indentation probe and button position.

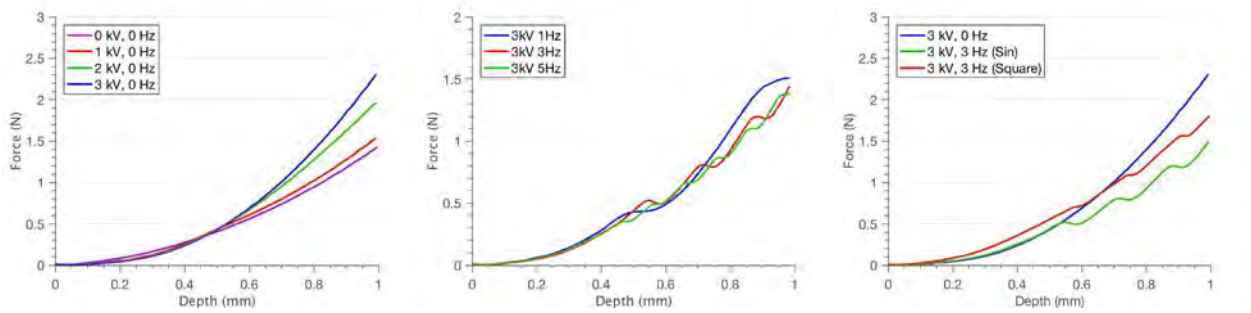

(a (b) (c)

Figure 4. (a) Results of the kinesthetic test under varied input voltages, **(b)** Results of the haptic test under varied input frequencies, **(c)** Comparison of response under varied input waveforms

Acknowledgments

This work was partially supported by the "Undergraduate Research Award" funded by the Office of Research for Undergraduates at Miami University and by the Ohio Space Grant Consortium.

References

1. Srinivasan, M., Basdogan, C., "Haptics in virtual environments: taxonomy, research status, and challenges," Comput. & Graphics 21(4), 393-404 (1997).
2. Hoggan, E., Brewster, S.A., Johnston, J., "Investigating the effectiveness of tactile feedback for mobile touchscreens," Proc. of CHI ACM, 1573-1582 (2008).
3. Poupyrev, I., Maruyama, S., and Rekimoto, J., "Ambient touch: designing tactile interfaces for handheld devices," Proc. of UIST ACM, 51-60 (2002).
4. Coles, T., Meglan, D., John, N., "The role of haptics in medical training simulators: A survey of the state of the art," IEEE Transactions on Haptics 4(1), 51-66 (2010).
5. Park, J., Khatib, O., "A haptic teleoperation approach based on contact force control," The Int. J. of Robotics Research 25(5-6), 575-591 (2006).
6. Laycock, S.D., Day, A.M., "Recent developments and applications of haptic devices," Computer Graphics Forum 22(2), 117-132 (2003).
7. Song, A., Morris, D., Colgate, J.E., "Haptic telemanipulation of soft environment without direct force feedback," Proc. of the 2005 IEEE International Conference on Information Acquisition, 21-25 (2005).
8. Bianchi, M., Scilingo, E.P., Serio, A., et al. "A new softness display based on bi-elastic fabric," Proc. of the third joint eurohaptics conference and symposium on haptic interfaces for virtual environment and teleoperator systems, 382-383 (2009).
9. Fujita, K., Ohmori, H., "A new softness display interface by dynamic fingertip contact area control," Proc. of the 5th World Multiconference on Systemics, Cybernetics and Informatics, 78-82 (2000).
10. Adams, R.J., Moreyra, M.R., Hannaford B., "Stability and performance of haptic displays: theory and experiments," Proc. of ASME international mechanical engineering congress and exhibition, 227–234 (1998).
11. An, J., Kwon, D.S., "Stability and performance of haptic interfaces with active/passive actuators-theory and experiments," The Int. J. of Robotics Research 25(11), 1121–1136 (2006).
12. Jansen, Y., Karrer, T., Borchers, J., "MudPad: Localized tactile feedback on touch surfaces," Proc. of UIST, 385-386 (2010).
13. Yang, T.H., Kwon, H.J., Lee, S.S., et al., "Development of a miniature tunable stiffness display using MR fluids for haptic application," Sensors and Actuators A: Physical 163, 180–190 (2010).

14. Yang, T.H., Koo, J.H., Kim, S.Y., Kyung, K.U., Kwon, K.S., “Application of magnetorheological fluids for a miniature haptic button: Experimental evaluation,” Journal of Intelligent Material Systems and Structures 23(9), 1025-1031 (2012).
15. Whittle, M., Bullough, W. A., “The structure of smart fluids,” Nature 358, 373–373 (1992).
16. Whittle, M., Atkin, R.J., Bullough, W.A., “Dynamics of an electrorheological valve,” Int. J. of Modern Physics B 10(23-24), 2933–2950 (1996).
17. Bullough, W.A., Johnson A.R., Hosseini-Sianaki, A., Makin, J., Firoozian, R., “The electro-rheological clutch: design, performance characteristics and operation,” Proc. Inst. Mech. Eng. 207, 87–95 (1993).
18. Han, S.S., Choi, S.B., Cheong C.C., “Position control of X–Y table mechanism using electro-rheological clutches,” Mech. Mach. Theory 35, 1563–77 (2000).
19. Wen, W., Huang, X., Yang, S., Lu, K., Sheng, P., “The giant electrorheological effect in suspensions of nanoparticles,” Nature Materials 2, 727-730 (2003).

Control of Dynamic Stall Over an Airfoil Using NS-DBD Plasma Actuators

Student Researcher: Matthew N. McCannon

Advisor: Dr. Mo Samimy

The Ohio State University
Department of Mechanical and Aerospace Engineering

Abstract
Dynamic stall is a phenomenon which can affect things like rotorcraft, maneuvering fixed wing craft, and wind turbines. Research is being conducted at The Ohio state University's Aerospace Research Center (ARC) to understand the flow physics of dynamic stall and how it can be controlled using nano-second pulse driven dielectric barrier discharge plasma actuators (NS-DBDs). NS-DBDs are being used as an active flow control technique to manipulate the natural instabilities in the flow.

Project Objective
Active and passive flow control devises have been researched and proven to delay separation or even reattach separated flow. The big challenge is to find a practical flow control device that can be used at high speed cruise conditions, while minimizing complexity of the system, and adding minimal weight to the structure. The purpose of this study is to see if nano-second pulse driven dielectric barrier discharge plasma actuators (NS-DBDs) are a viable option, as they add minimal weight and complexity to the structure. Figure one below shows a schematic of the flow control device.

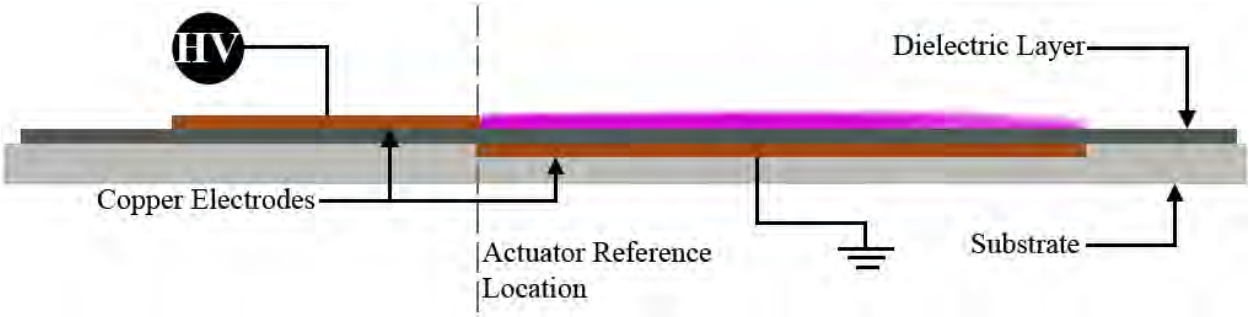

Figure 1. NS-DBD plasma actuator schematic. Vertical dimensions exaggerated for clarity [5].

Preliminary testing at the ARC concluded that although the flight conditions dictate the necessary actuation frequency to maximize the benefits of the NS-DBDs, it has been observed to break up the shear layer and reduce separation at all actuation frequencies.

For current testing, modifications to the experimental setup will be implemented in order to reduce error in measurement. The goal for this experiment remains unchanged; understand the flow physics and learn how to control the flow.

Methodology Used
The dynamic stall research at The Ohio State University focused primarily on understanding its effects in rotorcraft applications. The preliminary work used a NACA 0015 which is not a typical cross section you would see on a rotorcraft. However, its static flow characteristics were well characterized therefore it was used but this equates to less relevant results for rotorcraft applications. The current work will use a

NACA 0012 which is a thinner airfoil and more representative of what might be seen on a rotorcraft in comparison to the NACA 0015. This increases the relevance of the results to rotorcraft applications. For better synchronization between all control systems and measurement instruments, the current work will integrate all systems into a National Instruments CompactRIO. As seen in figure 2 below, the preliminary work used timing belts to control the airfoil pitching mechanism. These belts could be subject to deformations that could lead to phase delay and therefore increased error in the results.

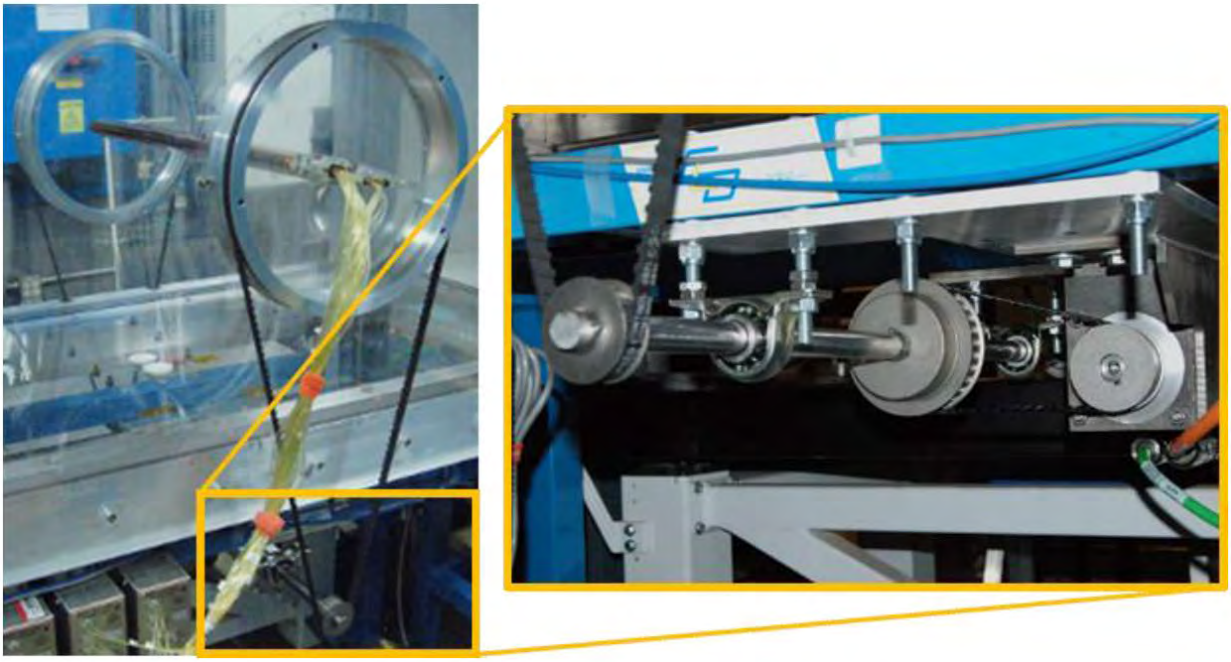

Figure 2. Preliminary Work Pitching Mechanism [5]

To help mitigate this error, the current work incorporates a direct-drive servo which will allow for more accurate pitching angles over the preliminary setup. It's important to understand how lift and drag are affected to understand the flow physics of dynamic stall. The preliminary work used an array of 35 pressure taps. The measurements from these pressure taps where integrated to obtain the lift and drag. This method could introduce error due to the potential three-dimensionality of the flow. To decrease the potential for error, the current work will use a load cell to directly measure the lift and drag. For more information on the preliminary work experimental test setup please reference Singhal [5].

Status of Project

The current work experiment is still in the process of being set up. Currently the team is trying to work out some bugs in the LabVIEW coding so that measurements can be taken. It is expected that the first test will be run within the next few weeks. Therefore, there are no results at this time.

References

1. Little, J., Takashima, K., Nishihara, M., Adamovich, I., Samimy, M., “Separation Control With Nanosecond-Pulse-Driven Dielectric Barrier Discharge Plasma Actuators,” AIAA Journal, Vol. 50, No. 2, February 2012.
2. Clifford, C., Singhal, A., Samimy, M., “Flow Control over an Airfoil in Fully Reversed Condition Using Plasma Actuators,” AIAA Journal, Vol. 54, No. 1, January 2016.
3. Visbal, M., “Numerical Exploration of Flow Control for Delay of Dynamic Stall on a Pitching Airfoil,” AIAA Aviation, 16-20 June 2014.
4. Visbal, M., “Control of Dynamic Stall on a Pitching Airfoil Using High-Frequency Actuation,” AIAA SciTech, 5-9 January 2015.
5. Singhal, A., Castañeda, D., Webb, N., Samimy, M., “Control of Dynamic Stall over a NACA 0015 Airfoil using NS-DBD Plasma Actuators,” The Ohio State University, 2017.

Carbon Nanotube-Copper Composite Sheet for EMI Shielding of Aerospace Structures

Student Researcher: Colin W. McConnell

Advisor: Dr. Vesselin Shanov

University of Cincinnati
Department of Chemical and Environmental Engineering

Abstract

This research project focused on combining copper with Carbon Nanotube (CNT) sheets in order to create a more desirable material for electromagnetic interference (EMI) shielding. As electronic devices become ever more present in the world, it is necessary to devise lighter and less expensive material to protect sensitive aerospace equipment from EMI so that they can continue to function safely. During the project, spinnable CNT arrays were fashioned into sheet structures and then brush electroplated with copper to form a thin CNT-Cu structure. The voltage applied during electrodeposition was adjusted as was the duration of the electrodeposition process. These samples were then tested for shielding effectiveness (SE) on two frequency bands; the C-band (5.85-8.2GHz) and the X-band (8.2-12.4GHz). Initial results, normalized by material thickness, indicate that the pure CNT sheet had the greatest SE, mostly due to how thin the material was. Lower frequencies need to be tested in order to see if the copper is truly adding SE to the CNT sheet.

Project Objectives

As more electronic devices are used, more electromagnetic radiation is being produced. This radiation has the potential to interfere with the functioning of sensitive aerospace devices used for navigation and other purposes. This phenomenon, called electromagnetic interference (EMI), has already happened on several previous occasions [1][2][3]. Current EMI shielding material is often comprised of metals [4], which tend to be heavy (weighing down the aircraft) and costly to manufacture. Carbon Nanotube (CNT) based materials are an excellent candidate to improve upon metal-based EMI shielding constructs due to their light weight and conductivity [5][6]. Previous reports of CNT based coatings show good SE for higher frequencies (8.2-12.4GHz) [7]. Copper, on the other hand, excels at lower frequencies (2-10 GHz) [8]. Therefore, this project aims to investigate CNT sheets electroplated with copper to achieve a more versatile EMI shielding material.

Experimental

A CNT spinnable array (Figure 1) was wrapped around metal shim on a Teflon rod to form a sheet 100 layers thick. The sheet was then exposed for ten rotations to a soft, atmospheric plasma in order to enhance hydrophilicity. The sheet was then densified with acetone. The sheet was then electroplated with copper using a copper sulfate solution. A “brush” electroplating setup was used (figure 2). The brush is a strip of gauze wrapped around a copper tube with holes drilled into it. The copper sulfate solution is then pumped into the gauze and wets the brush. The brush is moved close to the CNT sheet, so that a thin liquid film forms. The positive electrode of a power-source is attached to the copper tube and the negative electrode is placed against the metal shim underneath the CNT sheet. This results in the copper cations electroplating on the CNT sheet. Two sets of samples were made. One set was electroplated using 2.5V and one used 5.0V. For each set, a sheet was electroplated for 30, 60, and 120 rotations. An unmodified 100-layer CNT sheet and 25um copper shim was used for comparison.

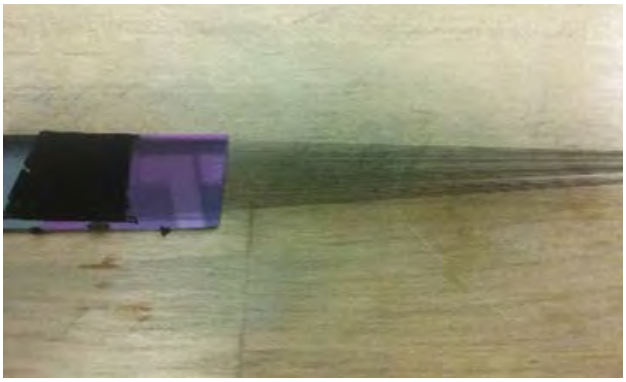

Figure 1. A spinnable CNT array

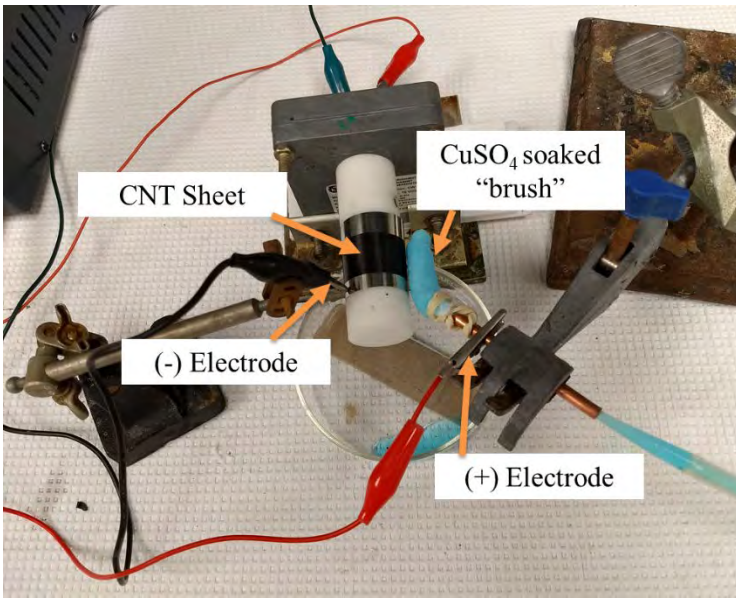

Figure 2. Brush Electroplating Setup

SE of the samples were evaluated using an Agilent Network Analyzer (figure 3). Two different wave guides were used to expose the samples to two different frequency ranges, the X-band (figure 4, bottom) and the C-band (figure 4, top). These two wave guides have a frequency range of 8.2-12.4GHz and 5.85-8.2GHz, respectively. For the X-band, samples were tested twice so that the grain of the material was parallel and perpendicular to the polarity of the wave. For the C-band, samples were not large enough to test them perpendicular to wave polarity. The Network Analyzer measures by how many dB the signal was reduced by over the frequency range. This value is given as S_{21}. Using the equation $SE = -10\log|T|\,(dB)$ with $T = |S_{21}|^2$ [9], the SE over a frequency was calculated and averaged. This average was then divided by sample thickness, measured using a micrometer, in order to normalize the results.

Figure 3. The Agilent Network Analyzer

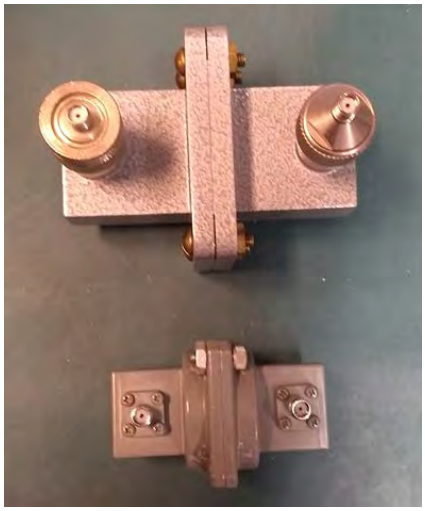

Figure 4. The C-band waveguide (top) and the X-band waveguide (bottom)

Results

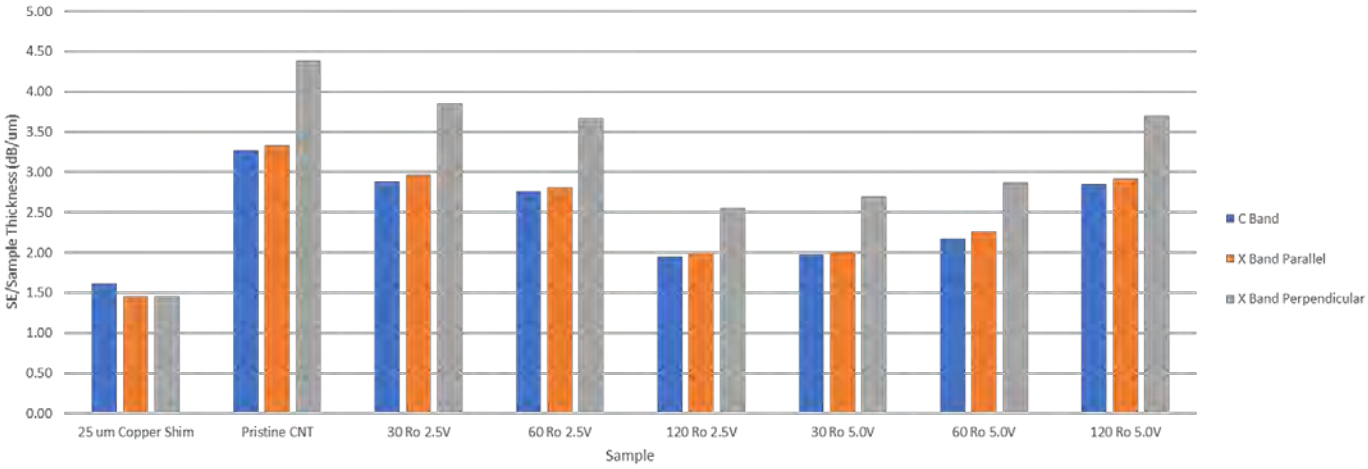

Figure 5. Graph showing thickness-normalized shielding effectiveness results.

Overall, the unmodified, pristine CNT sheet had the best EMI shielding performance. This is mostly due to the fact that the material provided descent SE while still being fairly thin (around 7 um) when compared to the other samples. One unexpected result was the anisotropy of the samples. When samples were positioned perpendicular to the polarity of the wave, SE increased significantly. It also appears that adding additional copper (in the form of increasing the voltage and rotations of electroplating) did not significantly improve the SE of the material. This could be caused by the fact that high frequencies are still being used and in order for the copper to have a greater effect, sub C-band frequencies should be used.

Future Work

The brush electroplating setup still needs to be refined and optimized to more reliably coat samples. Samples should also be tested at sub C-band frequencies to see if copper can increase the SE of the composite samples. The effect on SE of creasing/deforming the samples also should be evaluated. Finally, mechanical testing of the samples is planned.

Acknowledgments

The Author would like to acknowledge Dr. Vesselin Shanov for serving as the advisor for this project, Dr. Kelly Cohen for serving as the OSGC coordinator for the University of Cincinnati, Dr. David Mast for providing the Network Analyzer, and Dr. Rachit Malik for introducing me to CNT research.

References

1. Ladkin, Peter B. "Electromagnetic interference with aircraft systems: why worry." *Technical Report* (1997).
2. Donham, Bruce. "Electromagnetic interference from passenger-carried portable electronic devices." *Boeing Aero Magazine* 10 (2000).
3. Leach, R. D., and Margaret B. Alexander. "Electronic systems failures and anomalies attributed to electromagnetic interference." (1995).
4. Geetha, S., et al. "EMI shielding: Methods and materials—A review." *Journal of applied polymer science* 112.4 (2009): 2073-2086.
5. Smalley, Richard E. Carbon nanotubes: synthesis, structure, properties, and applications. Eds. Mildred S. Dresselhaus, Gene Dresselhaus, and Phaedon Avouris. Vol. 80. Springer Science & Business Media, 2003.
6. Baughman, Ray H., Anvar A. Zakhidov, and Walt A. De Heer. "Carbon nanotubes--the route toward applications." science 297.5582 (2002): 787-792.
7. Yang, Yonglai, et al. "Novel carbon nanotube− polystyrene foam composites for electromagnetic interference shielding." *Nano letters* 5.11 (2005): 2131-2134.
8. Kim, H. M., et al. "Electrical conductivity and electromagnetic interference shielding of multiwalled carbon nanotube composites containing Fe catalyst." *Applied Physics Letters* 84.4 (2004): 589-591.
9. Zhang, Lu, et al. "Preparation and characterization of graphene paper for electromagnetic interference shielding." *Carbon* 82 (2015): 353-359.

Design, Modeling, and Experimental Testing of a Variable Stiffness Structure for Shape Morphing

Student Researcher: Collin E. Mikol

Advisor: Dr. Haijun Su

The Ohio State University
Department of Mechanical and Aerospace Engineering

Abstract

Shape morphing structures that are both actively controlled and greatly variable in stiffness offer unique solutions in aerospace applications. Current aerospace industry trends show increased interest in shape-adaptive structures capable of carrying high loads for improved aerodynamic performance and fuel efficiency. One limiting factor in present applications is the ability to actively morph structures and control stiffness using the same type of actuation system. This research focuses on developing an actively controlled, variable stiffness structure that uses a pneumatic system for both morphing and locking the structure shape. Design prototypes that use various pneumatic actuation technologies and beam designs will be iteratively tested for feasibility and reliability. Layer jamming, which utilizes varied friction between thin sheets based on pressure, will be used to control the variable stiffness. The shape morphing and layer jamming will be analyzed in a setup using a force tester to show the ability of the structure to actively morph and control its stiffness using a pneumatic control scheme. This novel research would positively impact both the aerospace and robotics fields by creating lightweight morphing structures that are flexible and easily deformed, but also stiff with high load-carrying capability.

Introduction and Objectives

Both shape morphing and variable stiffness structures have received increased interest in the research community as well as the aerospace and robotic fields in recent years. Morphing structures are interesting due to their excellent performance, lightweight and reduced structural complexity [1]. Morphing structures also show significant advantages in performance and efficiency compared with traditional linkage designs [2]. Variable stiffness structures have also garnered increased interest, as their ability to transfer from a fluid-like state to a solid-like state using only air pressure has many applications, such as supporting high loads at high stiffness while being very flexible at a low stiffness. This research primarily focuses on the combined aspect of both shape morphing and variable stiffness incorporated into a single structure that is able to be actuated from a single energy source.

Although there has been previous research performed regarding both shape morphing and variable stiffness structures separately, little research has been done to combine the two. Previous shape morphing research has utilized a variety of different actuation methods to achieve a deformable structure, including shape memory alloys (SMA's), piezo-electrics, and cable driven stringers. However, there are many drawbacks to most of these methods, including slow actuation time and limited actuation frequency. These designs also lacked locking features, forcing the actuators to withstand the full loading force while holding a morphed shape [3]. Previous methods of achieving variable stiffness also contain many drawbacks. Layer jamming, the method to achieve variable stiffness in this research, has only been shown to have stiffness variations of as much as 10x [4]. The actuation frequency between stiffening and de-stiffening could also be improved.

The primary purpose for this research is to develop an actively controlled, variable stiffness structure that uses a simple pneumatic system for both shape morphing and locking the structure shape. The objectives are to:

1. Design and develop a compliant structure with integrated actuators
2. Model the design using a pseudo-rigid-body model
3. Test and validate the structure to develop a control model for actuation and explore the range of stiffness variation.

Methodology

By current standards, the main approach to achieve a shape changing structure has been accomplished through the use of conventional mechanisms. Conventional mechanisms are used throughout engineering in both the aerospace field and robotics field, such as in hinged airplane flaps and robotic linkages. However, the many drawbacks of these bulky and inefficient mechanisms leads to a new design strategy to create more efficient, lightweight, shape morphing structures. One of the main challenges in the design strategy for creating a shape morphing structure is the conflicting requirements between compliance, load-carrying capabilities, and weight [5]. Many other constraints were placed on the design of the structure, including integrated actuators that used pneumatics as their source of actuation, as well as the structure having flat and planar sides to apply layer jamming. In order to meet all of these requirements, many design prototypes were created and analyzed. Designs that integrated McKibben air muscles to achieve shape morphing were found to work best and were therefore used as the integrated actuators in the final design.

Once a viable actuation method was realized, the goal was to derive an experimental relationship between the position of the mechanism and the input actuator pressure. This relationship would help in developing a control model for the mechanism to predict the beam curvature or endpoint position based on the input pressure to the actuators. To derive this relationship, static test measurements of the structure were taken in 0.5 psig increments of actuator pressure. Tracker software was used to accurately track 9 positions along the length of the structure [6]. Figure 1 shows the morphing capabilities of the structure being morphed at three various internal actuator pressures. Experimental test data were imported into MATLAB to be analyzed and interpolated. Since data points were taken in discrete increments, interpolation equations were calculated in MATLAB to develop a model which gauged structure curvature based on input pressure. Tests were also performed to confirm the repeatability of the actuation method and to quantify any errors that could arise out of this type of shape morphing.

Development of a theoretical model of the structure curvature was also important as a means to help predict structure performance and enable design for specified performances. The Pseudo-Rigid-Body Model (PRBM) was used as a modeling tool. The PRBM provides a simple method of analyzing systems that undergo large, nonlinear deflections. The concept is used to model the deflection of flexible members using rigid-body components that have equal force-deflection characteristics [7]. For this model, the small-length flexural pivot PRBM approach was used. In this modeling approach, the more complex flexible mechanism can be simplified by modeling the system as two rigid links joined at a pin joint, called the characteristic pivot. This section may be approximated as a torsion spring that the structure bends about, having a spring constant K of:

$$K = \frac{(EI)_l}{l}$$

Use of this spring stiffness value along with the applied torque to the segment gives an estimate of the bending angle of the segment. Since the designed structure was comprised of multiple segments, the y-displacement of each segment over the entire length of the beam was summed to determine the overall position of the endpoint, which was calculated as:

$$y_{total} = \sum_{i=1}^{n} \left(L_i + \frac{l}{2} \right) * sin\theta_i$$

The accuracy of the PRB Model to the experimental data will be compared in the results section. The capabilities of the structure stiffness variability were also explored in this research. A test setup was created that supplied both positive and negative pressure inlets to the structure design, allowing both the supply of air to the internal actuators for morphing and the ability to create a vacuum for layer jamming. The structure stiffness and load-carrying capabilities were measured as some of the structure parameters were varied; namely the number of layer jamming sheets applied per side of the beam, the applied vacuum levels, stiffness at equilibrium vs. morphed positions, and comparison between the internal actuators being on and off.

Stiffness testing was performed using a MARK-10 force tester and a digital travel display. For the layer jamming sheets, laminar sheets of 0.005" thick matte polyester film were attached to the sides of the structure. Once the layer jamming sheets were applied, the entire structure was sealed inside a polyurethane enclosure to allow application of a partial vacuum to achieve variable stiffness. After being clamped in place, the structure was loaded with a force until it was displaced by 5mm, and then was unloaded back to its equilibrium position. The stiffness of the structure was measured during the loading phase of the experiment. The true stiffness of a structure at a location x is defined as:

$$k_x = \left. \frac{\partial F}{\partial x} \right|_x$$

However, if the slope of the force vs. displacement curve is slightly non-linear, the stiffness of the structure will change over the course of the 5mm displacement, if ever so slightly. Instead, the stiffness value can be fairly accurately estimated by taking the slope of the curve over the endpoints of the data in the more linear elastic range. The range of stiffness values and maximum loading capabilities achieved by this variable stiffness method are discussed in the results.

Results and Discussion

Figure 1 shows the final structure containing the integrated McKibben actuators being morphed at various input pressures. The structure was tested over the range of 0-35 psig for the input actuator pressures, and was capable of achieving a morphing endpoint position of slightly over ±90°. The repeatability of the structure was also tested by running the same experiment a total of five times to check the errors between experiments. The maximum error that occurred between tests was a difference of 0.57%. This indicates that the actuation method using McKibben air muscles as the actuators is fairly repeatable and has the potential to be accurately controlled.

A comparison of the structure curvature was also made between dynamic tests and the static model that was developed. From Figure 2, it can be seen that the interpolated model and dynamic tests agree very closely with one another, especially at lower internal actuator pressures. As the internal actuator pressure is increased, the model slightly underestimates the curvature results from the dynamic tests. The error in the data is largest at the endpoint of the structure, which is to be expected because the positional error is compounded when moving towards the endpoint of the beam. One possible cause of this error is the way in which the initial axes are defined and the initial points are chosen in Tracker. Since the resolution of the software is limited, selection of the starting positions could have differed by as much as 2mm, which would impact the comparison between the dynamic and static tests.

A control model to calculate the endpoint of the mechanism based on input internal actuator pressure was also calculated. Figure 3 shows the control model for the structure as well as a comparison between the experimental data and the pseudo-rigid-body model. From Figure 3 (a), the experimental data points were fit with a piecewise function. A linear relationship was fit between 0-10 psig and the data points between 10-35 psig were fit with a 5^{th} order polynomial. Looking at Figure 3 (b), the pseudo-rigid-body model is shown to closely approximate the actual experimental data of curvature. The PRB model shows that it is useful as a guide in the design for a specified structure performance.

Testing of the possible ranges of stiffness variation of the structure also showed significant improvements from previous research. Figure 4 shows the plots from the stiffness tests of the structure tested when the structure was at a morphed position. There are quite a few important observations to note from the figure as well as the numerical results shown in Table 1. The first is that the maximum load carrying capabilities of the structure are increased with the internal actuators on. At each of the vacuum levels and independent of the number of layer jamming sheets used, the maximum force is highest with the internal actuators on. This is also true for the maximum stiffness variation (stiffness variation compared to the structure stiffness at a 0 psig vacuum level). Comparing the data at the highest vacuum level of -12.2 psig using 4 layer jamming sheets, it can be seen that the stiffness variation is increased from 63.05X to 75.01X when the actuators are kept on. The stiffness variation using 4 layer jamming sheets is always larger than that using 6 sheets under the same vacuum and actuator position conditions. Therefore, even though 6 layer jamming sheets allow achievement of a higher loading force, a larger stiffness variation is attained using 4 layer jamming sheets. This stiffness variation of as much as 75X is a large improvement of current standards of only about 10X for layer jamming.

Figures

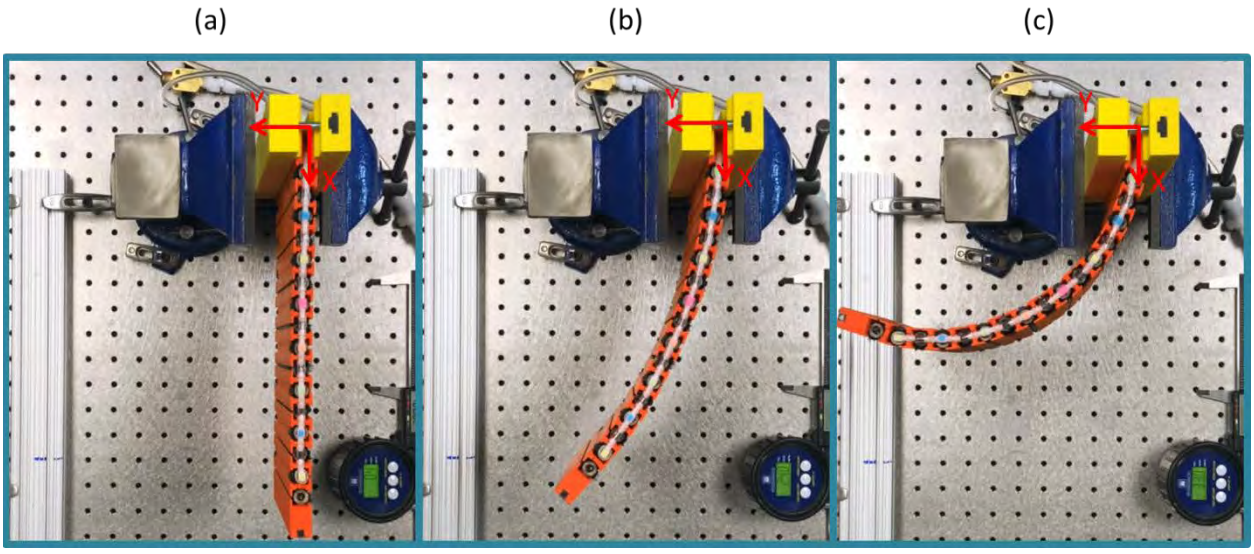

Figure 1. Actuated structure at three various pressures (a) 0.4 Psig (b) 24.0 Psig (c) 33.0 Psig

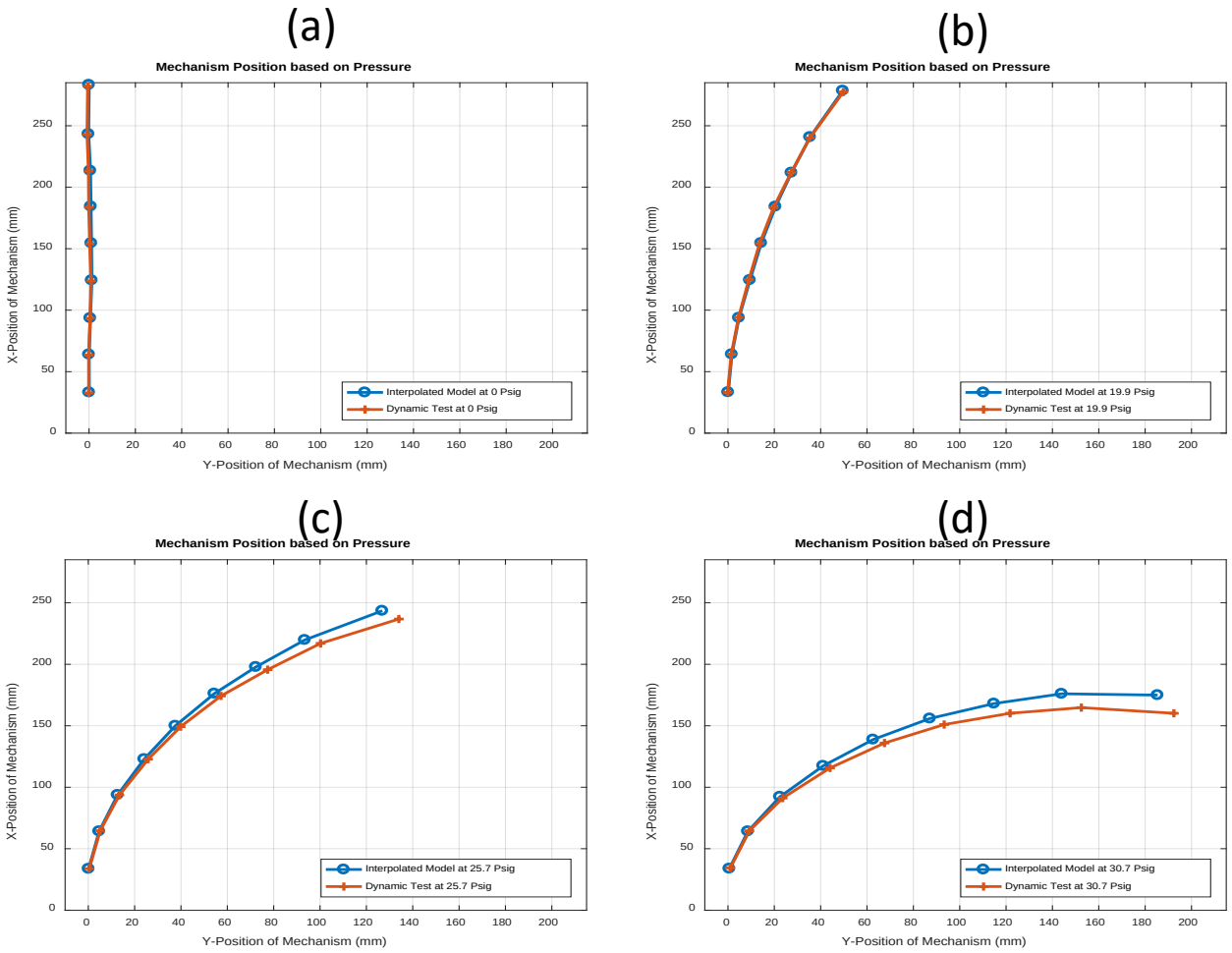

Figure 2. Comparison of Dynamic Tests vs. Interpolated Model at various pressures

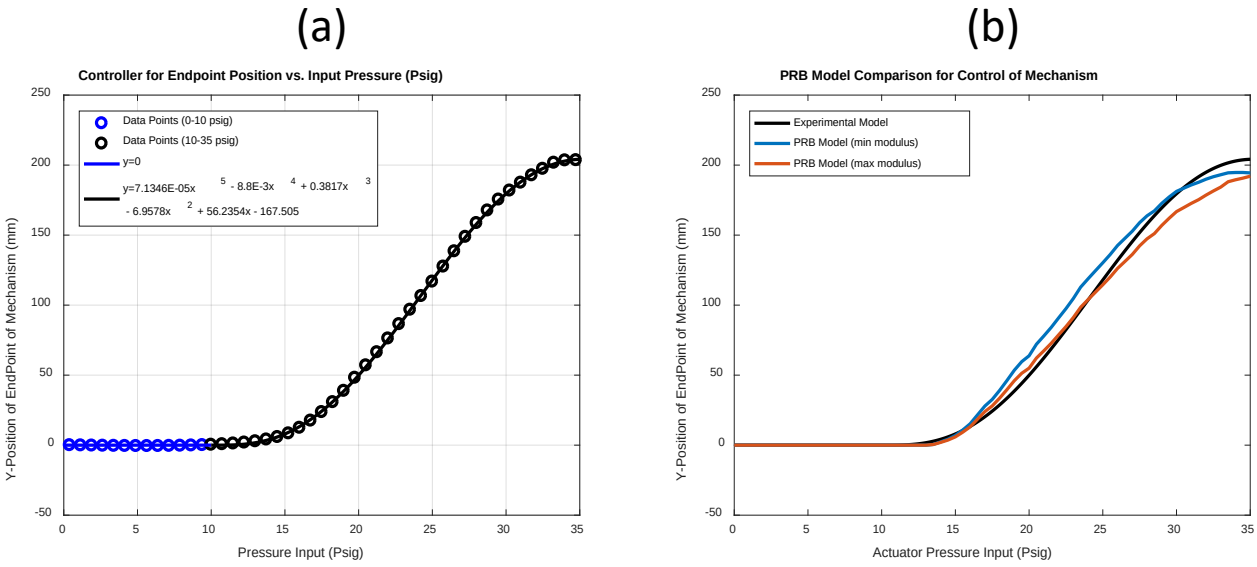

Figure 3. (a) Control Model (b) Control Model compared with PRB Model

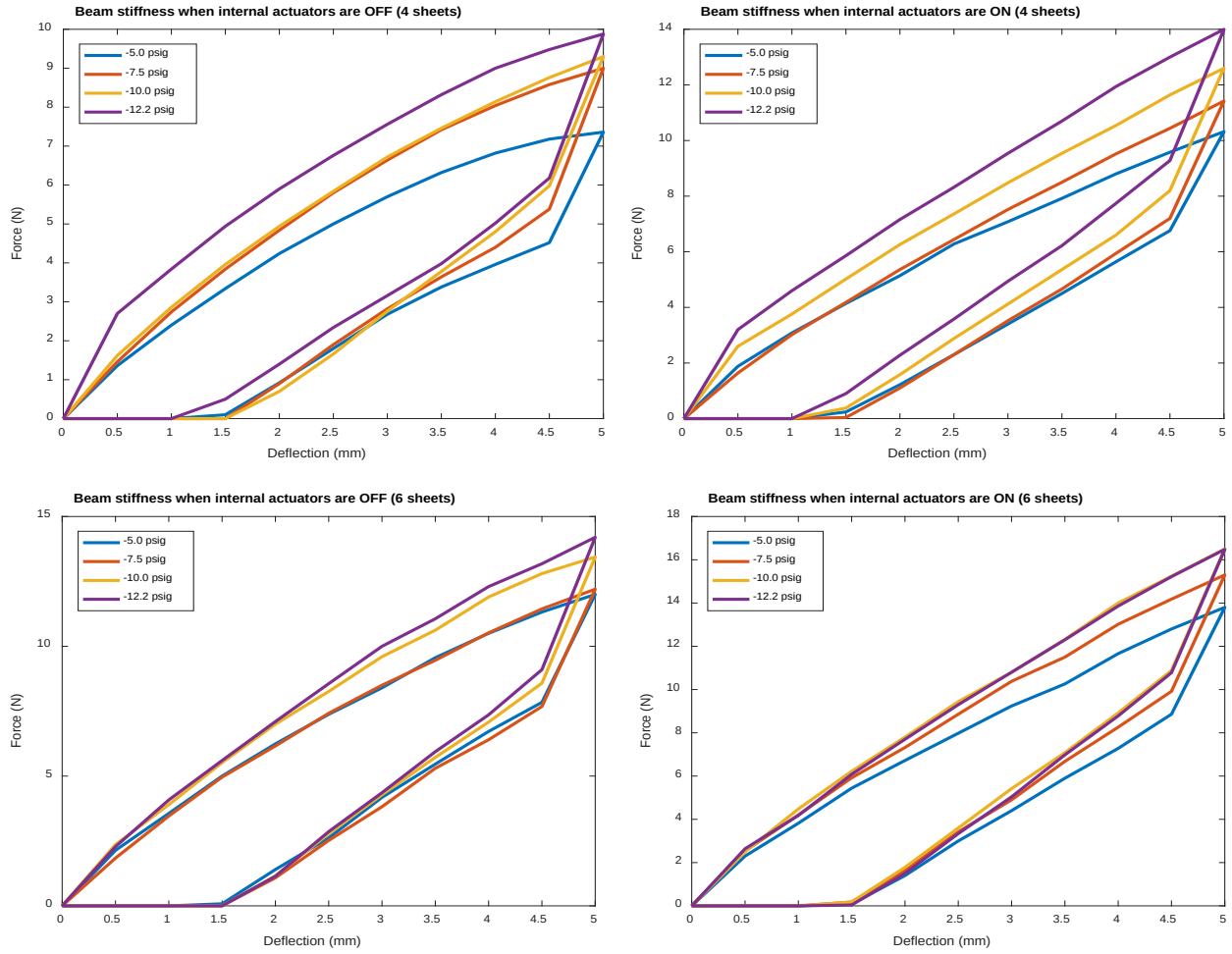

Figure 4. Stiffness Test Comparisons

Table 1. Effect of Internal Actuators on Structure Stiffness

Vacuum Level (Psig)	Actuator Position	# of sheets	Max Force (N)	Stiffness (N/mm)	Stiffness Variation
-5.0	OFF	4	7.36	2.3114	40.48 X
		6	12.00	3.4657	39.12 X
	ON	4	10.32	2.9229	51.19 X
		6	13.80	3.7514	42.34 X
-7.5	OFF	4	9.00	2.6371	46.18 X
		6	12.20	3.3771	38.12 X
	ON	4	11.42	2.8886	50.59 X
		6	15.30	4.1000	46.28 X
-10.0	OFF	4	9.30	2.7457	48.09 X
		6	13.44	3.8171	43.08 X
	ON	4	12.60	3.5971	63.00 X
		6	16.50	4.3029	48.57 X
-12.2	OFF	4	9.88	3.6000	63.05 X
		6	14.20	3.8914	43.92 X
	ON	4	14.00	4.2829	75.01 X
		6	16.48	4.1771	47.15 X

Acknowledgments
The author would like to thank the Ohio Space Grant Consortium for their support and funding of this research. Funding for shape morphing research at the Design Innovation and Simulation Lab at OSU was also provided by the NSF CMMI-1637656 grant and the Department of Mechanical and Aerospace Engineering. Special thanks to Dr. Haijun Su for his support and guidance on this research, as well as collaboration with all other DISL members. The author would also like to thank Dr. Mo Samimy, the campus representative for the OSGC, for his assistance in applying for the OSGC fellowship.

References

1. Q. Ai, P. M. Weaver, and M. Azarpeyvand, “Design and mechanical testing of a variable stiffness morphing trailing edge flap," *Journal of Intelligent Material Systems and Structures*, p. 1045389X17721028, 2017.
2. W. Raither, E. Furger, M. Zundel, A. Bergamini, and P. Ermanni, “Variable stiffness skin concept for camber-morphing airfoils," *Journal of Intelligent Material Systems and Structures*, vol. 26, no. 13, pp. 1609-1621, 2015.
3. S. Barbarino, O. Bilgen, R. M. Ajaj, M. I. Friswell, and D. J. Inman, “A review of morphing aircraft," *Journal of intelligent material systems and structures*, vol. 22, no. 9, pp. 823-877, 2011.
4. M. Manti, V. Cacucciolo, and M. Cianchetti, “Stiffening in soft robotics: A review of the state of the art," *IEEE Robotics & Automation Magazine*, vol. 23, no. 3, pp. 93-106, 2016.
5. S. Daynes and P. M. Weaver, “Review of shape-morphing automobile structures: concepts and outlook," *Proceedings of the Institution of Mechanical Engineers, Part D: Journal of Automobile Engineering*, vol. 227, no. 11, pp. 1603-1622, 2013.
6. D. Brown, “Tracker video analysis and modeling tool," 2018.
7. L. L. Howell, Compliant mechanisms. John Wiley & Sons, 2001.
8. H. Su, Carter Hurd and Xu Pei, “Variable stiffness robotic arm via layer jamming”, US Patent Application Serial No. 62/519,378, June, 2017.
9. C. Hurd, “Variable Stiffness Robotic Arm for Safe Human-Robot Interaction Using Layer Jamming”, *Undergraduate Honors Thesis*, The Ohio State University, May 2017.

Fabrication of Periodically Poled Lithium Niobate Waveguides for Frequency Conversion

Student Researcher: Matthew A. Mircovich

Advisor: Imad Agha

University of Dayton
Physics Department

Abstract
Lithium niobate (LN) is a noncentrocymmetric crystal (3M) in which χ (2) nonlinear processes can occur. In telecommunications, information is carried at a wavelength of 1550nm; however, there are no readily available and low-cost devices to detect single photons in the infrared. LN waveguides can be used to create high efficiency conversion mechanisms through the process of periodic poling.

Project Objectives
Nonlinear optics is the study of the phenomena that occur when the response of a material system to an applied optical field depends upon the strength of the optical field in a nonlinear manner [1]. The field of nonlinear optics spans a wide area of study ranging from tunable laser light generation, biomedical imaging, optical signal processing, high-speed telecommunications, and quantum optics.[2][3][4][5]

Three-wave mixing is an example of a nonlinear process (e.g. frequency generation) whereby two photons, or elementary particles of light, combine in a nonlinear medium to produce a photon of a different frequency. The energy of the created photon is equal to the energy of the two starting photons, obeying the conservation of energy. As with any form of scattering, the conservation of momentum must be obeyed. Unlike the conservation of energy which is satisfied by the generated photon (Fig. 1a), conservation of momentum is satisfied through both the photon and the medium in which the mixing process takes place (Fig. 1b). The conservation of momentum is referred to as phase matching. Lithium niobate (LN) has strong nonlinear properties that allows for high efficiency three-wave mixing processes; however, phase-matching is generally difficult to achieve in bulk lithium niobate. To promote phase matching, a process called poling is applied to the crystal in which the electrical domains of the crystal along the optical axis are swapped. By periodically reversing the electrical domains, phase matching occurs via an extra momentum “kick” provided by the crystal itself; this extra momentum compensates for the momentum mismatch between the three photons due to their different frequencies.[4][6][7][8]

Methodology Used
In order to fabricate PPLN, a 0.5 mm thick, z-cut MgO doped LN wafer (Mg:LN) is diced into 20.050 mm square pieces. One facet of the wafer is polished using a Buehler ecomet variable speed grinder/polisher equipped with a 9 μm diamond grit for 15 minutes at 20rpm. Then a 3 μm polish is applied for 15 minutes at 20rpm. This is followed by a 1 μm and a 0.5 μm polish for 20 minutes at 10rpm. At each stage of the polishing process, metrology of the crystal face is preformed to look for smoothness and defects. Defects include polishing at two different angles, large buildup of particles on the crystal face, and large scratches above the grit size. If the polished edge shows any defects, then the crystal is polished at a larger grit for half an hour or until the defect goes away.

Before fabricating waveguides loss measurements need to be done on a larger piece of Mg:LN using nondestructive optical loss characterization.[9] Poling will be explored using metal and liquid electrodes, along with circular and flat electrodes. For optimum conversion efficiency, a 50% duty cycle of domain walls is needed. To create a 50% duty cycle domain, the electrodes must be patterned at a 25% duty cycle to take account for the electric field expanding outward from the electrode, or electric field fringing. A solution to the issue in which domain walls expand past the electrodes is to use circular electrodes. Circular electrodes create less electric field fringing as shown in Figure 2.B. Interference lithography will be used to pattern the wafer; nickel chrome electrodes will then be patterned on top of the sample. In interference lithography, the photoresist develops in a sinusoidal fashion, allowing for the electrode to contact the wafer at the center of the domain. The applied electric field then propagates downward strongly at the center of the electrode. The amplitude of the electric field decreases near the edges of the electrode because of the photoresist acting as an insulator. This reduces the fringing of the electric field, as the field is not as strong near the edges of the domain.

Results Obtained

Fabrication equipment is set up to be automated and easily changeable using LabVIEW software. Initial testing shows the experimental setup is functioning properly. We successfully cut and polished lithium niobite to prepare samples for poling and loss measurements.

Significance and Interpretation of Results

We have created all the necessary steps to fabricate PPLN at various poling periods. All the processes are automated and theoretically modeled, this allows us to readily fabricate and design new waveguide designs. The modeling of the circular electrodes makes it easier to fabricate PPLN with very short periods on the scale of microns.

Figures/Charts

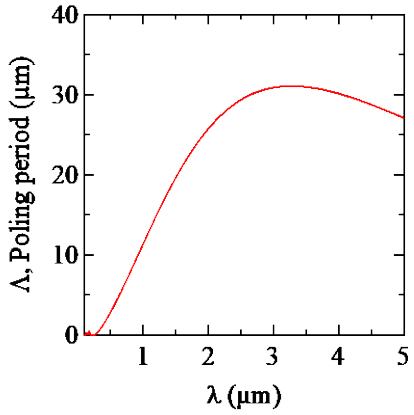

Figure 1. Poling period for SFG using a varying pump, signal at 1550 nm, and an idler at the SFG wavelength.

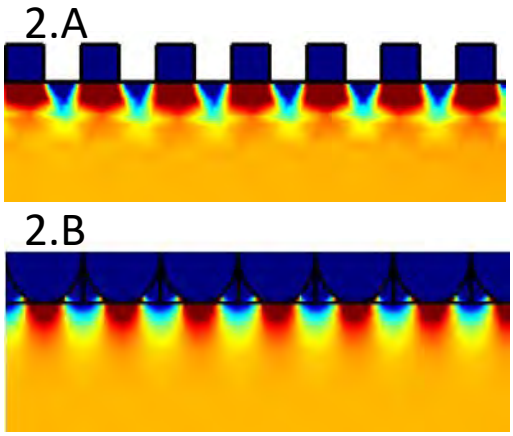

Figure 2. A: Comsol simulation of square electrodes patterned on a wafer with a 50% duty cycle. B: circular electrodes with a 50% duty cycle exhibit less electric field fringing.

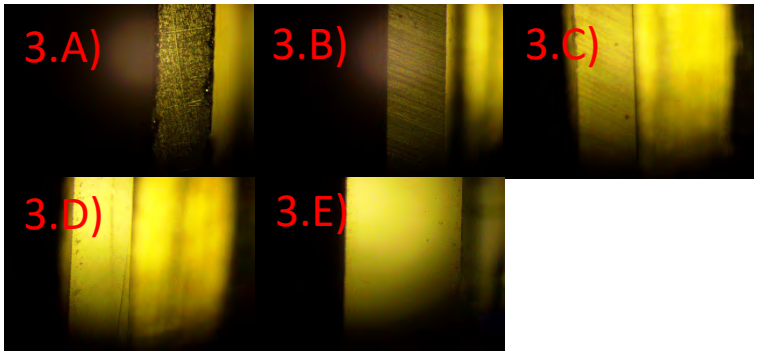

Figure 3. Mg:LN at various stages of polishing; A: unpolished, B: 9 µm, C: 3 µm, D: 1 µm, and E: 0.5 µm.

Acknowledgments

I would like to thank my college David Lombardo for preforming all the lithography necessary for this project.

References

1. R. Boyd, “Nonlinear Optics,” (Academic Press, Burlington, 2008), 3rd Edition.
2. C. Langrock, E. Diamanti, R. Roussev, Y. Yamamoto, M. Fejer, and H. Takesue, "Highly efficient single-photon detection at communication wavelengths by use of upconversion in reverse-proton-exchanged periodically poled LiNbO3 waveguides," Opt. Lett. 30, 1725-1727 (2005)
3. I. Agha, S. Ates, M. Davanço, and K. Srinivasan, "A chip-scale, telecommunications-band frequency conversion interface for quantum emitters," Opt. Express 21, 21628-21638 (2013).
4. C.M. Kaleva, M. Munro, T.D. Roberts, T. Chang, and P. Battle, “Type II Sum Frequency Generation in KTP Waveguides: a Technique for Pre and Post Screening,” in Nonlinear Frequency Generation and Conversion: Materials, Devices and Applications VII, Proc. SPIE Vol. 6875 (2008).
5. M. Rakher, L. Ma, O. Slattery, X. Tang, and K. Srinivasan, “Quantum transduction of telecommunications-band single photons from a quantum dot by frequency upconversion,” Nature Photonics **4**, 786-791 (2010).
6. R. Byer, “Quasi-phasematched nonlinear interactions and devices,” Journal of Nonlinear Optical Physics & Materials 6, 549-592 (1997).

7. L. Myers, R. Eckardt, M. Fejer, R. Byer, W. Bosnberg, and J. Pierce, “Quasi-phase-matched optical parametric oscillators in bulk periodically poled LiNbO3.”
8. L. Myers, R. Eckardt, M. Fejer, [8] R. Byer, and W. Bosenberg, “Multigrating quasi-phase-matched optical parametric oscillator in periodically poled LiNbO3,” Optics Letters **11**, 591-593 (1996).
9. D. Lombardo, I. Agha, A. Sarangan "Non-destructive optical loss characterization using designed scattering features," in *Frontiers in Optics 2017*, OSA Technical Digest (online) (Optical Society of America, 2017), paper JTu2A.39.

Coral Reefs: "Canaries" of the Sea

Student Researcher: Meghan G. Mulligan

Advisor: Dr. Ann Mackenzie

Miami University
Department of Teacher Education

Abstract
My lesson plan will focus on the ecological issue of coral bleaching. Students will explore their current understandings of reefs with others and identify any misconceptions they may have about coral reefs and any risks they face. Once students have identified these risks and have had opportunities to research information and discuss how their understanding has changed, they will develop a product to help educate others about coral reefs. I have not yet had the opportunity to implement this lesson plan in a classroom, but I plan on implementing it in my future classroom, and possibly next year during my student teaching. This activity helps students to understand how studying coral reefs can help scientists gauge the health of the ocean, and of the planet as a whole.

Lesson
This lesson uses resources from both NASA and NOAA websites, including information about CORAL, coral reefs, and coral bleaching. In Ohio, we don't have any coral reefs in our backyards, but we are still able to connect with the ocean through research and education. Students will consider different viewpoints to understand why coral bleaching is an issue that we should care about, even in Ohio. Students will be given an opportunity to create a product which can be shared with others and showcased in the school to inform others about coral bleaching.

Objectives
- To identify the importance of coral reefs.
- To explain coral bleaching and why it occurs.
- To communicate the effects of coral bleaching to others.

Alignment
Ohio Department of Education High School Biology "Diversity and Interdependence of Life."

NGSS (HS-LS2-6).

Methodology
This lesson plan is centered around constructivist pedagogy using the 5-E (Engage, Explore, Explain, Elaborate, Evaluate) Lesson Plan Format. In the Engage section, students will engage with what they already know about the term "bleaching." Living in Ohio, many students may not have had much prior exposure to the idea of coral bleaching, but they will likely be familiar with the uses of bleach and its ability to remove stains from clothing. After engaging with their prior knowledge, students can make connections to better understand the meaning of coral bleaching, how it is similar to what they know about bleaching, and how it is different. Students will have an opportunity to Explore coral bleaching through class discussion. This discussion will bring out any misconceptions the students may have. Students will use articles from NASA and NOAA to Explain coral bleaching and identify any information that changed their prior thinking. Since students in Ohio will likely not have the same viewpoint as others who interact with marine life on a regular basis, students will have the opportunity to Elaborate

in their thinking, and consider the perspective of a Marine Biologist, Fisherman, marine organism, or other individual. Finally, students will make a product which communicates a summary of what they have learned throughout the lesson, on which they will be Evaluated.

Materials/ Resources

Throughout this 5E lesson plan, students will need to be provided with clear cups, water, food coloring, bleach, large sheets of paper, and markers. Students will also need access to the internet in order to read the assigned articles and perform research in the Elaborate and Evaluate portions. If this is not possible, teachers should print copies of these resources for students to read and look for other articles which will help students research and develop their products.

Acknowledgments

I would like to thank my advisor, Dr. Ann Mackenzie, for supporting me and guiding me throughout this process.

References

1. Buis, A. (2016, June 2). *Five Things About Coral and CORAL*. Retrieved from NASA: https://www.nasa.gov/feature/jpl/five-things-about-coral-and-coral
2. NASA Jet Propulsion Laboratory: California Institute of Technology. (2018). *About CORAL*. Retrieved from NASA Jet Propulsion Laboratory: https://coral.jpl.nasa.gov/about-coral
3. National Oceanic and Atmospheric Administration. (2018). *NOAA's National Ocean Service*. Retrieved from National Ocean Service: https://oceanservice.noaa.gov/
4. National Oceanic and Atmospheric Administration. (2018). *What is Coral Bleaching?* Retrieved from National Ocean Service: https://oceanservice.noaa.gov/facts/coral_bleach.html

Design of a Raspberry Pi-Based Drone Prototype

Student Researcher: Daniel Dennis Musci

Advisor: Dr. Jed E. Marquart

Ohio Northern University
Department of Electrical and Computer Engineering and Computer Science

Abstract
Drones are becoming increasingly influential in today's society, as they are often used in a wide range of areas including defense, research, and surveillance. With their increasing popularity, it would be beneficial to have a simple platform to implement drone control and testing, especially from a research perspective. This paper lays out the groundwork for this system by assessing the design and construction of a Raspberry-Pi based drone. Raspberry Pis are small, versatile, and inexpensive devices that function as low-powered computers. They provide a lot of functionality onboard, such as Bluetooth and 802.11n Wi-Fi capabilities, and work well with a lot of well-developed software libraries and external hardware. Because of their versatility and low cost, they are perfect for prototyping platforms, and thus are valid candidates for implementing a simple drone control system [7].

This paper discusses the design process went through in order to create a prototype of a Raspberry Pi-based drone, as well as the results and future considerations gained from the process. The design process was broken down into the following categories: project inception, choice of raspberry pi model, brushless vs. brushed DC motors, circuit design & theory, prototyping, results, and future considerations.

Keywords: Raspberry Pi, Drone, DC Motor, Optocoupler, Integrated Circuit (IC), Python

Project Inception

Autonomous unmanned aerial vehicles (UAVs), otherwise known as drones, are finding their way into many different areas of society, from various industries to personal hobbies. On another hand, the maker movement (or maker culture), which is "a technology-based extension of DIY culture that intersects with hacker culture" [6] has also been growing in popularity. This movement has "a strong focus on using and learning practical skills and applying them to reference designs" [6] and would thus value from a simple, inexpensive drone platform. This project aims to merge the growing drone industry with the maker movement by creating a simple, inexpensive drone platform that can easily be constructed.

Choice of Raspberry Pi Model

When choosing the Raspberry Pi model to use for this project, there were numerous parameters to consider. The two models that were chosen between were the Raspberry Pi Model B 3.0 and the Raspberry Pi Model ZERO. Table 1 below summarizes the differences in specs between the two models.

Table 1. Raspberry Pi Model B 3.0 vs. Raspberry Pi Model ZERO Specs [3, 8]

Model B 3.0	**Model ZERO**
SoC: Broadcom BCM2837	SoC: Broadcom BCM2835
CPU: 4× ARM Cortex-A53, 1.2GHz	CPU: 1× ARM11, 1.0GHz
RAM: 1GB LPDDR2 (900 MHz)	RAM: 512MB LPDDR2
Networking: 10/100 Ethernet, 2.4GHz 802.11n wireless	Networking: 2.4GHz 802.11n wireless
Bluetooth 4.1 Classic, Bluetooth Low Energy	Bluetooth 4.0
Storage: microSD	Storage: microSD
GPIO: 40-pin header, populated	GPIO: 40-pin header, unpopulated
Ports: HDMI, 3.5mm analogue audio-video jack, 4× USB 2.0, Ethernet, Camera Serial Interface (CSI), Display Serial Interface (DSI)	Ports: mini-HDMI, 2x micro-USB
Weight: 45g	Weight: 9g

With respect to the scope of this project, the following parameters were taken most into consideration: processor speed, available RAM, available wireless communication protocols, and weight. With respect to processor speed, Table 1 shows that the Model B 3.0 contains the faster processor clocked at 1.2GHz. The Model B 3.0 also has 4 available processor cores opposed to the single core on the ZERO, but since multi-threading was not utilized this had little effect. With respect to RAM, Table 1 again shows the Model B as the superior choice with almost double the RAM. This was a large factor, because if more advanced control systems were to be utilized on this system in the future then they would have higher RAM demands. With respect to wireless communication protocols, the only significant difference between the two models was the Ethernet capabilities of the Model B 3.0. As this project concerned a wireless drone, this had no impact on the decision since any and all communications would inherently be wireless. With respect to weight, Table 1 shows the Model ZERO coming out on top by a large margin. The Model B 3.0 is actually five times the weight of the ZERO, which is important for power conservation when dealing with a drone.

After taking the above information into consideration, the Raspberry Pi Model B 3.0 was chosen for the original prototype. This was largely due to the faster processor and greater available RAM.

Brushed vs. Brushless DC Motors

A significant choice in the design process of this project was the choice to use either brushed or brushless DC motors for the drone propellers. DC motors were required as opposed to AC, because drones are battery powered and therefore only have DC power available. The pros and cons of both motor types are shown below in Table 2.

Table 2. Brushed & Brushless DC Motors Pros & Cons [2]

Brushed	Brushless
Pros: • Simple in construction • Inexpensive • Only two wires as inputs to motor coils Cons: • Lower efficiency & output power	Pros: • High efficiency & output power • Smaller size Cons: • Require use of an Electronic Speed Controller (ESC) to work properly • Three "phases" of driving coils • More complex • More expensive

Brushless motors are commonly used for quadcopters due to their reduced size and high efficiencies, but they require an ESC to function. Incorporating an ESC to the design would have further complicated the circuit and inflated the project cost, and thus was deemed inappropriate for the design. For these reasons, DC motors were chosen for the first prototype.

Circuit Design and Theory

The circuit was a large part of the design, as it was responsible for taking inputs from the Raspberry Pi and properly controlling the motors. Figure 1 below shows the breadboard view of the portion of the circuit that controls two of the motors. The other two motors would be controlled by an identical circuit with different general-purpose input/output (GPIO) pin inputs from the Raspberry Pi.

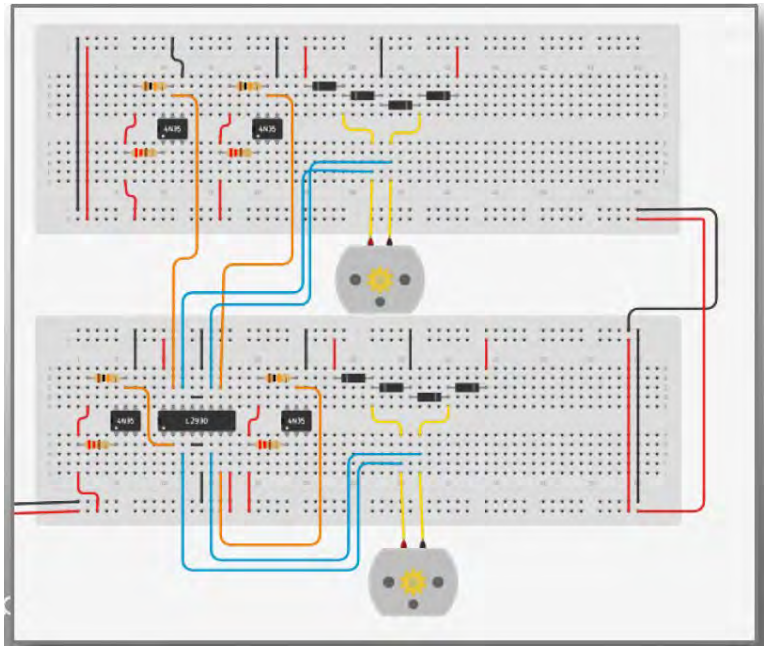

Figure 1. Portion of Circuit Controlling Two Motors

The circuit shown in Figure 1 does not show the inputs to the L293D motor driver IC from the Raspberry Pi GPIO pins. When incorporating these inputs, the circuit works as follows. The GPIO pins on the Raspberry Pi are programmatically changed to either HIGH (~3.3V) or LOW (~0V) voltage using a Python script, and are then each sent to an optocoupler. The optocoupler is used to electrically isolate the GPIO pins, and therefore the Raspberry Pi, from the motor coils. The optocoupler contains an internal infrared (IR) light-emitting diode (LED) that when energized from the GPIO pin emits IR light inside the IC. This light then causes an internal phototransistor to conduct which directs power to the L293D IC [8]. The L293D then outputs either HIGH or LOW voltage on the output pins, which are wired directly to the motor coils, thereby causing the motor to spin. The motor coils are also wired to a protective diode bridge. See Figure 2 below to see this.

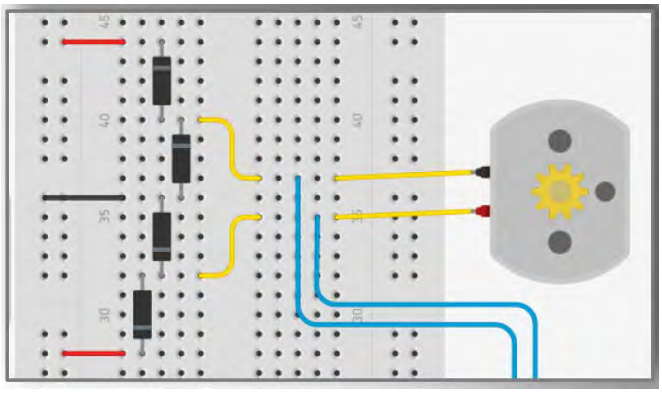

Figure 2. Diode Bridge for Protecting Motor Coils

This diode configuration is a pretty common method of protecting motor coils. This is to protect the motor from inductive kickback voltage that is developed from changing motor currents. The motor coils can be modeled as inductors, and thus their voltage-current characteristic can be seen through the following equation for the voltage across an inductor: $V_L = L\frac{di_L}{dt}$. That is the voltage across the inductor is linearly proportional to the time derivative of the current through the inductor with slope L (inductance of inductor) [10]. When the current through the motor rapidly changes (changing rotation direction), the time derivative of the current spikes, and thus the developed voltage spikes as well. The diodes are used to provide a short circuit path to ground when this occurs in order to protect the circuit from overvoltage.

It should be noted that this circuit is largely based off a circuit from SunFounder website used for simple motor control. This website is a hub for forums and blogs covering DIY projects among other things [5].

Prototyping

Prototyping was used throughout this project, and one of the valuable tools used was computer-aided design (CAD) software. The software used for the project was TinkerCAD, a free-to-use, online CAD tool developed by AutoDesk. The software has functionality for 3D modeling, as well as circuit modeling. The 3D modeling features were not used for the original prototype, but the circuit modeling functionality was thoroughly used. Both Figure 1 and Figure 2 above are images taken from the prototype circuit designed in TinkerCAD. The software can be used to model circuit components (resistors, capacitors, inductors, diodes, etc.), some IC's (operational amplifiers, motor drivers, logic gates, etc.), simple motors, power supplies, voltmeters, and even Arduinos. Through this I was able to test out my circuits in the software before physical testing occurred. Figure 3 below shows a picture of the actual prototype.

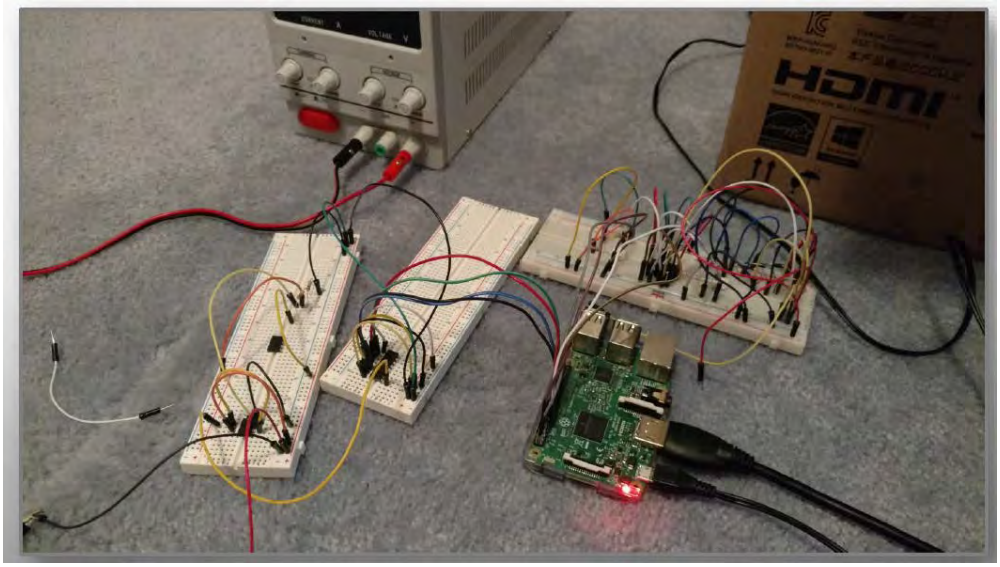

Figure 3. Circuit Prototype

Results and Future Considerations

Due to time limitations on the project, the current prototype was not able to achieve enough thrust to actually overcome its weight and achieve flight. There were a few large contributing factors to this that were observed. One of the factors was the weight of the breadboard. The breadboard weight was very high relative to the rest of the circuit, and even heavier than the Raspberry Pi. Another contributing factor was current/voltage limitations on the IC's used. The L293D motor driver IC could only handle so much motor current, and therefore had limitations on how fast it could drive the motors. The python 3 program controlling the GPIO pins functioned correctly however, and the circuit functioned to turn the motors.

After considering the results gained from the first prototype, the following are future considerations for continuing this project.

- Look into using the Raspberry Pi ZERO model due its significantly reduced weight. A heavy final product strongly contributed to the failure of the first prototype to achieve flight.
- Look into the possibility of using brushless motors as opposed to brushed for higher efficiencies and reduced weights.
- Look into a circuit redesign with high-power rated transistors as opposed to IC's. This will allow for more customizability, as well as stronger control over power limitations.
- Look into designing a body to house the circuitry and Raspberry Pi. 3D printing could be utilized here for prototyping.
- Look into batteries for the drone. The first prototype ran off a variable DC power supply, but eventually a battery will be needed when flight is achieved.

Conclusion

This project explored the design and construction of a Raspberry Pi-based drone prototype in order to create a link between the ever-growing field of drone technology and maker culture. The results were not perfect, and a lot of future improvements are necessary in order to achieve the original goal, but some takeaways were obtained. It was discovered that some inexpensive IC's have power limitations that prevent the motors from generating enough thrust for flight. It was also discovered that the Raspberry Pi Model B 3.0, while it has the best specs in terms of processing power, may be too heavy for an inexpensive drone prototype. Through these results, future considerations were obtained that can help lead to success in the future.

Acknowledgment

This work was funded by the Ohio Space Grant Consortium.

References

1. A Guide to Understanding LiPo Batteries. (n.d.). Retrieved March 21, 2018, from https://rogershobbycenter.com/lipoguide/
2. Brushed DC Motors Vs. Brushless DC Motors. (2017, January 24). Retrieved March 21, 2018, from https://www.motioncontrolonline.org/blog-article.cfm/Brushed-DC-Motors-Vs-Brushless-DC-Motors/24
3. Burgess, M. (2017, February 28). The Raspberry Pi Zero W is a £10 computer with Wi-Fi and Bluetooth. Retrieved March 21, 2018, from http://www.wired.co.uk/article/wireless-raspberry-pi-zero-price-specs
4. Joshi, D. (2017, July 13). Exploring the latest drone technology for commercial, industrial and military drone uses. Retrieved March 21, 2018, from http://www.businessinsider.com/drone-technology-uses-2017-7
5. Lesson 7 How to Drive a DC Motor. (n.d.). Retrieved March 21, 2018, from https://www.sunfounder.com/learn/Super_Kit_V2_for_RaspberryPi/lesson-7-how-to-drive-a-dc-motor-super-kit-for-raspberrypi.html
6. Maker culture. (n.d.). Retrieved March 21, 2018, from Maker culture
7. Musci, D. D. (2017). Feasibility of Creating a Home Drone System Controlled by a Raspberry Pi. 1-8. Retrieved March 21, 2018.
8. RASPBERRY PI ZERO: THE $5 COMPUTER. (n.d.). Retrieved March 21, 2018, from https://www.raspberrypi.org/blog/raspberry-pi-zero/
9. Rouse, M. (n.d.). Optoisolator (optical coupler or optocoupler). Retrieved March 21, 2018, from http://searchnetworking.techtarget.com/definition/optoisolator
10. Sedra, & Smith. (n.d.). Microelectronic Circuits (7th ed.). Oxford University Press.

Catalytic Gasification of Waste Materials

Student Researcher: Uchechukwu N. Obiako

Advisor: Dr. Jorge Gatica

Cleveland State University
Chemical Engineering

Abstract
Waste management has proven to be a challenge in aerospace and municipal areas. Catalytic gasification is one potential solution to tackle this challenge. Waste types commonly include plastic, paper, food scraps, human waste, etc. Catalytic gasification promotes thermal degradation of waste substrates at low temperatures to produce synthetic gas. A laboratory scale procedure has been developed to study and characterize the production of syngas from several waste substrates, including polyethylene and cellulose. Results from gasification of polyethylene show expected trends in reaction rates; however, catalytic gasification of cellulose has proven to present several additional design challenges and thus requires two complementary routes of in-depth research and analysis. Indeed, an essential stage in ensuring a successful scale-up and design for this project requires characterizing mixing, particle dynamics, and transport phenomena associated with the degradation (gasification) of cellulosic substrates. In this project, it is demonstrated how computational fluid dynamics (CFD) can serve as a powerful tool for characterization and optimization.

Project Objectives
Reprocessing waste as an alternative for waste management is an essential technology that optimizes utilization of available resources. With landfills reaching capacity and energetic and environmental impacts of incinerators, waste management and in-situ resource utilization have attracted the attention of engineers and scientists worldwide. Catalytic waste gasification transforms a carbon-based material, such as municipal waste or biomass, into synthetic gas and, in turn, energy. In the gasification process investigated in the Chemical Reaction Engineering (CRE) Laboratory at Cleveland State University, typically referred to as Wet-Thermal Catalytic Oxidation (WTCO), a slurry of solid substrates, catalyst, and water is combined in a controlled oxidizing environment. Common waste substrates are polyethylene, cellulose, and nylon, among others. This project focuses on the catalytic gasification of polyethylene, as well as that of cellulose. Cellulose has proven to present additional challenges when developing WTCO beyond laboratory scale. Indeed, unlike low melting temperature substrates such as polyethylene, cellulose remains in particulate form during most of the gasification process. Computational fluid dynamics (CFD) is used to understand the dynamics of fluid flow and substrate and catalyst particles during the reaction.

Methodology Used
Two specific waste substrates are analyzed in the lab; polyethylene and cellulose. The materials utilized are as follows:

- 100 mL batch reactor with an air-tight closure system (stirred tank pressure vessel)
- Enclosed heater
- Distilled water
- Catalysts: Ruthenium on alumina and platinum on alumina.
- Gas chromatograph
- Small sample gas cylinders from Swagelok

The schematic of the batch reactor which is a stirred tank pressure vessel is shown in figure 1. A picture of the set-up is also shown in Figure 2.

The experimental methodology for a typical gasification run is as follows:

1. A specific mass of waste substrate (polyethylene or cellulose) is weighed.
2. A specific mass of catalyst (ruthenium or platinum) is weighed.
3. 20 mL of water is measured, and all three components added to the reactor vessel.
4. The cap of the vessel has an in-built impeller; this is inserted into the 100mL vessel and is fitted with an air-tight closure system.
5. The batch reactor vessel is then pressurized with air to about 140 psi.
6. The stirrer speed is set to 356 rpm and the agitator turned on.
7. The heater is turned on to heat the reactor up to 310^{o}C; this typically takes an hour.
8. The reaction is left to run for a certain reaction time.
9. Once specified reaction time is reached, the heater is turned off and the reactor left to cool down to about 40^{o}C.
10. Using the gas sample cylinder, the resulting gas produced from the reactor is collected.
11. This gas sample is then run through a gas chromatograph for the identification and quantification of the gas components.
12. These steps are then repeated for different reaction times, different waste substrates and different catalysts.

The reaction mechanism can be seen in table 2. CFD modeling was done in both two dimensions (2D) and three dimensions (3D). The 2D model allowed for faster simulations runs. Two main physics interfaces were utilized. The first interface was the rotating machinery turbulent flow interface, because it works well for incompressible flows at high Reynolds number. The second interface was the particle tracing interface; which allowed for the computation of particle motion in the background fluid. Time-dependent studies showed the dynamic effects of different operating and design process variables on the reactor performance. The methodology utilized for CFD modeling in COMSOL is as follows:

1. Upon opening COMSOL, the dimension, physics interface and study type were selected.
2. The geometry was created using the reactor dimension shown in table 1 below.
3. Water was added as the fluid, and the rotating wall and domain allocated.
4. The rotating domain was set to an impeller speed of 356 rpm.
5. Cellulose particle characteristics were added.
6. Extra fine mesh elements were allocated to the interface between the stationary and rotating domains.
7. Finer free triangular mesh elements were used for the remainder of the geometry.
8. Pressure point constraint and symmetry constraints were also specified.
9. The study time was set to go from 0 – 5 seconds with increments of 0.02 seconds.
10. The simulation was then set to run until completion and the results analyzed, as will be discussed in a later section

Table 1. Reactor vessel and impeller dimensions

Dimension parameter	Value
Vessel height [in]	4.6
Vessel inner diameter [in]	1.3
Impeller clearance [in]	0.625
Impeller height [in]	4.125
Impeller sahft diameter [in]	0.1875
Blade length [in]	0.26
Blade width [in]	0.18

Table 2. Reaction Mechanism

Oxidation of Polyethylene

$$(C_2H_4)_n + 3nO_2 \rightarrow 2nCO_2 + 2nH_2O$$

$$(C_2H_4)_n + 2nO_2 \rightarrow 2nCO + 2nH_2O$$

Water-Gas Shift

$$CO + H_2O \rightleftarrows CO_2 + H_2$$

Sabatier

$$CO_2 + 4H_2 \rightleftarrows CH_4 + 2H_2O$$

Results Obtained

The gasification results for polyethylene are first discussed. These runs were completed to validate the experimental protocol by verifying the expected trends during the reaction. The compositions of the gaseous products were quantified by gas chromatography. In figure 3, the composition of hydrogen is shown for different reaction times. From the reaction mechanism, hydrogen is produced in the water-gas shift reaction and consumed in the Sabatier reaction. From figure 3, the mole fraction is seen to slightly increase between the third and fifth hour. This indicates the occurrence of the water-gas shift reaction. The hydrogen mole fraction is also seen to decrease between the fifth and sixth hour; which indicates the occurrence of the Sabatier reaction. The change in the CO composition with reaction time can be seen in figure 4. From figure 4, the CO mole fraction is seen to increase between hours three and five. Since CO is consumed in the water-gas shift reaction, this depletion implies that this reaction occurs between the third and fifth hour as previously shown by the hydrogen trend depicted in figure 3. The change in CO_2 composition during the reaction at various times is seen in figure 5.CO_2 is produced in two steps in the reaction mechanism; thus, a continuous increase in CO_2 was expected as seen in the figure above. The change in the methane composition with reaction times is shown in figure 6. The methane mole fraction is seen to increase continuously starting at the fourth hour. This also suggests that the Sabatier reaction commences between the fourth and fifth hour. On the other hand, cellulose has presented some challenges because it remains in particulate form during the gasification reaction and it produces little or no desired products. This warranted the need for CFD study on the process. The flow regime in the reactor was first analyzed via a determination of the Reynolds number; this was estimated to be 4300 at the reactor conditions. Since the Reynolds number was above 2300, the flow was considered a fully developed turbulent flow. As previously mentioned, two physics interfaces were used to create a CFD model of the mixing process in the reactor vessel. The 3-D dimension model of the reactor geometry can be seen in figure 1 while the 2-D dimension in shown in figure 7. For simplicity, an initial modeling step consisted in calculating the fully-developed flow velocity profile assuming that the reactor vessel was filled with water. The fully-developed 3D velocity profile field is shown in figure 8. From figure 8, the direction of flow in a revolving fashion was observed; this was expected as it is typical for this impeller type. The particle tracing interface was successfully used to model the 2D cellulose particles distribution within the reactor vessel. This is shown in figure 9. An even spread of the cellulose particles was observed.

Future Work

As it is important to determine the particle-particle interaction between the substrate particles and the catalyst (particles), such an analysis is envisioned in the future. The next steps in this project, therefore, involve a more in-depth analysis of the fluid flow which would investigate the air-water interface in the reaction system. This would enable an understanding of the vortex shape and how mixing parameters affect the area of mass transport of oxygen from the gas phase to the liquid phase. Also, a complete

analysis of the catalyst-waste substrate particle interaction in the liquid phase would be studied. The gas phase reaction kinetics (Sabatier and water-gas shift reactions) have been successfully studied. In addition, a study of the kinetics of the liquid phase oxidation reactions would be completed to provide insight into the reaction rates.

Figures

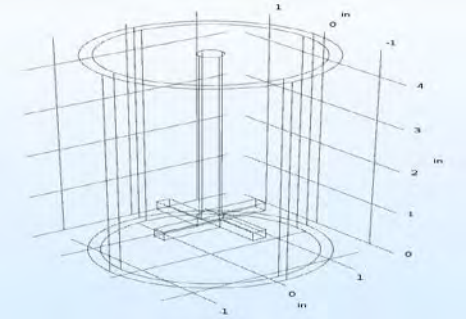

Figure 1

Figure 2

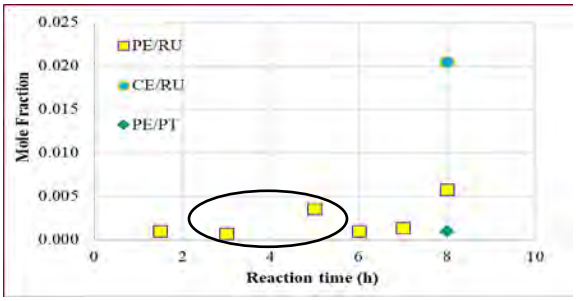

Figure 3

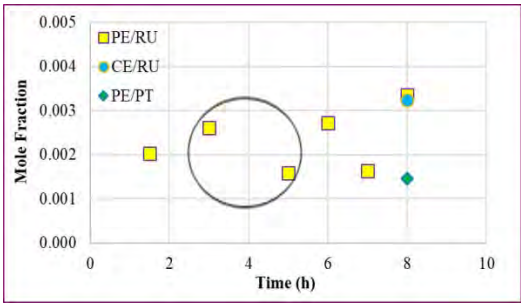

Figure 4

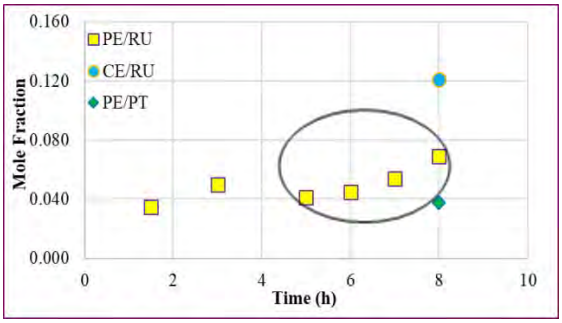

Figure 5

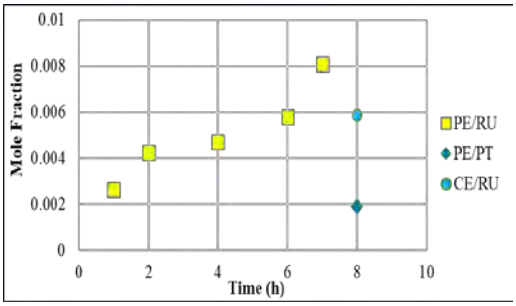

Figure 6

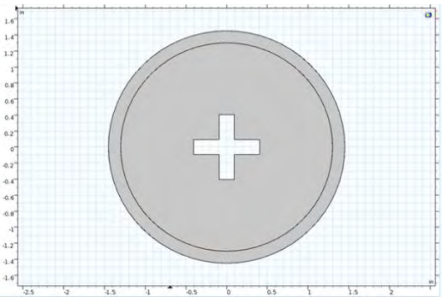

Figure 7

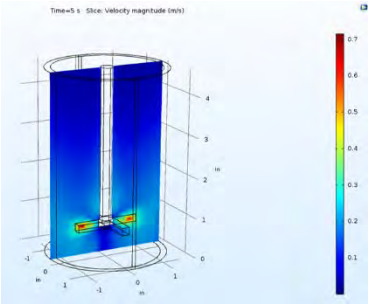

Figure 8

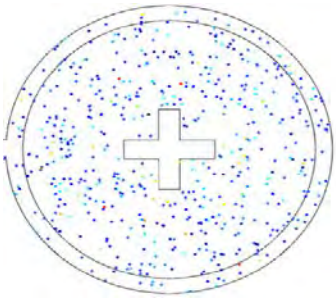

Figure 9

Acknowledgments
I would like to thank OSGC, NASA, the McNair Scholars program and the Mandel Honors College at CSU, the Chemical and Biomedical Engineering department at CSU, my advisor, and my fellow lab members (Mason Lang, Michael Matrona, Eric Lange, Samuel Sanya) for their support on this project.

References

1. "Catalytic Gasification." *National Energy Technology Laboratory*, www.netl.doe.gov/research/Coal/energy-systems/gasification/gasifipedia/catalytic
2. Elordi, G., et al. "Product Distribution Modelling in the Thermal Pyrolysis of High Density Polyethylene." *Journal of Hazardous Materials,* vol. 144, no. 3, 2007, pp. 708-714.
3. "SpaceX capsules." *SpaceX,* www.spacex.com

Usability Assessment for Caregiver Behavior Analysis Using Gaming Technology

Student Researcher: Alexandrea C. Oliver

Advisors: Tanvi Banerjee, Ph.D. (Department of Computer Science & Engineering), Jennifer Hughes, Ph.D. (Department of Social Work), Noah Schroeder, Ph.D. (Department of Leadership Studies in Education & Organizations)

Wright State University
Department of Computer Science and Engineering

Abstract
The proposed research focuses on developing a mobile application for Android systems that will detect changes in behavior and activity patterns of those who are primary caregivers for dementia patients. This application will be used to detect fluctuation in the behavior and the task performance of the caregivers as a measure of caregiver stress. By detecting these changes in behavior, the goal is to analyze the effects of caregiving to evaluate caregiver burnout. A usability study was conducted for this application to find the optimal design factors and features that benefit the target user: the caregiver.

The purpose of this research project is to develop a revised and expanded version of the application based on the results of a prior small-scale usability study [1], and then conduct a more in-depth and in-situ usability study of the revised application. Primary caregivers of dementia patients were the target of the data collection. This data will be used for the continuing design and development of the application. In short, the original application included a word-scramble game and an established caregiver stress scale survey [2]. Based on the results of the prior usability study, a basic reminder functionality was added, improvements occurred to the user interface, and development occurred for a reward system to incentivize the daily use of the application.

Objectives
The application, titled the Caregiver Assessment using Serious gaming Technology (CAST), assesses the feasibility of using gaming technology to assess task performance and stress levels of caregivers for dementia patients. For both version 1.0 and 2.0, the application was developed in Android Studio to remain consistent between testing periods and lessen the opportunity for unexpected variables to arise during the research process. The objective of this study is to evaluate the participant's experience and test the application for usability, feasibility, and interest levels from the participants.

During the first usability study for CAST 1.0, a small sample of caregivers were given CAST 1.0 to assess during the Research and Science Night event organized by Alzheimer's Association Miami Valley in November of 2017. During the study, participants gave feedback on the application and shared how the project could be altered to better accommodate them as well as other caregivers regarding ease of use, reoccurring use, and their overall interest in the application itself [1]. From these responses, one main concern centered on the difficulty of viewing the font and reading the text in the application. Legibility proved to be an issue in other regards concerning the color and contrast in CAST 1.0 with items such as the buttons, text, and boldness of text. A reward system was also requested to encourage the use of the application and some voiced complaints on the complex design of the application and noted their desire for the navigation across the app to be more straightforward and simplified [1]. These reoccurring issues became the focus of the updates for CAST 2.0, as well as other features that could benefit the caregivers based on their comments and concerns from the first trial.

Methodology Used

As with the prior study, the research method for CAST 2.0 continued the focus on qualitative data collected from individual use and evaluation. The prototype of CAST 2.0 was presented to a sample of caregivers at the Miami Valley Alzheimer's Association Research and Science Night in November of 2017. Ten caregiver participants were shown the application and were asked a series of questions regarding their opinions on features shown and were also asked for their overall thoughts on the application as well as other feedback that they felt could aid in improving the project. Using a verbal interview format, we collected the data and the caregiver's responses were recorded and later transcribed after the completion of the event. NVivo software was used to analyze the collected data.

Results Obtained

Four main aspects of CAST 2.0 remained the focus of the study with the caregiver participants. A "Reminders" section of the application was a new addition for CAST 2.0 as seen in Figure 1. The purpose of this feature is for the caregiver to easily set reminders for appointments or medication within the app to keep the information in a centralized location. The alarm within this feature works in the same way as the alarm for any phone. The sampled group responses proved positive and focused on the helpful aspects of having an aid for reminders of smaller caliber appointments and miscellaneous reminders.

One of the main features of the application is the included word scramble game shown is Figure 2. The word scramble game is a central point in the data collection to aid in the determination of the levels of caregiver stress from the user. The purpose of the game is to track user task performance over time regarding the time that they spend on each question, as well as their responses to words of different difficulty levels. This is done using artificial intelligence to compare the caregiver's performance across the days in which they use the application. Changes in behavior can be detected by analyzing the differences in their performance with the game.

The word scramble was updated for clarity as well as improved to provide a more straightforward interaction with the caregiver while providing clear feedback on the correctness of their response. The alterations to this area of the application include the feedback to the caregiver to remind them if they skipped the question or if their response was correct or incorrect before they rated the difficulty of the question. The elements of the section were also structured differently in CAST 2.0 to make the purpose and goal clearer by underlining the area in which they were to insert their answer and making the buttons for interaction larger and easier to use (given that most of our users were of age 65 and above). Responses from the demo ranged greatly from the caregivers. Some enjoyed the addition of the game and other did not feel that the inclusion of it was necessary or that it was not something that most would enjoy. The clarity of instruction also seemed to be lacking for some participants.

The other large addition to CAST 2.0 is a reward system requested from study with version 1.0. The reward or incentive system's goal is to encourage continued use of the application as well as to allow the caregiver to gain a sense of fulfillment while participating in the repetitive tasks that do not give immediate feedback. As seen in Figure 3, the reward or incentive is delivered in the form of a fact-providing system. Every few questions that the caregiver responds to, they are provided with an interesting fact that relates to caregivers, Alzheimer's, and dementia. Caregiver participants stated that the incentives were encouraging and an interesting addition to the game phase though some recommended that the facts stay more focused on the caregivers themselves to make them feel that the focus of the application remains on them.

The final change that occurred for updated application regarded the overall appearance and ease of use for CAST. Based on the feedback from the first trial, this was a major request from caregivers to increase the ease of use of the system. Edits were made throughout the application regarding the appearance and ease of use by altering font sizes, colors, and the sizes of elements such as the sizes and text to increase readability throughout as seen in Figure 4. The design in the various areas within the app were simplified for better understanding and the colors of buttons as well as fonts were changed to create a higher contrast against the background color. The screen size on each page was also maximized rather than leaving empty areas on the screen as shown in Figure 5. Font sizes were also enlarged to better accommodate those that would have difficulty reading the text. The caregiver participants in the second trial felt that these changes within CAST 2.0 gave the application a "newer" feel and that it felt more colorful and modern. The caregivers that were able to compare the two versions pointed out that it was easier to read text in CAST 2.0.

Analysis of Results and Future Work

In conclusion, the majority of the caregiver participants of the CAST 2.0 application usability study found the application to be an interesting concept and stated that once the application became fully deployed, they could see themselves using it routinely to aid them in evaluating the quality of their lives. Regarding the altered design and features, most participants felt that the game was interesting, but the difficulty level may be too high for the average user. The consensus regarding the reminders feature centered on the usefulness of an addition for those that easily forget medicine or appointments or those they prefer to keep caregiver related information centralized. The suggestions that were received for the reminders section of the application showed that more customizations and options should be available for the reminders. In response to the other addition of the incentives, participants relayed that they would encourage them to continue playing and the facts are interesting to read while using the application. Concerning the overall appearance and feel of the application, most participants felt that version 2.0 of CAST holds a more modern and "newer" look and it is easier to read the text throughout the various sections of the application.

As this is an ongoing study, the feedback received through the usability studies allow for the continuation to make changes to optimize the design of the application to allow for both adequate and efficient data collection, while maintaining a user-friendly interface for the caregiver. Such an interface would not only enable the caregiver to use it, but also encourage the caregiver to want to use the system routinely. The future outlook of this continuing study allows for the continuing optimization of the design and functionality of the application. Other than the feedback regarding the displayed features, caregiver participants also voiced other suggestions that could further improve CAST. Additions that are currently being integrated into the project include a setting menu to allow for customization per the desires of the caregiver such as the font size. An additional game is under development to allow a choice for those that feel that the word scramble game is too challenging or would prefer another option. Help interactions will be added through the application so the caregivers can easily access instructions features at any time. Upon the completion of these additions, a usability study will be conducted to ensure that the changes progress the application. This study is built on an existing NIH funded project (#1K01LM012439) titled "Managing Dementia through a Multisensory Smart Phone Application to Support Aging in Place**.**"

Figures/Charts

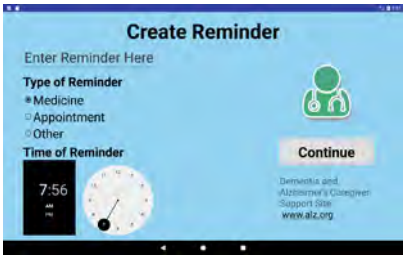

Figure 1. Reminder Screen - CAST 2.0 (New Addition)

Figure 2. Word Scramble Game CAST 1.0 (left) CAST 2.0 (Middle and Right)

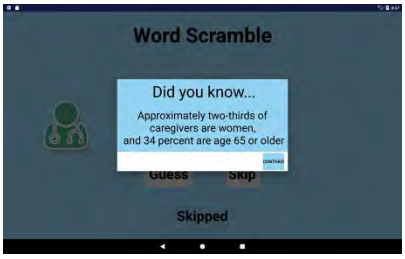

Figure 3. Incentive Fact - CAST 2.0 (New Addition)

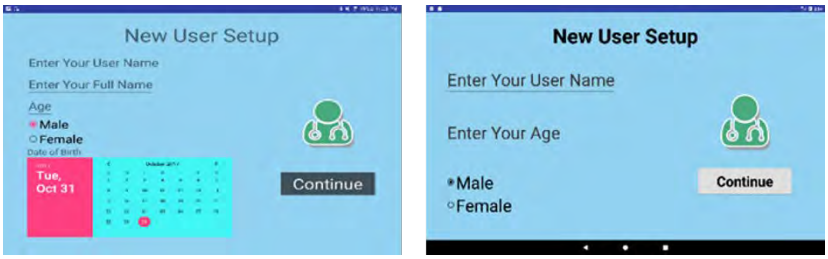

Figure 4. New User Setup Screen CAST 1.0 (left) CAST 2.0 (Right)

Figure 5. Activity Selection Screen CAST 1.0 (left) CAST 2.0 (Right)

Acknowledgments and References

1. Hughes, J. C., Banerjee, T., Goodman, G., & Lawhorne, L. (2017). A Preliminary Qualitative Analysis on the Feasibility of Using Gaming Technology in Caregiver Assessment. Journal of Technology in Human Services, 1-16.
2. Zarit, S. H., Reever, K. E., & Bach-Peterson, J. (1980). Relatives of the impaired elderly: correlates of feelings of burden. The gerontologist, 20(6), 649-655.

Effect of Curved Boundary Layer Fences on Aerodynamic Efficiency

Student Researcher: Asa E.E. Palmer

Advisor: Dr. Sidaard Gunasekaran

University of Dayton
Department of Mechanical and Aerospace Engineering

Abstract
During lift production, the air from the high-pressure region on the bottom surface of the wing curls towards the low-pressure region on the upper surface at the wingtip causing a spiraling vortex. These vortices induce downwash which in turn creates induced drag. Since every lift-generating wing causes these vortices, induced drag is inevitable. Passive control devices such as end plates, winglets, and wingtip sails are currently being employed in full scale airplanes to reduce the strength of wingtip vortices.

This research explores the use of curved boundary layer fences (CBLFs) of different arc lengths on an AR 4 NACA 0012 wing to affect the spanwise flow which is hypothesized to reduce the strength of the wingtip vortex resulting in an increase in aerodynamic efficiency. Force based experiments were conducted in the University of Dayton Low Speed Wind Tunnel (UD-LSWT) to determine the changes in aerodynamic lift with and without CBLFs. Sensitivity study was also performed by changing the location and orientation of the CBLFs along the span of the wing.

Introduction
The effects of induced drag are most prevalent during takeoff and landing where the lift production, hence the strength of wingtip vortices, is higher. Modern wingtip devices such as end plates, winglets, etc. result in drag reduction of only a few percent. Apart from higher induced drag, non-uniform flow separation across the span occurs in low aspect ratio (AR) wings which results in non-uniform lift distribution and pitching moments. Therefore, unconventional passive methods of improving aerodynamic efficiency under these conditions must be explored. One such passive method is the use of boundary layer fences (BLFs). Apart from being used to prevent stall from propagating across the span of a wing, BLFs have been shown to provide aerodynamic benefits in the form of an increased lift coefficient. Walker and Bons [1] observed a 14.3% increase in $C_{L\,max}$ by placing traditional BLFs on the upper surface of a swept wing. Recent research done by Goodman and Gunasekaran [2] showed that the near-wake from the lower surface showed the same trend as the near-wake from the upper surface. This is expected since the spanwise flow is more likely to occur on the lower surface as well. Therefore, curved boundary layer fences (CBLFs) were designed to be mounted on both the upper and lower surface of the wing to decrease the spanwise flow and in turn reduce the strength of wingtip vortices.

Objective
The objective of this research is to determine the changes in aerodynamic efficiency with the use of CBLFs on an AR 4 NACA 0012 wing. Force based experimentation as well as several methods of flow visualization were used to determine these effects. By placing a CBLF on the surface of a wing, spanwise flow is blocked which affects the pressure difference at the wingtip. This change in pressure difference is hypothesized to affect the wingtip vortex and in turn, the lift induced drag and aerodynamic efficiency.

Methodology

Experimental data was collected by conducting force based testing and several forms of flow visualization in the University of Dayton Low Speed Wind Tunnel (UD-LSWT). 3-D rendering of the CBLFs was done using Dassault Systèmes SolidWorks 2016-2017 Student Edition. Three different CBLFs with different arc lengths were designed to be mounted on the upper and lower surfaces of the wing. The three CBLFs varied only in the fraction of the semi-span of the wing that they covered; half span, third span, quarter span. All were 5 mm thick and their curvature was created using the spline function.

Computational Fluid Dynamics (CFD)

The SolidWorks Flow Simulation tool was used to gain insight into the effects of CBLFs. Assemblies were created using a baseline AR 4 NACA 0012 wing as well as two sets of CBLFs for each side of the wing. The flow simulation consisted of an external flow of air at 25 m/s with pressure of 101.325 kPa and density of 1 kg/m^3. 1,600,000 total mesh cells were used (~550,000 solid cells). Simulation was done at 0, 2, 4, and 6 degrees angle of attack (AoA). The surface goals that were calculated were SG Force (X) aka "drag" and SG Force (Y) aka "lift" measured in SI units (Newtons).

Force Based Testing

All force based testing on the half-span NACA 0012 wing was done at a velocity of 25 m/s and at AoAs ranging from -15^o to 15^o. The CBLFs were tested in 4 different configurations that differed in their spanwise location on the wing and their direction of curvature. The configurations were as follows; middle inward (Fig. 1a), middle outward (Fig. 1b), wingtip inward (Fig. 1c), and wingtip outward (Fig. 1d). The ATI Mini-40 force transducer was used to measure the aerodynamic forces along with the Griffin rotary stage, controlled using Galil motion software which was used to change AoA.

Flow Visualization

Three different flow visualization techniques were used during experimentation to attempt to visualize the flow on the surface of the wing with CBLFs; tuft visualization using fluorescent fishing line and white sewing thread, oil flow visualization using fluorescent dye, and smoke visualization using smoke streaklines. Small sections of fluorescent fishing line (approximately 1 inch in length) were cut and put together on strips of tape covering the splitter plate and the baseline wing. Unfortunately, the fluorescent tufts were not effective because the fishing line was too rigid so sewing thread was used instead. This thread was much less rigid than the fishing line which produced noticeable oscillations. Individual pieces of sewing thread (approx. 1 inch in length) were spaced along rows of tape that were then placed on the upper and lower surfaces of the wing. The thread was more spread out than the fluorescent tufts to avoid entanglement when the flow on the surface became turbulent.

Oil flow visualization was also used to determine the changes in the flow field on the surface of the wing using fluorescent dye. Drops of dye were placed on the splitter plate and then spread onto the baseline wing using a paint brush during testing. Only the baseline wing was done because of time constraints and a separation line was clearly seen on the surface of the wing. This test may be done more accurately in the future if it is believed that useful results can be obtained. In order to capture the bending and separation due to the CBLFs, a smoke visualization was performed. This setup involved placing a thin nichrome wire directly in front of the wing in the test section inlet. Current was then run through the wire using a variable voltage autotransformer that pulled voltage from a wall socket and outputted around 10% of that voltage (approx. 10-11 V) across the nichrome wire. The heated wire then burned fog liquid that was applied with a paint brush during testing. This setup produced streaklines of smoke however it was difficult to line the streaklines with the leading edge of the wing without needing multiple wires.

Results

CFD Results

The lift and drag force data obtained on the wings from the SolidWorks Flow Simulation tool were analyzed in order to calculate the coefficients of lift and drag from Equations 1 and 2 below.

$$C_L = \frac{2L}{\rho V^2 A} \quad (1)$$

$$C_D = \frac{2D}{\rho V^2 A} \quad (2)$$

The same planform surface area (A) was used for the baseline and the wings with CBLFs when calculating the lift and drag coefficients. It was assumed that the thickness of each CBLF was negligible. Further, density (ρ) and velocity (V) values were the same for all cases. The plot comparing the lift coefficients vs. angle of attack for each case is shown in Figure 2. It can be clearly seen that there is an increase in the lift coefficient when compared to the baseline wing for every BLF especially at higher AoAs. Although this range only went up to 6^o AoA, it can be seen that CBLFs affect the lift coefficient especially as angle of attack increases.

Force Based Testing Results

The Mini-40 force transducer measures normal and axial forces in Newtons [*N*]. The normal and axial forces recorded by the sensor were then used to calculate the lift and drag forces on the wings with Equations 3 and 4.

$$L = N\cos\alpha - A\sin\alpha \quad (3)$$

$$D = N\sin\alpha + A\cos\alpha \quad (4)$$

Unfortunately, the Mini-40 force transducer isn't sensitive enough in the axial force direction to give an accurate reading for drag. For that reason, a partial drag force was calculated for each case using only the $Nsin\alpha$ term from Equation 4. This allowed for a partial calculation of the drag coefficient to be made using Equation 2 and plotted to be compared for each case. The coefficient of lift was calculated for each case using Equation 1. Similar to the CFD data, the same planform surface area (A) density (ρ) and velocity (V) values were used for the baseline and the wing with CBLFs in calculating the lift coefficient and partial drag coefficient. The results of the force based testing showed a significant increase in coefficient of lift for every CBLF in every configuration when compared to the baseline wing which is consistent if the CFD data. These plots also show an increase in partial drag coefficient especially for the half span CBLF. This is to be expected though because more surface area was in contact with the freestream casuing more parasitic drag which would increase the total drag force. Plots of coefficient of lift and partial coefficient of drag for each BLF orientation compared to the baseline wing are shown in Figure 3a-f. The slopes of the increase of coefficient of lift with respect to angle of attack were determined from -8^o to 8^o AoA to determine the percentage increase in slope. This range of AoA was used to observe the most linear section possible. The largest percentage increase was seen in the quarter span wingtip outward orientation with an increase of 22.4%. Following that were the third span wingtip inward and quarter span middle outward orientations with percentage increases of 21.6% and 18.7% respectively. The highest percentage increases for coefficient of lift and partial coefficient of drag for each CBLF is shown on the Figure 3 plots.

Flow Visualization Results

As stated earlier, only some of the flow visualization experiments yielded sufficient results. The smoke streakline flow visualization was too unclear to determine what was actually happening to the flow on the surface of the wing. The fluorescent dye experiment showed some separation of the flow on the surface of the baseline wing but CBLFs were not tested with this method. The sewing thread flow

visualization did appear to show a delay in flow separation with the CBLFs as AoA increased. Further, flow remained attached closer to the root and wingtips when CBLFs were used. For the baseline, it appeared that the flow separated everywhere on the wing at the same time. This delay in flow separation, which can be seen in Figure 4a-d, could be an indication as to why an increase in lift coefficient is seen in the force based testing especially at higher AoAs.

Status

Although significant increases in lift coefficient can be seen with the addition of CBLFs through force based testing and CFD, the partial drag coefficient is also increased. For this reason, it is difficult to determine how CBLFs affect aerodynamic efficiency. It appears that flow remains attached to the surface of the wing in more locations when CBLFs are put onto the wing. The influence of the CBLF on the wingtip vortex has yet to be quantified using Particle Image Velocimetry (PIV) and is currently in progress. These results will tell more about how CBLFs actually affect the induced drag. Further, sensitivity analysis will be performed by having CBLFs on the upper and lower surfaces independently.

Figures

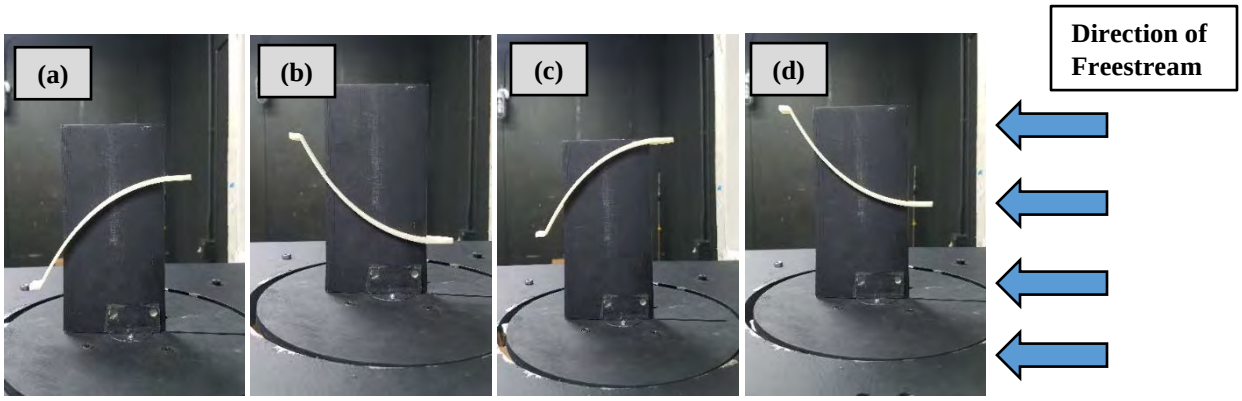

Figure 1. Half Span CBLF test configurations; a) middle inward, b) middle outward, c) wingtip inward, d) wingtip outward. The same orientations and positions were done for other CBLFs (third span and quarter span).

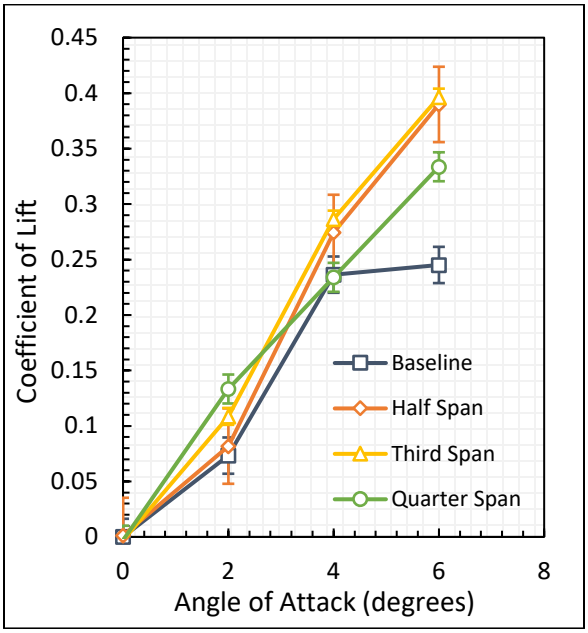

Figure 2. Plot of coefficient of lift vs. angle of attack for the CFD data. A distinct increase in lift coefficient can be seen for all cases when compared to the baseline wing without CBLFs.

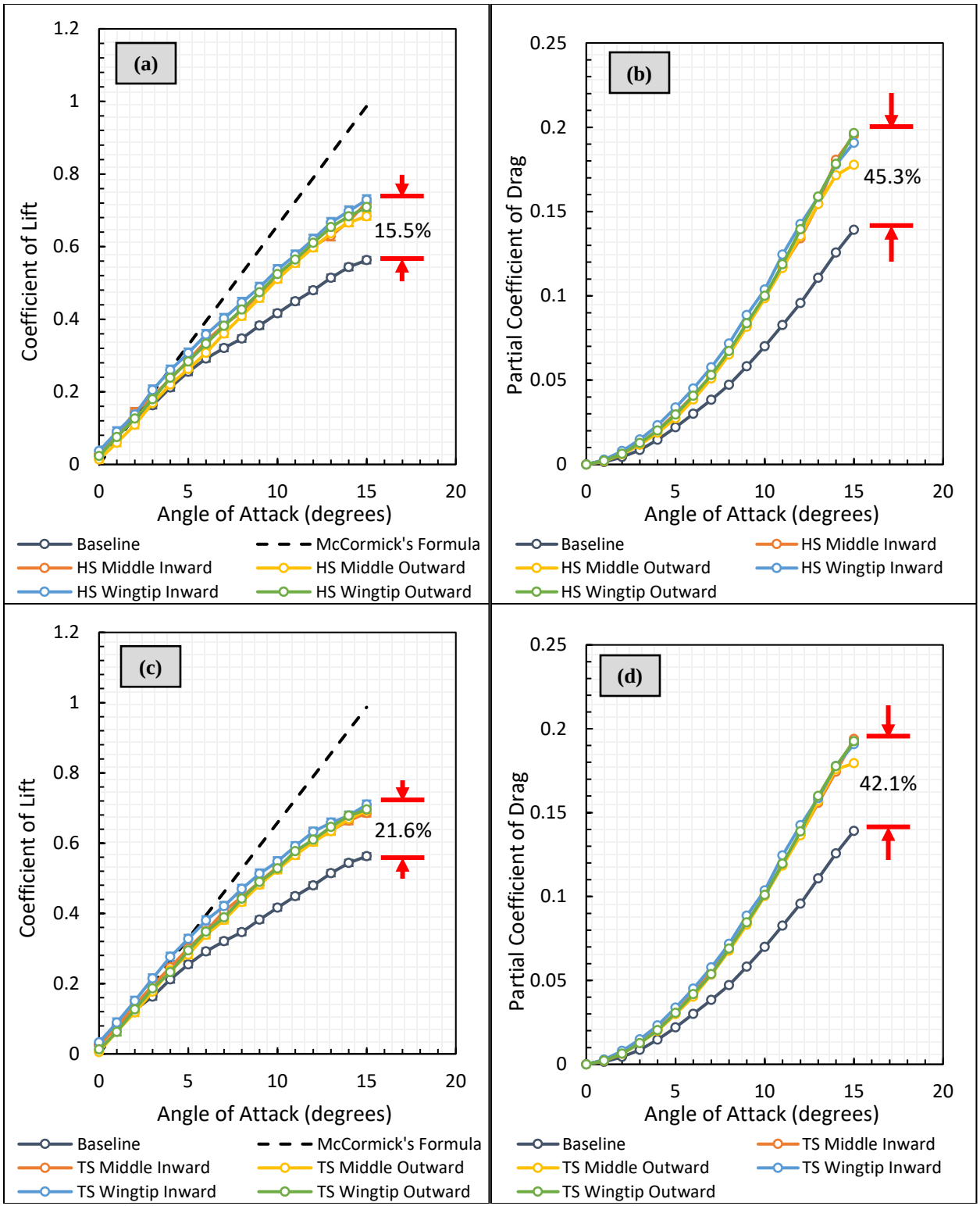
(a)
Coefficient of Lift
Angle of Attack (degrees)
15.5%
Baseline
McCormick's Formula
HS Middle Inward
HS Middle Outward
HS Wingtip Inward
HS Wingtip Outward
(b)
Partial Coefficient of Drag
Angle of Attack (degrees)
45.3%
Baseline
HS Middle Inward
HS Middle Outward
HS Wingtip Inward
HS Wingtip Outward
(c)
Coefficient of Lift
Angle of Attack (degrees)
21.6%
Baseline
McCormick's Formula
TS Middle Inward
TS Middle Outward
TS Wingtip Inward
TS Wingtip Outward
(d)
Partial Coefficient of Drag
Angle of Attack (degrees)
42.1%
Baseline
TS Middle Inward
TS Middle Outward
TS Wingtip Inward
TS Wingtip Outward

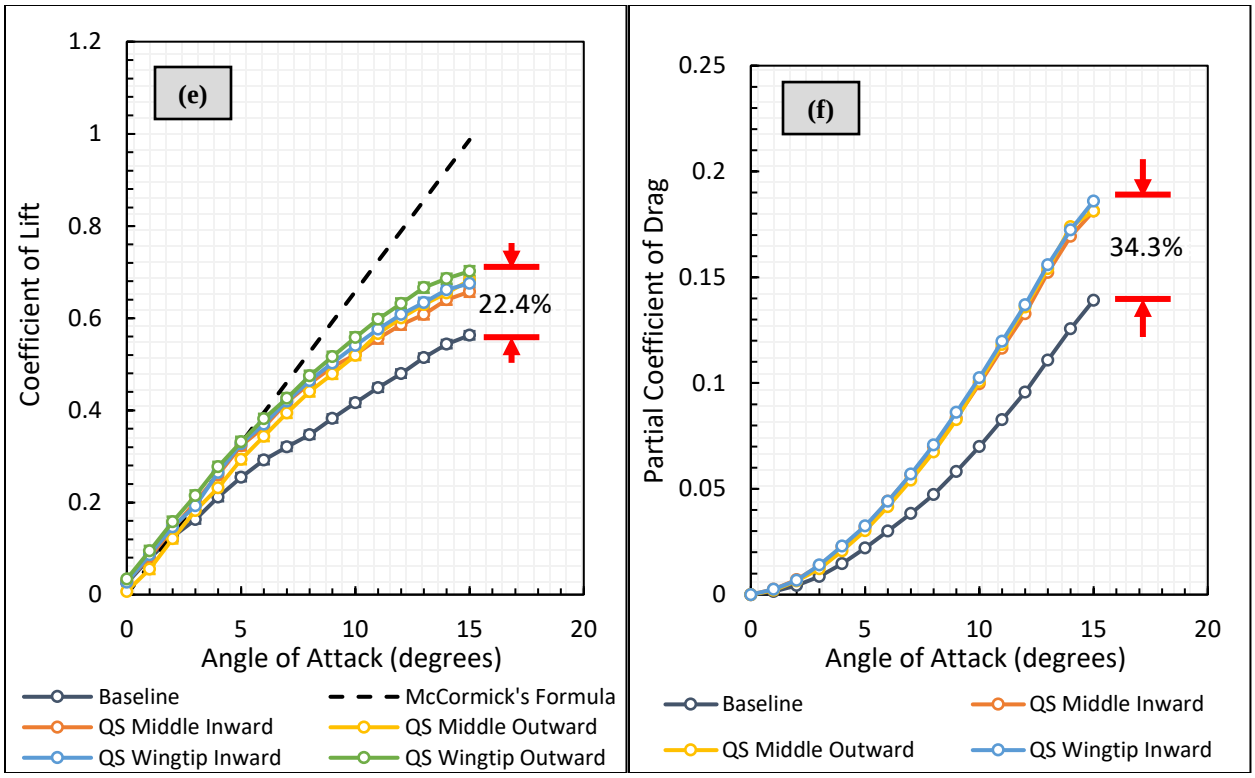

Figure 3. Force based test data for each CBLF. Coefficient of lift plots are complete with error bars; a) half span, c) third span, e) quarter span. Partial coefficient of drag data uses only the normal force component of drag and is used only to compare the trends for each CBLF; b) half span, d) third span, f) quarter span.

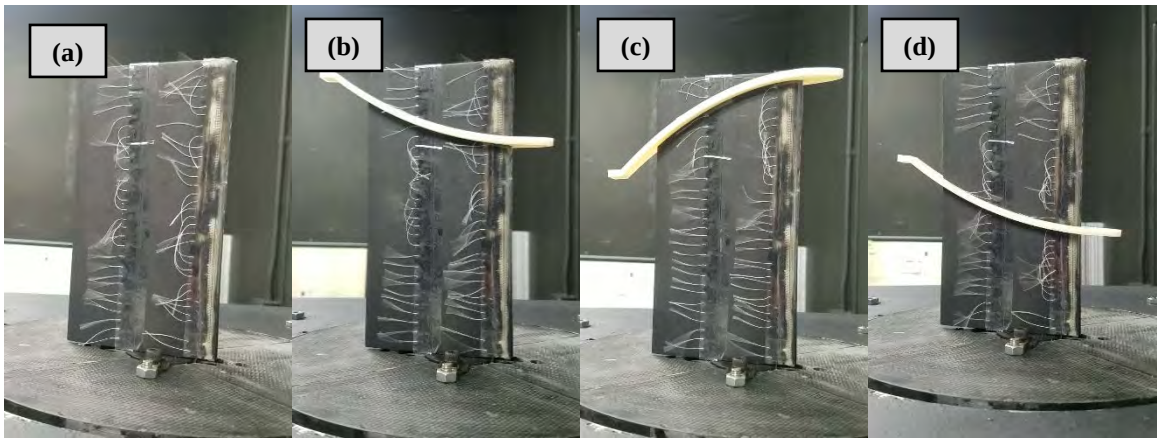

Figure 4. Sewing thread tuft visualization for the top three CBLF cases and the baseline at the instant that flow begins to separate; a) baseline wing shows that flow separates at every location at the same time, b) quarter span wingtip outward saw the highest increase in C_L, c) third span wingtip inward saw the 2nd highest increase in C_L, d) quarter span middle outward saw the 3rd highest increase in C_L.

References

1. Walker, Michael M.; Bons, Jeffrey P. “The Effect of Passive and Active Boundary-Layer Fences on Swept-Wing Performance at Low Reynolds Number”. The Ohio State University. Columbus, OH. 2018.
2. Goodman, Stephen; Gunasekaran, Sidaard. “Correlation Between Near Wake Turbulent Fluctuations and Aerodynamic Efficiency of SD7003 Airfoil”. University of Dayton. Dayton, OH. 2018.

Triangulation Using Antennas in the Near-Field

Student Researcher: DeGrafth A. Palmore

Advisor: Dr. Nathan Ida

University of Akron
Department of Electrical and Computer Engineering

Project Objectives

Antennas can be used in a multitude of applications. Most of the applications can be separated into two subcategories, near-field and far-field. Far-field is mostly used for transmission of data wirelessly such as radio communication or Bluetooth. Near-field is mostly used for coupling devices such as RFID tags.

The purpose of this project is to detect the location of a body part, such as a hand, using antennas in the near-field. Using an allocated bandwidth from the FCC, all antennas will have to operate at different center frequencies. The measurement of frequency change and amplitude change will be used to detect location and speed respectively. Possible applications of this technology will be military combat simulation, virtual reality simulation and distant learning environments.

Abstract

The circuit is based off the famous Theremin instrument. The frequency range of the circuit is normally higher than the range of human hearing. This is done to have complete audio isolation from the output. The signal is then passed through a mixer and is converted to the human audio range. This instrument used two antennas: one for frequency shifting and the other for amplitude modulation. There are four things that the triangulation circuit must have to function property: an antenna, an oscillator circuit, a filter, and an amplitude detector (sample and hold circuit). These elements are shown in figure 1.

Methodology

When it comes to electromagnetic spectrum, the FCC regulates what frequencies that are allocated for use. Using antennas in the near-field are best done at lower frequencies because the wavelengths are longer. To operate in the near field, activity must be between the antenna and theoretically 2π wavelengths away or at most 3 wavelengths for practical purposes.

The actual dimensions of the antennas are arbitrary to a point in this application because it is used only to change the frequency and amplitude and not to transmit power. Too small and the capacitance of the object will saturate it; too large and it will not have an adequate frequency change to detect. In the near-field, antennas act as inductors and capacitors. This means that in the circuit, the resonance frequency of the oscillator circuit will change because the added values on inductance and capacitance.

With these two stipulations in mind, the best possible bandwidth to use is 3.5-4MHz. The three antennas must operate on different frequencies and have a wide enough bandwidth to change center frequency. Using the frequencies selected above, the useable near-field range at this frequency is sufficient for this application. The center frequency for the circuits are found using the equation $f_c = \sqrt{f_1 x f_2}$. f_0,f_1 and f_2 means center frequency, leading edge frequency and trailing edge frequency respectively. The three frequencies aref_{C1}, f_{C2} and f_{c3}.

An oscillator circuit must be implemented. A crystal only oscillates at a specific frequency, so it will not be idea in a frequency modulation circuit. The "Tank Circuit" provides the oscillation while the rest of the circuit provides stability and amplification as shown in figure 2. At 4MHz, the Colpitts Oscillator will be the most effective oscillator design due to its stability at high frequencies and ability to produce a pure signal.

$$f_c = \frac{1}{2\pi\left(\sqrt{\frac{LC_1C_2}{C_1 + C_2}}\right)}$$

Ideal Filters have what is called a brick wall characteristic which means that there is no transition band between the attenuation band and the gain band. First-order filters are usually made with passive components while higher order circuits are made with an operational amplifier and passive components.

Practical filters will have a transition band. This is non-ideal because it will allow unwanted frequencies to pass at an attenuated amplitude. This cannot be eliminated but can be reduced by higher order filter stages cascaded together. Although increasing the order of the circuit will increase efficiency, it will also decrease gain while increasing cost and complexity. This is important because it the effects on the amplitude should be minute. The amplitude will measure how fast the motion occurs and the frequency change will determine the location of the moving object.

This means that the filter must have a practical initial frequency before the ideal initial frequency. The detection of amplitude means a constant gain in a designated bandwidth that contains the change in frequency. Filter design that experience oscillation in the bandwidth such as Chebyshev is not ideal even if with a smaller transition band.

With that, the perfect design to implement is referred to as a narrowband filter because the range of frequency that it passes is very small. The bandgap depends on the quality factor denoted as Q. The formula for finding Q changes as the topology of the circuit changes. The gain must also be divided between each filter stage for maximum efficiency.

All components have a frequency where the operation is less than ideal. For example, for a ceramic capacitor will behave close to idea for frequencies under 40MHz but about 60MHz it will act as an inductor.

Results Obtained

In the simulation, the capacitor above must be higher than the capacitor below in the tank circuit. If the values are reversed, the wave will become distorted. Also, the capacitors and inductors must be on the same magnitude. If not, the wave will be distorted.

The filter stage has three different design for each Colpitts Oscillator center frequency. f_{C1} is shown in figure 3. It is a 6th order system because the roll off must have a steeper slope. f_{C3} is also a 6th order system. f_{C2} is an 8th order system because the center frequency is between the two other frequencies. The magnitude plot of all the filters in this design is shown in figure 4.

Acknowledgments

The author of this paper would like to thank Ohio Space Grant Consortium (OSGC) for funding as well as the University of Akron. The author would also like to thank Dr. Nathan Ida for advising this project and Dr. Julie Zhao for her cooperation on the project.

Figures and Tables

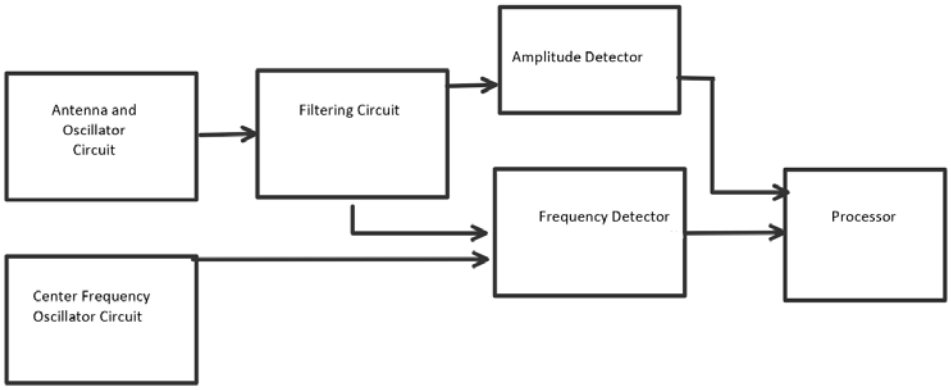

Figure 1: Block Diagram

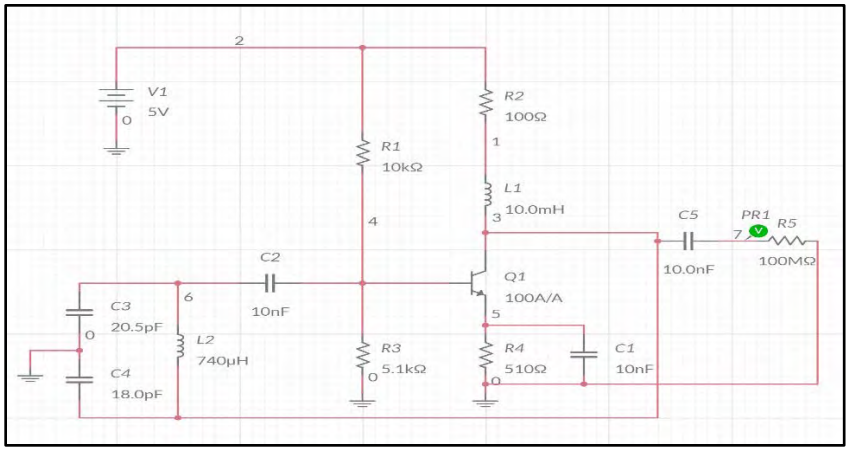

Figure 2: Colpitts Oscillator

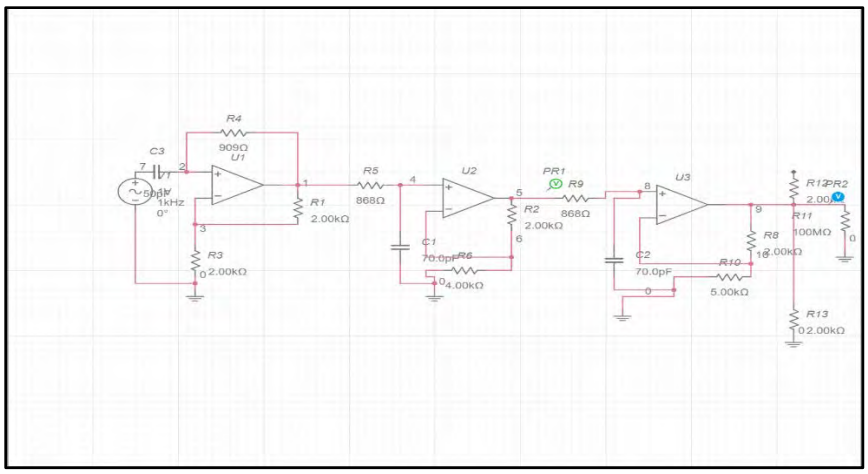

Figure 3: Filter Circuit Sample

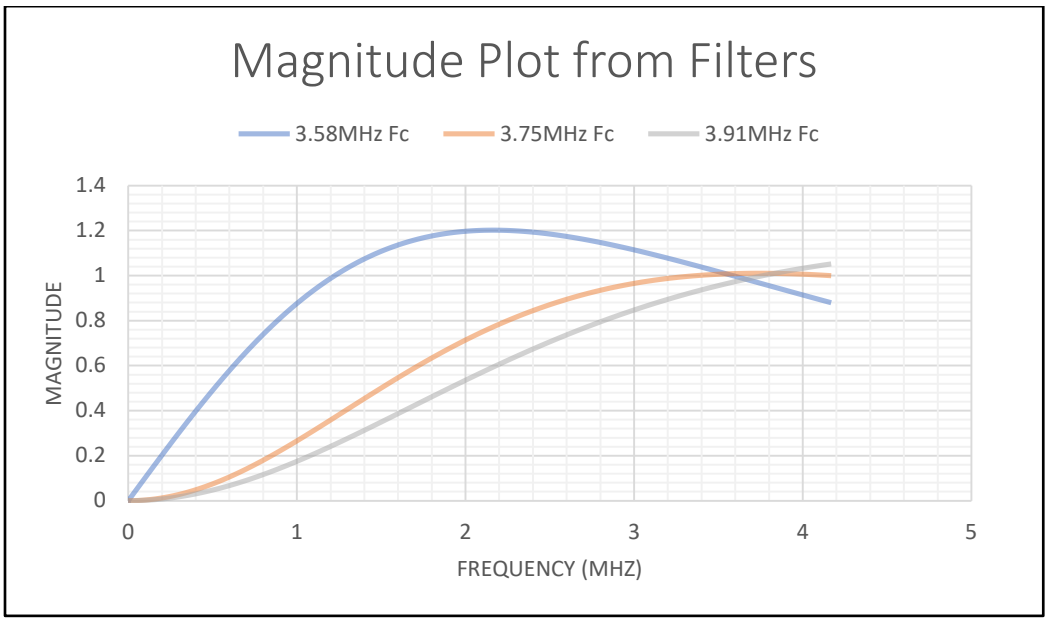

Figure 4: Magnitude Plot for the three Filters

References

Colpitt Oscillator using BJT's. (n.d.). In A. Electronics.

FCC. (n.d.). Retrieved from https://www.ntia.doc.gov/files/ntia/publications/2003-allochrt.pdf

Grimes, G. (2018). *How a Theremin Works.* Retrieved from https://electronics.howstuffworks.com/gadgets/audio-music/theremin2.htm

Ida, N. (n.d.). Engineering Electromagnetics.

Valk, R. S. (2001). Design of Analog Filters. nburg, Oxford University Press.

Reducing Passive Muscle Force: A Process for Patient Specific Muscle Parameter Calibration in RTSA Patients

Student Researcher: Kayla M. Pariser

Advisors: Dr. Allison L. Kinney (University of Dayton) and Dr. David R. Walker (Rehoboth Innovations)

University of Dayton
Department of Mechanical and Aerospace Engineering

Abstract

Currently there is not a standardized, objective method for a surgeon to position a reverse total shoulder arthroplasty (RTSA) in a patient. Simulation and optimization methods have been used to analyze how surgeries affect muscle function with generic models. However, the effect of patient-specific muscle parameters on modeling realistic muscle function in the RTSA population is unknown. Calibration of patient-specific parameters via optimization is feasible, but can be time consuming. Due to the fast workplace environment, surgeons cannot afford to wait hours for optimizations to converge. To decrease convergence time and apply these tools clinically, muscle parameter optimizations must be provided a realistic initial guess representative of the patient's muscle function. To our knowledge, previous studies have not established guidelines for adjusting muscle parameter values from literature sources to patient-specific values, but one possible mechanism is reduction of passive force. The purpose of this study was to investigate how much deviation from the literature muscle parameter values is necessary to reduce passive force and produce more realistic muscle activations for patient-specific cases. Patient-specific shoulder models were generated for eight subjects with two different implants. The literature muscle parameter values for the three deltoid muscles were modified via scaling factors that were manually chosen to reduce passive muscle force and find common factors across all subjects for each deltoid. Following the parameter sensitivity study it was determined that reduction of passive force produced more realistic muscle forces and activations for all subjects. Common scaling factors were found across all of the subjects for two of the three deltoids. There was inconsistency amongst the subjects as to which deltoid required the most parameter adjustment, emphasizing the importance of patient-specific muscle parameter adjustment. Once the parameters were adjusted, the muscle activation and force contribution became more realistic for all three deltoid muscles for all subjects.

Introduction

A reverse total shoulder arthroplasty (RTSA) is a common treatment used to stabilize the shoulder and improve range of motion in patients with rotator cuff muscle tears or severe arthritis. The RTSA implant is designed to enable the deltoid muscle to become the primary stabilizer thereby increasing the stability of the joint [1]. Greater stability is due to an increase in the deltoid muscle moment arm, which decreases the required deltoid force to achieve the required torque about the glenohumeral joint for shoulder movement. Previous research suggests that a more medial and inferior placement of the center of rotation for the RTSA implant is ideal, however, implant placement is complex given the multiple degrees of freedom of the shoulder joint [2]. In addition, there is no standardized, objective way for a surgeon to position an implant on a specific patient.

Simulation and optimization methods have been used to understand moment arms and their effect on muscle function, to predict muscle forces, to analyze how surgeries affect the muscle moment arms with general models, and to analyze the effect of muscle parameters on muscle function [3]. However, the effect of patient-specific muscle parameters on modeling realistic muscle function in this population is unknown. Muscle parameters influence how much force a muscle can produce. The force-length curve (FLC) defines the relationship between the muscle-tendon length and muscle force produced (Figure 1). Physiologically, muscles primarily act in the left region of the curve (0.5-1 x optimal fiber length (LMo)) and produce active force. Muscles typically do not produce much passive force. Muscles have protective measures against this, because passive force production is analogous to an overstretched spring and can lead to injuries like muscle tears. At the optimal muscle fiber length (1 x LMo), the muscle will produce its maximum isometric force. Every patient has their own unique set of muscle parameters and sits on different regions of the FLC. Using generic literature muscle parameters based off cadaveric studies can cause muscles to act on the passive force region of the FLC. Therefore, obtaining patient-specific muscle parameters is necessary to predict realistic muscle forces and apply simulation tools clinically.

Project Objective

Calibration of patient-specific parameters via optimization is feasible, but can be time consuming. Due to the fast workplace environment, surgeons cannot afford to wait hours for optimizations to converge. In order to decrease convergence time and apply computational tools clinically, muscle parameter optimizations must be provided a realistic initial guess that is representative of the patient's muscle function. To our knowledge, previous studies have not established guidelines for adjusting muscle parameter values from literature, especially across a group of subjects. Reduction of passive force produced by muscles may be a mechanism for adjusting parameter values. Therefore, the purpose of this study is to investigate how much deviation from the literature muscle parameter values is necessary in order to reduce passive force and produce more realistic muscle activations for patient-specific cases.

Methodology

Eight subjects with two different RTSA implants participated in this study (age: 73±6 years, height: 1.67±0.07 m, mass: 77.28±9.62 kg). Electromyographic (EMG) muscle activity, motion capture, and fluoroscopic data were collected previously and provided by Rehoboth Innovations, LLC [4-5]. A combination of the fluoroscopic images and the motion capture data was used to define the motion in a shoulder model for each subject. The models were modified from Holzbaur et al. [6] to include the RTSA implant and were scaled to the subject specific dimensions. Each model included two degrees of freedom at the shoulder (abduction/adduction and flexion/extension) and 15 major shoulder muscles (anterior, middle, and posterior deltoid; four rotator cuff muscles; thoracic, lumbar, and iliac latissimus dorsi; clavicular, sternal, and costal pectoralis major; upper trapezius; and teres major). OpenSim, an open-sourced software, was used to perform biomechanical modeling and to calculate musculotendon lengths, muscle moment arms, and joint moments for the three deltoid muscles [7]. These values were calculated for the deltoid muscles for each subject as the subject performed isometric muscle contractions at arm elevation angles of 0, 45, and 90 degrees.

The optimal fiber length and tendon slack length values of the anterior, middle, and posterior deltoid muscles were modified from the literature values [8] using scaling factors. Scaling factors were chosen manually with the goal of determining common factors for each deltoid muscle across all eight subjects so that the muscle-tendon length (lMtilda) values were within the active force range, 0.5-1.0 x LMo, on the FLC. A custom MATLAB code was used to generate plots of the lMtilda values, predicted muscle activation as compared to the experimental EMG data, and force contribution from each of the three deltoid muscles before and after the literature muscle parameter values were modified.

Results / Discussion

Reduction of passive force produced more realistic muscle forces and activations for all eight subjects. Scaling factors larger than one were chosen for all three deltoid muscles for all eight subjects, as scaling factors above one caused a shift of the muscle to operate in the left, active-force, region of the FLC. Common scaling factors were found for the middle and posterior deltoids across all eight subjects, but not for the anterior deltoid (Table 1). Two of the subjects required scaling factors for the anterior deltoid that were much higher than that for the other subjects. This demonstrates the importance of patient-specificity in terms of muscle parameters. The ranges for the average lMtilda values across all eight subjects for each of the deltoid muscles using the literature parameters had upper bounds outside the ideal range of 0.5-1.0 x LMo. After adjusting the parameters, the lMtilda ranges were all within the ideal region of the FLC (Table 2). Some of the subjects had lMtilda values for one or more deltoids within the desired range prior to parameter adjustment, but others, as depicted by the ranges in Table 2, produced large passive forces. There was an inconsistency among the subjects as to which deltoid muscle required the most parameter adjustment, further emphasizing the importance of patient-specific muscle parameter adjustment.

Using the literature parameter values, many subjects displayed a trend in which the muscle activation was minimal, but the predicted muscle force was very large due to the large passive muscle force contributions. Following parameter adjustment, the muscle activation and force contribution became much more realistic for all three deltoid muscles of all eight subjects. Figure 2 depicts the results for the anterior deltoid of Subject 1. With the literature value parameters, the anterior deltoid for this subject was not active, but produced 20,000 N of force. It is not realistic for a muscle to be inactive and to produce such a large amount of force. In addition, the lMtilda values for this subject reached as high as 2.4 at 45 degrees of arm elevation. This value is in the extreme right/passive-force region of the curve and is not typically represented on the curve, as physiologically muscles do not produce this much passive force. By adjusting the parameters to reduce passive force production and shift the lMtilda value for each of the three arm elevations into the desired range, the anterior deltoid muscle activation and force became more realistic. When the muscle was inactive it did not produce force, and when the muscle was around 30% active it produced approximately 250 N of force, a reasonable magnitude for the anterior deltoid muscle. The resulting muscle activation after parameter adjustment mimicked the trend observed in the experimental EMG data. Additional adjustments are necessary to further calibrate the parameters to the individual subject, but the results from this parameter sensitivity study should provide the calibration optimization with a more realistic initial guess to speed up the time to convergence. This will facilitate application of simulation methods in a clinical setting.

Conclusion

RTSA patients have varying height, weight, and muscle force capacity. Therefore, it is important that RTSA implants be placed in patient-specific locations to have optimal deltoid muscle function after surgery. To determine patient-specific implant placement, patient-specific models are needed. It is not adequate to scale the models in terms of the subjects' heights only. This study illustrates the need for adjustment to the commonly used literature muscle parameter values to generate patient-specific models that more accurately reflect a patient's muscle force capacity. Reduction of passive force appears to be a feasible process to adjust muscle model parameter values and improve patient-specific calibration of models. Future work should focus on automating the calibration process and continuing to test passive force reduction as a mechanism for producing realistic results in a larger subject population.

Figures and Tables

Table 1. Scaling factors

	Deltoid		
Patient	Anterior	Middle	Posterior
1	1.79	1.13	1.25
2	1.5	1.13	1.25
3	1.5	1.13	1.25
4	1.5	1.13	1.25
5	1.5	1.13	1.25
6	1.5	1.13	1.25
7	2.22	1.13	1.25
8	1.5	1.13	1.25

Table 2. Average lMtilda values for deltoids across all eight subjects before and after parameter adjustment

	Average lMtilda	
Deltoid	Literature Parameters	Adjusted Parameters
Anterior	1.4-3.05	0.7-0.91
Middle	0.85-1.05	0.625-0.82
Posterior	0.84-1.08	0.675-0.84

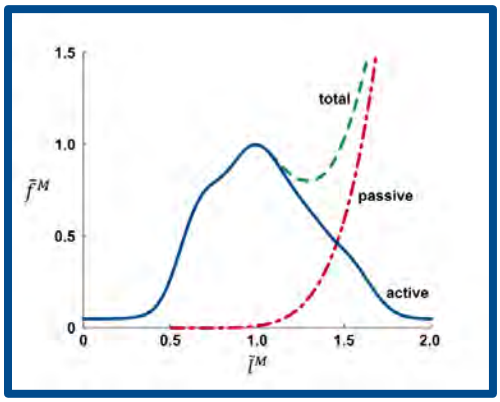

Figure 1. Force-length curve

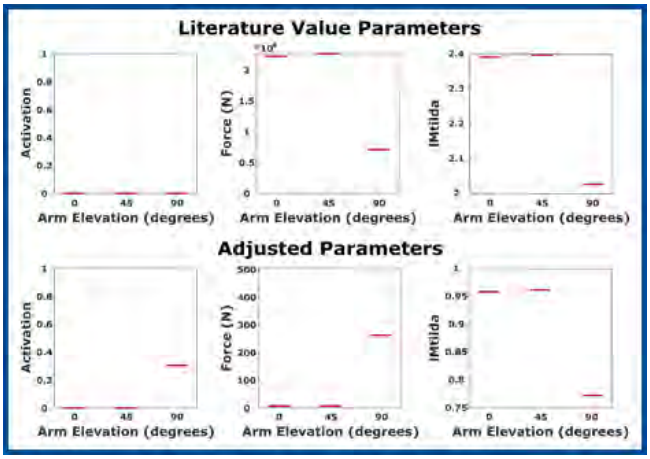

Figure 2. Anterior deltoid activation, force, and lMtilda for literature and adjusted muscle parameters for a representative subject

Acknowledgments and References

1. Ackland DC, et al. *J Anat.* **213**, 383-390, 2008.
2. Hoenecke H., et al. *J Shoulder Elbow Surg.* **23**, 1128-1135, 2014.
3. Pandy M.G., et al. *Annu Rev Biomed Eng.* **12**, 401-433, 2010.
4. Walker D., et al. *J Shoulder Elbow Surg.* **24**, 1129-1134, 2015.
5. Walker D., et al. *J Shoulder Elbow Surg.* **23**, 166-172, 2014.
6. Holzbaur KRS., et al. *Ann Biomed Eng.* **33**, 829-840, 2005.
7. Delp, S., et al. *IEEE Trans Biomed Eng.* **54**, 1940-1950, 2007.
8. Saul K., et al *Comput Methods Biomech Biomed Engin.* **5842**, 1-14, 2014.

Funding for this research was provided by the Berry Family Foundation, the University of Dayton University Honors Program, the University of Dayton School of Engineering Summer Undergraduate Research Experience, and the Ohio Space Grant Consortium.

Heated Clothing

Student Researchers: Lynnae S. Frisco and Kylon J. Payne

Advisor: Augustus Morris, Jr., Ph.D.

Central State University
Department of Manufacturing Engineering

Abstract
Every year throughout the U.S., there are a tremendous amount of reports of people freezing to death. We believe the reason for these major causes of death by hypothermia is because people are not properly equipped to handle such extreme weather. This problem can be improved by installing heating systems similar to heated blankets, warming pads and heated chairs. Heated clothing is a current product on the market but is not well known. Our goal is to modify the existing model to make it more affordable, accessible and to improve the quality of the jacket.

A variation of people can benefit from our improved heated clothing. The main idea of our clothing is to ensure warmth to the person wearing the clothes, reduce the number of hypothermic deaths, assist those who suffer from anemia and for the comfort of those who don't enjoy the cold weather.

The plan for the heated clothing is to begin with a basic design of a jacket. The jacket will have multiple layers that will help to keep the heat trapped inside. Before we can begin the design, there are some things we need to consider such as the battery life, the technology inside the jacket and its materials. Once, all of these factors have been considered we can then begin to implement the design.

Project Objectives
We want our jacket to have a long battery life, in order to ensure that people who wear our clothing can have the comfort of heat at any time they wish. There are many types of batteries on the market that can be used. The battery that we choose must have a slow decaying time, low risk for flammability and be able to store a high amount of energy. Lithium Ion batteries are at the top of our list.

Methodology Used
Lithium ion batteries are made of about 80% Lithium and 20% carbon (How Stuff Works). Most lithium ion batteries are highly reactive and can store a lot of energy in its atomic bonding (How Stuff Works). This is useful because the batteries store a lot of energy which means they have a longer life and can be very powerful. Generally, most lithium batteries can accumulate up to 150 watts/hour of power. Another benefit of using the lithium ion battery is that it can survive in extremely cold weather. In fact, these batteries have life in -40°F weather and has a decay rate of about 5% a month (How Stuff Works.) This is a good thing for our clothing because we want our jacket to be able to thrive in cold temperatures. One downfall to using the lithium battery is that it is flammable, as seen in the Samsung Galaxy telephones the batteries have be known to explode. They are also known to have about a three year from manufactured date life span (How Stuff Works).

The jacket will be designed using a lithium ion battery and we need it to produce about 12 volts with 2 amps of current which is about 24 watts of power to our heating system. Now, that we know where our power source is coming from we should now talk about how the heating system will work.

Our heating system will use nichrome as the wire that will be inserted into heating tubes. We considered two metals when trying to determine the best heating source for our clothing which were nichrome and copper. Copper is a good conductor of heat but the nichrome is an even better conductor. Nichrome is used in toasters, electric irons and many other common household items. This material is highly resistant to heat and high temperature oxidation. When nichrome is coiled it produces a specific electrical resistance and then electric current is passed through the wires to produce heat (Chemistry Learner). Nichrome is a nickel chromium alloy with non-magnetic properties and is our best option for heating our jacket.

Now that we know what our conductor is we will use the nichrome by using heating tubes and inserting the nichrome through them. The heating system will be layered between a material that will insulate the heat being produced. A layer of waterproof material will also be used to prevent any damage to our system. The outer layer of the jacket will be a polar fleece material. This material was chosen due to its comparability to wool and its cheaper price. Polar fleece is a highly breathable, great insulating and hydrophobic material. In our jacket design this will benefit us because it will help add extra waterproof protection. Polar fleece traps air between its fibers and the heat given off from the body heats the air that is trapped inside the materials fibers (Thermax).

The clothing will be controlled by an app that will allow you to control how much heat the user would like; it would be the user's personalized settings. As it has been stated before we want to help prevent hypothermic deaths. We would like to insert a sensor in the jacket that will turn on the heating system when body temperature begins to drop. Our sensor will be a temperature gauge that will alert the person when weather conditions are extreme and the person is at risk for hypothermia as well as when their body temperature is dropping. The heater will remain on until body temperature has reached the standard temperature of 98.6°F (Summit Medical Group), or if it's manually turned off. On the app you can also personalize the temp settings in your jacket; if you prefer to be warmer you can adjust it to your own needs.

Problem

This past winter we have experiences some of the coldest weather. Homeless people are out on those streets even when the temperature is well below 0. There have been multiple cases of people freezing to death on the street and we want to resolve this problem. Not only the homeless but people who have diseases that causes them to be cold and not able to regulate body temperature is another problem that our clothing can fix.

Idea

To create clothing that will help people stay warm and regulate your body temp.

Risk

- With the wiring there could be a risk factor if water were to be near.
- Overheating
- Material can withstand the amount of heat being applied
- Does it have a battery life? How long can it stay heated for?
- Is there a control system and what is its durability?

Features

- Temperature control: heating and possibly cooling.
- Charging port and Bluetooth speaker (Hood)

- The ability to focus the heat on a certain area
- Body regulator
    - Keeps track of heart rate
    - Gives exact body temperature
    - Steps taken

Research
Blaze wear: heated clothing has three main areas they target the heat at. Also, includes features with charging capabilities and adjustable thermostat.

- Waterproof abilities that can be turned off/on
- Powered by a 5v USB power bank
- Temperatures range from 38-55 degrees Celsius with a 13-hr. battery life.
- 2.1 Amp output

Information on the design of heated clothing. Coated the gloves with a material that still allowed the current to flow without getting to hot.
Massachusetts School Abstract on Heated Clothing

Activate
https://www.activheat.com/Heated-Clothing-How-it-Works-s/87.htm

-Uses a battery and very thin nonmetallic carbon fiber bundles for wiring.
-Uses a material that prevents heat from seeping through.
-Jacket has 6 layers from the outside to the skin. Each layer is different but helps with insulation
-Wiring is placed normally on back in chest and heat will be directed in this area.
-Runs on less the 12 V

Nichrome
https://electronics.stackexchange.com/questions/67462/why-does-the-nichrome-heat-up

-Has a higher resistance per unit length
-Has a higher resistance, High Melting point and can remain hot without oxidizing or burning out.
- Resistive alloy and its nonmagnetic.
-high electron mobility is a good conductor
-Low electron mobility is a good insulator

Common metals ranked by thermal conductivity

Rank	Metal	Thermal Conductivity [BTU/(shrift·°F)]
1	Copper	223
2	Aluminum	118
3	Brass	64
4	Steel	17
5	Bronze	15

http://www.chemistrylearner.com/nichrome.html

-This material is highly resistant to heat and high temperature oxidation. Due to this property, Nichrome is used in building toasters, soldering iron, hair dryers and electric ovens. In these instruments, Nichrome wires are wound in coils to produce a specific electrical resistance and then electric current is passed through the wires for producing heat.

-This substance is also used to build thermocouples.

-Nichrome is also used by hot wire foam cutters in industrial and other arenas.

-Nichrome wires and ribbons can be bought from shops that sell electrical wires and goods. 24 gauges of round Nichrome wires having .020 inches diameter with 25 inches coil can cost about $15 to $16. Flat Nichrome ribbons having dimensions of 1/16 inches width and .010 inches thickness cost around $2.20 per feet.

https://lightsngear.com/best-aa-batteries-for-winter/

-Lithium batteries have a life in -40-degree F and in C.
-Most energetic and rechargeable batteries on the market.

https://electronics.howstuffworks.com/everyday-tech/lithium-ion-battery.htm

-One downfall is that they have been known to explode.
-Highly reactive atom which can store a lot of energy in its atomic bond
-A typical lithium-ion battery can store 150 watt-hours of electricity in 1 kilogram of battery
-A NiMH (nickel-metal hydride) battery pack can store perhaps 100 watt-hours per kilogram, although 60 to 70 watt-hours might be more typical.
-Lead-acid battery can store only 25 watt-hours per kilogram.
-A lithium-ion battery pack loses only about 5 percent of its charge per month, compared to a 20 percent loss per month for NiMH batteries.

Materials

https://www.thermaxxjackets.com/5-most-common-thermal-insulation-materials/

-Fleece material is:
-Highly Breathable
-Soft to the Touch
-Less expensive than Wool
-Easy Care (machine washable)
-Durable
-Available in different weights for a wide range of temperature & insulation needs
-Hydrophobic (holds less than 1% of its weight in water)
-Retains insulating powers, even when wet
-Quick Dry
-Great alternative for those allergic to Wool
-Vegan alternative to Wool
-Polar heat traps air between its fibers and when against the skin can warm air

Nano Cloth

-Use tiny fibers 10 nanometers long usually in cotton or linen.
-Waterproof and increases the density and surface tension of the outside layer that prevent water from leaking through.

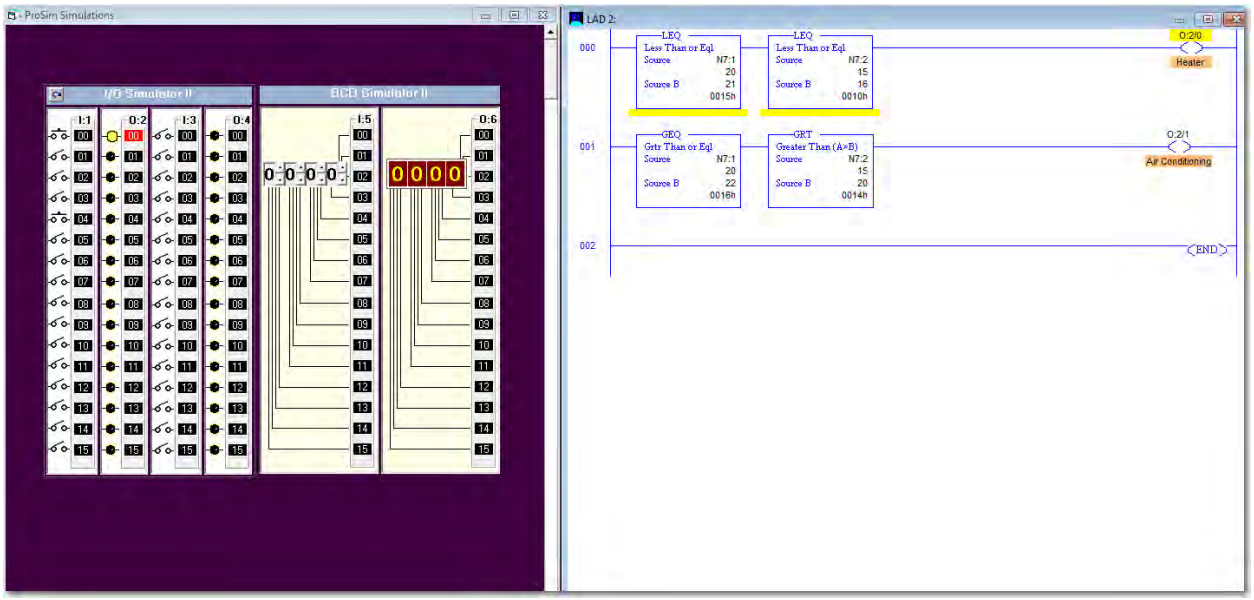

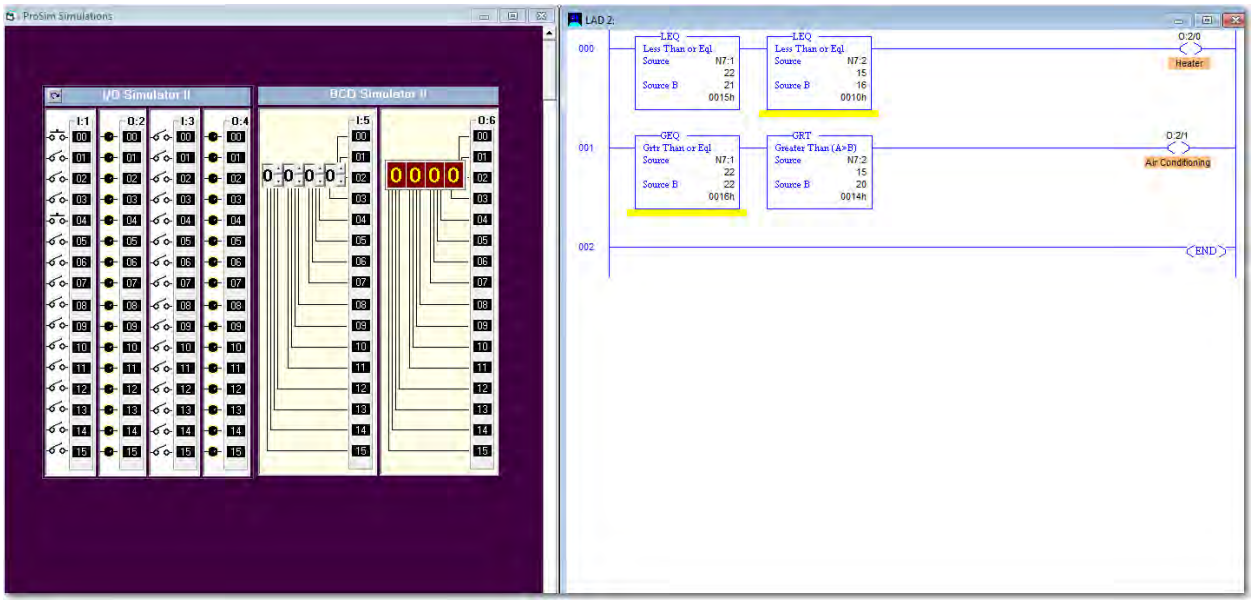

Figure 1. A model similar to how the sensor will work.

Conclusion

In conclusion we hope to improve the lives of others with this jacket and to decrease the number of hypothermic deaths. We strongly believe that with our design we can improve the overall design of the original product on the market by adding these features. We believe that with the improvement of the battery life, technology and the material our design can help reach our goal and change lives.

References

1. "Best AA Batteries for Winter -." *Lightsngear*, 29 Nov. 2014, lightsngear.com/best-aa-batteries-for-winter/.
2. *Chemistry Learner*, www.chemistrylearner.com/nichrome.html.
3. Cox, Brad. "Is Heat or Cold Worse for a Battery?" *The Charge*, 23 May 2016, thechargebyventev.com/heat-cold-worse-battery/.
4. "Heater Wire for Electric Blanket (for 1-Wire Type) | Products." *TOTOKU - TOTOKU ELECTRIC CO., LTD.*, www.totoku.com/products/heater/cat1/heater-wire-for-electric-blanket-for-1-wire-type.php.
5. "How Do Heated and Cooled Seats Work?" *Streetsville Hyundai*, www.streetsvillehyundai.com/faq/sales/how-do-heated-and-cooled-seats-work/.
6. "How Lithium-Ion Batteries Work." *HowStuffWorks*, HowStuffWorks, 14 Nov. 2006, electronics.howstuffworks.com/everyday-tech/lithium-ion-battery.htm.
7. "How to Make DIY Heated Insoles." *YouTube*, YouTube, 16 Dec. 2015, www.youtube.com/watch?v=SpJZ3bCi8d8.
8. Ingraham, Christopher. "Cold Temperatures Kill More Americans than Hot Ones, CDC Data Show." *The Washington Post*, WP Company, 17 Dec. 2016, www.washingtonpost.com/news/wonk/wp/2016/12/17/cold-temperatures-kill-more-americans-than-hot-ones-cdc-data-show/?utm_term=.79bddc91d36a.

9. “Make a Carbon Heated Blanket - DIY Crafts - Guidecentral.” *YouTube*, YouTube, 20 Apr. 2015, www.youtube.com/watch?v=T1GQRiGlocc.
10. “Our Tech.” *Blaze Wear Heated Clothing*, www.blazewear.com/blazeweartech.
11. Piddledigit. “12 Volt vs 24 Volt Solar Setup Pros and Cons.” *YouTube*, YouTube, 18 Aug. 2014, www.youtube.com/watch?v=UQeK5TrGijM.
12. “QuickStats: Number of Hypothermia-Related Deaths,* by Sex - National Vital Statistics System, United States,† 1999–2011§.” *Centers for Disease Control and Prevention*, Centers for Disease Control and Prevention, 4 Jan. 2013, www.cdc.gov/mmwr/preview/mmwrhtml/mm6151a6.htm.
13. Thompson, Dennis. “More Americans Dying From Hypothermia, CDC Says.” *Consumer HealthDay*, 19 Feb. 2015, consumer.healthday.com/environmental-health-information-12/environment-health-news-233/more-americans-dying-from-hypothermia-cdc-says-696679.html.
14. “Why Does the Nichrome Heat up?” *Current - Why Does the Nichrome Heat up? - Electrical Engineering Stack Exchange*, electronics.stackexchange.com/questions/67462/why-does-the-nichrome-heat-up.
15. “Why Does the Nichrome Heat up?” *Current - Why Does the Nichrome Heat up? - Electrical Engineering Stack Exchange*, electronics.stackexchange.com/questions/67462/why-does-the-nichrome-heat-up.
16. “Why Does the Nichrome Heat up?” *Current - Why Does the Nichrome Heat up? - Electrical Engineering Stack Exchange*, electronics.stackexchange.com/questions/67462/why-does-the-nichrome-heat-up.
17. “Why Does the Nichrome Heat up?” *Current - Why Does the Nichrome Heat up? - Electrical Engineering Stack Exchange*, electronics.stackexchange.com/questions/67462/why-does-the-nichrome-heat-up.
18. “Www.activheat.com.” *Battery Heated Clothing - How It Works | ActiVHeat*, www.activheat.com/Heated-Clothing-How-it-Works-s/87.htm.

Validation of Variable Star Photometry utilizing the Burrell Telescope

Student Researcher: Kyle S. Pellegrin

Advisor: Dr. Peter Hoekje

Baldwin Wallace University
Department of Physics and Astronomy

Abstract
This research project aims to prepare the Burrell Memorial Observatory telescope for use in studying variable stars with the intent of submitting collected data to the American Association of Variable Star Observers (AAVSO), while also laying the foundation for an observing program at the university. This will begin by quantifying the characteristics of the telescope and CCD camera system, as well as developing procedures for successful observations. A well-known variable star will then be studied by utilizing the technique of differential photometry, in order to ensure the results acquired are in agreement with the known variations of the star. After successful completion of these tasks, the observatory will then be ready to select a section of the AAVSO to work with, and begin acquiring data on current target variable stars for submission to the AAVSO.

Project Objectives
The goal of the project was to create an observing program at Baldwin Wallace University that would allow for the acquisition of data on variable stars. To achieve this goal, the university collaborated with the American Association of Variable Star Observers (AAVSO). The AAVSO provides guidelines and other resources for independent astronomers on how to collect astronomical data. The immediate objective is to calibrate the university's telescope and camera so that the data from here could be contributed to the AAVSO's database of observations.

The variable star Algol was chosen as a test case for verifying the equipment and procedures. Algol is a classic example of an eclipsing binary star, where two stars are orbiting each other in a system. The variability of Algol is caused by the dimmer star of the system moving in front of the brighter one. The net effect is that the binary system appears dimmer that when neither star is being blocked by its companion.

Observations were taken at the Burrell Memorial Observatory located on campus at Baldwin Wallace University in Berea, Ohio. The observatory is home to a 14-inch refracting telescope built in 1940 by Warner and Swasey. A unique aspect of the telescope is that due to its age, the telescope is completely manual with no computer controls available, which introduces some difficulty in data acquisition.

Methodology
The technique needed to study variable stars is known as differential photometry. By taking a picture of a standard star (whose brightness is known) and of a target star (whose brightness is not known) information is captured about how much light was received from each star. Knowing how much light from the standard star is in the picture, the light contribution from the target star can be calculated. Since stars emit light at all wavelengths, further refinement of these results is obtained by utilizing standard photometric filters to 'slice up' regions of the electromagnetic spectrum. This allows for each region of the electromagnetic spectrum to be measured more accurately than an unfiltered observation would permit.

Additionally, by measuring the brightness of standard stars though each photometric filter, and comparing it to the actual known brightness, the CCD camera's response to various wavelengths of light can be quantified. By conducting this procedure, a number called a transformation coefficient can be determined, which is utilized in the final calculation of standard magnitudes so that multiple observers can then directly compare their magnitude values with each other.

Error reduction occurs through a collection of calibration images. These images are effectively pictures of the sources of noise in the science image, and can be subtracted from the actual science image thus removing that sources contribution to the desired signal in the science image. Calibration images are comprised of flat fields, dark frames, and bias frames. The function of the flat field is to remove deviations in the light path due to the telescope's optics, as well as capturing any dust residing on optical surfaces. The dark frames capture the thermal noise caused by the operation of the electronics, and the bias image captures any defects in the CCD chip itself.

A typical observing session at the observatory begins with setting the telescopes position indicators to correspond with the current time and date. Next an eyepiece is placed into the telescope, and the target stars are found visually. The position indicators on the telescope is then marked for each target (usually a target star and a standard star), and then the telescope is set up for taking images. This corresponds to removing the eyepiece and attaching the CCD camera with a focal reducer to the telescope. Standard photometric filters are then inserted into the camera housing as needed. Once set up, images are taken of the target star and then of the standard star at regular intervals until the end of the observing session.

A set of images of star cluster M67 were taken in order to determine the transformation coefficients, and Algol was selected as the variable star that would be studied in order to test the procedures and equipment. As mentioned in the objectives section, Algol is an eclipsing binary type of variable star, and the minima's of Algol occur about every 2.38 days. This leads to the difficulty of not only having to have clear sky's for observing, but for clear weather to occur during a minimum as well as the minimum occurring during a time the star is above the horizon at night.

Results

The weather conditions during the research period comprised the largest limiting factor. The only minimum of Algol that was able to be measured occurred on January 18th 2018, and only half of the minimum was able to be captured due to clouds rolling in during the minimum. Figure 1 shows the data collected that night. It is important to note that the graph's data corresponds to average digital counts from the CCD camera over the entire image. These digital counts correspond to the amount of light each pixel received from the star. This dataset shows that utilizing the current procedures and equipment, it is possible to detect the variability of Algol, thus providing evidence that it is possible to then take measurements of other variable star targets successfully.

To determine the transformation coefficients, Images of M67 were taken with a B and V filter and then analyzed. The analysis required the measured brightness of standard stars in M67 to be compared to the actual brightness of the same star, provided by the AAVSO. A linear trend line was applied, and the slope of that trend line corresponds to the coefficient required, which was found to be -1.8515 for the B magnitude transform and -0.0358 for the V magnitude transform which can be seen in figures 2 and 3. The x-axis of both graphs is the AAVSO B filter magnitude minus the V filter magnitude, while the y-axis is the known magnitude (B or V) minus the measured magnitude through the same filter.

Throughout this research project, the procedures and resources utilized in gathering data were carefully documented and compiled into a user guide for future students. This included creating step-by-step how to sections for each of the aforementioned parts of this research, as well as providing insight into what was found to work well. With these results, the astronomy group at Baldwin Wallace University is now prepared to measure stellar magnitudes according to AAVSO guidelines for submission to their research database.

Figures and Charts

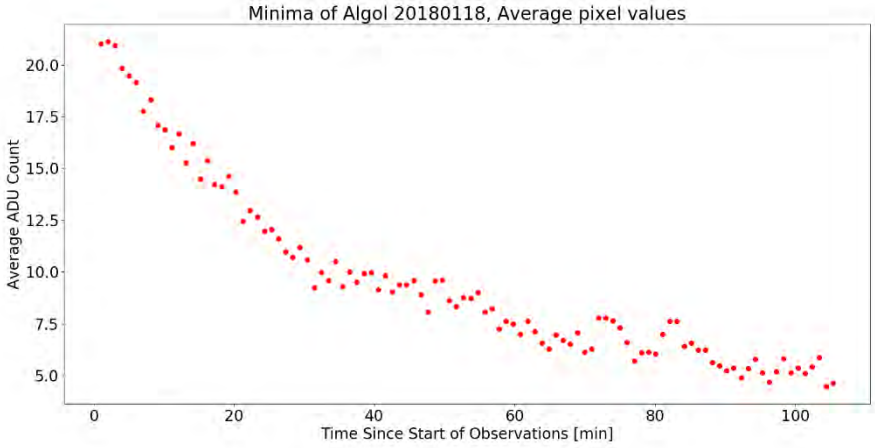

Figure 1. Minimum of Algol data from January 18, 2018

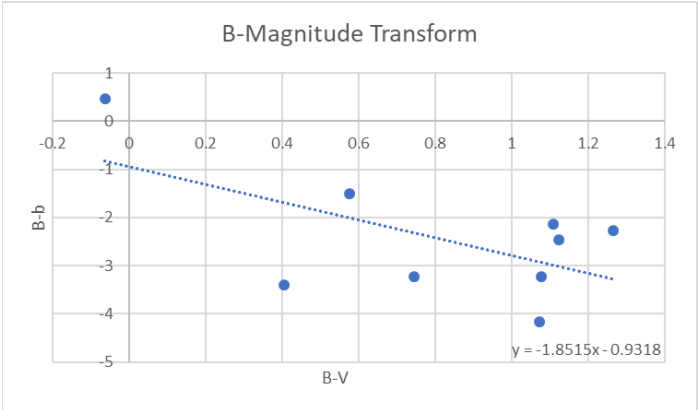

Figure 2. B-Magnitude Transform

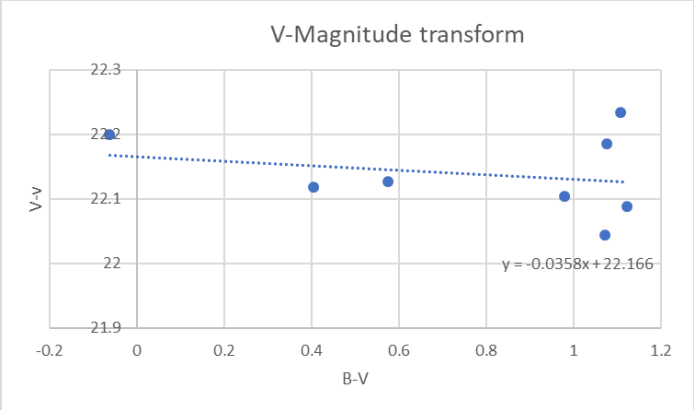

Figure 3. V-Magnitude Transform

Acknowledgments

The author of this paper would like to thank the Ohio Space Grant Consortium and the Ohio Aerospace Institute for this wonderful opportunity to conduct and present this research. They would also like to thank Dr. Peter Hoekje and Gary Kader for their support and insight with this project. Finally, they would like to thank senior physics major James Corkish for his assistance with compiling the student user guide.

References

1. "The AAVSO Guide to CCD Photometry." AAVSO.
2. "AstroImageJ." *AstroImageJ (AIJ) - ImageJ for Astronomy*, 3.2.0, University of Louisville, www.astro.louisville.edu/software/astroimagej/.
3. "AutoStar Suite." Meade Instruments, www.meade.com/support/downloads/software/.
4. Craig, Matthew, et al. "6.3. From Counts to Magnitudes." *6.3. From Counts to Magnitudes - ObsAstro 0.1 Documentation*, image-analysis.readthedocs.io/en/latest/06_photometry_intro/instrumental_mags_and_the_beauty_of_photometry.html.
5. King, Bob. "When Algol Winks, Will You Wink Back?" *Sky & Telescope*, Sky and Telescope, 19 Nov. 2014, www.skyandtelescope.com/observing/behold-algol-star-secret/.
6. *Meade Deep Sky Imager: The Basics*. Meade Instruments.

Incorporating STEM into ELA: Humans on Mars?

Student Researcher: Kristen E. Pierce

Advisor: Sean Thompson

The Ohio State University
Department of Teaching and Learning

Abstract

The goal of these lesson plans is to incorporate STEM education into an English Language Arts (ELA) classroom. Following Ohio's Common Core Standards, they will learn about informational and narrative writing, speech and listening skills, and various forms of technology. The topic of the project will be centered around NASA's space exploration plan to send humans to Mars and include topics such as spacesuits, shuttles, rovers, the history of human exploration, and fitness in space. Students will work in groups to create a transmedia storytelling poster that contains QR codes that link to an informational writing essay about their chosen topic, a narrative writing piece incorporating facts about Mars, a timeline, and an activity designed by NASA.

Learning Standards and Objectives

While this lesson can be adapted to incorporate Ohio Common Core Standards for ELA from other grade levels, the lessons were planned with the eighth grade standards in mind.

Ohio Common Core ELA Writing Standards 8.2, 8.3, 8.6, and 8.8

- **W.8.2:** Students will be able to synthesize their research into an informational paragraph that conveys relevant, well-chosen facts and concrete details.
- **W.8.3:** Students will be able to create a narrative of an imagined experience about traveling to Mars that incorporates relevant and factual descriptive details about Mars.
- **W.8.6:** Students will be able to publish their informational paragraph and narrative on Google Docs.
- **W.8.8:** Students will be able to gather relevant information about their topic from credible sources to be incorporated into their informational essay and narrative.
- **W.8.8:** Students will be able to develop a timeline that demonstrates the history of their chosen topic.

Ohio Common Core ELA Speaking and Learning Standards 8.1 and 8.5

- **SL.8.1:** Students will be able to work together towards a common goal of creating a transmedia poster.
- **SL.8.5:** Students will be able to construct a transmedia poster that displays all four pieces (informational essay, narrative, timeline, and activity) as QR codes in order to add interest.

Methodology

This project is student-centered, incorporates cooperative learning methods, and is culturally relevant. The unit starts off with the teacher presenting the requirements of the project. Student groups can be chosen by the teacher or chosen by the students. The five topics explained in this written report are spacesuits, shuttles/spaceships, rovers, history of human exploration, and fitness in space. The requirements of the project are an informational essay about a given topic, a narrative of an imagined experienced about going to Mars that incorporates factual information about Mars, a project/activity, and a timeline.

Students are given two to three class periods (a class period=48 minutes) to complete the two writing components of the project. A graphic organizer is provided for both types of writing that provides a visual of the things that need to be included. A mini-lesson can be given about credible vs non-credible sources as well as an overview of how to search Nasa.gov for resources to help students find relevant information.

The next lesson has students working on their activity, three to five class periods, and putting together their presentation of their activity. Each activity is different for each group. The spacesuits group is doing the "Suit Yourself" activity from *Exploring Space Through Math* series. This activity can be considered an enrichment activity for my eighth graders since the topics in the activity are Algebra 1 topics (a ninth grade level class). The way the Spacesuits group will present their information is through a lightboard video, which shows their work for their calculations. The Shuttles group will be putting together a paper model of Orion, which is a NASA educational resource titled "Orion Desktop Model." The History/Future of Human Exploration group will be making a 3D model of a human habitat of Mars and can use the NASA article titled, "Nine Real NASA Technologies Used in 'The Martian'" to help them come up with ideas for their model. The Rover group will be doing the "Rover Race" activity, which has students learning about how rovers receive signals from Earth and the challenges that come with that. The Fitness in Space group will be creating a fitness video using green screen technology (*Camtasia* or the *DoInk* app) that demonstrates exercises that astronauts do in space. They can use the "Train Like an Astronaut" video series to help give them ideas.

The fourth part is a timeline, which students create either using technology (Tiki-Toki is a good online resource) or by hand, that shows important events about their chosen topic. For example, the Spacesuits group will do a timeline about when spacesuits were created and when they were changed, while the History/Future of Human Exploration will have a timeline about when and where NASA sent humans to space and when and where NASA is planning to send people.

The final step would be to create a multimedia, interactive poster that should take 1 to 2 class periods to complete. The poster (which could be any size) includes a labeled QR code that links to each part of their project that is online. So, there will be one QR code for their informational essay and one for their narrative that links to the Google Docs location. They will also have one for their activity, that links either to a uploaded video (spacesuits, rovers, and fitness and space) or a photo (shuttles and history/future of human exploration) and one to their timeline. A QR code is like a barcode, but they link to a website url instead of a product. A QR code can be made for free online by doing a search for 'QR code generator.' The students can then decorate the poster as they see fit.

Results

This lesson was implemented into two different eighth grade ELA classrooms in an intercity middle school. The classes were mixed ability in English Language Arts from below grade level readers and writers to gifted and talented. The incorporation of math and science and the student-centered approach actively engaged nearly all of my students, including the ones who are not normally engaged in ELA. The posters and activities looked different in each group, but reflected the students' achievement of most of the learning objectives. Something that I could have done differently was incorporate more formative assessments during the project to assess students' ability to work collaboratively.

Acknowledgments and References

1. Dunbar, B. (n.d.). SUIT YOURSELF. Retrieved March, 2018, from https://www.nasa.gov/audience/foreducators/exploringmath/algebra1/Prob_SuitYourself_detail.html
2. Dunbar, B. (2013, January 04). Rover Races Activity. Retrieved March, 2018, from https://www.nasa.gov/audience/foreducators/topnav/materials/listbytype/Rover_Races_Activity.html
3. Fox, S. (2015, August 13). Nine Real NASA Technologies in 'The Martian'. Retrieved March, 2018, from https://www.nasa.gov/feature/nine-real-nasa-technologies-in-the-martian
4. Gushanas, T. (2015, February 06). Train Like an Astronaut. Retrieved March, 2018, from https://www.nasa.gov/audience/foreducators/trainlikeanastronaut/home/index.htm
5. Orion Desktop Model. (2016). Retrieved March, 2018, from https://www.nasa.gov/sites/default/files/atoms/files/2016_orion_desk_model.pdf

Digital Analysis of Manduca Sexta Wings for Micro Aerial Vehicle

Student Researcher: David B. Prigg

Advisors: Roger D. Quinn, Ph.D. and Kenneth C. Moses

Case Western Reserve University
Mechanical Engineering

Abstract
The development of small robotic moth drones would provide beneficial in search and rescue situations with rough terrain and tight spaces. In order to mimic the efficient flight mechanics of a moth, artificial wings must be designed to function similar to their biological counterpart. This report features digital methods of image processing through Matlab to measure and alter the makeup of Manduca Sexta wings. Templates are created for the manufacturing of artificial wings to mimic the properties when manufactured. These methods allow for quick, accurate and repeatable documentation of many wings to create a variety of templates with differing sizes and shapes.

Background
This project is a part of Kenneth C. Moses's Robo-Moth Ph.D. project. The overall goal of the project is to create a small efficient drone that could be used for search and rescue operations exceeding in hazardous or tight spaces. The micro aerial vehicle will be powered by a flapping mechanism driven by a DC motor. This propulsion system allows for some energy storage and energy efficient flight. One of the main reasons why the Manduca Sexta was choses, was due to its size and passive wing structure. Unlike bats, birds and other larger flying creatures, the hawkmoths wings are passive and feature simple actuation via two main muscles. Although the actuation of the hawkmoth wings is relatively simple, the wings motion is very complex. As the moth flaps its wings, the wing supinates, creating a vortex propelling the hawkmoth. This motion is due to the physical structure of the wing and is the primary interest of this project.

Project Objectives
The goal of this sub-project is to develop software to convert a biological hawkmoth wing to a manufacturable template with similar shape and properties as well as gather important parameters such as length, chord, area and centroid. Digitizing this process will make gathering many samples much quicker and more accurate as opposed to manually measuring and plotting small values.

Methodology Used
Wing Scans

The first step to digitizing the moth wings is to get high resolution scans of the wings. The wing specimens are extracted from the Hawkmoths and descaled. The wings are scanned with a known pixel density. The scanner used in this project had a resolution up to 12800 DPI (dots per inch). Figure 1 shows a sample scan of a Manduca Sexta forewing.

Figure 1. Manduca sexta forewing scan at 12800 DPI.

Image Processing

The color image from the scan is difficult to work with due to the gradient in color. Overall geometry such as the outline of the wing on the white background can be hard to trace. In order to make a robust program able to calculate our desired parameters, a black and white image is desired. Matlab's Image Processing Toolbox has built in functions to help with converting an RGB color image to a black and white (BW) image.

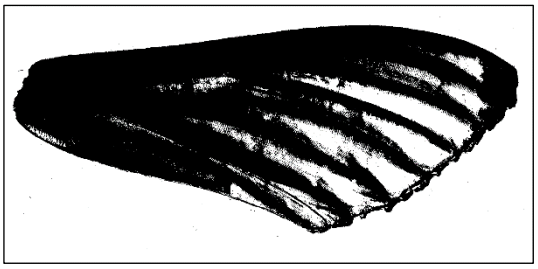

Figure 2. *im2bw* function with a threshold of 0.75.

Area Calculation

To compute the total area of the wing, a BW image contrasting the entire wing from the background is desired. This is achieved by using the Matlab function im2bw. This simple thresholding method could be used as the wing differs enough from the white background to get a reliable BW image depicted in Figure 2. The next step is to fill the holes with imfill, as seen in Figure 3. Now obtaining the area is simple by using Matlab's regionprops(BW,'Area') function.

Length / Chord Calculation

For the length of the image, the user clicks on the root of the wing then the tip. The distance between the two points is calculated and converted from pixels to inches using the DPI of the scanned image. The image is rotated so that the length is horizonal. The rotated image is converted to BW as discussed above. For our purposes, the chord is the maximum width of the wing perpendicular to the measured length line and is found by iterating through each column of the BW wing image and finding the maximum. These properties are stored in a Microsoft Excel document.

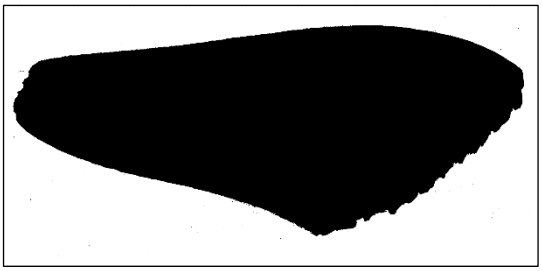

Figure 3. Wing image after *imfill* function.

Flexural Stiffness

For artificial wings to act the same under loads the mass properties as well as flexural stiffness must be similar to that of biological wings [1]. The veins were represented as concentric circles with the inner radius equal to 0.732 times the outer radius as an average [1]. The membrane was assumed to be of uniform thickness. The flexural stiffness of the membrane and veins are added separately and set equal to that of the manufactured design.

$$(E_m I_m)_R + (E_v I_v)_R = (E_m I_m)_M + (E_v I_v)_M$$

The membrane width and vein diameter is determined by a Matlab script. The total area should remain the same to insure the same forces on the wing due to air drag. Therefore, since the material properties of the moth and materials used are known, the only unknown is the width of the carbon fiber strip. These are then recorded for each column of pixels and compiled into a template as seen in Figure 4.

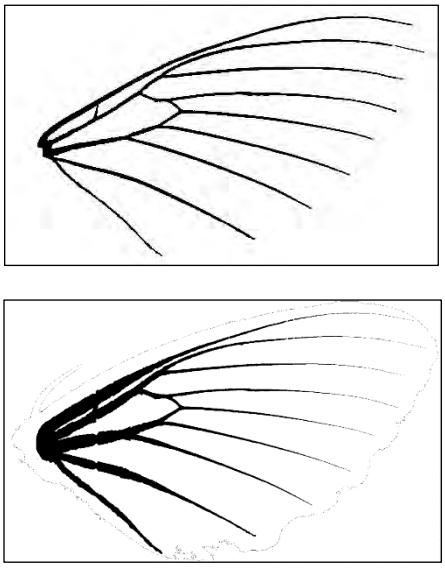

Figure 4. Biological vs Template

Results

Although the manufactured wings have yet to be produced from the templates, the process is promising. Using carbon fiber and mylar, a physically similar wing can be made. Further testing on these wings to determine how close they perform to their biological counterparts.

Reference

1. O'Hara R. P., "The characterization of material properties and structural dynamics of the Manduca sexta forewing for application to flapping wing micro air vehicles Department of Aeronautics and Astronautics Report (Air Force Institute of Technology, Wright-Patterson AFB, OH)", 2012.

Unprecedented Whiskey Flavors Created by a Novel Accelerated Pressure Aging Process

Student Researcher: Ryan A. Reffner

Advisors: Dr. Regan Silvestri, Dr. Leanna Ergin

Lorain County Community College
Science and Mathematics Division

Abstract

Our partners at Cleveland Whiskey use a unique, rapid pressurization process to accelerate the maturation of whiskey. Varying pressure of the bourbon allows traditional oak wood to absorb the bourbon like a sponge, and subsequent release of pressure forces the bourbon from the wood while carrying its unique flavor, a process which only takes a few days. This variable, rapid pressurization process allows for the use of other types of wood other than the traditional oak barrels, such as cherry, hickory, apple, maple, and honey locust which are not traditionally used to store whiskey, giving new experimental flavor compounds to the product. We identified these distinct flavor compounds using Gas Chromatography – Mass Spectrometry (GC-MS), and compare the uniquely processed whiskey to a traditional whiskey, whiskey with unique wood flavoring, and the raw distillate. The results of the GC-MS testing indicate similar compounds are present between the traditionally aged bourbon from a competitor brand and the pressure aged bourbon with the addition of steric acid with pressure aging. The use of cherry wood while pressure aging adds the unique flavor compound furanone which has a sweet, fruity, maple nuance, and ethyl octanoate, further sweetening the bourbon while lending additional creamy, waxy, cognac notes. The pressure aging process used on light oak aged bourbon loses ethyl hexanoate, while adding furfural, which has a woody, nutty, caramel nuance.

Project Objective

Use straight injection Gas Chromatography – Mass Spectrometry to identify and profile the chemical compounds which contribute to the flavoring of whiskey from the rapid pressure aging process used by our industry partners at Cleveland Whiskey, and compare the data to the flavor compounds found in traditionally aged whiskey, whiskey pressure aged with specialized wood, and raw distillate.

Results Obtained

Routine straight injection GC-MS results from different comparison tests between raw distillate, light oak aged, pressure aged, Black reserve, competitors' bourbon, and cherry bourbons.

Production of the pressure aged Black Reserve. (Left: Short Retention, Right: Long retention)

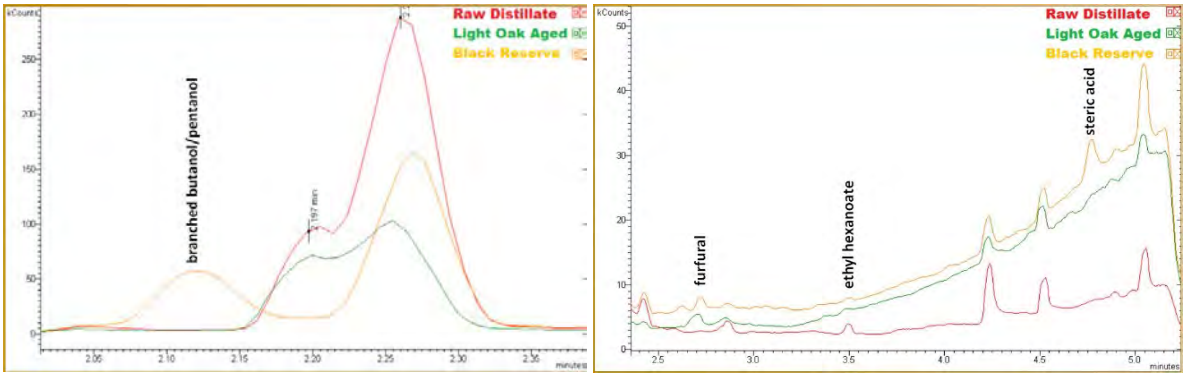

Initial light oak aging loses ethyl hexanoate, adds furfural. Further pressure aging adds steric acid and a branched long chain alcohol.

Comparison of pressure aged Black Reserve and traditionally aged competitor. (Left: Short Retention, Right: Long retention.

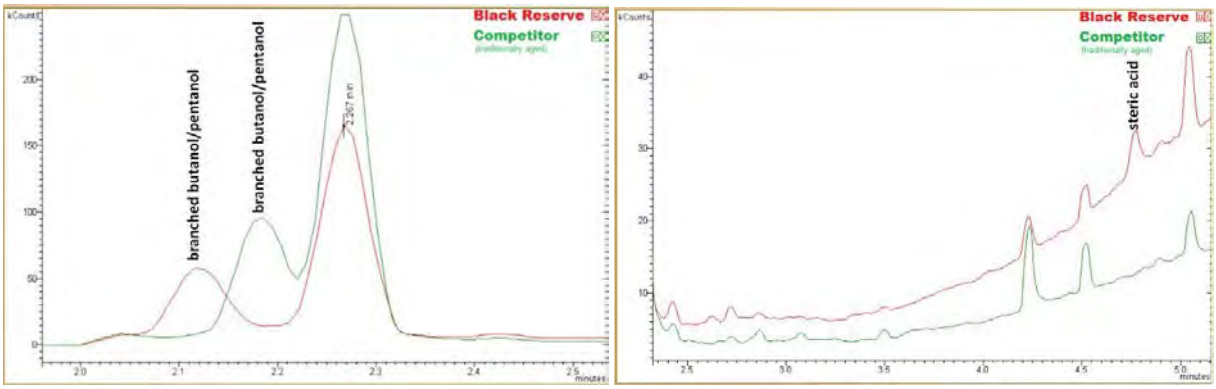

Black reserved is comparable to traditionally aged bourbons, with the addition of steric acid.

Comparison of pressure aged bourbon with Cherry wood and pressure aged Black Reserve. (Left: Short retention, Right: Long retention)

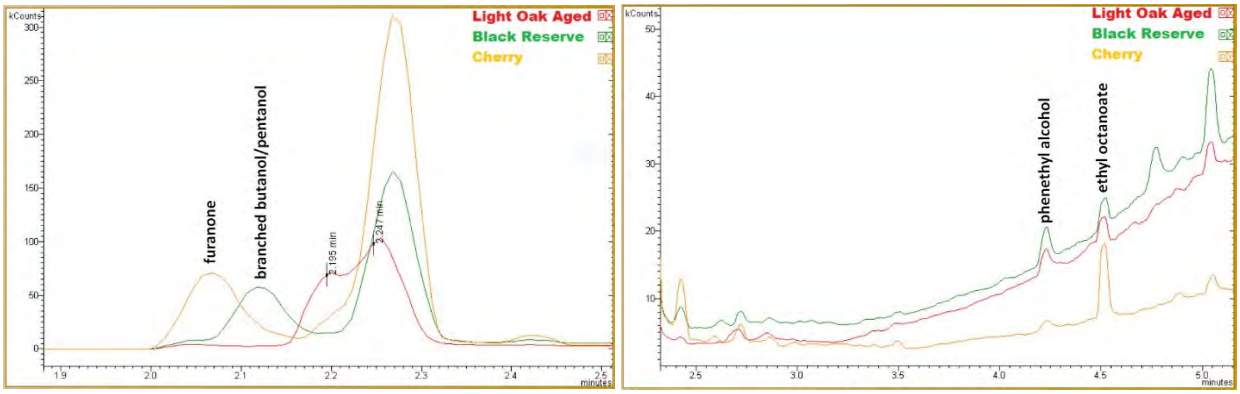

Pressure aging with cherry wood adds furanone and ethyl octanoate, whilst reducing phenethyl alcohol.

Interpretation of Results

Results indicate noticeable changes and additions of flavorful compounds in the unprecedented pressure aged whiskey products. Initial oak aging loses flavors found in ethyl hexanoate, while producing furfural, which adds the woody, sweet, caramel nuance. Comparison of the standard Black Reserve created through rapid pressure aging and a traditional competitors bourbon indicates a smaller difference with the addition of steric acid. The last set of tests compared the experimental cherry wood flavoring with the standard black reserve. These results indicated an addition of furanone with its sweet, fruity, maple note, and ethyl octanoate, which has a creamy, waxy, cognac nuance.

References

1. Silvestri, Regan. “Distilling Lessons From A Whiskey Research Program”, *inChemistry*, January 11, 2017.https://inchemistry.acs.org/content/inchemistry/en/acs-and-you/distilling-lessons-from-a-whiskey-research-program.html
2. *Ohio Academy of Science Newsletter.* Fall (Part II) 2017. Pages 1-2. https://static1.squarespace.com/static/545d32b5e4b0719cb5aae580/t/59f2380753450aa9d1360622/1509046281513/Fall+2017+Part+II.pdf

Mini-Excavator Modification

Student Researcher: Zachary D. Reser

Advisor: Professor Abigail Yee

Cincinnati State Technical and Community College
Mechanical Engineering Design

Multi-use hiking and biking trails are becoming more popular over time and the demand for these trails on both public and private land is increasing. Based on input from local trail builders in the Cincinnati area, a need for modifications of mini-excavators was discovered. Trail builders could increase their trail-building efficiency by taking a vibration plate compactor, or tamper, deep into the trails. However, mini-excavators do not have enough auxiliary power to use tampers as attachments, and standalone tampers are too heavy to push to the site. This research focuses on commonly used mini-excavators to determine the most feasible way to equip a mini-excavator with a tamper.

The John Deere 17G mini excavator was selected for its small size making it ideal for multi-use trail building. Important trail building properties of this excavator are a width of just over three feet, and a weight of 3790lbs. This short width and light weight allows trail builders to navigate the worksite while avoiding trees and causing minimal damage to the environment. It has a reach of up to 12'6" making it able to reach portions of the trail that may be too uneven for the excavator to safely traverse. The size and functionality of the John Deere 17G make it an ideal tool for creating multi-use trails.

With the auxiliary power being too low for a vibration plate compactor, a standalone push-style compactor must be retrofitted to the arm of a John Deere 17G mini excavator arm. In order to attach the compactor to the arm, a steel bracket will have to cut out to the shape of the quick connect that is standard to the John Deere mini excavators. There are 2 problems with attaching an excavator arm directly to a standalone tamper: (1) a solid connection between the arm and tamper can cause the arm to absorb most of the vibrations, which takes away from the effectiveness of the tamper, and has the possibility of causing damage to the excavator arm. (2) the force that the arm can put out can cause damage to the tamper. With no feedback in the controls, there is no way to feel whether the arm is putting too much force onto the tamper. These issues required the design of a quick connect adaptor with a hinge joint between the quick connect and the tamper. With a hinged joint, the excavator operator could lower the tamper to the ground without worrying about putting too much force onto it. The hinged joint would also ensure that the tamper sends most of its vibrations through the earth because the tamper will be operating with its own weight just as it would be as a stand-alone tamper pushed by hand.

The Wen Plate Compactor was selected due to its availability and its larger base plate. It's also gas powered so it would use the same fuel as other trail-building equipment. The compactor is capable of delivering up to 4496 lbs. of force up to 5400 times per minute.

With the demand for trail building equipment on the rise, there will be a need for modification until more commercial solutions are developed.

Enhanced Concussion Recovery Prognosis with Deep Neural Networks: Proof-of-Concept for Decision Support

Student Researcher: Nathaniel L. Richards

Advisor: Dr. Kelly Cohen

University of Cincinnati
Aerospace Engineering and Engineering Mechanics

Abstract
Physicians currently do not have standardized methodologies or models to predict time-to-recovery for pediatric concussion patients. Such predictive models would aid physicians in predicting long-term effects and help influence proactive, rather than reactive, treatment strategies. This research explores the training of a Deep Neural Network (DNN) model to predict the number of days from initial concussion injury to return to play clearance ("Days Out") from each patient's self-reported injury profile, pre- and post-concussion symptoms and history. Modern training techniques (e.g. dropout regularization, learning rate scheduling, adaptive optimizers) prevent the network from overfitting the training data and yield acceptable performance on the test cases. The DNN is a more accurate predictor of Days Out than four traditional regression methods, including both linear and nonlinear algorithms.

Introduction and Objectives
Up to 3.8 million sports and recreation related concussions are diagnosed annually, with children accounting for over 800,000 of these injuries and over $100 million in direct medical costs.[1,2] Children may exhibit longer durations of post-concussion symptoms than adults,[3,4] and recovery times are difficult to predict. Zonfrillo et. al. highlight the lack of standardized procedures for diagnosis and prognosis for pediatric concussion care.[5] The authors also issue a call for decision support tools to aid physicians in the post-concussion treatment process. This research responds to that call by delivering a proof-of-concept model to predict time-to-recovery for pediatric concussion patients from electronic medical record data.

Standardized Concussion Information
The Division of Sports Medicine at Cincinnati Children's Hospital has developed the *New Head Injury Questionnaire* (NHIQ): a standardized set of forms that are used to obtain standardized information from pediatric patients with suspected head injuries. Included within these forms is the *Post-Concussion Symptom Inventory* (PCSI),[6,7] a standardized questionnaire with pre- and post-concussion self-reported symptoms (e.g., headache, fatigue, dizziness)—along with general questions about the head injury and the patient's medical history. Thus, at the completion of the NHIQ the physicians have a patient concussion profile that is used to inform treatment strategies.

The NHIQ was constructed based on physician heuristics for optimizing relevant information to aid in concussion prognosis and the development of treatment plans. However, current concussion treatment is based on a "one size fits all" approach. That is, the same treatment plan is implemented for every patient, and more aggressive treatment strategies are utilized only when a patient's symptoms are not subsiding following up to a week of standardized care. The current project is designed to support a precision medicine based approach to concussion treatment. Specifically, the development of a predictive model of concussion recovery can support physicians in the development of personalized

treatment plans to improve recovery times through targeted interventions earlier in the recovery timeline.

Physicians must consolidate a multitude of patient-specific variables and then combine them with their own practical knowledge for the development of meaningful concussion treatment plans. The NHIQ forms and PCSI tests yield a large number of factors (>10) that physicians must weigh in order to provide treatment; adding other potential predictive factors only increases the complexity of the problem at hand. Research approaches that only consider a single factor cannot capture the complex interactions between multiple factors and thus lead to less accurate predictions of recovery times. Thus, multivariate regression models are needed to assist physicians in predicting recovery times from all of the available potential predictors.

Advanced Decision Support Tool

Neural networks, a set of layered linear algebra operations that loosely model the human brain, exhibit desirable characteristics for this multivariate prediction problem. The potential predictive factors include a heterogeneous combination of variable types; neural networks can accept this combination, while some regression algorithms cannot or perform poorly. Recent improvements in computational power allow the neural networks to scale with an increasing number of input features and increased model complexity and predictive power.

Deep Neural Networks (DNNs)—networks with more than one hidden layer—are modern, more powerful networks and can take on a variety of architectures (e.g. feedforward, recurrent, convolutional). DNNs have been successfully applied to prediction, image classification, and speech recognition tasks.[8] The model trained for this research is a traditional feedforward architecture applied to a regression problem; modern advances in training recurrent and convolutional architectures can also be applied to feedforward networks. The methodology section details key differences in traditional and modern techniques for training such networks.

The DNN models trained will provide physicians with recovery time predictions for new concussion cases, using data collected from the NHIQ forms and PCSI tests. This process can be automated and combined with electronic medical records (EMR) into a easy-to-use tool to aid treatment decisions and recovery prognosis. Further, the models can be retrained on new data as more concussion patients are evaluated and treated, potentially leading to more accurate estimates.

Methodology

The dataset includes the pre- and post-concussion information of 29 patients and the number of days ("Days Out") from injury until they were released to unrestricted activity by the same physician—i.e., the total recovery time. The input features include a mixture of continuous (real-valued), integer, ordinal, and binary variables. The continuous and integer variables include age, days out from initial injury, and the four Standardized PCSI scores for the physical, cognitive, emotional, and fatigue subscale scores. Ordinal variables include pain intensity, pain frequency, and pain duration following the injury, along with the patient's baseline academic performance. Binary variables include whether the athlete completed the sport contest following the injury, whether the athlete lost consciousness, suffered anterograde or retrograde amnesia, if head pain following the injury worsens with activity, and whether the patient was on ADHD medication at the time of injury.

Data Preprocessing

To test the generalization performance of the regression algorithms, the data was split into a training set (80%) and a test set (20%). Because this dataset is quite small (only 29 samples), random sampling of the 80/20 split has the potential to introduce significant sampling bias, where the resulting distribution of the train and test sets are significantly different than that of the original dataset.[9] To combat this sampling bias, the concept of Stratified Splitting is borrowed from classification problems and applied to this regression problem. Stratified Splitting performs the 80/20 split such that the resulting distributions of the train/test splits, shown in Figure 1, closely match the original dataset for the single output variable, "Days Out."

Each variable was normalized to reduce the effects of different scales and variances between variables. Binary variables were converted to [-1, 1], and ordinal variables were converted to evenly-spaced bins on [-1, 1]. Continuous variables were normalized by a z-score transformation, resulting in zero mean and unit standard deviation. Both the train and test sets were normalized by the mean and standard deviation of the train set – otherwise, there would be information leakage from the test set to the train set.

Traditional Regression Algorithms

Four traditional regression algorithms were used to baseline the performance of the neural network model: Linear Regression, LASSO, Support Vector Regression, and K-Nearest Neighbor Regression. Traditional Linear Regression attempts to find regression coefficients and a bias term to minimize the loss function. Least absolute shrinkage and selection operator (LASSO) is similar to linear regression but penalizes the absolute value of the regression coefficients; this penalty drives some of the weights to zero, effectively performing input feature selection. Support Vector Regression (SVR) utilizes radial basis kernel functions to perform nonlinear multivariate regression. Finally, K-Nearest Neighbor (KNN) Regression, where k=3 for this research, identifies the three nearest neighbors to a sample point in the input space and performs a weighted average of the output variable, where the neighbor weights are inversely proportional to the Euclidean distance from the sample point.

Loss Function

The root-mean-square error (RMSE) loss function was used to compare all of the traditional regression algorithms and the neural network performance. The RMSE performance of an algorithm can be interpreted as the standard deviation of the prediction from the true value. For example, an RMSE of 15 days means the prediction will be within ±15 days of the true value for 68% of the samples; the prediction will be within ±30 days of the true value for 95% of the samples, and within ±45 days for 99% of the samples.

Deep Neural Network Training

The hyperparameters of a neural network define its architecture (layer width, depth) and tuning process. The depth of the network defines the number of hidden layers; the width of the network defines the number of neurons within each hidden layer. The network trained for this research consisted of four hidden layers with sizes 512, 256, 128, and 64 neurons, respectively. Figure 2 visualizes the four-layer feedforward architecture of the DNN**.** Modern neural networks have moved away from sigmoid and hyperbolic tangent activation functions used in the hidden layers; the Rectified Linear Unit (ReLU) has been empirically shown to perform better in deeper networks.[10] The DNN trained in this research uses a variant of ReLU called the "Leaky ReLU," which has a small negative slope for inputs less than zero, whereas the ReLU has a slope of zero for inputs less than zero.

Hand-tuning such networks is an iterative process, where the size of the model (width, depth) is increased until the model overfits the training set. Then, regularization strategies are applied to reduce overfitting and improve generalization performance on the test set. Traditional regularization strategies include limiting the number of neurons per layer and adding a weight penalty. For this model, the L2 penalty was kept to a small scalar (1e-8). However, more modern techniques, including "dropout regularization," are more effective at improving test set generalization.[11] Dropout randomly turns hidden layer neurons off (with probability = 0.4) during training, which forces the neurons and weights to build redundant connections and learn patterns (i.e. generalize), rather than memorize training samples (i.e. overfit).

The ADAM optimization algorithm,[12] a form of stochastic gradient descent with adaptive learning rates, was used as the optimizer for tuning the model's weights and biases. The network was trained for 2000 full passes through the training set, known as epochs. The base learning rate for ADAM was changed during epochs [0, 1000] using a cosine annealing schedule,[13] decreasing from 0.01 to 0.005, as the right plot of Figure 3. shows. During epochs [1000, 2000], the learning rate was kept constant at 0.005. The network construction, regularization strategies, optimizers, and learning rate scheduling are all implemented in the PyTorch Python package.[14]

Results and Discussion

The limited number of training samples requires larger learning rates in order to escape local minima. Some minima yield low training RMSE but poor test performance. The left plot in Figure 3. shows the train and test RMSE scores over the 2000 training epochs. The apparent large variance in both signals is due to the stochastic nature of the optimizer, the large learning rate, and the small number of samples in the dataset. The resulting time histories show the optimizer attempting to find local minima that perform well on the training set while preventing overfitting, allowing those minima to generalize to the test set as well.

Successful Generalization Strategies

Dropout regularization is the largest contributor to acceptable generalization performance – without it, the model, with over 180,000 parameters, would catastrophically overfit and yield poor test set performance. The model never exhibits acceptable test performance when only traditional L2 regularization are applied. Dropout (p=0.4), applied to all four hidden layers, forces the model to build redundant and robust connections between layers, and subsequently learn the underlying patterns in the data. Smaller dropout probabilities ($p<0.3$) do not provide enough regularization and the model overfits to the training set. Conversely, the network is too restricted and does not converge on either the training or test sets with dropout probabilities that are too high ($p>0.6$).

Learning rate scheduling with restarts was also investigated; this strategy of restarting the cosine half-wave after a fixed number of epochs has been applied successfully to other domains.[13] For this research, resetting the learning rate to a high value resulted in improved training performance at the cost of generalization; therefore, a simple annealing schedule with no restarts was found to yield better train and test performance.

Generalization Performance Comparison

Table 1. presents the train RMSE, test RMSE, and Days Out predictions of all five regression algorithms. The true Days Out values for the six test cases are presented and span a wide range—[9, 55] days. The nonlinear regression algorithms (e.g. SVR, KNN, DNN) exhibit the capability to overfit and yield low train

RMSE scores. Conversely, the linear methods (e.g. Linear Regression, LASSO) have limited expressive power and exhibit unacceptably high train RMSE scores.

Linear Regression catastrophically fails to generalize to the test set with an RMSE of over 50 days, and it even predicts negative days out for some test cases. Interestingly, LASSO performs quite well on the test set with an RMSE of about 9 days. The algorithm even gives insight on which input features contributed to optimization; LASSO drives the regression coefficients of the unimportant features to zero. However, LASSO still performs poorly on the training set and cannot capture underlying nonlinearities in the data.

Inspecting the predictions for individual test cases, the DNN predicts about 12 days for both of the 9-day cases; the other algorithms have completely disparate predictions for the two cases. The predictions of all regression algorithms, including the DNN, degrades as the number of Days Out increased. The distribution of Days Out is significantly skewed towards fewer days, as shown in Figure 1. With only ten training samples in the middle and right bins combined, the algorithms do not generalize as well to predicting higher Days Out compared to lower Days Out.

The predictions by the DNN model yield a train RMSE of 3.53 days and a test RMSE of 8.31 days. The DNN model best learned the patterns in the data and outperforms the other algorithms by simultaneously scoring both low train and test RMSE, whereas the other algorithms perform well on one of the sets or diverge altogether. As a result of effective regularization, the DNN did not excessively overfit the training set. This allowed for the test RMSE to be closer to the train RMSE – an indicator of generalization.

Impacts and Future Work

The current standard for in-clinic concussion care forces physicians into a *reactive*, one-size-fits-all approach to treatment that increases patient burden throughout recovery. Thus, there is an urgent need to develop tools that will empower physicians to be proactive in their treatment strategies for patients following concussion. The results of this project provide a proof-of-concept tool, based on DNN, as a first step toward the realization of a precision medicine approach to concussion treatment. The 8.31 days test RMSE provides a promising baseline on a relatively small dataset. With more data, the training procedure is likely to have more reliable convergence and improved training and test performance.

Current efforts are underway to pull over 800 additional cases from electronic medical records to further refine and train the existing DNN model. Further experiments will include intelligent feature selection and dimensionality reduction; factor analysis may indicate which features are most predictive and which features may just be noise. This is a critical step necessary to motivate physician adoption for clinical care. In addition, comparisons will be made across a variety of machine learning approaches in an attempt to balance prediction accuracy with varying levels of model interpretability.

Figures

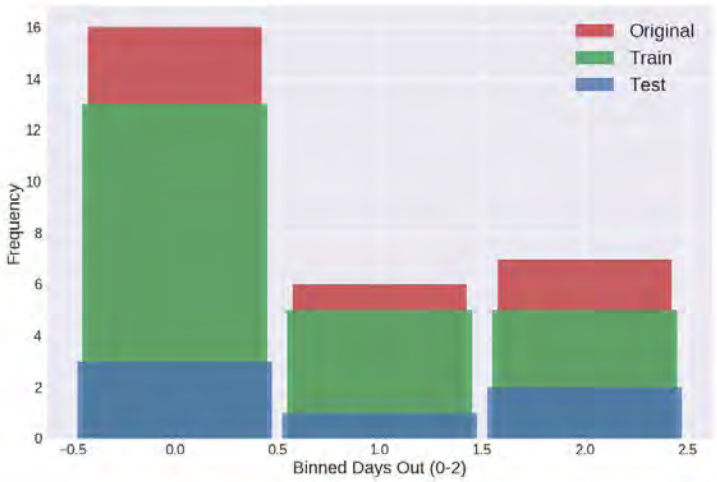

Figure 1. Stratified Splitting of train and test sets.

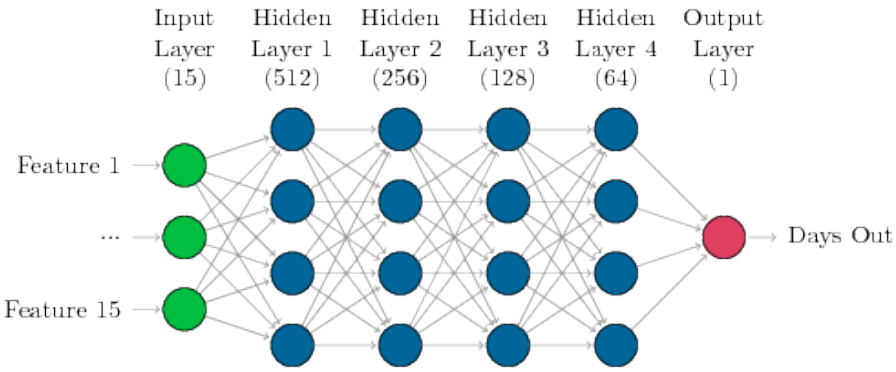

Figure 2. Four-layer, feedforward DNN model for regression.

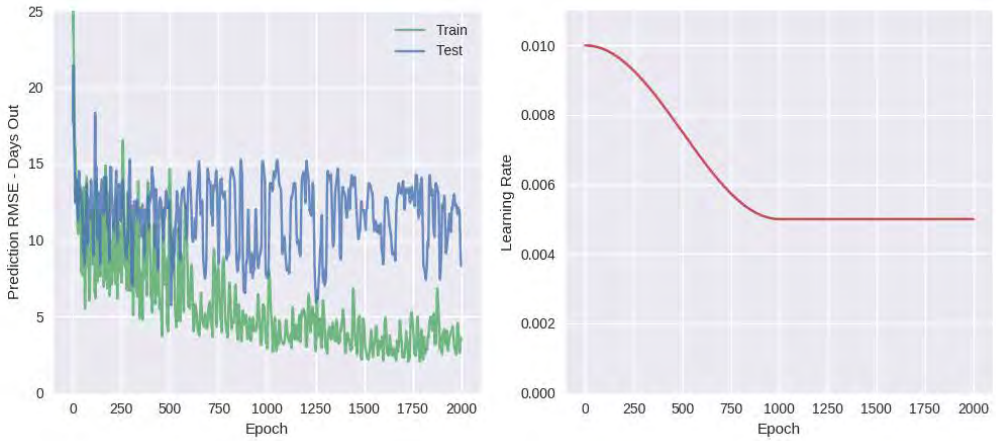

Figure 3. DNN train/test performance and learning rate during training.

Table 1. Generalization performance comparison of regression algorithms.

	Predicted Days Out					
	Linear Reg.	LASSO	SVR	KNN	**DNN**	True Days Out
Test 1	29.93	2.82	12.88	11.79	**12.62**	9.00
Test 2	58.24	24.63	39.13	51.27	**41.42**	34.00
Test 3	103.68	40.42	43.14	40.99	**54.26**	45.00
Test 4	38.89	39.20	27.20	30.44	**39.24**	55.00
Test 5	0.49	18.88	29.54	28.13	**12.23**	9.00
Test 6	-93.97	20.39	24.71	38.80	**19.34**	18.00
Train RMSE	14.23	18.38	2.48	7.75E-07	**3.53**	
Test RMSE	53.75	9.13	14.63	16.95	**8.31**	

Acknowledgments

I would like to thank the Ohio Space Grant Consortium for supporting my graduate studies and this research. Many thanks to Adam Kiefer, PhD, Gregory Walker, MD, Emma Klug, Christy Reed and Jackson Elpers at Cincinnati Children's Hospital for preparing the data and providing valuable insights. Most of all, I would like to thank Professor Kelly Cohen for supporting my academic, personal, and professional development throughout my undergraduate and graduate careers.

References

1. Rivara FP. Sports-related concussions in youth. *Journal of the American Medical Association. 2013.* https://doi.org/10.1001/jama.2013.282985.
2. Colvin JD, Thurm C, Pate BM., Newland JG, Hall M, Meehan WP. Diagnosis and acute management of patients with concussion at children's hospitals. *Archives of Disease in Childhood*. 2013. https://doi.org/10.1136/archdischild-2012-303588.
3. Giza CC, Hovda DA. The neurometabolic cascade of concussion. *Journal of Athletic Training.* 2001;36:228-35.
4. Field M, Collins MW, Lovell MR, Maroon J. Does age play a role in recovery from sports-related concussion? A comparison of high school and collegiate athletes. *Journal of Pediatrics.* 2003;142:546-53.
5. Zonfrillo M, Master C, Grady M, et. al. Pediatric providers' self-reported knowledge, practices, and attitudes about concussion. *Journal of Pediatrics*. 2012;130(6):1120-1125.
6. Gioia G, Janusz J, Isquith P, et al. Psychometric properties of the parent and teacher post-concussion symptom inventory (PCSI) for children and adolescents. J Int Neuropsych Soc 2008;14(Suppl 1):204
7. Schneider J, Gioia G. Psychometric properties of the Post-Concussion Symptom Inventory (PCSI) in school age children. Dev Neurorehabil 2007;10:282..
8. *Advances in Neural Information Processing Systems 30*. 2017
9. Geron A. Hands-on machine learning with Scikit-Learn and TensorFlow. *O'Reilly Media*. 2017.
10. Ramachandran P, Zoph B, Le, QV. Searching for activation functions. *arXiv preprint.* ArXiv:1710.05941, 2017.
11. Srivastava N, Hinton G, Krizhevsky A, Sutskever I, Salakhutdinov R. Dropout: A simple way to prevent neural networks from overfitting. *Journal of Machine Learning Research.* 2014;15:1929-1958.
12. Kingma D, Adam BJ. A method for stochastic optimization. *arXiv preprint.* arXiv:1412.6980, 2014.
13. Loshchilov I, Hutter F. SGDR: Stochastic gradient descent with warm restarts. *arXiv preprint.* ArXiv:1608.03983, 2016.
14. PyTorch: Tensors and dynamic neural networks in Python with strong GPU acceleration. PyTorch website. http://pytorch.org/. Accessed March 16, 2018.

Building a Better Model: The Solar System

Student Researcher: Kaycie R. Riley

Academic Advisor: Dr. Todd Edwards

Miami University
Mathematics Education Department

Abstract

This project reinforces the circle theorems of geometry, inequalities and their constraints, and writing equations with two or more variables in an introductory geometry course. Students engage in the construction of a scaled replica of the solar system over a week-long period. Through a series of scaffolded experiences, students develop more complex models than typically explored in the high school curriculum. Students employ a cross-disciplinary approach in their model building---integrating science and mathematics with technology--- as they collect and analyze data from NASA websites; build mathematical equations from distance data; and construct digital models using DESMOS, a freely available online calculation and visualization tool. The model construction brings content alive for students and serves as an alternative assessment of their understanding, actively engaging learners in ways that are difficult---nay impossible--- with traditional, paper-and-pencil tests.

Students begin their work with https://solarsystem.nasa.gov/ as they gather information about objects within the solar system and compare planet data. As students progress through the lesson, they process and enter scaled data into DESMOS to build a digital model. This work is non-trivial and addresses a variety of Common Core State Standards for Mathematics (CCSSM). For instance, students manipulate circle equations to model planets, use scaled distances to position circle centers, and shade using inequalities. Knowledge of inequalities and similarity is a prerequisite for this work. At the end of the project, students write up their process and reasoning in detail, compare solar systems while discussing problems and errors they encountered along the way, as well as possible project extensions and areas for future research.

Standards Involved

CCSS.MATH.CONTENT.HSA.CED.A.3
Represent constraints by equations or inequalities, and by systems of equations and/or inequalities, and interpret solutions as viable or nonviable options in a modeling context
CCSS.MATH.CONTENT.HSG.C.A.1
Prove that all circles are similar
CCSS.MATH.CONTENT.HSA.CED.A.2
Create equations in two or more variables to represent relationships between quantities; graph equations on coordinate axes with labels and scales.

Rationale and Required Materials

This project is designed as an alternative to a quiz or test assessing student understanding of circle equations. It also serves as a review of proportions, size-change transformation and scaling, and circle theorems (e.g., all circles are similar). Students use technology as they build scaled models that are more scientifically and mathematically accurate than those constructed with foam balls or other hands-on materials. Students write up their research, detailing the mathematics they employed along with a link to their online model. The project culminates with a whole-group conversation of common mistakes, different approaches, and project extensions.

Students will need the following materials to complete the project:

- Calculator
- Paper
- Pencil
- Computer (or handheld device) with internet access

Project Process

Day 1. The project begins with an introduction to the solar system and its magnitude. Students explore the NASA website and its various resources. The guidelines of the project are then discussed along with a demonstration of the graphing capabilities of DESMOS. At the end of class and for homework, students review ratios, inequalities, and circle theorems (particularly with regards to circle similarities).

Day 2. Students explore the NASA solar system website in more detail. In particular, they search for data relevant to the project and consider strategies for modeling the solar system to scale within the DESMOS environment. Students begin to scale the data into graphable numbers. This step requires students to keep track of their data and mathematical processes in a clear and organized manner, as the quantity and length of the numbers can become confusing if work is unclear. Students write circle inequalities for each planet in our solar system. Figure 1 illustrates several planet equations in DESMOS.

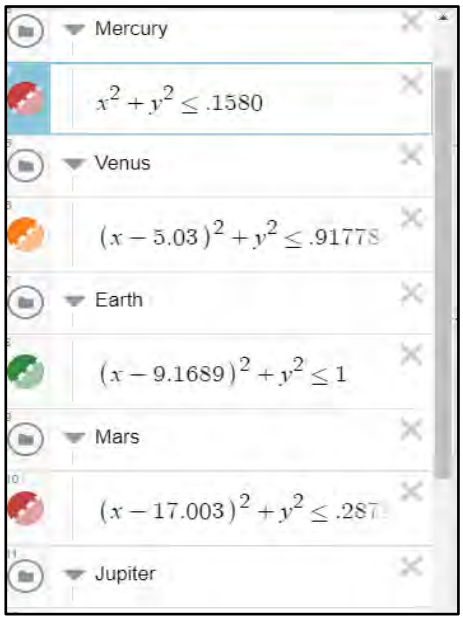

Figure 1. Equations for planets in DESMOS graphing environment.

In Figure 1, the equation for Venus is as follows:$(x-5.03)^2+y^2\le .91778$

Note that -5.03 shifts Venus the scaled distance away from Mercury (centered at the origin). The parameter .91778 is the scaled r^2value for Venus. Figure 2 illustrates the model generated by the inequalities in Figure 1.

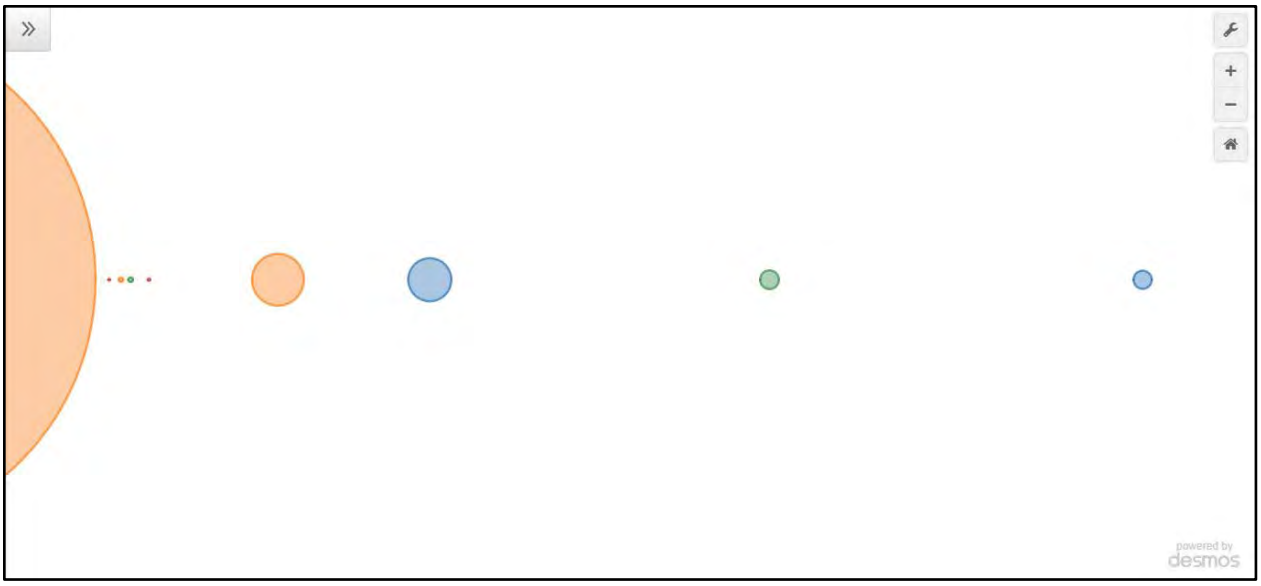

Figure 2. Solar system model in DESMOS generated by inequalities in Figure 1.
Figure 2 illustrates a completed model in DESMOS, with planets and the distances between them scaled to size. Note that the sun is only partially shown. This allows all planets to be visible on a standard computer screen. Students provide a link to their graph.

Day 3. Students work individually and in small peer-editing teams to write a 1-2 page paper that documents and summarizes the mathematics they employed in their modeling work.

Day 4. Students turn in their work and discuss their processes as they compare their models linked on a class website. To close out the project, students engage in a conversation over common errors, misconceptions and extensions.

Possible Extensions

Students engage in an open-ended brainstorming session on Day 5, considering ways to extend the project. This is a crucial part of the project, as it encourages students to think critically about the mathematics they employed and other aspects of the solar system that were not addressed in their work. One area of possible extension involves modeling the orbits of the planets with circles or ellipses. A sample of circular orbits in DESMOS is shown in Figure 3.

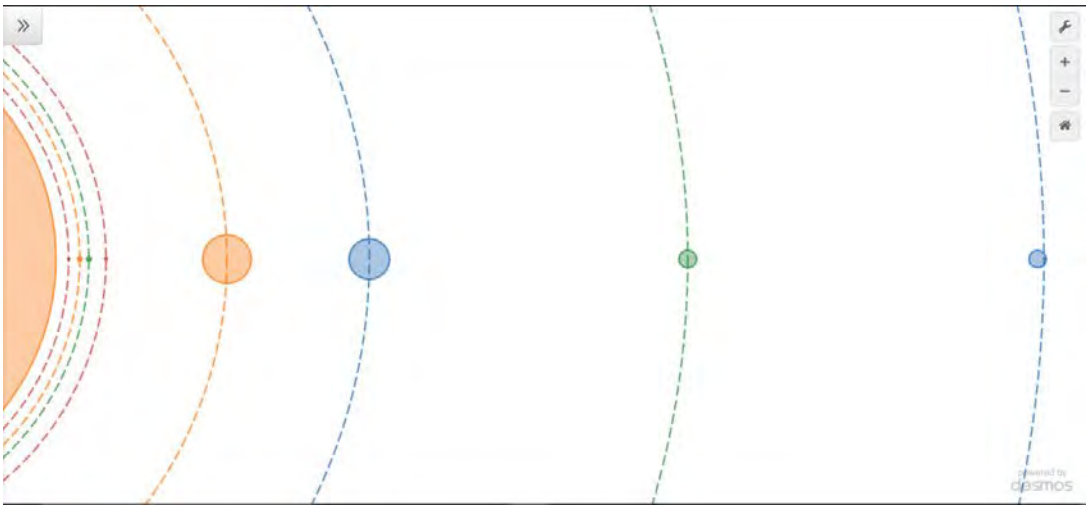

Figure 3. An example of ideal orbital patterns in DESMOS

The circular paths are not accurate since planets have elliptical orbits. However, within the context of the project, students may find it interesting to examine the orbital paths as circles. These pathways can be drawn in DESMOS using an r^2value equivalent to *the scaled radius of the sun + scaled distance between planet and sun*. Due to calculator constraints, this equation becomes less accurate the further the planet is from the sun. The round-off error involved in computer-based models is a topic for further discussion while visual representations of planetary orbits provide the impetus for discussions of animation within the software (using tools such as sliders).

Final Thoughts

This project includes a review into circle theorems, inequalities, and ratios, and gives students a chance to creatively use their math skills to build an accurate model of a familiar concept. Additionally, the students use real life data and explore the NASA website to gain new understanding of old topics. This project also allows for cross-disciplinary collaboration between science and math classrooms. Students will tie their knowledge of math to their knowledge of the solar system and will have a more in-depth understanding of how to create equations, as well as learning how to use a new technological resource.

Characterization of sand grains of the Tensleep Sandstone (Pennsylvanian-Permian), Wyoming, USA

Student Researcher: Sarah C. Rouse

Advisor: Dr. John Whitmore

Cedarville University
Science and Math Department

Abstract
The Tensleep Sandstone, a Pennsylvanian-Permian oil-bearing formation that outcrops in the Bighorn Mountains of north-central Wyoming, has attracted much research relevant to oil production. Few previous studies, however, have provided a detailed quantitative description of the Tensleep's petrographic characteristics. This project aims to analyze grain size, sorting, composition, and porosity through the study of thin sections and hand samples taken from four Tensleep outcrops. The results of thin section analysis are compared with results from other methods, including laser diffraction and image processing. Additionally, the Tensleep Sandstone and the similar Coconino Sandstone (Permian) of Arizona are stated to be equivalents. This project's research is compared to corresponding Coconino data in order to provide an initial statistical correlation of the textural and compositional natures of these widespread sandstones.

Project Objectives
The goal of this project is to characterize the sand grains that constitute the Tensleep Sandstone. Grain size, sorting, composition, and porosity will be obtained through the study of samples that were collected near the Bighorn Mountains of Wyoming by Dr. John Whitmore (Figure1). These measurements can then be compared with other methods, as well as with the characteristics of the Coconino Sandstone, an equivalent to the Tensleep that appears in the Grand Canyon (Figure 2). The results of the comparison may provide insight into the Tensleep's relation to other widespread deposits of the same age.

Methodology
Materials studied include 28 hand samples collected from four different outcrops as well as the thin sections made from each sample. 21 thin sections are studied in detail as Tensleep samples, while the remaining 7 were taken from units directly above and below the Tensleep for context. The data obtained is compared to data from the Coconino Sandstone that was gathered in a similar manner by Dr. Whitmore (2014). Equipment includes a Nikon Eclipse 50i Pol microscope with the Br software package for direct measurement of the grains. The necessary statistical analysis can be performed either within the software or by exporting the data to Microsoft Excel or IBM SPSS. The procedure involves systematically examining carefully selected regions of each thin section, generally at 100x magnification. Grain size and sorting are calculated by measuring the long axes of every grain in the selected regions, while composition and porosity are estimated by recording the presence or absence of minerals at regularly spaced points across the regions. At least 300 grains per slide are examined in this way. Raw measurements are evaluated according to the guidelines proposed by Johnson (1994). Composition and porosity are calculated as percentages for straightforward comparison to Coconino data. For comparison, the hand samples corresponding to the thin sections were disaggregated for particle size analysis, performed by Sarah Maithel of Loma Linda University. Images of thin sections were also processed with MatLab as an alternative method for determining porosity.

Results Obtained

Grain size data from each location are summarized in a histogram, as in Figure 3. This allows for visual comparison with the results of particle size analysis, shown in Figure 4. An examination of mean grain size from both methods suggests that a simple correction factor could be applied, as the difference between the two is small and consistent (Figure 5). Comparison between the point counting and image processing methods of determining porosity is less conclusive (Figure 6), suggesting that one or both methods are less reliable. When grain size and sorting are plotted against each other, Coconino and Tensleep data appear to correlate well (Figure 7). Additionally, the overall compositions of these sandstones is very similar, particularly in quartz content and porosity (Figure 8). Therefore, based on comparison on a microscopic scale, the Coconino and Tensleep sandstones indeed seem to be equivalent.

Acknowledgements

The author would like to thank Dr. John Whitmore for advising this project as well as for providing materials and Coconino Sandstone data. Dr. Lindsey McCarty and Dr. Timothy Tuinstra also provided valuable guidance with analyzing the data. Finally, the author would like to thank Sarah Maithel for advice on methods and for processing the disaggregated samples.

Figures and Tables

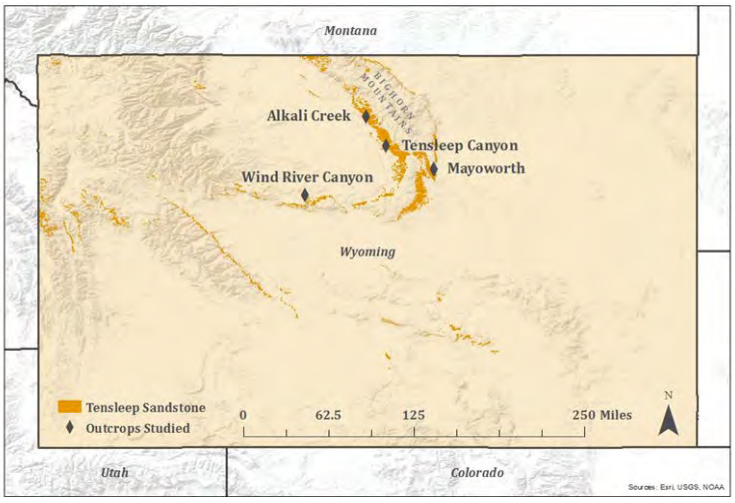

Figure 1. Location of outcrops in north-central Wyoming.

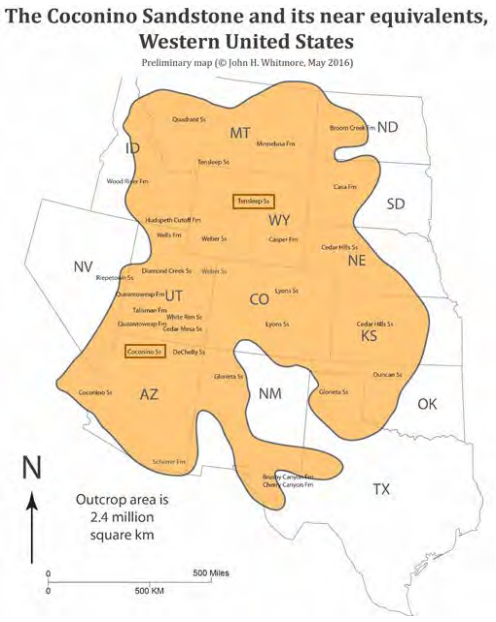

Figure 2. Map of Coconino and equivalents, with Tensleep Sandstone highlighted.

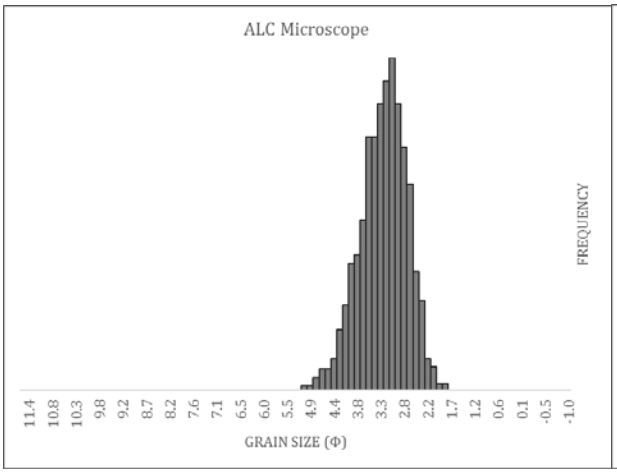

Figure 3. Summary of grain size data from Alkali Creek obtained by microscope work.

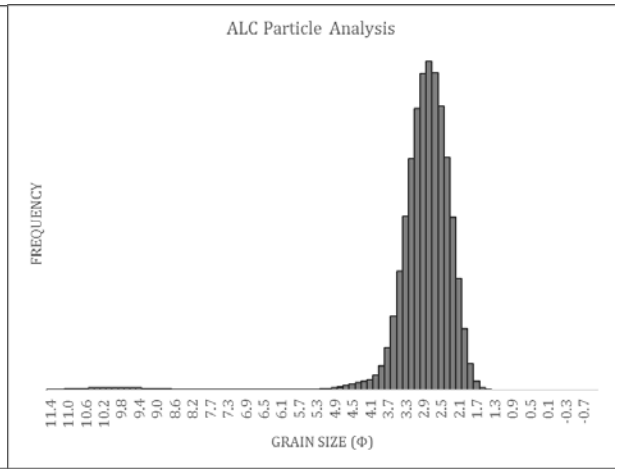

Figure 4. Summary of data from Alkali Creek obtained by particle size analysis.

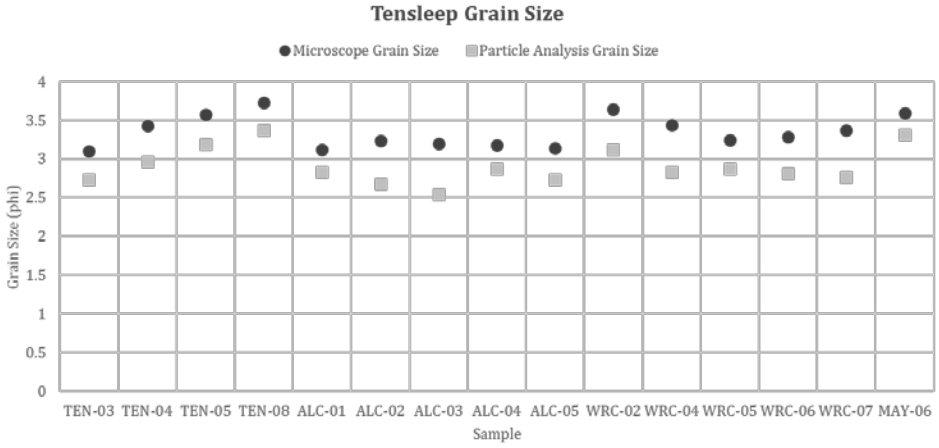

Figure 5. Comparison of mean grain size obtained by microscope work and particle analysis.

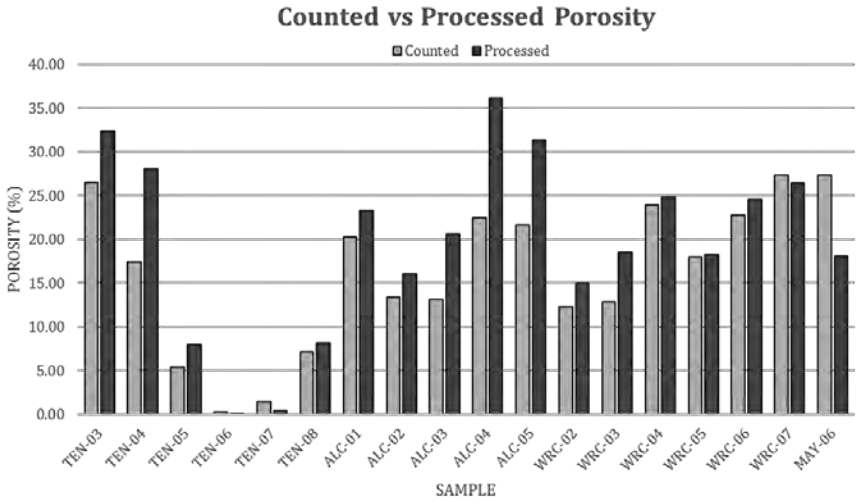

Figure 6. Comparison of porosity obtained by point counting and image processing.

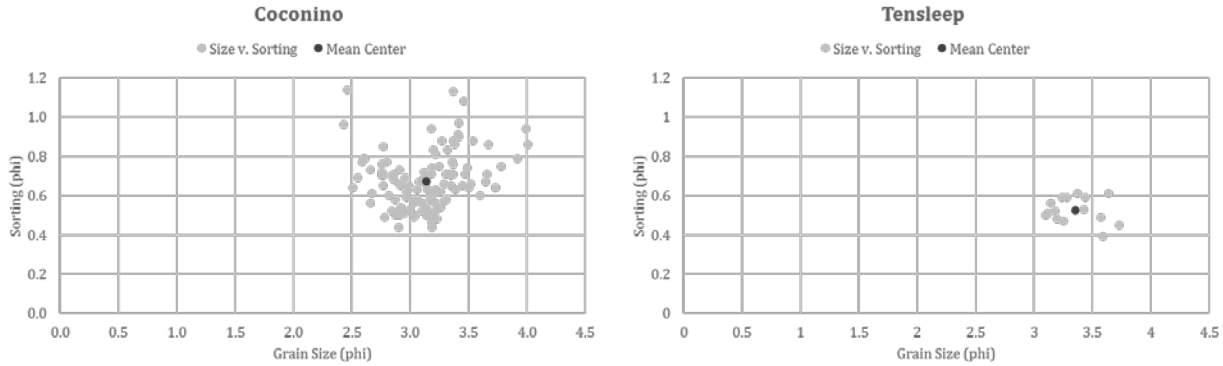

Figure 7. Comparison of Coconino and Tensleep textural data.

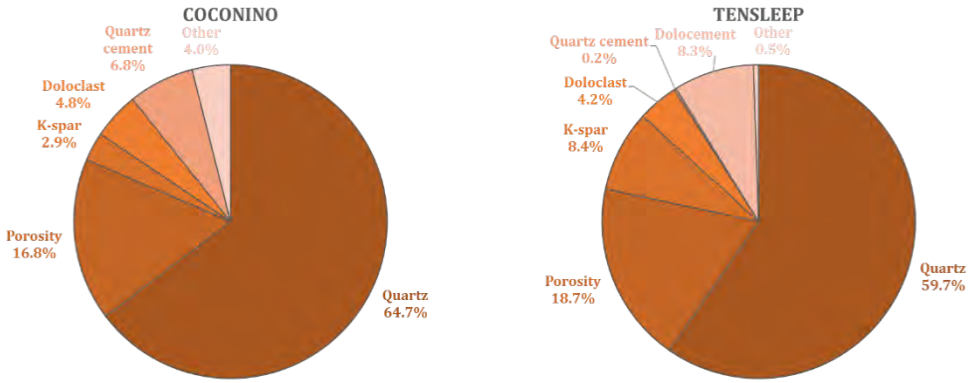

Figure 8. Comparison of Coconino and Tensleep compositional data.

References

1. Jafri, M. K. (2015). Petrophysical evaluation of the Tensleep Sandstone Formation using well logs and limited core data at Teapot Dome, Powder River Basin, Wyoming, USA. *Arabian Journal for Science and Engineering*, *41*(1), 223-247. doi: 10.1007/s13369-015- 1741-7.
2. Johnson, M. R. (1994). Thin section grain size analysis revisited. *Sedimentology*, *41*, 985-999. doi: 10.1111/j.1365-3091.1994.tb01436.x.
3. Mankiewicz, D. and Steidtmann, J. R. (1979). Depositional environments and diagenesis of the Tensleep Sandstone, Eastern Big Horn Basin, Wyoming. *Society of Economic Paleontologists and Mineralogists*, *26*, 319-336. doi: 10.2110/pec.79.26.0319.
4. Morgan, J. K. (2015). Stratigraphy and tectonic implications of the Tensleep Sandstone, NE Bighorn Basin, WY. (Master's thesis). Retrieved from University of Houston. (http://hdl.handle.net/10657/1249).
5. Whitmore, J. H. et al. (2014). The Petrology of the Coconino Sandstone (Permian), Arizona, USA. *Answers Research Journal*, *7*, 499-532.
6. Wibowo, R. A. (2003). Petrophysical properties of the Tensleep Sandstone at Sage Creek Field, Bighorn Basin, Wyoming. (Doctoral dissertation). Retrieved from GeoRef. (2005-009550).
7. Zhang, Q. (2005). Stratigraphy and sedimentology of the Tensleep Sandstone at the Teapot Dome and in outcrops, Wyoming. (Doctoral dissertation). Retrieved from GeoRef. (2007-0-6691).

Augmented Reality in Construction Coordination

Student Researcher: Katherine M. Rucker

Advisor: Dean Bortz, MA, CSI, CDT

Columbus State Community College

Construction Management and Sheet Metal

Abstract

Technology is the driving force behind most paradigm shifts. Such is the case for many aspects of construction. Construction coordination is known for being an in depth process of comparing 2D prints, 3D modeling, and physical construction to meet the requests of the Owner. Common BIM, Building Information Modeling, practices have aided blueprints by bringing the 2D into 3D format, but Augmented Reality has kicked it up a notch.

With Augmented Reality (AR), the capability of seeing what the Architect and Engineer have designed is put into perspective. Imagine looking through a lens on the purposed construction site and being able to see a 3D digital image of the new building on the landscape in front of you. AR creates that ability to put the digital design into the spatial capacity of the planned site. Being able to walk the site both literally and virtually, aides in construction coordination by being able to see exactly what the finished product will look like down to the details. Alterations and coordination clashes can be spotted and prevented before they become costly corrections. The design team can interact with the different areas of the building to insure complete client satisfaction.

Project Objective

My objective is to research the capabilities of augmented reality, the use of augmented reality in the construction coordination process, and the benefits this technology has provided to the construction industry.

Methodology Used

The bulk of my research has come from industry presentations, both in person and published online. Autodesk is a software company who develops computer aided drafting and similar platforms. They hold conferences, Autodesk University (AU), throughout the year to show case immerging technology and professional development. During the recent conference in November of 2017, multiple presentations involving Augmented Reality had focused on the implementation of AR devices into construction projects. These presentations were harnessed for research to see how the industry is using this technology.

The videos published online through Lynda Learning, took a directed path of technology advancement and specific construction projects using the technology. The Banner University Medical Center Tucson (BUMCT) project in Arizona that had incorporated technology from the project kick-off, was explored as a case study. The video went into depth of their processes with both the engineer and the manager of the virtual elements of the job.

Results Obtained

The results of this research, has led to an understanding of the evolution of how far augmented reality has progressed in development, where and how to incorporate AR into projects, and the benefits of this technology to the construction industry. Augmented reality is credited to Morton Heilig for first creating a covered screen with sensory engaging activities associated with a film called the Sensorama. Products out today are compact headsets such as the Oculus Rift developed by Palmer Luckey. Construction projects can use AR capabilities from the beginning design stage allowing a clearer image of function and style. Using AR during the construction process can correct clashing objects after construction of the initial frame of the building, but before installation of trades.

Significance and Interpretation of Results

As being a member of the construction industry, the outlook of increasing technology implementation into the building process is exciting. The programs of the past focus more on virtual reality and it is easy for clashes to be overlooked. Correction of clashes after product installation can be very costly to projects in both time and money. Having the ability to literally walk the job site and be able to see the design in its entirety, has the potential for completing projects ahead of schedule and to complete client satisfaction. It will be interesting to see the significant evolution of using technology on job sites and in the detailing departments.

References

1. Rogers, J. (2017, June 15). Retrieved February 2018, from https://www.lynda.com/CAD-tutorials/Construction-Management-Technology-Jobsite/606060-2.html
2. Benham, J. (2017, April 24).Retrieved February 2018, from https://www.lynda.com/CAD-tutorials/Construction-Technology-Industry-Snapshot/574682-2.html
3. Myers,B. (2017, November). *Future of Virtual Reality*. Lecture presented at Columbus Revit User Group in Elford, Inc, Columbus.
4. Shyu, M., Mai, I., Xie, F., & Heath, C. (2017, November). *A New Design Paradigm in Mixed Reality-Using HoloLens for Architectural DesignI [PDF]. Autodesk University*
5. Jahangiri, B., Keane, D., &Tang, W. (2017, November). *Augmented Reality: Practical Applications for RealWorld Problems* [PDF/PPT]. Autodesk University
6. Barr,C.(2018, June 29). Retrieved February, 2018, from https://www.lynda.com/CAD-tutorials/VR-design-tool/574683/632947-4.html?autoplay=true
7. Sundt Construction. (2017). Banner University Medical Center Tucson (BUMCT). Retrieved February, 2018, from http://www.sundt.com/projects/banner-university-medical-center-tucson-bumct/

Micromachining of Glass

Student Researcher: Ann M. Rumsey

Advisor: Dr. Muhammad Jahan

Miami University
Department of Mechanical and Manufacturing Engineering

Abstract
The development of microfluidics heavily relies on the optimization of machining techniques and choice of substrate material. This project focuses on the micromachining, more specifically micro milling of polycarbonate glass for micro fluidic applications. The amorphous structure, chemical and thermal stability, optical transparency, and electrical insulation of glass make it an obvious material choice for the related applications. Emphasis will be placed on evaluating the relationship among various process parameters and optimizing machining performance based on these variables. Experiments will be conducted to observe the effects of surface finish based on tool diameter, machining feed, speed, and depths of cut. The results of the milling experiments will then be analyzed for trends and relationships among the variables. Conclusions from the micromilling tests will aid in determining the optimal machining parameters for glass materials for microfluidic applications.

Project Objective
The goal of this project is to investigate the machinability of glass by experimenting with various machining parameters and investigating their effect on micromilling performance of glass for use in microfluidic applications. More specifically, the focus of the project is the optimization of machining parameters so that the overall micromachining performance is improved. The expected accomplishments of this project include determining the machining parameters and conditions that optimize glass micromachining using micro milling. To specify these conditions, it is imperative that each one is sufficiently observed and its influence is evaluated from experimental investigation.

Literature Review
Microfluidics, or the manufacturing of materials for fluid flow on a micrometric scale (Casquillas, G. V., & Houssin, T., n.d.), has progressed over the years in terms of material choice and manufacturing techniques. There exists a wide spectrum of microfluidic chip applications, most of which are focused on biological functions that take advantage of the chemical and physical properties of the fluid and material (Casquillas et al., n.d.). Technological advancements and material development have led to experiments with machining techniques including milling, turning, and grinding. Glass has emerged as a promising material due to its amorphous structure (Ren, K., Zhou, J., & Wu, H., 2012), optical transparency (Illiescu, C., Taylor, H., Avram, M., Miao, J., & Franssila, S., 2012), chemical and thermal stability (Whitesides, G. M., 2006), and electrical insulation (Ren, K., Zhou, J., & Wu, H., 2012). Glass machining focuses on the brittle-ductile transition, a theory that states that any brittle material, like glass, can be machined as a ductile material to create a crack-free surface (Foy, K., 5-2008). Literature reviews on topics including microfluidics, glass material properties, and machining techniques have been completed to provide evidence of the ductile regime and information on machining characteristics for optimization. The next step in refining and improving glass machining for microfluidic applications involves focusing on the features and constraints of the manufacturing processes.

Results Obtained

The expected accomplishments and results of this project include determining the machining parameters and conditions that optimize glass micromachining using micro milling. To specify these conditions, it is imperative that each one is sufficiently observed and its influence is evaluated from experimental investigation. Finally, the flow characteristics of the micro channels will be evaluated by running microfluidic experiments on the channels. Experiments to be completed include variations in tool diameter, rotational speed, depth of cut, and feed rate. The micromachining performance of polycarbonate glass will be evaluated by material removal rate, tool wear, surface finish, and the flow characteristics of the micro channels. Depth of cut experiments have begun, using polycarbonate glass slides with 0.3mm diameter end mills. Various depths of cut were chosen based on literature reviews of glass micromilling along with FeatureCam recommendations based on selected material and tooling. The results of 0.15mm depth of cut are shown below and the surface finish will be analyzed once all depth of cut tests are completed.

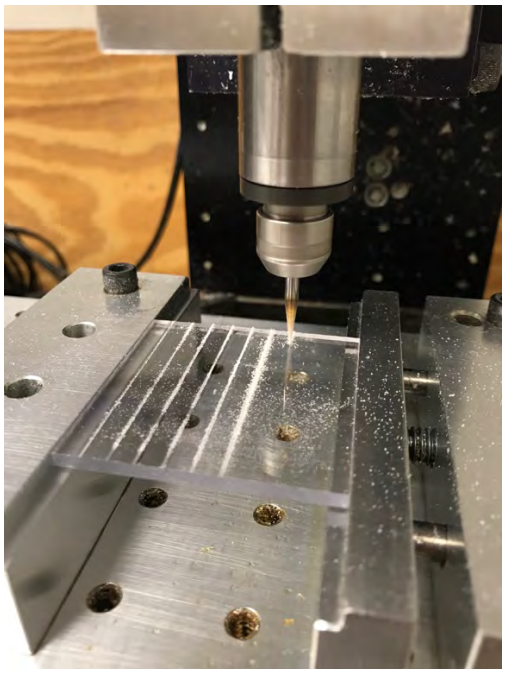

Figure 1. Micromilling Test Set-Up

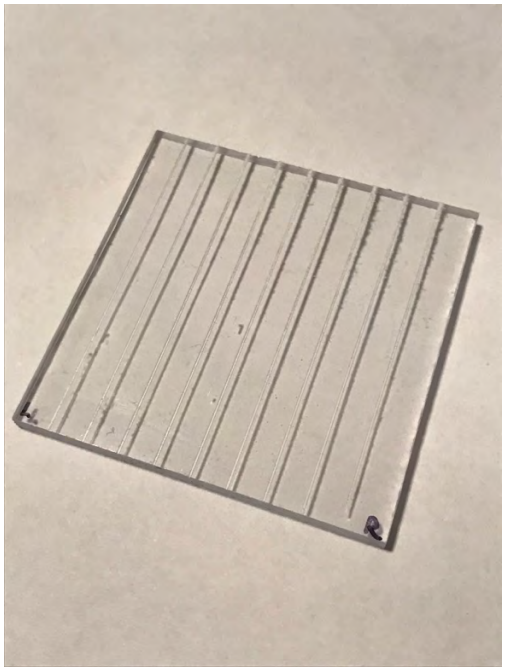

Figure 2. 0.3mm End Mill and 0.15mm Depth of Cut

References

1. Casquillas, G. V., & Houssin, T. (n.d.). Microfluidics and Microfluidic Devices: A Review. Retrieved from http://www.elveflow.com/microfluidic-tutorials/microfluidic-reviews-and-tutorials/microfluidics-and-microfluidic-device-a-review/
2. Foy, K. (2008a). *Ductile-Regime Machining of Glass Using the Micromilling Process* (Master's Thesis). Retrieved from All Theses. (Paper 359).
3. Illiescu, C., Taylor, H., Avram, M., Miao, J., & Franssila, S. (2012). A practical guide for the fabrication of microfluidic devices using glass and silicon. *Biomicrofluidics. 6(1).* doi: 10.1063/1.3689939.
4. Ren, K., Zhou, J., & Wu, H. (2012). Materials for Microfluidic Chip Fabrication. *Accounts of Chemical Research. 46(11), 2396-2406.* doi: 10.1021/ar300314s.
5. Whitesides, G. M. (2006). The origins and the future of microfluidics. *Nature. 442.* doi: 10.1038/nature05058.

Investigating Storage Systems for Alternative Sources of Energy

Student Researcher: Reannah N. Rymarz

Advisor: Professor Craig Rabatin

Marietta College
Petroleum Engineering

Abstract

Over the past 10 years alternative energy research has made leaps and bounds in production as well as accessibility. Solar panels especially have become more attainable to consumers as they can be found in neighborhoods all over the country. Though the push for greener energy is justified, it is difficult to accumulate this energy for large consumption. Once energy is produced it is difficult to store in an efficient, but also environmentally friendly way. Batteries are the main storage system for alternative energies which, though effective, are not as environmentally conscious as the energy producing counterpart. Alternatives do exist but are not ready for commercial use. To progress alternative energies forward into larger scale accessibility efficiency of storage systems must surpass that of the battery.

This study will provide insight to the types of storage systems for alternative energy that are currently available or in development. An overview of each type of storage system will be conducted including mechanics, cost, implementation, and the system's ability to store energy. Accessibility will also be investigated as the system is simpler to judge once it is used on a consumer level. Each type of storage system will be compared to the currently used storage system type, batteries. A conclusion of strengths and weaknesses of each type of storage system will be determined.

Introduction

The energy industry has developed extensively in finding, creating, and using sources of energy, but an area receiving less focus is that of means to store the energy. Methods of storage do exist but are not as evolved as battery power. In terms of alternative energy, batteries appear to be an ill-favored option as the contents of batteries are not entirely eco-friendly in nature. Though battery power is simple, there are more efficient means of storage that are quickly becoming available. Multiple alternatives are investigated in this study. Characteristics of each type are compared to determine the best conditions for each to thrive, or if applicable, the conditions in which are not yet available but could be in the future. The alternatives investigated are Pumped Hydroelectric Energy Storage (PHES), Compressed Air Energy Storage (CAES), Battery Energy Storage (BES), Superconducting Magnet Energy Storage (SMES), Molten Salt Battery, and Solar Ponds

Findings

Pumped Hydroelectric Energy Storage (PHES);

> Consists of two large reservoirs at different elevations separated by an impermeable mass (dam). Potential energy is stored at the higher elevation until it is needed. The water uses gravity to flow through the turbines inside the dam to produce electricity.

Compressed Air Energy Storage (CAES);

> Compressed air is forced by surplus energy into underground aquifers for later use. When needed the compressed air is released, heated, and used to burn natural gas in combustion chambers which is then expanded in a turbine expander to produce electricity.

Battery Energy Storage (BES);

Store electric energy, from all sources, in electrochemical form as in a conventional battery though this is on a larger scale. Two electrodes are immersed in an electrolyte while a chemical reaction generates a current when needed. In a flow battery two charged electrolytes are pumped to a cell stack where the chemical reaction occurs to generate a current

Superconducting Magnet Energy Storage (SMES);

Energy is stored within a magnet field that is created by the flow of direct current power in a coil of superconducting material that has been cooled cryogenically. The stored energy is released to the network by discharging the coil. The system uses an inverter/rectifier to convert alternating current to direct current or direct current to alternating current.

Molten Salt;

Store solar energy in the form of heat that is converted to superheated stream to power steam turbines to generate electricity. The molten salt used has a much higher heat capacity than regular table salt allowing it to hold large amounts of heat without changing state.

Solar Ponds;

A pool of water containing layers of salt solutions that increase concentration with depth. The pond absorbs solar energy causing the density gradient prevents heat from the lower layers from moving upwards by convection. The trapped heat is used to heat or to drive a turbine.

Conclusions

Based on the investigation the best large scale alternative options are Pumped Hydroelectric Energy Storage (PHES) and Compressed Air Energy Storage (CAES) due to the high capacity potential. In addition to capacity these options are also low in cost. Compared to batteries, the strongest advantage of the alternative options is the decreased environmental impact. Though rechargeable batteries are affordable and accessible it is nonsensical to store clean renewable energy in a nonrenewable medium. Similarly, effective, molten salt and solar ponds are strong candidates for energy storage. Molten salt combines solar and thermal energy to provide a renewable storage mechanism, though it is not yet ready for large scale application. The materials for molten salt plants and solar ponds are low cost and simple to install which is essential to the advancement of the systems. Finally, the best small-scale candidate is Superconducting Magnet Energy Storage (SMES). SMES is capable of quick turnaround but is limited to small scale due to the high installation and material cost. This method has large scale capabilities as it is about 95% efficient. Though no method has completely positive outputs, this investigation provides insight into the current mechanisms on the market that provide positive outputs that are also economical.

References

1. “Compressed Air Energy Storage (CAES).” *Energy Storage Association*, 2018, energystorage.org/energy-storage/storage-technology-comparisons/caes.
2. “Energy Storage.” *Wikipedia*, Wikimedia Foundation, 9 Mar. 2018, en.wikipedia.org/wiki/Energy_storage#Mechanical_storage.
3. “Operating Flexibility of Power Plants with CCS.” *Global Carbon Capture and Storage Institute*, IEA Greenhouse Gas R&D Programme, 1 June 2012, www.globalccsinstitute.com/publications/operating-flexibility-power-plants-ccs.
4. “Pumped Hydro-Power.” *Energy Storage Association*, 2018, energystorage.org/energy-storage/energy-storage-technologies/pumped-hydro-power.
5. “Solar Energy.” *Wikipedia*, Wikimedia Foundation, 20 Mar. 2018, en.wikipedia.org/wiki/Solar_energy.
6. “Solar Pond.” *Wikipedia*, Wikimedia Foundation, 28 Feb. 2018, en.wikipedia.org/wiki/Solar_pond.
7. “Thermal Energy Storage.” *Wikipedia*, Wikimedia Foundation, 12 Mar. 2018, en.wikipedia.org/wiki/Thermal_energy_storage#Molten_salt_technology.
8. Wagner, Leonard. “Overview of Energy Storage Methods.” *Mora Associates*, Dec. 2007, www.moraassociates.com/reports/0712%20Energy%20storage.pdf.

Space Plants: Growing Peas as NASA Scientists

Student Researcher: Rachel E. Sauder

Advisor: Dr. Todd France

Ohio Northern University
Department of Biological and Allied Health Sciences, Department of Chemistry and Biochemistry, Department of Education

Abstract
The Space Plants Unit, designed for a high school biology classroom, will allow students to apply content knowledge of photosynthesis to grow plants in experimental conditions mimicking those of space. Students will use background resources from NASA and other sources to design an experiment and build devices to allow growth in suboptimal conditions.

Project Objectives

1. Design and implement a well-researched experiment on the manipulation of photosynthetic variables.
2. Calculate mean growth rate and percent difference between the typical plant and experimental plant.
3. Present methods and results to the class in a verbal presentation.

Methodology to be Used

Day 1: Introduction of Project: Students will learn how plants are grown in space conditions using NASA resources. The project challenge, to grow a pea plant as a NASA scientist, will be introduced to students using an informational/project guidelines packet.

Days 2-3: Space Conditions Research: Students will research the growing of plants in space conditions using academic databases accessible through the school library, and texts from reputable scientific sources like NASA. At the end of this segment, students will submit a project proposal outlining their experimental condition, supported by resources.

Days 4-5: Experimental Device Design: Students will design an experimental device to allow their plants to grow in the aforementioned experimental condition. At the end of this segment, students will submit a diagram and materials list necessary to build their device.

Days 6-7: Build Devices: Students will construct their devices using materials gathered or purchased based on materials lists submitted on Day 5.

Day 8: Pot Plants, begin experiment: Students will plant pea sprouts and begin growing the plants; three pots will be in the experimental condition, and three pots will be in optimal growing conditions, like a windowsill or greenhouse.

Days 9-10: Teach data techniques, introduce presentation: Students will learn how to collect data for the experiment and begin collecting data. Additionally, students will be introduced to the final assessment of the project, a presentation covering the experimental condition, device used, results, and conclusions as a NASA scientist.

Days 11-25: Daily data collection, resume normal class: Students will collect data at the beginning of every class period. During this period, normal class will resume.

Days 26-27: Work on presentations: Students will work on compiling and analyzing data and creating their final presentations.

Days 28-30: Student Presentations: Students will give their presentations and be graded by the teacher. Classmates will pay attention and ask relevant questions of their peers.

Significance and Interpretation of Results

Students will gain experience in scientific research as well as interdisciplinary work. Through this experience, they will understand how different fields work together for scientific advancement.

Figures/Charts

Suggested materials for the unit are found in Tables 1 and 2, below.

Table 1. Reusable Materials

Part Description	*Vendor/Source*	*Part # / Link*	*Qty./Team*	*Qty./Class*	*Total Qty.*	*Cost/Qty.*	*Total Cost*
Plastic Pots	Home Depot	#T55BL817	2	20	80	$29.69/ 50 pots	$59.38
Watering Can	IKEA	PS 2002	N/A	2	2	$0.99 each	$1.98
Potting Soil	Home Depot	# 72790430	N/A	0.5 bag	2	$13.47/ 50qt. bag	$26.94
Fridge	Access somewhere in school	N/A	N/A	N/A	1	N/A	N/A
Grow Light Strip (1m)	Amazon	B01LO55GAS	N/A	N/A	1	$11.95	$11.95
						Total:	**$100.25**

Table 2. Non-reusable Materials

Part Description	*Vendor/Source*	*Part # / Link*	*Qty./Team*	*Qty./Class*	*Total Qty.*	*Cost/Qty.*	*Total Cost*
Pea Seeds (200 pack)	Burpee	62405A	N/A	0.25	1	$4.99	$4.99
Introduction Packet	N/A	N/A	3	24	96	N/A	N/A
Masking Tape	Walmart	001290428	1’	8’	32’	$1.66/ 159’	$1.66
Vinegar	Walmart	009278075	8 fl.oz	16 fl.oz	64 fl.oz	$2.48/128 fl.oz	$2.48
pH paper	Amazon	SG6623169139	16	32	128	$3.99/160	$3.99
						Total:	**$13.12**

Acknowledgments and References

Thank you to Dr. Todd France for guidance and feedback throughout the project.

Remote Sensing of Water Quality Parameters Influencing Coral Reef Health, US Virgin Islands

Student Researcher: Hannah L. Schlaerth

Advisor: Dr. Joseph D. Ortiz

Kent State University
Geology

Abstract
Nearly a quarter of ocean species are constrained to coral reefs, making reefs important resources to island tourism and fishing. Increases in development and changes in land use have created an influx of sediment and nutrients entering the coastal waters of the US Virgin Islands (USVI), causing detrimental effects on water quality. As a consequence, coral reefs have started to degrade. We employ remote sensing as a method of water quality monitoring, which offers a spatial advantage and cost effective alternative over traditional water quality monitoring. This study integrates NASA Landsat 8 (L8), Landsat 7 (L7), and Landsat 5 (L5) data with field spectroscopy in order to determine bio-optical properties and to quantify changes in water quality parameters that effect coral reef health in the USVI. Surface reflectance imagery was collected for clear days from January 1985 through August 2017. The images were systematically analyzed by taking the derivative of the measured visible/near infrared spectra and then using Varimax-rotated Principal Component Analysis (VPCA) decomposition to identify color producing agents (CPAs) in the water column. VPCA loadings were standardized and results were matched to libraries of reflectance derivative spectra for known pigment and mineral standards. Research campaigns were conducted to provide in-situ surface reflectance data for comparison with the VPCA-decomposed imagery. A spectroradiometer (ASD Fieldspec HH2) was used to measure surface reflectance from 350-1075 nm and data were averaged to 10 nm resolution. Preliminary results show changes in the spatial distribution of CPAs over time, which may suggest changes in coastal water quality. The detection and analysis of water quality parameters is a necessity in current and future remediation efforts and VPCA-decomposition will likely prove beneficial as an inexpensive method of near real time water quality monitoring.

Project Objectives
Recent and widespread coral degradation in the Caribbean necessitates an increase in water quality monitoring in coastal areas. Traditional water quality monitoring involves labor intensive, in-situ water sampling and expensive research campaigns that can cost thousands of dollars per day. Since NASA satellite data is easily accessible and available free-of-cost from USGS Earth Explorer, remote sensing data provides an inexpensive method of water quality monitoring over large spatial extents. However, optical properties of shallow coastal waters complicate remote sensing in places like the US Virgin Islands. Coastal water is a heterogeneous mix of microbes, sediments, and organic matter, so identifying individual water quality parameters is a challenge of active research in the remote sensing community. This study uses a method of spectral unmixing called VPCA-decomposition on Landsat data to identify CPAs in the shallow, coastal waters of the USVI. In addition, this study takes advantage of the extensive archives available from USGS Earth Explorer to create a time series of water quality in the USVI that goes back to 1985.

Methodology

Atmospherically corrected, Landsat surface reflectance products were collected from USGS Earth Explorer for winter and spring months from 1985 to 2016. These months coincide with the field campaigns described below. Surface reflectance imagery were systematically analyzed using VPCA-decomposition (Ortiz et al., 2013). Water pixels in each image were isolated by creating masks that cover land, clouds, and cloud shadows, following Hollister et al (2016). Then, the centered, first derivative of each valid water pixel was calculated and a VPCA was performed using the computer software ENVI/IDL. Principle components were ranked, with the first component accounting for the greatest percentage of variance in the data matrix and each successive component contributing less. Standardized loadings representing the spectral signature for each principal component were then plotted against wavelength definitions (ultra-blue, blue, green, red, and near-infrared(NIR)) and matched by their spectral patterns. Groups of matching spectral signatures were averaged to obtain an average spectral signature to use for identification. Spectral libraries of known, standard CPAs were averaged to the spectral resolution of each Landsat sensor and a stepwise multiple linear regression was used to determine the combination of CPAs associated with each component for identification.

Three field campaigns have been conducted in May 2016, December 2016, and May 2017. Sampling locations ranged from heavily populated bays of St. Thomas to the relatively unaffected watershed of St. John, an island which is mostly national park land. At each of the eleven sampling sites, surface reflectance was measured from 350-1075 nm using an ASD Fieldspec HH2 spectroradiometer. Data obtained were averaged to 10 nm resolution and analyzed using the VPCA-decomposition described above (Ortiz et al., KSU NASA EPSCoR Annual Report 2016).

Results

Fifty-four components representing spectral patterns of CPAs were retrieved from the eighteen time-series images processed. Of these components, forty-nine were separated into four major groups on the basis of spectral shape: Match 1, Match 2, Match 3, and Match 4.

Match 1 is comprised of twelve components with highest reflectance in the blue range of the electromagnetic spectrum followed by a sharp drop in reflectance in the green and red, and a slight increase in the NIR. Match 1 is further subdivided as Match 1a and Match 1b, depending on the magnitude of reflectance in the NIR. Match 1a has lower NIR magnitudes than Match 1b, which is either due to differences in CPAs present or differences between sensors. Match 1a consists of primary components from five L8 images from November 2013 to December 2015. Spatial distribution of components in Match 1a were abundant near shore and gradationally decreased moving off shore. Match 1b consisted of seven components from L5 and L7 imagery from 1985 to 2001. Similar to Match 1a, Match 1b had high spatial distribution on shore and low spatial distribution off shore. However, the region of high spatial distribution in the early images (1985-1999) is significantly smaller than the region of high spatial distribution in more recent images (1999-2015). On first approximation, the Match 1 group is similar to spectral signatures matched to phaeophorbide-B and chlorophyta.

Match 2 is comprised of thirteen components with reflectance values that decrease moving from the blue to green ranges of the electromagnetic spectrum and increase in the red and NIR ranges. Match 2 can be further subdivided as Match 2a and Match 2b, with Match 2a consisting of five L8 components from 2013 to 2015 and Match 2b consisting of eight L7 and L5 components from 1985 to 2001. Match 2a has highest concentrations in onshore areas to the north and abruptly decreases on the north side of the USVI. South of the USVI, concentration decreases in a gradational manner. Match 2b has highest concentrations near shore and grades rapidly to low concentrations moving off shore. Plumes of high

Match 2b concentration are confined to areas directly around islands and do not extend far offshore like those of Match 2a. On first approximation, the Match 2 group is similar to spectral signatures matched to phycocyanin.

Match 3 is comprised of nineteen components and has highest reflectance in the blue and lowest reflectance in the NIR. Match 3 can be further subdivided as Match 3a, Match 3b, and Match 3c depending on the slope between the green and NIR points on the graph. Match 3a consists of five components from L8 imagery between the 2013 and 2015. Spatial abundance is lowest close to shore and grades to high moving away from shore. Match 3b consists of ten components from L5 and L7 imagery between 1986 and 2001. The spatial distribution of Match 3b is highest near Puerto Rico and offshore of the USVI. In some images, the high concentration off of Puerto Rico creates a gradational plume of high concentration moving east. Match 3c consists of three components from L5 and L7 images from 1985, 1987, and 2000. These images show highest abundance northeast of the USVI. Very low concentrations are localized in near shore areas. In general, the Match 3 distribution seems to move from high abundance offshore to high abundance near shore and then back to high abundance offshore. On first approximation, Match 3 is similar to the spectral signatures matched to chlorophyceae.

Match 4 consists of six components from L7 and L5 imagery between 1987 and 2001. These spectral patterns have highest reflectance in the green and red ranges and lowest reflectance in the blue and NIR ranges. Spatial abundance is low near shore and grades to moderate off shore. This group has the highest variability between components and has not yet been matched to the spectral signature of CPAs. Further work will be done to update the spectral libraries in use and identify Match 4.

Five major components were revealed from the VPCA-decomposition of the *in situ* hyperspectral measurements, which are graphically similar to the spectral patterns described above. Future efforts will be targeted at identifying the CPAs present in each match group beyond first approximation and quantitatively comparing spectral signatures of Landsat imagery to ASD measurements.

Significance and Interpretation of Results

VPCA-decomposition of Landsat imagery is a reproducible method of extracting spectral signatures of CPAs in the water column. Indeed, this study produced matching spectral signatures from 1985 through 2015, despite changes in cloud cover and sensor specifics of the three different Landsat missions. Variability within major match groups was reduced by placing signatures into sub groups. This variation can be attributed to two things. First of all, the band designations for L5, L7, and L8 are different, which might affect the measurement of reflectance data. L8 also has an additional band (“ultra-blue”) that is not included in the L5 and L7 thematic mapper sensors. The other possible explanation for the observed variation within match groups is that the CPAs present in the water column, and therefore the water quality, have changed over time. Reflectance spectra represent the different proportions of CPAs in the water column and when these proportions change, so too do the spectral signatures retrieved. Whether the observed variation is a consequence of differences in Landsat sensors, changes to water quality, or a combination of these two factors remains ambiguous. However, the spatial distribution of CPAs has, in general, extended to encompass more close-to-shore areas. This change in CPA abundance and distribution can be interpreted as changes in the associated local water quality.

With increases in development and population, anthropogenic activity is likely having negative effects on coral reefs, particularly those located near shore. For this reason, the detection and analysis of water quality parameters is integral to remediation and environmental policy concerning reef mortality. Although comparison of VPCA results between sensors is an area of active research, this project offers a

timely, cost effective method of remotely sensing water quality by systematically analyzing surface reflectance imagery. Moreover, these results show that the distribution of material in the water column has changed between 1985 and the present day. When verified with ground spectroscopy, VPCA-decomposition of remote sensing data could potentially be used to identify algal species and mineral detritus from satellite imagery alone, making near real time water quality monitoring a possibility.

Acknowledgements
An extension of gratitude to my advisor, Dr. Ortiz, Dulci Avouris, the faculty of the geology department at Kent State University, and all others who contributed over the semester. This project is in collaboration with the College of Charleston and the University of the Virgin Islands. Undergraduate research was made possible thanks to the Ohio Space Grant Consortium and NASA EPSCoR, grant number NNX15AM74A.

References

1. Grimsditch, G. (2005). A study of potential coral reef bioindicators in the Mamanucas region, Fiji, using Coral Cay Conservation Reef Check data. (Unpublished doctoral dissertation). UCL, London.
2. Hollister, K., Ortiz, J. D. (2016). Historic Water Quality Trends in the US Virgin Islands and Future Implications on Coral Reef Health (Unpublished McNair Scholars Report). Kent State University.
3. Kerrigan, K. (2015). Development of a regional bio-optical model for water quality assessment in the US Virgin Islands (Master's thesis).
4. Ocean Conservancy. (n.d.) The state of the coral reefs of the US Virgin Islands. Retrieved from http://act.oceanconservancy.org/site/DocServer/Reefs_USVI_part2.pdf.
5. Ortiz, J. D., Schlaerth, H., Hollister, K., Avouris, D. (2016). Annual Report, 2016 for Using NASA's Ocean Color Sensors to Identify Effects of Watershed Development and Climate Change on Coastal
6. Marine Ecosystems of the US Virgin Islands. Grant number NNX15AM74A. (p 1-18).
7. Ortiz, J. D., Witter, D. L., Ali, K. A., Fela, N., Duff, M., and Mills, L., Evaluating multiple color producing agents in Case II waters from Lake Erie, International Journal of Remote Sensing, 34 (24), 8854-8880, 2013.
8. Ortiz, Joseph D., Avouris, Dulcinea, Schiller, Stephen, Luvall, Jeffrey C., Lekki, John D., Tokars, Roger P., Anderson, Robert C., Shuchman, Robert, Sayers, Michael, Becker, Richard. Intercomparison of Approaches to the Empirical Line Method for Vicarious Hyperspectral Reflectance Calibration. Frontiers in Marine Science 2017. V4 (p 296). Retrieved from https://www.frontiersin.org/articles/10.3389/fmars.2017.00296/full.

An Isolated DC-DC Converter with Bidirectional Current for Interfacing the Voltage Busses of the Dragon Capsule and ISS

Student Researchers: Benjamin D. Shaffer, Nicholas D. Wolford

Advisor: Dr. Mark Scott

Miami University
Department of Electrical and Computer Engineering

Abstract
With spaceflight becoming more frequent, and long term operational reliability of spaceflight devices ever more important, the challenges of designing robust electrical power supplies to support satellites and crew capsules are at the forefront of research and innovation. This case study of the ISS-Dragon interface considers the specific power conversion requirements of the interface as design parameters for a prototype of an isolated, bidirectional current, DC-DC converter topology. The topology was chosen based on theoretical advantages over similar topologies given the operating environment. The efficiency of the prototype will be measured at varying loads to determine its suitability for the target application.

Objectives
This research project aims to study the requirements and challenges of designing a power supply for space-grade applications. To do so, an understanding of the environmental hazards and the existing systems is required, so that operating parameters which affect the design choices may be determined. Appropriate components for the environment must be chosen, as well as a circuit topology that can theoretically meet all needs of the application. Finally, simulation and prototyping must be performed to verify the potential solution. Following the background research, we chose three topologies that can support the power requirements and are typically used at the required voltage and power levels. Each is analyzed and simulated to determine whether it is the best solution based on our evaluation criteria. The chosen topology is then manufactured to conduct final experiments which verify the design choices.

Methodologies
To build a baseline for understanding the design challenges, we researched the systems currently employed on the space station and their expected performance. We also interviewed a power supply engineer who works on satellites to gain valuable information and a starting point. With the baseline formed, our advisor provided the three topologies known to be used at the determined power point. Given these topologies, we analyzed their design and performance characteristics. Using the data provided by the analysis, we simulated models of each topology and recorded their performance, providing the required information for evaluation. This determined an optimal solution to our design challenge, which we analyzed and simulated further. We then built a prototype of the chosen device and performed several experiments to measure its performance and validate our theoretical findings.

Results
Power electronics in space applications were found to be the highest percentage of causes for satellite failure. Furthermore, the primary cause of failure was not the control circuitry, but the power transfer devices. This failure regularly occurs due to lack of radiation hardened (or rad-hard) components in the device construction. These non-rad-hard components may absorb radiation and cause a Single Event Effect (SEE) which may cause failure [1]. SEEs do not always cause immediate device failure but do contribute to Total Ionizing Dose (TID), the dosage of radiation required to fully destroy the ability of a

semiconductor to operate properly. For a transistor to experience an SEE, it must be constructed with an oxide layer within the crystal lattice of the device which can absorb cosmic radiation. Without an oxide layer, the radiation will simply pass through the device and the system will remain unharmed. Common MOSFETs (Metal Oxide Semiconductor Field Effect Transistors) include the oxide layer that absorbs the radiation, but HEMTs (High Electron-Mobility Transistors) do not. For this reason, we chose HEMT devices for our primary power transfer circuit.

Based on our background research, the ISS and Dragon capsules run on one 120V DC bus and one 28V DC bus [2]. These busses carry power from the solar arrays and batteries and deliver it to the various systems and instruments on board. Various systems and devices use each of the busses, but the primary power supplies (solar arrays, batteries) of each vehicle only connect to one bus. Also, the two busses must remain electrically isolated from each other. Therefore, there must be a system between the two busses that can transfer power from one to the other, in either direction, while providing galvanic isolation. Based on our research, the power draw of the Dragon capsule is an average of 2kW with a peak of up to 5kW [2]. Given these parameters we may choose potential topologies to implement the power sharing device.

The three devices we chose to evaluate are each capable of bi-directional current flow, support 28V on one side and 120V on the other, support 2 to 5kW operation, and provide galvanic isolation via a transformer. They are the Push-Pull (Figure 1), an efficient topology but with high voltage stresses and a complex transformer [3]; the Dual Active Bridge (DAB, Figure 2), a simpler topology with lower voltage stresses but less efficiency [4]; the Resonant, Pulse Width Modulated (R-PWM, Figure 3) topology with simple control, low voltage stresses and high efficiency but complex mode of operation [5]. Following theoretical analysis, each topology was simulated to validate the predictions. Given the findings detailed in Table 1, we chose to prototype the R-PWM topology.

As previously stated, and as shown in Table 1, the R-PWM topology is expected to be more efficient than the DAB, despite similar construction. This is because of its resonant operation, the complex factor previously mentioned [5]. Unlike the DAB and the Push-Pull, the R-PWM resonates the inductance of the transformer with a set capacitance. This resonant action reduces the harmonics in the current passing through the transformer and thus reduces the energy lost in the transformer thereby increasing the overall efficiency of the device. The resonant circuit depends on several capacitor banks on the circuit board being matched to the inductance of the transformer. However, assuming the resonant circuit and the rest of the system is built correctly, we can accurately test the device to validate the predictions and its feasibility as a solution to the design challenge.

Preliminary experimental results, shown in Figure 5, confirm the prototype's ability to produce 120V output given a 28V input. The switching waveforms indicate proper timing between the switching signals, as well as the beginnings of the resonant action, but also indicate large ringing that needs mitigated for better results. The output load is too low to achieve the predicted characteristic sine wave, so higher power testing is required to further confirm functionality of the device. The experimental data, at the time of this report, is inconclusive on its suitability to the target application.

Table 1: Evaluation data for each proposed topology.

Topology	# of Active Switches	Voltage Stress	Transformer Complexity	Efficiency	Control Complexity
Push-Pull	**4**	**2x V_{IN} or 2x V_{OUT}**	**Complex**	**~95%**	**Complex**
Dual Active Bridge	**8**	**V_{IN} or V_{OUT}**	**Simple**	**~90%**	**Simple**
Resonant-PWM	**8**	**V_{IN} or V_{OUT}**	**Simple**	**~95%**	**Simple**

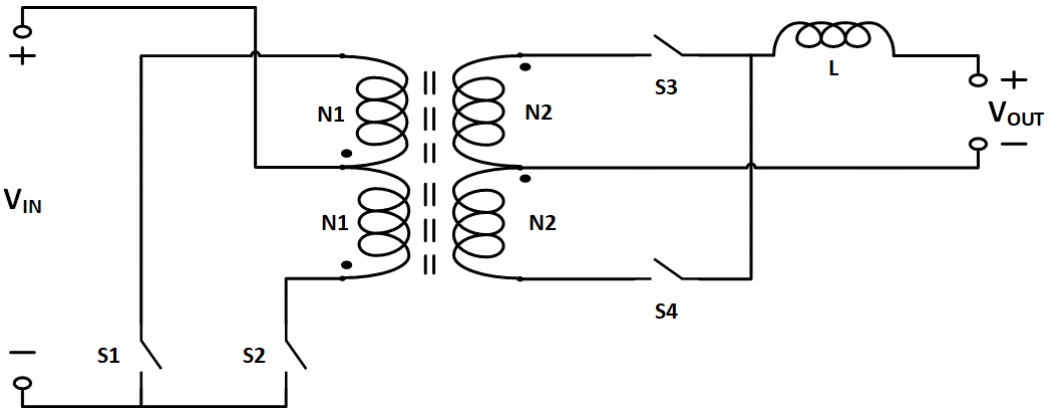

Figure 1. Push-Pull topology [3].

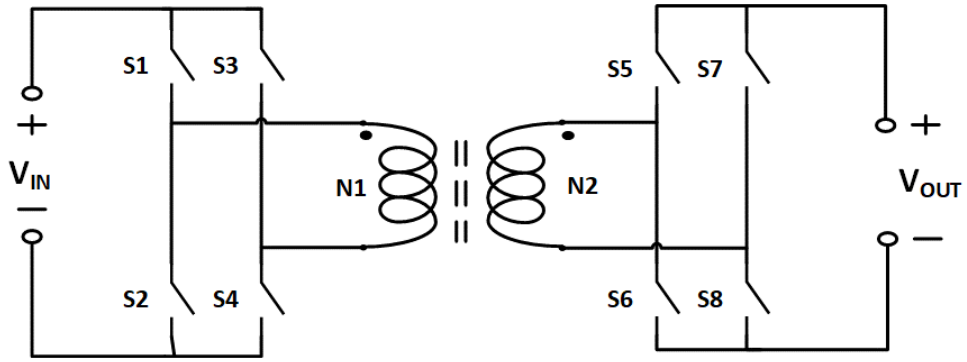

Figure 2. Dual Active Bridge topology [4].

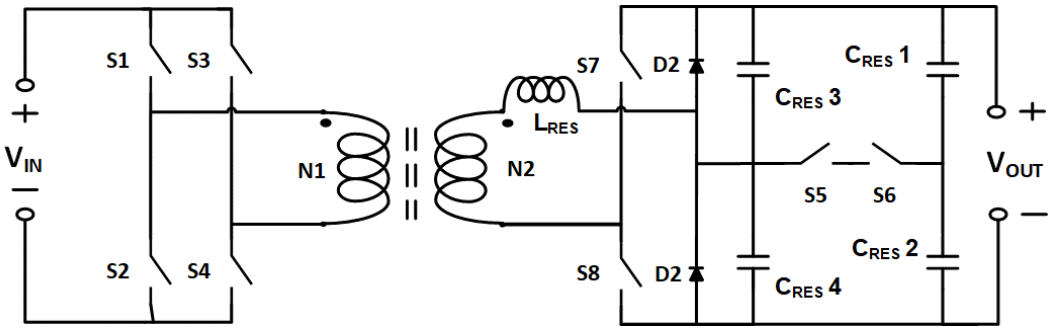

Figure 3. Resonant-PWM topology [5].

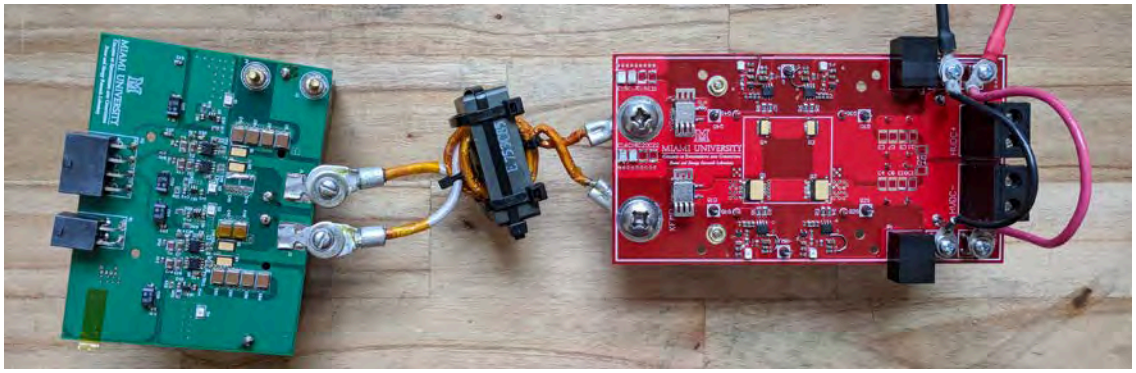

Figure 4. Prototype of the R-PWM topology.

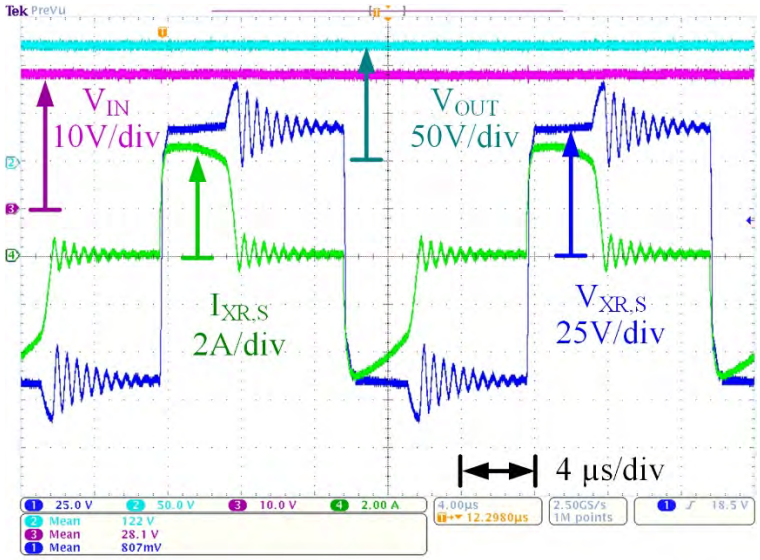

Figure 5. Preliminary experimental results.
Pink: Input voltage (V_{IN}). Light blue: Output voltage (V_{OUT}). Dark blue: Voltage output from the transformer (V_{XFMR}). Green: Current output from the transformer (I_{XFMR}).

Acknowledgments
Thanks to Dr. Alexander “Sasha” Isurin, of Vanner Inc., for help and guidance in understanding his topology.

References

1. “Single Event Effects,” NASA Radiation Effects and Analysis Group [Online]. https://radhome.gsfc.nasa.gov/radhome/see.htm [Accessed Dec. 8 2017].
2. Dragon Lab Fact Sheet. (2017). [ebook] SpaceX. Available at: http://www.spacex.com/sites/spacex/files/pdf/DragonLabFactSheet.pdf [Accessed 20 Oct. 2017].
3. Mohan, Undeland, Robbins, “DC-DC Converters with Electrical Isolation,” in Power Electronics, , Wiley, 2003, pp. 319-322.
4. R. W. A. A. De Doncker, D. M. Divan and M. H. Kheraluwala, "A three-phase soft-switched high-power-density DC/DC converter for high-power applications," in IEEE Transactions on Industry Applications, vol. 27, no. 1, pp. 63-73, Jan/Feb 1991.
5. A. Isurin and A. Cook, "A novel resonant converter topology and its application," 2001 IEEE 32nd Annual Power Electronics Specialists Conference (IEEE Cat. No.01CH37230), Vancouver, BC, 2001, pp. 1039-1044 vol.2.

Development of Small UAV Engine Capabilities at High-Altitudes

Student Researcher: Liberty M. Shockley

Advisor: Dr. Shaaban Abdallah

University of Cincinnati
Aerospace Engineering Department

Abstract

Current attainable flight times of Unmanned Aerial Vehicles (UAVs) at high altitudes greatly hinder potential mission capabilities. Two different engine systems for pushing the boundaries of this capability are explored, focusing on how to overcome the lack of oxygen for combustion at these altitudes. The goal of these UAV engines is to provide the air mass flow rate necessary to operate at 60% of maximum sea-level power while at 30,000 feet altitude. The first solution explores the Army's small UAVs propelled by automotive compression-ignition (CI) engines, which deliver the required high efficiency and low fuel consumption but lack the ability to ingest an adequate mass flow rate of low-density air into their compression cylinders. The combined system will be integrated on a dual shaft to allow for fan and compressor to rotate at different speeds. This hybrid fan-centrifugal compressor system will offer higher pressure and mass flow rate to the current Army UAV engines than standard turbochargers, while maintaining simplicity and manufacturability. The second solution explores the use of a modular microjet engine with a solid fuel grain that doesn't require an oxidizer. The main components explored are fuel type and structural design. The use of solid-to-gas burning fuel is being explored, specifically with HTPB. By using solid fuel, and finding a unique type and gradient that can extend the burn time by slowing the burn rate would improve the capabilities of UAVs. Developing this concepts involve remodeling the combustor to remove liquid fuel lines and injectors and including a solid fuel package that could be easily accessed and exchanged.

Project Objectives

The primary goal of this research was to design two options for small UAV engines that fulfill the following requirements. The two projects are a fan-centrifugal compressor system for operation with a 180-hp Compression Ignition engine and microjet engine that utilizes a solid fuel grain and features an exchangeable combustor package. A goal is to use off-the-shelf parts and keep manufacturing to a minimum to reduce time for development, keep simplicity, and prioritize low costs. The system will be designed:

1. For efficient operation at altitudes between sea level and 30,000 feet
2. For operation with required mass flow to achieve 60% power at maximum altitude
3. Aim for at least a 10 minute flight time
4. Operate within a temperature range of -60F to 130F
5. To avoid compressor surge, shaft vibration, and blade deflection
6. For a hardware life of 2,000 hours
7. To weigh no more than 15 lbs
8. Rapid refueling strategy

Methodology

Turbocharger

A proposal was written and submitted in February 2018 for a hybrid fan-centrifugal compressor boost charging system to deliver the required mass flow for CI engines at altitudes ranging from sea level to 30,000-ft. This was submitted as a partnership between the University of Cincinnati and Ubiquity Interface as a Small Business Innovation Research for the Army.

A schematic for the turbocharger concept is shown in Figure 1. Due to the difference in fan and centrifugal compressor functions, the fan must run at lower rotational speed as compared to the compressor. Therefore, dual shaft or gear box arrangements must be used to meet the optimum operations of these components. The large fan diameter (inlet area) will allow for ingesting large air mass flow compared to the air mass flow ingested by the centrifugal compressor alone. The fan speed as well as its dimensions will be designed to meet the 60% of the sea level power required at 30,000-ft altitude. Typically, fans deliver high mass flow and low pressures. The centrifugal compressor in the current design will benefit from the modest increase of the fan pressure above the atmospheric pressure. That increase in the pressure obtained by the fan will help increase the compressor pressure ratio. The use of fan-axial compressor system is well developed in Aviation Turbofan engines. The dual shaft technology is also as well developed in counter-rotating propellers for efficient UAVs and turbofan propulsion systems. Although the purpose of using the fan-axial compressor system and our design of fan-centrifugal compressor system is to deliver large mass flows, the function of the two systems is different. In the axial compressor system, the large mass flow is mostly delivered to a nozzle to generate thrust, while in the proposed centrifugal compressor system the large mass flow is completely delivered to the compressor of the turbocharger.

Microjet

A proposal is being prepared for an Air Force SBIR submission in June 2018 for a microjet engine that utilizes solid fuel and features an exchangeable combustor package. The microjet chosen is the JetCat P180 RXI-B shown in Figure 2, which has a centrifugal compressor and diffuser that feed air to the combustion chamber, and weighs only 4.9 lbs. A solid fuel package of Hydroxyl Terminated Polybutadiene (HTPB), which is good for the specific use at high-altitudes where a consequential problem is the lack of air for typical turbine engines. This will be submitted as a partnership between the University of Cincinnati and Ubiquity Interface as a Small Business Innovation Research for the Army.

The solid fuel will be in a unique donut design within the existing combustion chamber of the JetCat, placed with a connection point to the igniter. This will be made using a homemade fuel casing using Kraft paper and glue, with a process similar to the one shown in Figure 4. A pyrotechnical chemical will be electrically ignited to start fuel burn, and the gradient will specifically be designed in a gradient to provide 60% power at sea level and 100% power at the target altitude of 30,000 feet. The flight time will be set at 10 minutes for these calculations and experimentation goals, meaning the fuel will need to burn at the required power rates for this time. The burn rate of a solid fuel is determined by Saint Robert's Law:

$$r = ap_c^n$$

where r is the burn rate of the fuel, a is the burn rate coefficient, p_c is the combustion chamber pressure, and n is the pressure exponent. The terms for a and n are found experimentally. Based on prior research on HTPB, the fuel is found to burn at a lower chamber pressure when burning in the atmosphere. This means at the desired altitude there is a slower burn rate, extending flight time while

meeting the 60% power requirements of the engine. As the project progresses, the fuel will be purchased and tested by UC students in order to determine the optimal fuel grain cross-section geometry and the values for a and n. If HTPB isn't burning in a way conducive for this mission, a secondary solid fuel option is Glycidyl Azide Polymer (GAP), which is also thoroughly researched, but is known to have a higher burn rate.

An approach to reduce UAV refueling time opposed to batteries is an exchangeable combustor package. A view of the unmodified combustion chamber of the JetCat is shown in Figure 3. This assumes the use of a solid fuel gradient described above, which eliminates the need for fuel lines and a tank. The concept is to modify a microjet engine to allow a cartridge-like solid fuel gradient to be inserted through a door on the casing of the engine, directly into the combustor chamber. Figures 5, 6, and 7 show different angles of these changes made to the JetCat in Solidworks. Once a model is 3D printed for proof of concept, and the planned modifications fit within a purchased JetCat, then the engine parts can be actually modified and tested with a solid fuel grain. The next step is finding a UAV body to outfit with these modified engines, and wind tunnel testing.

Figures/Charts

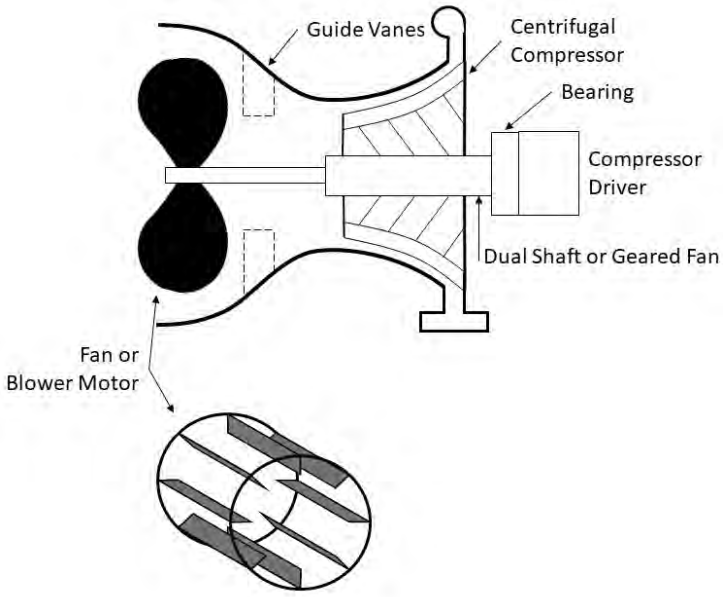

Figure 1. Fan-Centrifugal compressor system for a turbocharger

Figure 2. JetCat P180 RXI-B

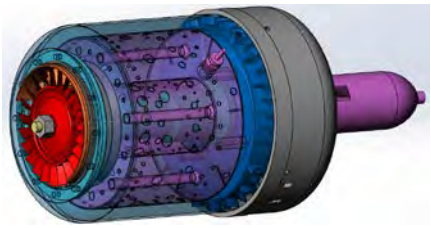

Figure 3. JetCat Solidworks cutaway view

Figure 4. Kraft paper wrapped around a dowel rod to make a pliable but strong fuel casing

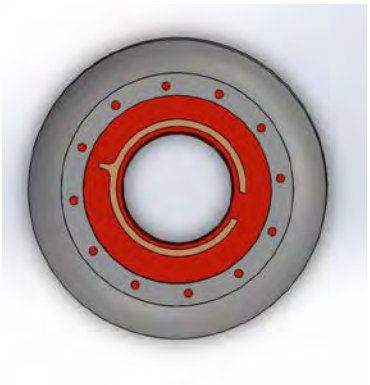

Figure 5. Side view ft. window and igniter

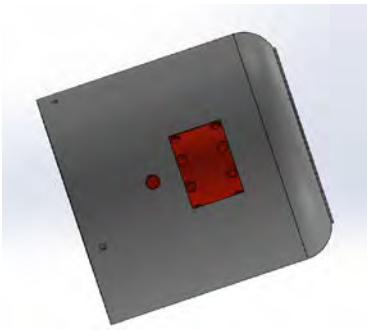

Figure 6. Top View of combustion chamber, envelope, and fuel grain

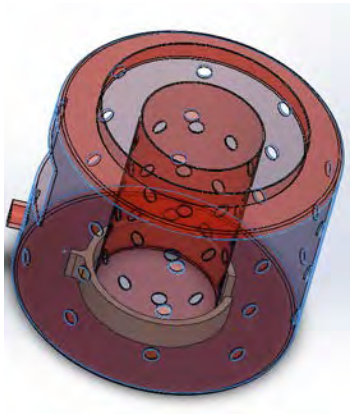

Figure 7. Transparent combustion chamber with fuel grain

Acknowledgments

The author would like to thank Dr. Shaaban Abdallah, her research advisor, for supporting her the past two years and giving her breadth and freedom to pursue to many different projects. McKenzie Kinzbach, for assisting in this research and always being willing to share her expertise and time. And finally, Dr. Kelly Cohen, for guiding me through this process during my undergraduate years.

References

1. J. Joy, “Solid Fuel Turbine Engine”, Patent number US5010728A, 1985.
2. Hobby Rocket Motor Paper Tubes <http://www.instructables.com/id/Hobby-rocket-motor-paper-tubes-parallel-/>
3. I. Komai, K. Kobayashi, K. Kato, “Burning Rate Characteristics of Glycidyl Azide Polymer (GAP) Fuels and Propellants “, NOF Corporation, Aichi Japan, AIAA (1999).
4. S. Krishnan and R. Jeenu, “Combustion Characteristics of AP/HTPB Propellants with Burning Rate Modifiers”, Indian Institute of Technology, Madras 600036, India, Journal of Propulsion and Power Vol. 8, No. 4, July-Aug 1992.

Flexible Wing Technology Applied to Drone Technology

Student Researcher: Anthony O. Smoktonowicz

Advisor: Brian Trease, Ph.D.

The University of Toledo
Electrical Engineering Technology with Mechanical Concentration

Abstract
Flight has been a topic of study, artistic expression and scientific design for an extensive duration of time. While the theories of fixed wing and rotor flight have been developed and engineered since the 1800's, the field of flapping wings is still relatively new to the scientific community with respected to applied sciences. There are considerable theories and even models such as ornithopters developed that duplicate flapping flight, yet the mathematics behind design, and application of flapping winged drones has yet to be commonplace. There have been successes by a few universities nationwide regarding mimicking the flight of a hummingbird or hawk.

Project Objectives
This researcher will work towards the implementation of flapping wing technology into a functional autonomous drone that mimics the takeoff, flight and landing of an avian.

Results
Currently, this researcher is still experimenting with the children's toys and balsa wood constructions of bird-like flapping models. The mathematics behind vorticity and incompressible fluids is still several semesters beyond my current level. I will continue to build various models utilizing various modes of locomotion including DC motors with gearbox mechanisms and shape memory alloys. There are quite a few variables regarding how a bird actually flies. A few are that a bird has control over the shape and angles of the wings during flight. Plus, even the aeroelasticity of the bird's skin contributes to the bird's ability to take and sustain flight. This researcher will start with the initial area of flapping to achieve takeoff.

Conclusions
My research is still in the initial stages, my first objective is to construct a model that will not only utilize the principles of aerodynamics but also mimic the flapping motion of birds in flight for locomotion. While working with multiple materials for lightweight yet high strength is proving to be a difficult area to find a balance. The locomotion method for the flapping motion is also presenting challenges. This area is more than a simple short term project, this researcher will pursue this area long term.

Publications
None

Elucidating the Pathway by which miR-146a leads to Upregulation in Phagocytosis

Student Researcher: Daniel J. Stank

Advisor: Dr. Kaleb Pauley

Cedarville University
Biology Department

Abstract
Sjögren's syndrome is an autoimmune disease that affects the salivary and other secretory glands. It has been shown that individuals with the disease have upregulated miR-146a. Previously, we found that increased levels of miR-146a increase phagocytosis. This may be the body's attempt to clean up the cells killed by the immune system. We sought to elucidate the pathway by which miR-146a leads to an upregulation in phagocytosis. We found that TNF Receptor Associated Factor 6 (TRAF6), a protein which has been linked to phagocytosis and miR-146a pathways, is not involved in this pathway. Further research is needed to determine the mechanism by which miR-146a upregulates phagocytosis.

Project Objectives
Sjögren's syndrome is an autoimmune disease that affects the salivary and other secretory glands. This leads to symptoms including dry mouth, dry eyes, and other GI tract issues. While the symptoms do not lead to death, as they do in some autoimmune diseases, research is still needed for these patients because it has a severe impact on their quality of life.

MiR-146a is a microRNA that is upregulated in Sjögren's patients (Konstantin et al. 2006) In previous studies, Pauley et al. linked upregulation of miR-146a to an increase in phagocytosis (2001). Later, Pauley et al confirmed this link using apoptotic E. coli. bacteria cells. Further, we have shown that upregulation of miR-146a is also linked to phagocytosis of apoptotic human cells, using a Jurkat line (manuscript in progress).

In the year under the OSGC grant, we began the work on elucidating the pathway by which miR-146a leads to upregulation of phagocytosis. We began this process by testing to see if TRAF6, a protein which has been linked to both phagocytosis and miR-146a, was in the pathway by which miR-146a leads to an upregulation in phagocytosis. We tested this by knocking down TRAF6 and seeing if this had an effect on phagocytic levels. When we found that knocking down TRAF6 had no significant effect on phagocytosis, we began testing metadherin, a protein linked to cytoskeletal development. We believe metadherin (MTDH) could be involved with phagocytosis since cytoskeletal redevelopment is an important factor in phagocytosis.

Methodology Used
For a model of patient cells, we used THP-1 cells which we then transfected with TRAF6 siRNA to see if this would decrease phagocytic levels. After being transfected the cells were allowed to grow and multiply for two days.

On the third day of the experiment, we prepared apoptotic Jurkat cells to serve as the model of dead cells in the secretory glands of Sjögren's syndrome patient. These cells accumulate in these locations when the patient's immune system kills them. We treated the Jurkats with etoposide to make them apoptotic. On day three we also treated the THP-1 cells with PMA to cause them to differentiate into macrophages.

On day four, we "fed" the apoptotic Jurkat cells to the differentiated THP-1 cells and measured the phagocytosis by staining the Jurkats with phrodo, which fluoresces in low pH, indicating the cell had been phagocytosed and was in the low pH environment of a digestive vacuole (caused by merging with lysosomes) and using immunofluorescence. We then measured the net fluorescence intensity of the mock group and the TRAF6 knockdown group on a plate reader.

Results Obtained

We found no significant changes in phagocytosis when TRAF6 is knocked down. The results of knockdown of TRAF6 on phagocytosis can be seen in Figures 1 and 2. In the first experiment, we had a mean fluorescence in the mock group of 50.42 and 52.35 in the TRAF6 knockdown group. In the second experiment, we had a mean fluorescence in the mock group of 296.9 and 302.2 in the TRAF6 knockdown group. These numbers are different because there were different concentrations of cells in the two experiments. With p values of 0.73 and 0.87 respectively, it is clear that there is no significant difference between the cells in which TRAF6 was knocked down and the ones treated with a mock solution, in regards to phagocytosis.

Significance and Interpretation of Results

Now that we have shown that knocking down the genes coding for TRAF6 does not affect phagocytosis levels, we can conclude that TRAF6 is not in the signaling pathway by which miR-146a is upregulating phagocytosis. We are still in the process of determining if MTDH is involved in this pathway. Once the pathway is known, this will open up more possible targets for drugs designed to help Sjögren's syndrome patients, but there is still much to be done and this is a long way down the road.

Figures /Charts

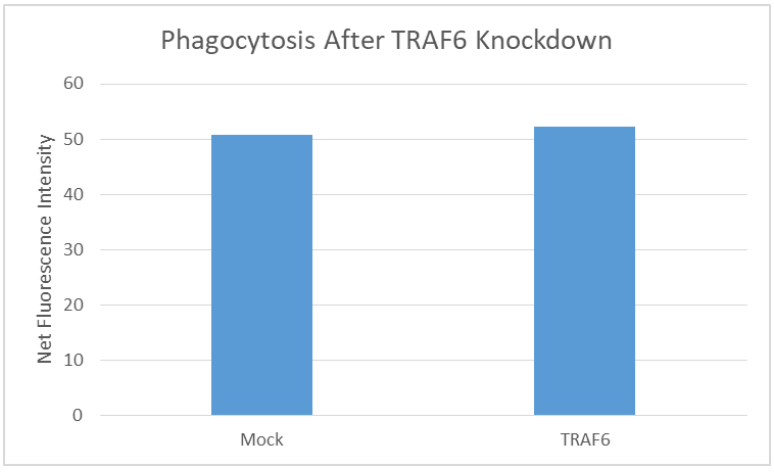

Figure 1. TRAF6 Knockdown Experiment 1

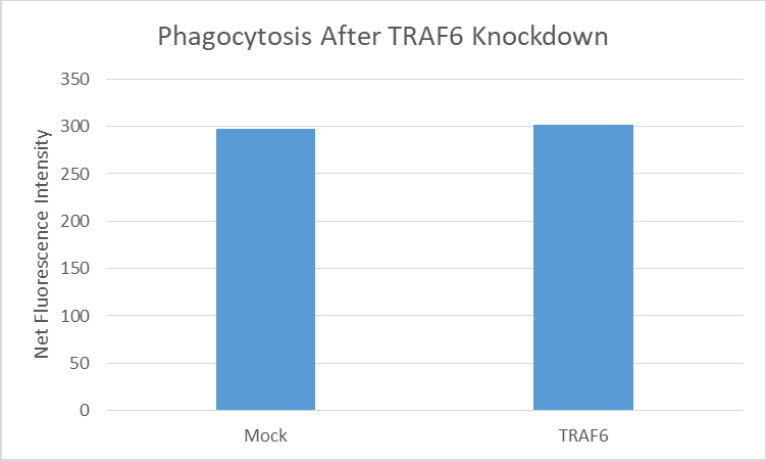

Figure 2. TRAF6 Knockdown Experiment 2

Acknowledgments
Many thanks to Dr. Pauley for her planning, assistance, and encouragement!

References

1. Konstantin D., T., Mark P., B., Kuang-Jung, C., & David, B. (2006). NF-κB-Dependent Induction of MicroRNA MiR-146, an Inhibitor Targeted to Signaling Proteins of Innate Immune Responses. *Proceedings of The National Academy Of Sciences Of The United States Of America*, (33), 12481. doi:10.1073/pnas.0605298103.
2. Pauley, K., Stewart, C., Gauna, A., Dupre, L., Kuklani, R., Cha, S., and Reeves, W. (2011). Altered miR-146a expression in Sjögren's syndrome and its functional role in innate immunity. *European Journal of Immunology*, 41(7), 2029-2039. doi:10.1002/eji.201040757.

Verification of Ideal Gas Law

Student Researcher: Kyle W. Strahm

Advisor: Dr. Jed E. Marquart

Ohio Northern University
Department of Mechanical Engineering

Abstract
The ideal gas law is a relationship used to model the behavior of ideal gases. An ideal gas is defined as point masses moving at a constant speed in a random, but straight-line motion. The objective of this project is to compare theoretical predictions using the ideal gas law to experimental results. To achieve the objective, the operation of an air compressor was analyzed, and compared with theory using the ideal gas law. Instrumentation was fitted to an air compressor and analysis software was incorporated to monitor and track the operation of the compressor. The reciprocating piston air compressor was fitted with the required pressure transducer(s), thermocouple(s), and an optical encoder to track the position of the rotating shaft. The pressure transducer and thermocouple were connected in line to the piston, and monitored the internal pressure and temperature in real time, relative to shaft rotation. The optical encoder was coupled to the input shaft that attached to the connecting rod of the piston. From the collected data the pressure, temperature, and shaft position were plotted, and compared with the ideal gas law.

This experiment demonstrated the usefulness of hardware and software inclusion on a real process for monitoring and validation purposes. It is essential that all equipment in aerospace applications be working properly, and this type of health monitoring is necessary to assure that operation.

Project Objectives
The objective of this research is to validate the ideal gas law and prove that pressure, volume, and temperature are proportional to each other experimentally.

Methodology Used
The study was conducted using a reciprocating air compressor instrumented with the following sensors: a k type thermocouple, a 1000 pulse per revolution (PPR) rotary encoder, and a 0 – 175 psig pressure transducer. LabVIEW was used to record the sensor outputs. For testing, the compressor and VI were started and data monitored during operation.

Preliminary Results Obtained
The results obtained proved that the concept and the method used were acceptable. Timing of the data acquisition hardware/software became an issue, and requires further testing and analysis. However, the correlation between experimental and theoretical results are confirmed.

Future Methodology Changes
In continuation of this project, the sampling rate for the data acquisition device will be increased to better capture the pressure and temperature data.

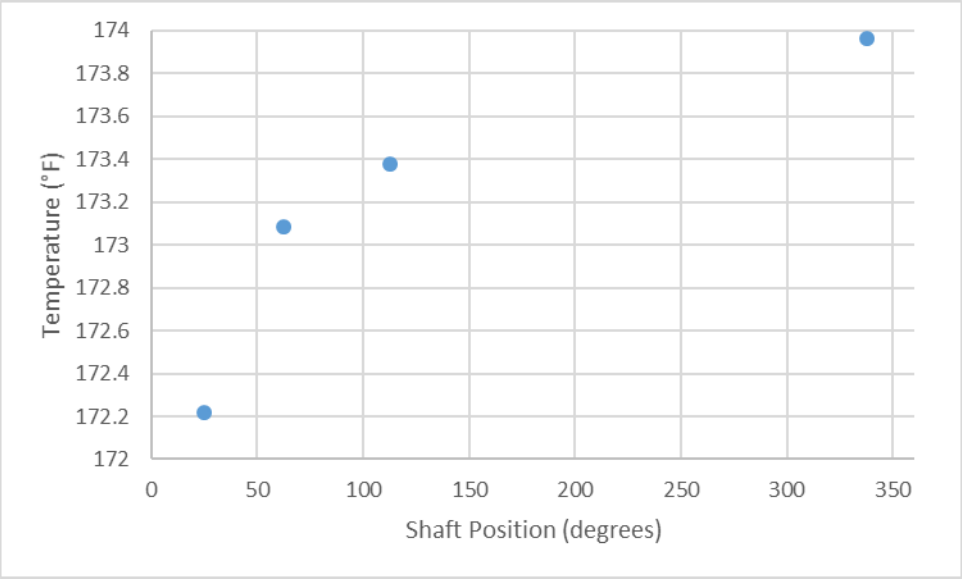

Figure 1. Shaft Position vs. Temperature

Design and Fabrication of Portable 3D Printed Cell Loader

Student Researcher: Robert P. Thoerner

Advisor: Dr. Marnie M. Saunders

The University of Akron
Biomedical Engineering

Abstract

When a human bone is exposed to microgravity, resorption ensues naturally due to the decrease in load on the osteocytes located within the bone matrix. The opposite can be seen in athletes where both the muscle and bone increase in mass to accommodate the increase in forces on their bodies. Testing of these cells traditionally requires a large loading machine able to apply ample load in order to stimulate these variances. When working in an adverse environment certain machines are deemed unusable due to spatial constraints or limited portability. A portable 3D printed machine is being developed that will overcome both of these constraints. The 3D printed machine will feature compatibility with in house developed labs on a chip. Labs on a chip are self-contained systems that are designed to simulate an area of the human body, in our case a bone system. This loading machine will allow for the sample to be loaded without altering the delicate system within the chip. The machine will allow for ease of loading and unloading of samples for extended periods of time while also being able to obtain an average surface strain between 15%-19% for extended periods of time to simulate physiological forces being applied on the chosen cells.

Project Objectives

Bone remodeling is a dynamic process that requires the communication and cooperation of the three primary bone cells: osteoclasts, osteocytes, and osteoblasts. In their simplest forms osteocytes are the cells that give off signals due to forces that tell other cells to remodel, osteoblasts are the cells that will lay down new bone and osteoclasts are the cells that resorb bone. Variance in this process can be characterized by malformation of the bone in question. Such examples being bisphosphonate-related osteonecrosis of the jaw (BRONJ), osteoporosis, and osteopetrosis. BRONJ is related to the degradation of the oral cavity and excessive bone loss when coupled with varying drug treatments[1].

Once more extensive space exploration occurs similar conditions may appear due to the introduction of varying gravitational forces being subjected on the human body. To simulate these forces expensive and large loading machines are used in lab settings. The loading machines can range in price to an incredible degree as well as requiring routine maintenance. As an alternative a microloading machine was developed that allows for a portable and potentially disposable unit for cell load testing. The machine utilizes mechanical loading in order to stimulate the cells from below using a circular platen. This system will allow for the sample to be put under load for extended amounts of time. Due to the nature of materials, once the machine is no longer able to operate properly it can be considered disposable and a new one printed.

In order to develop a machine such as this a few key points needed to be considered. The microloader must be able to apply a consistent load without the constant need for technician monitoring, the load being applied must be appropriate for the system in question, materials must be able to handle adverse environments, it must be operable by hand with no outside equipment needed and the device must be able to last multiple cycles before replacement is needed.

Methodology Used

The device was designed with the intent to house the previously created microfluidic labs on a chip. These chip are made of Polydimethylsiloxane or PDMS, a form of silicone. When designing the initial device precautions would have to be made to make sure that the device did not apply too much pressure as to break through the (.5mm) PDMS layer that will separate it and the cells. The platform that will house the chip consists of a baseplate (11 cm x 7 cm x 1.8 cm) with a hole directly in the center. This hole is where the 6-mm diameter platen will contact the PDMS and apply a force. The platen will transverse up to the base plate by using a screw located below it. In order to quantify the vertical displacement the thread pitch of the central screw was used. The device was designed so that one rotation of the base screw would translate to 1-mm displacement on the platen and subsequently on the cells. To help in quantifying one full rotation a dial was placed over the screw with tick marks spaced around it. This will allow a user to have a visual to how far the dial has been turned. To stop the platen from spinning and applying unintended torque on the cells as the screw turned a semi key lock system was utilized with small rectangular blocks printed onto the platen that restrict rotation. To help reduce preload on the cells, a chip holder was designed that allows for ease of transport before and after loading. A lid was then designed to make sure that as the load was being applied the chip did not simply move up with the platen. The baseplate and cover were designed so that the chip holder would fit within them and align the sample. To hold this cover with the base four screws were used in the corners of the system with thin hex nuts. Legs were utilized to allow for the system to not rest on the dial and allow for clearance if the dial needs to be turned more.

All components were created in SolidWorks 2017 in order to make easy changes and prepare for 3D printing (Figure 1). The design was 3D printed using Raptor series PLA as a material. This material is then annealed at 100°C for 15 minutes in order to increase its strength and heat resistance. The need for an increase in heat resistance results from the need of having cells within a bioreactor with regulated conditions including temperature and humidity. Early general tests showed that without having the material treated it would become malformed when load was being applied in the hot conditions of the biochamber.

In order to test properties before fabrication a finite element analysis (FEA) was conducted on the loading device using SolidWorks Simulation 2017. This was done to ensure that the PDMS would not fail during the experiment. For our specific case we are looking to load MLO-Y4 osteocyte cells. Previous works have shown that a 15-19% strain level is representative of a physiological environment. This strain range is conducive with a combination of both stimulation and traumatic strain levels[2]. When levels such as this are applied one would expect an osteocyte to give off numerous proteins and eventually necrosis. To quantify where these values would be located the average surface strain was modeled for various screw displacement and then a best fit line was created. The chosen values for the displacements were 1.2mm, 1.4mm, 1.6mm and 1.8mm. The PDMS was modeled as a nonlinear Mooney-Rivlin material due to its elastic nature[3].

Results and Discussion

Using the method outlined above a best fit line was created. Strain values versus displacement values can be seen in **Chart 1**. Using this best fit line equation the displacement value for an average surface strain of 15% was calculated to be 1.7226 mm and for an average surface strain rate of 19% the displacement was calculated to be 1.8947 mm. When these displacement values were then ran through the same analysis used to determine the best fit line the value of 1.7226 mm displacement showed to have a simulated average strain of 14.8% where as the input of 1.8947 mm showed an unexpected average strain of 16.5%.

The value for the predicted 15% strain matched to reasonable amount. The predicted value for the 19% strain varied greatly between actual strain and predicted. This variance is likely caused by the best fit line being used. In proceeding further with the project it may be import to run further material testing on the PDMS used in developing the chips before forming a more appropriate predictive equation.

Figures/Charts

Figure 1. Photoview 360 image of the complete prototype microloader. Slots on the top cover were included to allow for tubing to supply nutrients to the cells on the chip during loading.

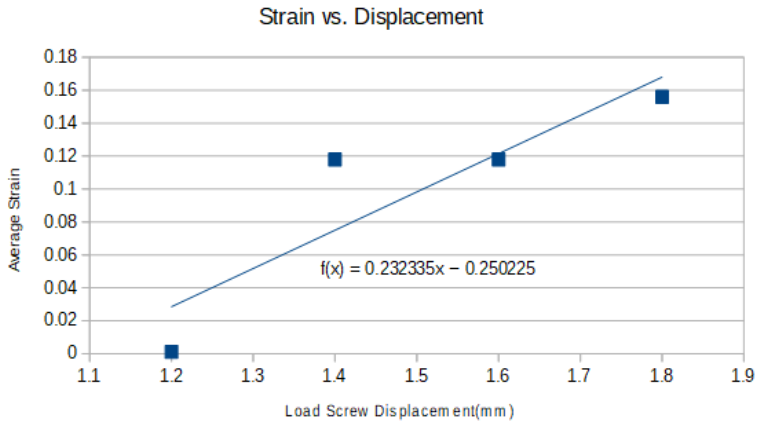

Figure 2. A comparison between the modeled average strain compared to the input load screw displacement. A best fit line was utilized to help form a general equation to help with future predictions.

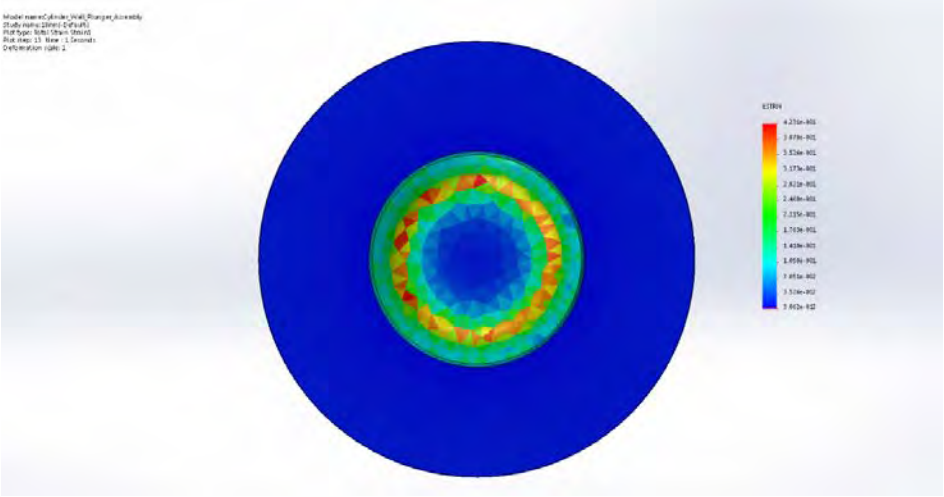

Figure 3. SolidWorks simulation 2017 top view strain analysis of loading well. Values calculated in the study consists of average strain it is important however to note the strain pattern of a circle around the edge of the platen. This high strain rate in these regions will likely result in cellular necrosis.

Acknowledgments
The author would like to thank OSGC for support, Dr. Saunders for guidance over multiple years and all the graduate students for their patience.

References

1. Ikebe, T., Pathophysiology of BRONJ: Drug-related osteoclastic disease of the jaw. Oral Science International, 2013. 10(1): p. 1-8.
2. York, S.L., P. Sethu, and M.M. Saunders, Impact of Gap Junctional Intercellular Communication on MLO-Y4 Sclerostin and Soluble Factor Expression. Annals of biomedical engineering, 2016. 44(4): p. 1170-1180.
3. Nunes, L.C.S., Mechanical characterization of hyperelastic polydimethylsiloxane by simple shear test. Materials Science and Engineering: A, 2011. 528(3): p. 1799-1804.

Exploring Transverse Myelitis

Student Researcher: Isis S. Tubbs

Advisors: George Armstrong, Abigail Yee

Cincinnati State Technical and Community College
Center for Innovative Technologies

Transverse myelitis is a neurological disorder caused by inflammation of the spinal cord and can have devastating neurologic effects with up to two-thirds of patients having a moderate to severe degree of residual disability. The term myelitis refers to inflammation of the spinal cord; transverse describes the position of the inflammation that is across the width of the spinal cord. Attacks of inflammation can damage or destroy myelin; the fatty insulting substance that covers nerve cell fibers.

Transverse myelitis interrupts the messages that the spinal cord nerves send throughout the body. Symptoms of this disease typically develop over hours or days and then worsen over a matter of days to weeks. Initial symptoms usually include weakness, localized lower back pain, paraparesis, sensory loss, and sudden paresthesias in the legs. Paraparesis often progresses to paraplegia. Some patients even experience autonomic dysfunction including bowel and bladder problems, temperature dysregulation or even bouts of hypertension. Motor symptoms often include weakness that preferentially affects the flexors of the legs and the extensors of the arms. Transverse myelitis is a relatively rare disease. The inflammation that causes such extensive damage to nerve fibers of the spinal cord may occur in isolation or in the setting of another illness. A number of conditions appear to cause transverse myelitis, including immune system disorders, viral infections, bacterial infections, fungal infections, parasities, vascular disorders, and other inflammatory disorders. Physicians diagnose transverse myelitis by taking a medical history and performing a thorough neurological examination. Researchers perform tests that can indicate a diagnosis of transverse myelitis and rule out or evaluate underlying causes, these test include magnetic resonance imaging, blood test, and lumbar puncture. The exact cause of transverse myelitis and extensive damage to nerve fibers of the spinal cord is unknown in many cases. Cases in which a cause cannot be identified are called idiopathic. Transverse myelitis is idiopathic in about 60% of cases.

Initial treatments and management of the complications of transverse myelitis include:

Intravenous corticosteroid drugs which may decrease swelling and inflammation in the spine and reduce immune system activity. These medications may also be given to reduce subsequent attacks of transverse myelitis in individuals with underlying disorders.

Plasma exchange therapy are used for people who do not respond well to intravenous steroids. Plasmapheresis is a procedure that reduces immune system activity by removing plasma (the fluid in which blood cells and antibodies are suspended) and replacing it with special fluids, thus removing the antibodies and other proteins thought to be causing the inflammatory reaction.

Pain medicines that can lessen muscle pain include acetaminophen, ibuprofen, naproxen. Nerve pain may be treated with certain antidepressant drugs, muscle relaxants, and anticonvulsant drugs.

Antiviral medications may help those individuals who have a viral infection in the spinal cord.

Transverse myelitis is researched daily to try to come to more conclusions of effective treatment. Along with treatments, follow initial therapy. It is very critical to keep the person's body functioning while hoping for either complete or partial spontaneous recovery of the nervous system. Many forms of rehabilitative therapy are available for people who have disabilities resulting from transverse myelitis. Strength and functioning of the body may improve with rehabilitative services, even years after the initial episode. Rehabilitative therapy teaches people strategies for carrying out activities in new ways in order to overcome, or compensate for permanent disabilities.

Transverse myelitis affects approximately 1400 people per year. Anyone can be affected by transverse myelitis, no matter the age or race of a person. Although rehabilitation cannot reverse the physical damage resulting from transverse myelitis, it can help people, even those with severe paralysis become as functionally independent as possible and attain the best possible quality of life.

Focusing on the adult crowd who are affected by transverse myelitis, they should not have to depend on caregivers if they desire to be as independent as possible. Individuals with transverse myelitis maneuver throughout life in a wheelchair, and along with this disability transportation barriers affect their lives in important ways. Over 20 years ago is when hand controls were introduced to the automotive industry. Hand controls are a set of controls in some cars, operated by hand that have the same function as the accelerator, brake and clutch pedals. Portable hand controls came along afterwards to add flexibility for disabled people. Portable hand controls are very useful because disabled people are able to drive any car they want without having to arrange ahead of time to get hand controls put on a vehicle. Another accessory that was introduced was the steering knob that attaches to the steering wheel to help turn the steering wheel. After hand controls were introduced, the automotive industry created a way for individuals to be able to operate a motor vehicle while in their wheel chair.

Although these solutions for driving are great and helpful, some suggested design improvements could help to make them better. Handicap vehicles that are operated by an individual maneuvering behind the wheel of a vehicle, while in their wheelchair should have special locks put in place, so that the wheelchair does not move while the vehicle is in motion. While doing some research for individuals that prefer to only use the portable hand controls, some found difficulty in installing them on to the pedals because they had to extend their arms so far under the steering wheel to tighten them. A knob at the top of the hand control should be put in place to prevent that struggle.

Particle Imaging Velocimetry Analysis of Wake Induced by Real Whiskers

Student Researcher: Jodi C.Turk

Advisor: Dr. Wei Zhang

Cleveland State University
Department of Mechanical Engineering

Abstract
Biomimicry has been utilized to create innovative solutions in a vast range of applications. One such application is the design of seal-whisker-inspired flow sensors for autonomous underwater vehicles (AUVs). In dark, cramped, and unstable terrain AUVs are not able to maneuver using visual and sonar-based navigation. Hence, it is critical to use underwater flow sensors to accurately detect minute disturbances in the surroundings. Certain seal whiskers exhibit a unique undulating three-dimensional morphology that can reduce vortex induced vibrations (VIVs) if the major axis of the whisker cross-section is aligned to the inflow. This allows the seal to precisely track prey fish upstream using solely their whiskers. The current study aims to understand the effect of a real seal whisker's morphology on the vortex shedding behavior. Despite extensive studies of the wake induced by scaled whisker-like models, the vortex shedding in the wake of a real seal whisker is not well understood. A series of experiments are conducted with a high-speed Particle Imaging Velocimetry (PIV) system in a water channel to examine the vortex shedding downstream from a smooth whisker and an undulating whisker at a Reynolds number of a few hundred. Results of the vortex shedding induced by real seal whiskers can provide insights on developing high-sensitivity underwater flow sensors for AUVs and other whisker-inspired structures.

Introduction and Objectives
Biomimicry takes shapes and forms from nature and finds ways to apply these designs to solve engineering problems and because of its success biomimicry has become an increasingly popular field of study. One potential nature inspired design has come from seal whiskers. The design came from the observation that harbor seals are found to be able to track their prey by capturing even minute disturbance of the ambient water solely by using their whiskers, instead of visual and auditory sensing capability[1,2]. This is attributed to the fact that a harbor seal whisker has a unique undulating morphology, as shown in Fig. 1b and is similar to the morphology of an elephant seal whisker[3]. The major and minor axes can both be seen as well as peak and trough locations on both axes. Research has shown that this unique morphology suppresses vortex-shedding in the wake flow and reduces vortex induced vibrations (VIV). This allows the seal to sense very small fluctuations within the incoming flow, such as the wake of a fish, and in turn this significantly enhance the seal's capability to track the fish[4] (Fig. 1a). It is of great interest to develop whisker-inspired flow sensors, by adopting and optimizing the whisker morphology, for autonomous underwater vehicles (AUVs). A need for high-sensitivity underwater flow sensors is critical for AUVs to smoothly navigate through dark, cramped, and unstable terrain because in this harsh environment, vison-based and sonar sensors usually do not function well.

Previous research has studied the effects of the parameters of the whisker morphology on wake structure using idealized whisker-like models with both experiments and CFD analysis[4,5,6]. These studies focused on a single wavy cylinder or idealized whisker inspired ellipse to try and understand the effects of different morphologies on the wake[7,8]. The studies found that the wake behind a whisker model and a circular cylinder are very different and benefits, such as a different von Kármán vortex sheet which leads

to reduced vibration, can be seen. Other studies have analyzed the vibrations of a whisker[4,9,10] and the mechanics of a whisker to understand how a seal is able to track prey in the water[11].

While these studies have focused on the wake effect of a single idealized whisker a real seal has many whiskers that have a natural variation in length, size and twist along the length of the whisker. Due to these parameters, it is not well understood how a real seal whisker changes wake flow. Some recent studies have started to quantify the wake of a real whisker[12] but the vortex shedding is still not well understood.

The uncertainty of the vortex shedding from a seal whisker hinders the capability to design whisker-inspired underwater flow sensors. This research uses high speed particle imaging velocimetry (PIV) to analyze the wake structure behind a real elephant seal whisker at a peak and trough location while comparing it to a California sea lion. By analyzing the vortex shedding behind a real elephant seal whisker, undulating morphology, and a California sea lion, smooth morphology, the effects of the whisker morphology can be understood and applied to developing high sensitivity underwater flow sensors.

Methodology

One real elephant seal whiskers and one real California sea lion were used. The elephant seal whisker has a unique undulating morphology and the California sea lion whisker has a smooth morphology, the geometric parameters are listed in Table 1. Due to the variation in dimensions the hydraulic diameter was used to perform the calculations to quantify the wake of the whiskers. The average hydraulic diameter was calculated for the peak and trough locations on the elephant seal whisker and for a specific location on the California sea lion, Table 1. The equations used are show in equations 4, 5, and 6.

Table 1. Average dimensions of the real elephant seal whiskers.

	Peak Diameter	Trough Diameter
Elephant Seal Whisker - Major Axis (mm)	0.9779	0.8255
Elephant Seal Whisker - Minor Axis (mm)	0.5207	0.4953
Elephant Seal Whisker Peak - D_h (mm)	0.650	
Elephant Seal Whisker Trough - D_h (mm)	0.601	
California Sea Lion - Major Axis (mm)	0.9906	
California Sea Lion - Minor Axis (mm)	0.6858	
California Sea Lion - D_h (mm)	0.797	

$$D_h = \frac{4*A}{P} \quad (4)$$

$$A = a * b * \frac{\pi}{4} \quad (5)$$

$$P = 2 * \pi \sqrt{\frac{a^2}{2} + \frac{b^2}{2}} \quad (6)$$

Where D_h is the hydraulic diameter, which is calculated from the area, A, and perimeter, P, of the whisker. For the area and perimeter, a is the major axis diameter and b is the minor axis diameter.

This study used elephant seal whiskers in comparison to previous studies that used harbor seal whiskers because they both have an undulating morphology. Table 2 shows the comparison between the eccentricity Eq. 5 of the harbor seal whisker and the elephant seal whisker[3].

$$\epsilon = \sqrt{\frac{a^2+b^2}{a^2}} \tag{7}$$

Table 2. Eccentricity of a real harbor seal whisker in comparison to a real elephant seal whisker[3].

	ϵ_{peak}	ϵ_{trough}
Harbor Seal Whisker	0.924	0.836
Elephant Seal Whisker	0.856	0.751

The closer ϵ is to 0 the more cylindrical the cross section is and the closer ϵ is to 1 the more parabolic the shape.

Table 2 shows that the harbor seal is more parabolic in shape but both are more parabolic than cylindrical in shape than. The other values of the two whiskers are similar[3] so a comparison between the studies using harbor seal whiskers is still relevant.

The real whiskers were mounted in the water channel at the Biofluid and Biomimic Research Center (BBRC) of Pohang University of Science and Technology (POSTECH) in Pohang, South Korea. The wake and vortex shedding were measured using the high-speed PIV system. The water channel has a test section of 0.30 m (W) × 0.25 m (H) × 1.20 m (L). The experimental setup can be seen in Fig. 2. The flow comes in from the left and a single whisker was placed in the center of the water channel in line with the laser light sheet and the water was a fully developed flow. The whiskers were also rotated to an angle of attack (AOA) of 0˚ and 90˚. When the minor axis is aligned with the inflow this is considered an AOA of 0˚ and when the major axis is aligned with the inflow this is considered an AOA of 90˚. The water was seeded with tracer particles (silver hallow spheres) of a diameter of 44 microns to visualize the flow. The water channel had a constant velocity of 0.49 m/s, giving a Reynolds number of 389 (California sea lion), 317 (elephant seal – peak), and 293 (elephant seal – trough), with a streamwise turbulence intensity of three to four percent.

To conduct these measurements a high-speed PIV system was used to capture the vortex shedding behavior induced by a seal whisker. The particle images were taken in the horizontal plane at a rate of 5000 frames per second (fps), with a Fastcam SA1.1 Photron High Speed Camera and a Nikon ED AF Micro Nikkor 200 mm 1:4D Lens (fitted with a Nikon L37c 62 mm filter). The laser light sheet was strategically aligned on the peak and trough locations on the elephant seal whisker as well as a similar diameter on the California sea lion whisker, Figure 3.

A total of 8000 images were captured for each location and analyzed using the window-based correlation method (DaVis 8.3 LaVision GmbH). A two-pass procedure was employed: initial interrogation window of 32 by 32 pixels followed by a reduced window of 16 by 16 pixels with 50% overlap in each pass. Instantaneous velocity fields were captured and then the frequency of the vortex shedding was captured for each of the whiskers.

Results and Discussion

Plots were created for the mean velocity and vorticity for each of the trials in the horizontal plane. The velocity component obtained in this experiment is the streamwise velocity, u (in the x direction).

The first set of images show an instantaneous capture of the vortex shedding for peak and trough locations as well as the smooth whisker, where the flow comes in from the right. The instantaneous flow shows a significant difference between the two AOAs, Fig. 4. The recovery time is faster with the AOA of 0˚ and the wake is narrower. The peak and trough locations also show a faster and more narrow recovery time in comparison to the smooth whisker.

The instantaneous vorticity shows a similar pattern to the instantaneous velocity fields, Fig. 5. Where the is even a larger difference between the AOA of 0˚ and 90˚. There does not seem to be a significant difference between the peak, trough, and smooth whiskers for an AOA of 90 ˚

From the instantaneous velocity fields the power spectral density was calculated for each of the whiskers, Fig. 6. To calculate the power spectral density (turbulent kinetic energy) a time series of the velocity was taken at two diameters behind the whisker and a FFT in MATLAB was run on the time series. The FFT was then put into terms of the power spectral density to compare the frequency and energy of the vortices shedding from the whisker. It can be seen that the smooth whisker has a higher energy but lower shedding frequency in comparison to the undulating whisker at the peak and trough locations. It is also shown that the AOA of 90˚ causes a significantly higher power spectral density in comparison to the AOA of 0˚ for all locations.

In conclusion, the whiskers show a shorter recovery time for the undulating whisker in comparison to the smooth whisker. Higher intensities are observed for the vorticity of a smooth whisker in comparison to the undulating whisker. There is a noticeable difference in vorticity and recovery time between the peak and trough locations of an undulating whisker. Distinct shedding frequencies for each measurement location on the smooth and undulating whiskers due to the location and the AOA are seen.

This research has shown that seal whiskers are able to reduce the forces and vibrations caused by fluid flow around its body in comparison to a sea lion whisker of similar dimensions at the same Reynolds number. The peak and troughs of the seal whisker have also been shown to cause a different wake structure as well as the AOA. However, it is still unclear as to how the vortices shed off of the whisker and how much the whisker itself vibrates in this process.

To continue this research, higher Reynolds numbers will be tested which are closer to what a seal experiences while hunting. Pressure calculations can be performed to understand what pressures are present due to the whisker and a deeper analysis of the vibration of the whisker and an uncertainty analysis will be performed. By conducting these future tests, a deeper and stronger understanding can be found that will help with the ultimate design of underwater flow sensors and airfoils.

Figures

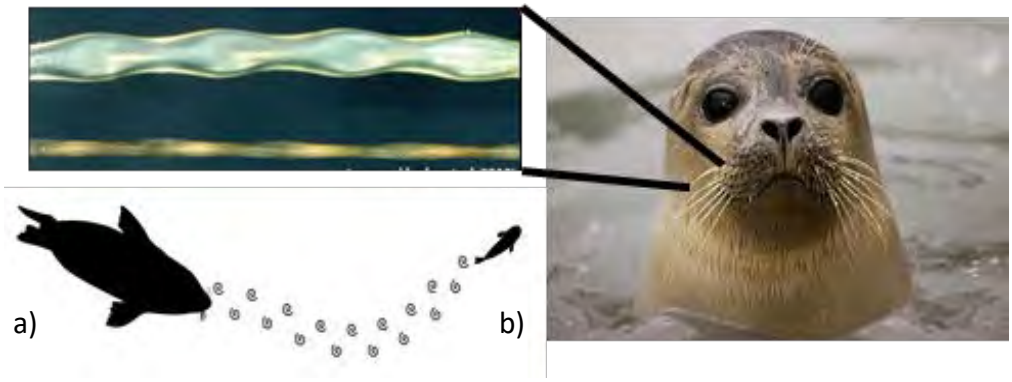

Figure 1. a) Harbor Seal has an exceptional capability to tracking it's prey using solely its whiskers[4]; b) harbor seal's whiskers on the seal and the zoom-in view of the whisker morphology[1]

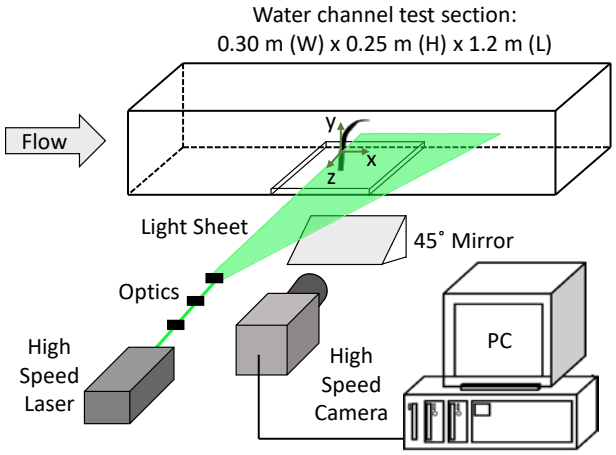

Figure 2. Experimental setup: A single whiskers mounted in a water channel and high speed PIV system setup.

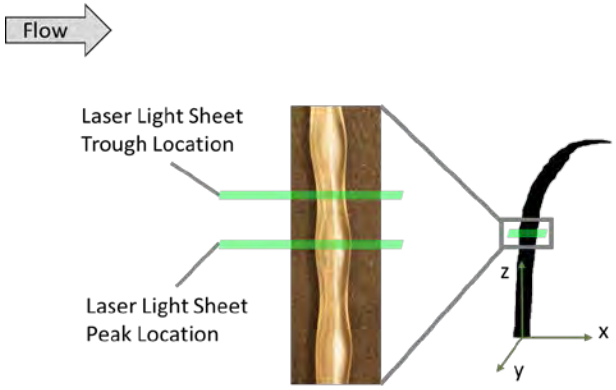

Figure 3. Schematics of the high-speed PIV measurement setup.

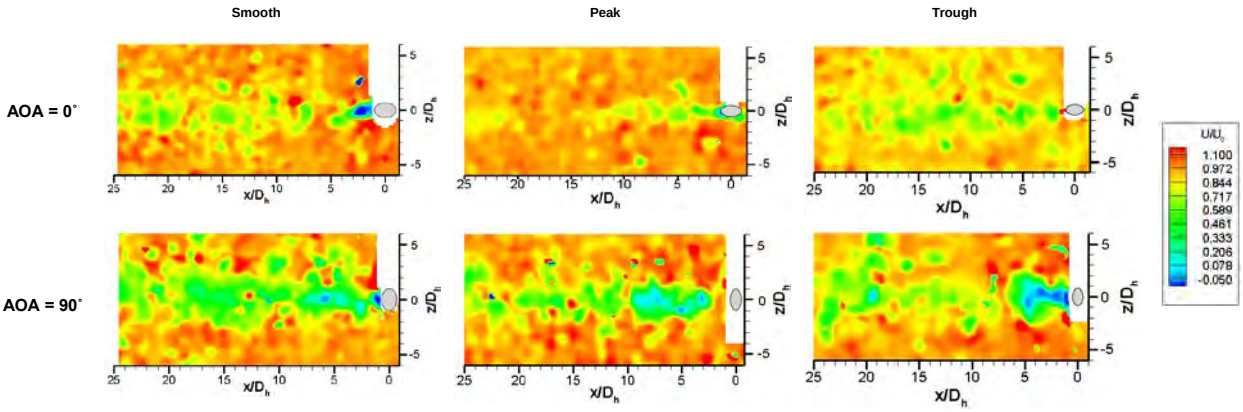

Figure 4. Instantaneous streamwise velocity fields in the horizontal plane for the smooth California sea lion whisker, elephant seal whisker at the peak location and an elephant seal whisker at the trough location for AOA of 0˚ and 90˚, flow from the right.

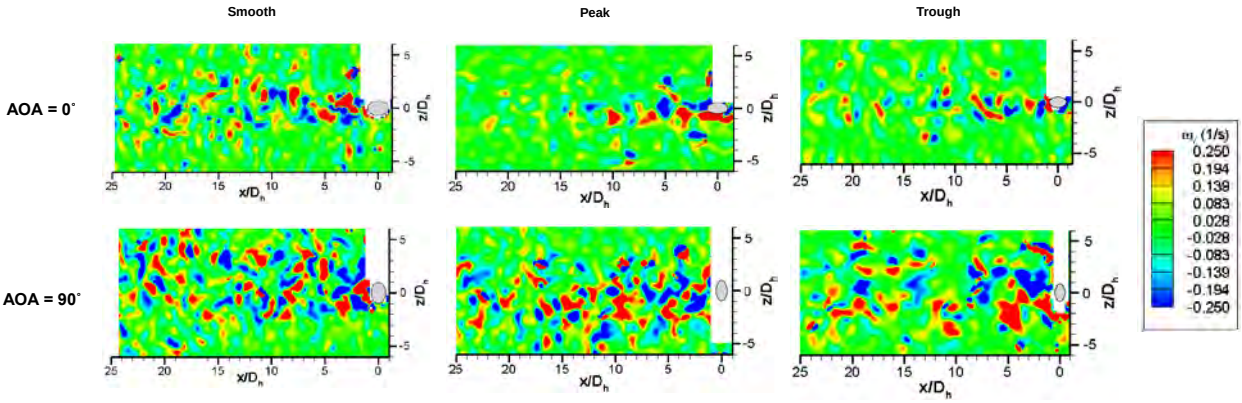

Figure 5. Instantaneous vorticity fields in the horizontal plane for the smooth california sea lion whisker, elephant seal whisker at the peak location and an elephant seal whisker at the trough location for AOA of 0˚ and 90˚, flow from the right.

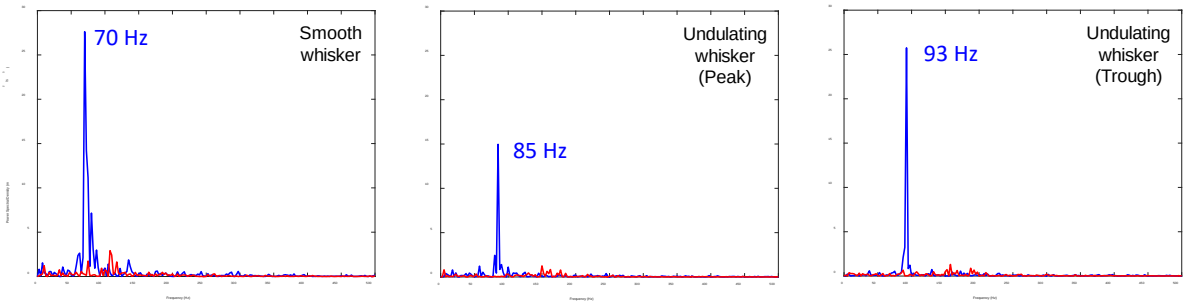

Figure 6. Power spectrum of the velocities at selective locations off the wake, the smooth whisker of a California sea lion, an elephant seal whisker at the peak location, and an elephant seal whisker at the trough location for AOA of 0˚ (red) and 90˚ (blue).

Acknowledgments
The author would like to thank the Ohio Space Grant Consortium for proving support for the author to complete her master's thesis, Ohio Aeronautics Institute for hosting the symposium, the National Science Foundation East Asia and Pacific Summer Institutes Fellowship (award number 1713991) for providing support to conduct the experiments at POSTECH, Dave Epperly for helping to fabricate the test plate, Dr. Wei Zhang for advising the author, and Dr. Sang Joon Lee for hosting and advising the author while she was at POSTECH.

References
1. Hanke, W., Witte, M., Miersch, L., Brede, M., Oeffner, J., Michael, M., Hanke, F., Leder, A., and Dehnardt, G., "Harbor Seal Vibrissa Morphology Suppresses Vortex-Induced Vibrations," The Journal of Experimental Biology, Vol. 213, 2010, pp. 2665-2672.
2. Hanke, W., and Dehnardt, G., "Vibrissal Touch in Pinnipeds," Scholarpedia of Touch, 2016, pp. 125-139.
3. Rinehart A, Shyam V, Zhang W, "Characterization of Seal Whisker Morphology Implications for whisker-inspired flow control applications", Bioinspiration and Biomimecahics, 2017.
4. Beem, H., and Triantafyllou, M., "Wake-induced 'slaloming' response explains exquisite sensitivity of seal whisker-like sensors," The Journal of Fluid Mechanics, Vol 783, 2015, pp.306-322.
5. Zhang, W., Daichin, and Joon Lee, S., "PIV measurements of the near-wake behind a sinusoidal cylinder" Experiments in Fluids, 2005, pp. 824-832.
6. Lin, Y., Bai, H., Mahbub Alam, Md., Zhang, W., and Lam, K., "Effects of Large Spanwise Wavelength on the Wake of a Sinusoidal Wavy Cylinder," Journal of Fluids and Structures, Vol. 61, 2016, pp. 392-409.
7. Ginter, C., Fish, F., and Marshall, C., "Morphological Analysis of the Bumpy Profile of Phocid Vibrissae," Marine Mammal Science, Vol. 26(3), 2010, pp. 733-743.
8. Ginter, C., DeWitt, T., Fish, F., and Marshall, C., "Fused Traditional and Geometric Morphometrics Demonstrate Pinniped Whisker Diversity," PLoS ONE, Vol. 7(4), 2012.
9. Murphy, C., Eberhardt, W., Calhoun, B., Mann, K., and Mann, D., "Effect of Angle on Flow-Induced Vibrations of Pinniped Vibrissae", PLoS ONE, Vol. 8, 2013, pp e69872-e69872.
10. Beem, H., Liu, Y., Barbastathis, G., Triantafyllou, M., "Vortex – induced vibration measurements of seal whiskers using digital holography," 2014.
11. Hans, H., Miao, J., and Triantafyllou, M., "Mechanical Characteristics of Harbor Seal (Phoca vitulina) Vibrissae under different Circumstances and their Implications on its Sensing Methodology," Bioinspiration and Biomimetics, Vol. 9, 2014.
12. Bunjevac, J., Turk, J., Rinehart, A., Zhang, W., "Wake Induced by an Undulating Elephant Seal Whisker," Journal of Visualization, Vol 21(2), 2018.

Water Filtration

Student Researcher: Matthew W. Walker

Advisor: Dr. Todd France

Ohio Northern University
T. J. Smull College of Engineering

Abstract
I will be using the idea of water turbidity and water filtration for the basis of my project. The project will span two to three days. Students at the 2018 fall "STEM Day" run by Ohio Northern University will be the first participants in this activity. In addition to the water aspect, the activity is also focused on student trial and error and having students learn through error. Students should work in groups of 3-4. This activity allows students to understand water turbidity and science through trial and error.

Lesson Plan
The lesson plan is focused on the student's ability to use science to discover properties of different materials and their relation to the process of water filtration. The activity should take approximately 3 days. 2 for prototyping and testing, and one for a debrief. Students will receive the top part of a pop bottle cut in half. They will then wrap coffee filters around the nozzle of the bottle using rubber bands. Students will be allowed to use any materials they want to fill the bottle. They should fill it layer by layer, that is, each material should get its own visible layer.

Once the students have completed their initial design, the teacher should have ready some water that is dirty (pond water, water with dirt mixed in/watery mud). The teacher will get a sample of water and use a turbidity meter to give the student group an initial value. They will then pour that sample through their filter and collect the filtered water. The teacher will take a sample of the now filtered water and use the turbidity meter on it. The change in turbidity will be the score of the group.

If the change isn't good or the students didn't like their result, they should be encouraged to empty their bottle and try to change materials. 2 or 3 prototypes are what students should build before they build their final product. The final product will be tested 3 times, and students can keep the best score.

Objectives
- To understand the idea of water filtration and turbidity
- To use discovery and trial and error to produce a good product

Alignment with Ohio Academic Content Standards

Grades 9-12 Ohio Extended Standards: *Identify a consequence of soil, water or air pollution*

Grades 9-12 Ohio Extended Standards: *Identify soil, water and/or air pollution*

Underlying Theory
The activity is focused on a trial and error learning. In this approach, it is the assumption that full immersion will force students to figure things out. When working on this project, students will begin to realize which materials work, and which don't. Through this error, they can continue to try with the materials that work and build the best product possible. The teacher will act as a facilitator working with students to help them decide the best materials through their own logic.

Student Engagement
The entirety of this activity is designed to be active. Students should be hands-on for everything but describing the project. The students will be involved because they will want their water turbidity to have the best number (As close to 1 NTU as possible)

Resources
Each group needs a pop bottle cut in half to create the base and holder for the filter system. The team will also require some other basic materials of their choosing to make the filter work. Activated charcoal, rocks, sand, gravel, cotton, and dirt are all great examples of possible water filtration materials. The team will also require rubber bands and coffee filters for the end of their pop bottle. This will help to filter out big chunks of material without impacting the turbidity too much. Students should also be encouraged to try and bring some of these items from home. Many of them are common household items and can save the teacher time and money by having their students bring it in instead.

Assessment
The assessment will come in the form of the water turbidity results. A before and after sample will be compared and the difference, their result. Students will keep track of how the materials impact turbidity and which ones most positively contribute to the biggest difference.

Manduca Sexta Flying Wing Micro-Air Vehicle

Student Researcher: Matthias S. Weisfeld

Advisor: Dr. Roger D. Quinn

Case Western Reserve University
Mechanical and Aerospace Engineering

Abstract
This project seeks to create a lifelike replica of the *Manduca Sexta* Hawkmoth, specifically revolving around creating a physical copy of the wings with similar mass and flexural characteristics as the real moth itself. This involves the careful selection of materials to serve as the membrane and as the venation structure and the careful repeated construction of sets of wings, replicating the moth's real life properties.

Project Objectives
This project seeks to replicate the flight characteristics of the *Manduca Sexta* Hawkmoth in a mechanical form. This is split into 3 major parts: creating wings of the correct dimensions, weight, and proportions; creating a control system; and creating a body that can effectively house the control system. This section of the project revolved around the processes behind designing, analyzing, and creating both the forewings and hindwings. The scope of this project includes investigating the appropriate ratio of venation to membrane material similar to a real *Manduca Sexta*, as well as investigating appropriate materials that can be used as either the venation or membrane, and then creating a physical replica of the wings.

Methodology Used
We began by extracting the wings directly from actual *Manduca Sexta* Hawkmoths. The Case Western Biology Department runs the Willis Lab that incubates *Manduca Sexta* Hawkmoths. We acquired a small number of male specimens, that were freeze killed and preserved. We could then extract both the forewings and hindwings from the specimens. From there, we removed the scales of the wings using a lightly damp q-tip and small amounts of rubbing. We then scanned the wings using a 12800 dpi flatbed scanner, giving us a high resolution image of the wings. We then edited a representative wing to form a template from which we could construct the physical replica wings.

Figure 1. A Sample Scan of a Manduca Sexta Right Forewing

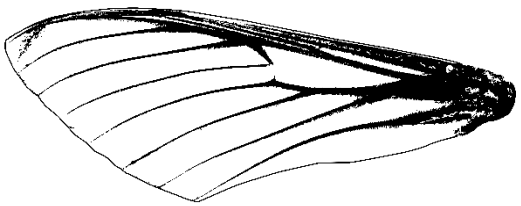

Figure 2. The Template Created from the Sample Scan

We tentatively chose Icarex Ripstop Nylon Polymer to act as the membrane material and unidirectional carbon fiber strips to act as the venation material. We cut thin strips of

Figure 3. A Manufactured Wing

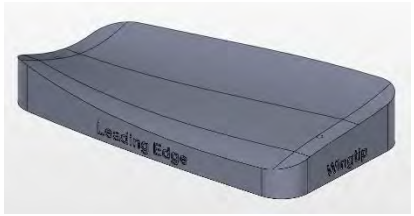

Figure 4. CAD Model of the Mold

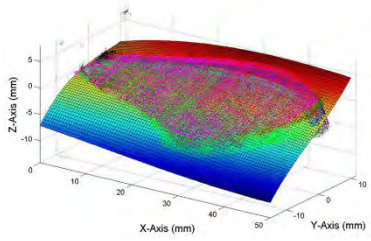

Figure 5. Graphical Depiction of the 3-Dimensional Curve Developed by O'hara and Palazotto, Fitting the Curve of the Forewing

unidirectional carbon fiber and attach them to the Icarex membrane in the appropriate position, making sure that they carefully match the mass of their corresponding opposite side, ensuring they roughly match. This is then placed onto a curved mold and baked in a vacuum sealed bag. After the mold has baked for an acceptable duration, it is removed and allowed to cool. The excess material is trimmed and the wing replica is weighed and compared to the average *Manduca Sexta* wing mass.

Our molds were based on an equation developed by R P O'hara and A N Palazotto.

Results Obtained

We sought to test if it was indeed possible to create a replica *Manduca Sexta* wing that had the appropriate mass characteristics and proportions. When we built our wings the best overall mass we managed to create was 0.0259 g. The average mass of a *Manuduca Sexta* wing was found to be 0.03521g from the O'hara Paper and 0.04116g based on our measurements. As our lowest number was quite a bit lower than the actual wings, we have found that it is indeed possible to create a wing with plausible mass characteristics. That being said, while it is certainly plausible, it is not practical. The average mass of our manufactured venation structure alone was found to be 0.02400g. This accounts for over half of the desired mass of the wings, where the venation structure should make up an estimated 10-20% of the overall mass of the wing.

While we were able to achieve acceptable mass characteristics for our wing replicas, we were not able to accurately ensure an appropriate venation pattern. Oftentimes, close together veins had to be combined, simply because it was practically impossible to cut thin enough carbon fiber with our current methods. This will be one of the next areas we work on. Additionally, we have not looked into also matching the flexural characteristics of the *Manduca Sexta* wing, and therefore will also be looking into this.

References

1. Ryan P. O'Hara, Anthony N. Palazotto, Richard G. Cobb, Peter J. Collins, (2006) "The Characterization of Material Properties and Structural Dynamics of the Manduca Sexta Forewing for Application to Flapping Wing Micro Air Vehicle Design," Air Force Institute of Technology.
2. Ryan P. O'Hara, Anthony N. Palazotto, (2012) "The Morphological Characterization of the Forewing of the Manduca Sexta Species for the Application of Biometric Flapping Wing Micro Air Vehicles," Air Force Institute of Technology.
3. Travis W. Sims, Anthony N. Palazotto, Richard Cobb, Eric Swenson, (2010) "A Structural Dynamic Analysis of a Manduca Sexta Forewing," Air Force Institute of Technology.

Variable Pitch Quadcopter Flight Control

Student Researcher: Austin M. Wessels

Advisor: Dr. Kelly Cohen

University of Cincinnati
Aerospace Engineering

Abstract
As small unmanned aerial systems (sUAS) have become more popular in the past few years, the desire for more maneuverable sUAS has grown. Traditional quadcopters use four separate motors to control the three rotational axes, roll, pitch, and yaw, and the one translational axis, altitude. The flight controller changes the rpm of each motor to achieve stable flight. The variable pitch multirotor has a single motor powering all four rotors, and a servo motor for each rotor to control the pitch of the blades. There are a few variable pitch quadcopters on the market currently; I will focus on the Stingray 500. One advantage of a variable pitch system is the ability to use a different power source such as an internal combustion engine. This would allow increased efficiency and longer flight time. The variable pitch multirotor is also more maneuverable given that the rotors are able to produce negative thrust. This allows to vehicle to maneuver upright as well as inverted. These flight characteristics can be achieved with slight modifications to readily available flight controllers already on the market, such as the Naze32 or FrSky F3FC. The Stingray 500 with this customized flight controller will be a stable yet maneuverable sUAS.

Purpose
The goal of this project was to develop a flight controller for a variable pitch quadcopter. The scope of this project will include modifying an off the shelf airframe to use an open source flight controller.

Flight Controller
Betaflight firmware seemed to be the obvious choice to control the Stingray. This firmware already supports 3D quadcopters. The firmware was modified slightly to support servos in place of electronic speed controllers and motors. There are many flight controllers that support Betaflight. Some flight controllers considered include the Naze32, FrSky F3FC, and the ReadyMadeRC Seriously DODO. All these flight controllers support servo outputs. The Naze32 was ruled out because it uses an older F1 processor. The FrSky F3FC has the newer F3 processor, but it uses an internal receiver. Ultimately the DODO flight controller was chosen. The DODO has an F3 processor and supports an external receiver.

Pre-flight Testing
Initial testing was performed using an analog for the multirotor, so as to not damage the vehicle. This analog used 4 four servos, and a Naze32 flight controller. This analog was used to test the modified firmware before use on the Stingray 500.

After the firmware was validated on the analog, testing moved to the actual flight hardware. The Stingray was set up with flight controller, electronic speed controller (ESC), receiver, and servos. The ESC's onboard battery eliminator circuit (BEC) powered all the servos through the receiver and flight controller. This configuration was tested by moving the control sticks without the motor active. It became clear the flight controller and the receiver would turn off briefly and reset. This is a critical failure and must be addressed before flight. The fault was traced to the servos drawing too many amps

for the configuration. Upon further testing, the ESC's onboard BEC had also been compromised. After an overcurrent event, the BEC would not reinitialize.

After these tests, the Stingray was reconfigured. Now the Stingray is equipped with a new ESC with onboard BEC to power the receiver and flight controller. Also, there is an external BEC to power only the servos. In this configuration the servos are allowed to draw more power with causing a voltage drop for the receiver or flight controller. The servos are able to handle the momentary voltage sag, unlike the receiver and flight controller.

Flight Testing

Flight testing began once the new configuration was completed. The Stingray was flown in our indoor flight area. The vehicle yawed and rolled; it was unable to maintain a stable hover. After this first flight, the Stingray was closely inspected. The inspection revealed three of the four rotor shafts were loose. This caused the rotor to be out of trim. The flight controller attempted to send a neutral signal, but the rotor was not neutral. The rotors were re-centered and tightened.

In the next flight, the vehicle bounced and oscillated in the roll axis. The orientation of the landing gear made this oscillation more pronounced. Once the quadcopter was in the air, it flew, but it oscillated about five degrees in pitch and roll. The vehicle was marginally stable. The flight controller needs to be tuned. Unfortunately, during that flight, the flight controller was not recording flight data.

In the next flight the PID gains were increased for the roll axis. In this final flight, the vehicle bounced and oscillated violently on the ground causing two rotors to strike the ground. This crash broke one blade grip and the main shaft pulley. The Stingray will need replacement parts before it can fly again. The blackbox log was recorded for this flight. It shows the oscillation as well as the poorly tuned flight controller.

Acknowledgments

I would like to give a special thanks to Dr. Kelly Cohen, Dr. Manish Kumar, and Bryan Brown for making this research possible.

Dynamic Stall Control over a Rotorcraft Airfoil using NS-DBD Plasma Actuators

Student Researcher: Nicole L. Whiting

Advisor: Dr. Mo Samimy

The Ohio State University
Mechanical and Aerospace Engineering Department

Abstract

Dynamic stall occurs in applications where airfoils are rapidly changing angle of attack, like rotorcraft or wind turbines. When the change is fast enough, flow over a pitching airfoil remains attached beyond the static stall angle. This results in the formation of a dynamic stall vortex on the leading edge of the airfoil, which eventually convects over the airfoil and sheds. Once the vortex sheds and the flow separates, unsteady aerodynamic loads are produced. These loads can lead to fatigue and eventually structural failure, making it essential to mitigate the effects of dynamic stall. Nanosecond Dielectric Barrier Discharge (NS-DBD) plasma actuators have shown promise at mitigating dynamic stall and reattaching the flow over a NACA 0015 airfoil, a thick, symmetric airfoil, significantly reducing unsteady loads. A high-voltage nanosecond pulse drives the actuator and creates rapid, localized heating that result in a thermal perturbation. The thermal perturbation then excites the flow's natural instabilities and generates coherent flow structures. Previous work has shown that high Strouhal number (non-dimensional frequency) excitation results in small structures that quickly develop, breakdown, and result in smooth, partial reattachment of the flow whereas low Strouhal number excitation results in large structures that are capable of fully reattaching the flow cyclically and lead to unsteady loads. This work aims at improving upon the previous work by upgrading the facility and data acquisition and reduction systems and using a thin airfoil to make the results more relevant to rotorcraft applications. A NACA 0012 airfoil is chosen because it is a well-documented, thin airfoil. Facility upgrades include integrating all systems into a National Instruments CompactRIO, which will allow for better synchronization between all control systems and measurement instruments. The airfoil pitching mechanism is being changed to a direct-drive servo, this allows for more accurate pitching angles over the previous setup, which used belts that could stretch and cause a phase delay. Previously the lift and drag on the airfoil were calculated by integrating pressure measurements which introduced error due to potential three-dimensionality in the flow. Therefore, a load cell will be used instead to directly measure the forces and momentums on the airfoil. Mitigating the negative effects of dynamic stall has the potential to increase the lifespan of blades and increase lift, which will allow rotorcraft to fly higher, faster, or carry larger loads.

Previous Work

A NACA 0015 airfoil was mounted in the recirculating wind tunnel located at the Aerospace Research Center. The airfoil was connected to an oscillating mechanism that varied the angle of attack sinusoidally. The plasma actuator was mounted just downstream of the airfoil leading edge at x/L=0.01. Baseline experiments were done with the plasma actuator installed but not on, to understand it's effect on the flow physics. Experiments were done for three Reynolds numbers based on the airfoil cord (Re=167,000, 300,000 and 500,000), at three reduced frequencies (k=0.025, 0.050, and 0.075) and 20 excitation Strouhal numbers ranging from 0 – 9.9. Detailed unsteady surface pressure measurements, and flow velocity and turbulence measurements were taken to assess the effect of control. The work resulted in a major conclusions [1]: low Strouhal number excitation results in large structures and high

Strouhal number excitation results in small structures, this results in the mitigation of the dynamic stall vortex and unsteady loads. This can be seen in Figures 1 and 2 below. They show the phase-averaged swirling strength at a Reynolds number of 300,000 and a reduced frequency of 0.050 while the airfoil is pitching down from 20 to 17 degrees. Figure 1 has an excitation Strouhal number of 0.35 whereas Figure 2 has an excitation Strouhal number of 9.9. In Figure 1, a large structure can be seen convecting over the airfoil, whereas in Figure 2, with an increased Strouhal number, several significantly smaller structures formed over the airfoil and disintegrate while convecting over the airfoil. The large structure convects over the entire airfoil and sheds from the airfoil, leading to oscillatory forces and moments on the blade. As the Strouhal number increases the oscillatory loads are significantly reduced, as shown in Figure 3. The figure shows the negative damping coefficient, which is directly related to unsteady loads [3].

Shortcomings of Previous Experimental Setup and Data Acquisition and Reduction System

Based on the previous research, NS-DBD plasma actuators show promise at suppressing dynamic stall and reattaching the flow over a NACA 0015 airfoil, significantly reducing unsteady loads. Due to design of the facility and the instrumentation used, there are some shortcomings in the repeatability, generating significant uncertainties in the collected data. The results are also not directly relatable to rotorcraft due to type of airfoil used. Therefore, the airfoil, force measurement system, servomotor and control system were all upgraded.

A NACA 0015 airfoil is characterized as a thick airfoil because its maximum thickness to chord ratio is 15 percent. Thick airfoils experience trailing edge stall. Rotorcraft, on the other hand, typically use thin airfoils because they are able to generate more lift, thin airfoils experience leading edge stall. Therefore, the previous results cannot be directly related to rotorcraft because the airfoil tested experiences a different type of flow separation. As a result, a NACA 0012 airfoil was manufactured for future experiments. It is a thin, symmetric airfoil with a maximum thickness to chord ratio of 12 percent. This specific airfoil was chosen because it is well characterized in literature.

In the previous setup, 35 static pressure taps were located on the surface of the airfoil in order to calculate the phase-averaged pressure coefficient. From the pressure coefficient the lift, drag and moment were calculated. Due to the long pressure tap lines, empirical lag/gain corrections were applied to the data. Overall, this system of calculating the lift, drag and moment introduced multiple sources of error. Therefore, the new system directly measures the lift, drag and moment using an ATI SI-660-60 6-axis force/torque transducer.

For dynamic stall experiments, the airfoil needs to be consistently changing angle of attack to simulate flight conditions; to do this the previous setup used a servomotor driven by timing belts. There are two main concerns with the previous setup, first the timing belts can stretch over time creating a phase delay and second the overall setup reduced the optical access. The servo was oscillated sinusoidally from 8 to 18 degrees at a frequency of 3.48 Hz. The individual cycles varied up to a degree, but the average result was similar to the desired motion. This is problematic from a repeatability standpoint, if the actual motion of the airfoil is unknown; the actual stall characteristics are also unknown. This can be attributed to the timing belts, over time they tend to stretch or slip. To counteract this, the new setup uses a direct drive servo that is accurate to a thousandth of a degree.

To secure the airfoil in the wind tunnel, its ends were connected to disks in the sidewall of the wind tunnel. The disks were then driven by the servomotor-timing belt combination. The disks in the sidewall of the wind tunnel obstructed the view near the trailing edge of the airfoil in Particle Image Velocimetry (PIV) measurements, therefore the vortex shedding over the trailing edge is obstructed, an example of

this is shown in Figures 1 and 2. PIV is a major optical measurement tool in obtaining detailed flow velocity and turbulence measurements. If the setup obstructs optical access to the model, it makes the tool significantly less useful in exploring flow physics. For that reason, the direct drive servomotor is installed in the floor of the wind tunnel with the load cell on top of it and the airfoil positioned vertically on top of them, therefore there will be no obstructions in the optical access, shown in Figure 4.

To control the system and collect data three data systems were used, these include a National Instrument Data Acquisition (NI-DAQ) system, three Scanivalve Pressure Scanners (SPS), and an ABB Servo Controller. To synchronize the NI-DAQ and the SPS a continuous chirp signal was used. The chirp was transmitted to the NI-DAQ using LabVIEW and it was transmitted to the SPS using a speaker. The constant lag between the inputs and outputs were determined and applied as a time correction. Synchronization between the NI-DAQ and ABB servo controller was achieved by aligning the analog output of the servo to the position given by the network connection. Having three data acquisition systems can introduce synchronization errors, which is extremely detrimental to dynamic stall tests since dynamic stall is time dependent. Therefore, the new system uses a NI-CompactRIO (CRIO). It has a real-time processor, a user-programmable FPGA, and interchangeable modules for each instrument, this ensures complete synchronization between each instrument.

Conclusion and Future Work

Dynamic stall occurs in applications where airfoils are rapidly changing angle of attack, when the change is fast enough, flow over a pitching airfoil remains attached beyond the static stall angle. This results in the formation of a dynamic stall vortex on the leading edge of the airfoil. The dynamic stall vortex eventually convects over the airfoil and sheds and the flow separates producing unsteady aerodynamic loads. These unsteady loads produce a rapid growth in blade torsion which can lead to fatigue and eventually structural failure. Due to these issues, dynamic stall is normally the limiting factor in the operational flight envelope of helicopters [2]. Therefore, in order to increase operating conditions of rotorcraft it is essential to mitigate the effects of dynamic stall. Previous research has shown promise at mitigating dynamic stall and reattaching the flow over a NACA 0015 airfoil using a NS-DBD plasma actuator. This work aims at improving upon the previous work by changing the airfoil to make it more relevant to rotorcraft, using a load cell to directly measure the forces and moments on the airfoil, changing to a direct-drive servo to mitigate the cycle-to-cycle motion variation, and incorporating all systems into one control system to ensure complete synchronization.

Future work for this setup includes static testing to ensure the results match literature. Detailed unsteady lift, drag, and moments and flow velocity and turbulence measurements will also be taken, at the same parameters tested with the old setup to see if the same trends occur. Overall, this research is being conducted to mitigate the negative effects of dynamic stall which has the potential to increase the lifespan of the blades and increase lift, which will allow rotorcraft to fly higher, faster or carry larger loads.

Figures

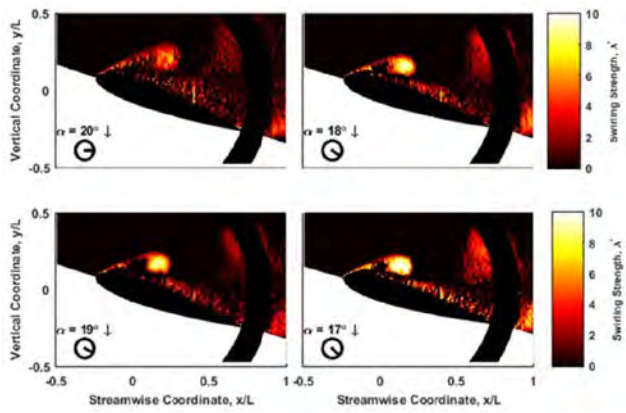

Figure 1. Re=300,000, k=0.050, and St_e=0.35 [1].

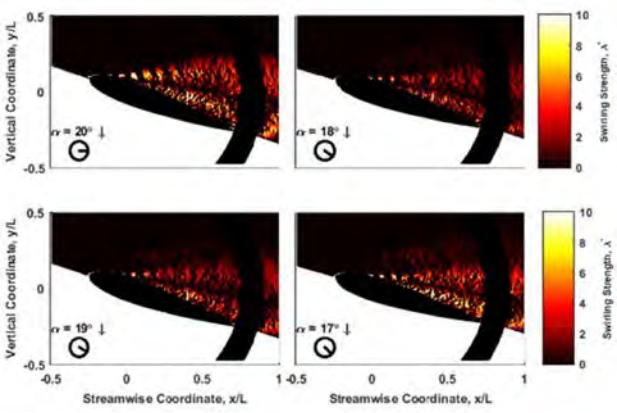

Figure 2. Re=300,000, k=0.050, and St_e=9.9 [1].

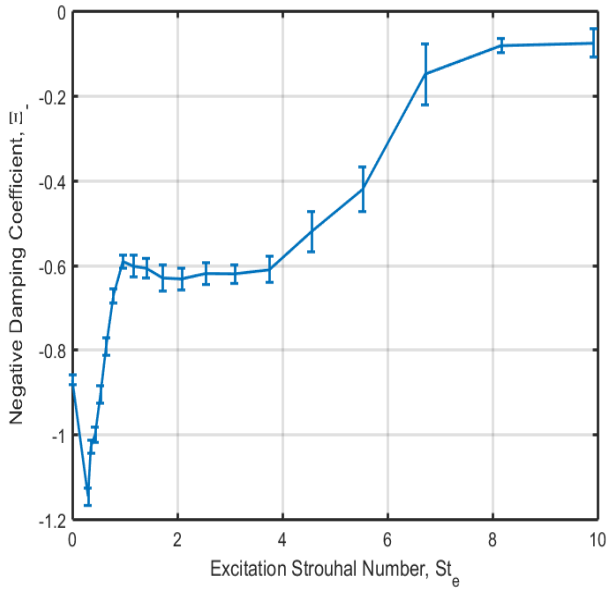

Figure 3. Negative damping coefficient at Re=300,000 and k=0.050 [1].

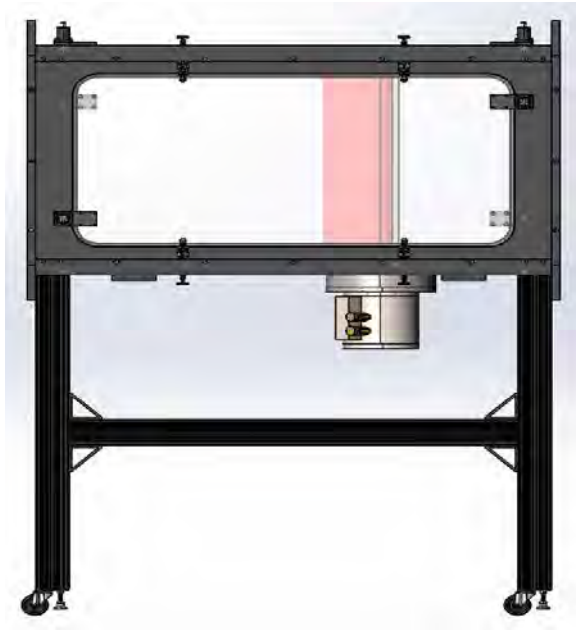

Figure 4. New experimental setup.

Acknowledgments

I would like to thank Dr. Mo Samimy, Dr. Nathan Webb, and David Castañeda for all of their guidance and help on this project. I would also like to thank the Ohio Space Grant Consortium for providing a scholarship for me to work on this project.

References

1. Singhal, A., Castaneda, D., Webb, N., and Samimy, M., "Control of Dynamic Stall over a NACA 0015 Airfoil using NS-DBD Plasma Actuators," AIAA Journal, Vol. 56, No 1, January 2018 – pp. 78-89.
2. Leishman, G. J. *Principles of helicopter aerodynamics*. Cambridge university press, 2006.
3. Corke, T.C. and Thomas, F. O., "Dynamic Stall in Pitching Airfoils: Aerodynamic Damping and Compressibility Effects," *Annual Review of Fluid Mechanics,* pp. 479-505, 2015.

Subsonic Wind Tunnel Development

Student: Robert R. Wilson

Advisor: D. Blake Stringer, Ph.D.

Kent State University
Aeronautics and Engineering

Introduction

A wind tunnel is an instrument used to measure aerodynamic forces and pressures applied to an object at a certain airspeed. There are generally two types: open and closed, both variations having their advantages and disadvantages. The wind tunnel at Kent State University is an open wind tunnel with a one-foot by one-foot test area. This wind tunnel serves as a sufficient academic tool for classroom work. But as the aerospace program rapidly expands, a new and improved wind tunnel is needed for academic, public and private use. This project serves to determine factors needed for design and development of a larger wind tunnel for the university

An open wind tunnel is a device that uses the air in the laboratory as its base for the air flow of the test section. The air is sucked into the test section by a fan and pushed out back into the lab where it circulates back into the wind tunnel. Advantages to an open wind tunnel include a lower construction cost and overall size. The space that the wind tunnel is operated in must be large enough that the walls of the lab will not affect air flow. Another advantage due to overall room volume is low temperature fluctuation. Some disadvantages to an open circuit wind tunnel are higher energy output/cost and lower flow quality. Open wind tunnels are generally smaller than their counterparts but can be very large. One of the largest wind tunnels is an open wind tunnel at NASA Langley capable of testing aircraft and spacecraft.

(A closed-circuit wind tunnel. John Calautit)

A closed wind tunnel differs from an open wind tunnel by inclosing the air used in the test section. The

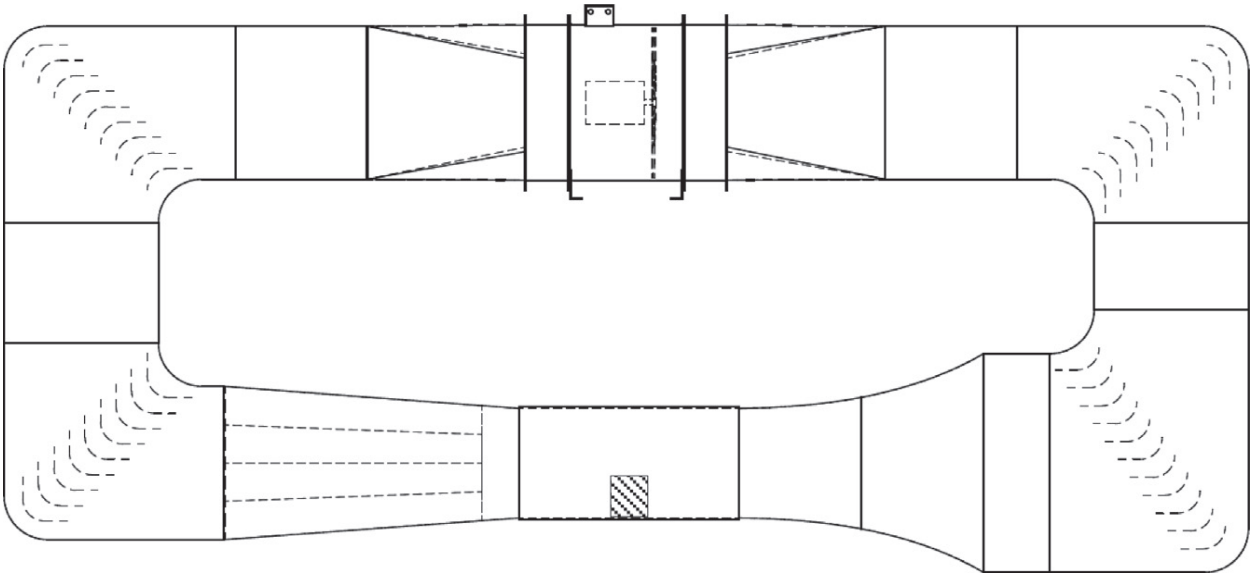

air is sent through the test section where it makes a 360-degree loop back to the test section. The difference is the air is enclosed in the wind tunnel as shown above. The advantages to a closed loop

wind tunnel include, better flow quality, higher operating speeds, and lower operating costs. Some disadvantages are a higher construction cost, and the overall size of the wind tunnel.

Wind Tunnel Section Identification

The first area of the wind tunnel is the test section. This is the most crucial area inside the wind tunnel because the flow quality. In general, the length of the test section should be maximized according to the cross-sectional area to maximize the flow quality. One factor to consider in design is the boundary layers of the test section and how these will interfere with the test data. “For a given cross section the length of the test section should not be made too large in order to avoid too much influence on the core flow from the wall boundary layers” (Lindgren).

The next area is the diffuser(s). The diffusers are found after the test section, in between the corners, and before and after the fan. These areas slow the air down as the diffuser expands. These areas use Bernoulli’s Principle which states that area and velocity have an inverse relationship with fluids in a container. The air inside the wind tunnel is treated as fluid because it is a uniform gas. The air slows because the entrance area is smaller than the exiting area.

The area following are the corners. The corners are another crucial area for air flow quality. In traditional closed loop wind tunnels, the corners have a ¼ circle approach where the cross-sectional area of the opening is equivalent to the cross-sectional area of the exit. Inside these corners are guide vanes that guide the flow around the 90-degree keeping the flow from transitioning from turbulent to laminar and decreasing build up or a blockage of air.

Another type of corner is an expanding corner. The difference is that the exit cross-sectional area is larger than the cross-sectional area of the opening. This combines the job of the corner and the diffuser in between the corners, optimizing spatial limits of the wind tunnel. The use of expanding corners shortens the total wind tunnel circuit length about 30%(Lindgren) In prior research, the use of expanding corners was not popular due to poorly designed guide vanes. In more recent articles, with newly designed airfoils that continued after the corner to decrease separation. This helped solve the flow quality issue.

The power plant is the area where the fan is kept. The layout changes the wind tunnel from a rectangular shape to a cylinder where the fan operates and back to a rectangle. “The use of axial fans can, however, create some flow quality problems, if they are subjected to very high loads, but even with more moderate loads they can create a low frequency pulsating variation of the streamwise flow component” (Lindgren). Usually there are silencers that help convert the cross-section shape(Lindgren), while dampening the sound of the fan.

Finally, the stagnation chamber is an extremely important piece because its design directly impacts flow quality in the test section. The wind tunnel starting at the end of the test section, works as on diffuser. Its area slowly increases to a point at the stagnation chamber. The chamber, also known as a contraction chamber, contracts at first in a concave configuration and after in a convex configuration. The contraction is the same from all four sides which forms an almost rectangular funnel. This is another prime use of Bernoulli’s Principle, and where velocity increases. The contraction must be done in a way to minimized turbulence so the length of the concave section should be maximized (Lindgren).

In the stagnation chamber the air is turbulent due to the increased velocity and low area. To fix this turbulence a honeycomb shaped screen is placed at the exit of the chamber. The honeycomb shape is

effective in breaking cross stream flows, as well as fully straightening the flow. The honeycomb by itself can still leave turbulence, to ensure great flow quality it is usually paired with screens that form a rectangular pattern to straighten the flow completely and ensure great flow quality.

The contraction ratio also plays into the section. “The contraction ratio, CR, i.e. the ratio between the largest cross section are, (found in the stagnation chamber), and smallest cross section area, (found in the test section)” (Lindgren). The optimal contraction ratio is 9. Some smaller wind tunnels can have lower contraction ratios such as 6-9 but usually for optimal flow quality the number is 9.

Flow quality defined by John Kaiser Calautit is the “uniformity of the velocity flow field, flow angularity and turbulence intensity” (Calautit). Ensuring that the quality of the flow is excellent is essential to receive accurate results in taking data. At the test section, the turbulence needs to be minimized which is crucial in the corner before the test section and the stagnation chamber.

Current Wind Tunnel

An open wind tunnel contains a stagnation chamber, test section, diffuser, and a fan in that order. The open wind tunnel at Kent State(KSWT) sucks air into the stagnation chamber that contains a single honeycomb screen at the entrance of the test section. Then after the test section a screen that leads into the diffuser that leads to the fan. The fan blows the air out of the wind tunnel and back into the lab where it circulates in the lab back to the front of the lab and into the stagnation chamber. The KSWT has a test section with a cross sectional area of 305mm x 305mm and a length of 600mm. The maximum velocity the wind tunnel can produce is 36 meters per second. The overall size of the KSWT is 3700mm x 1065mm x 1900mm and weighs 293 kg(TECQUIPMENT).

The boundary layer in the KSWT extended from the top and bottom about 35 mm- 40mm. These boundary layers influence the flow quality and can cause an error in data. This is the wall effect and the testing material must be small enough that the flow over the testing material is not interfered by the wall effect. The pressure difference from the KSWT can be seen below

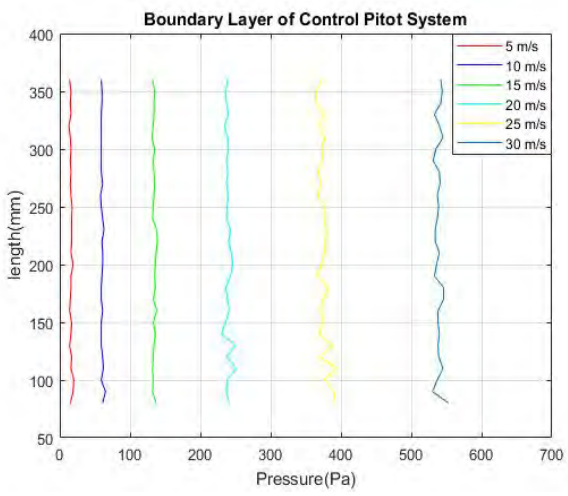

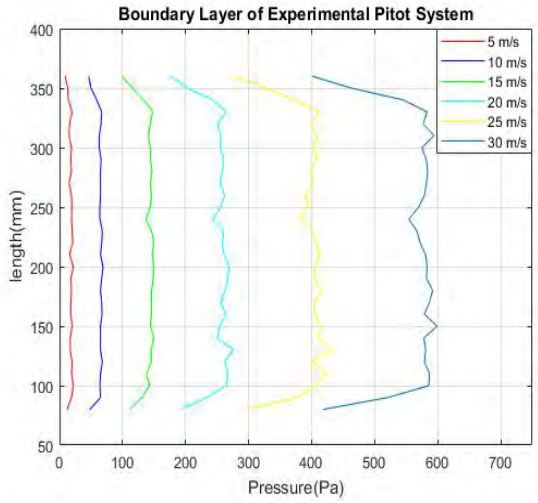

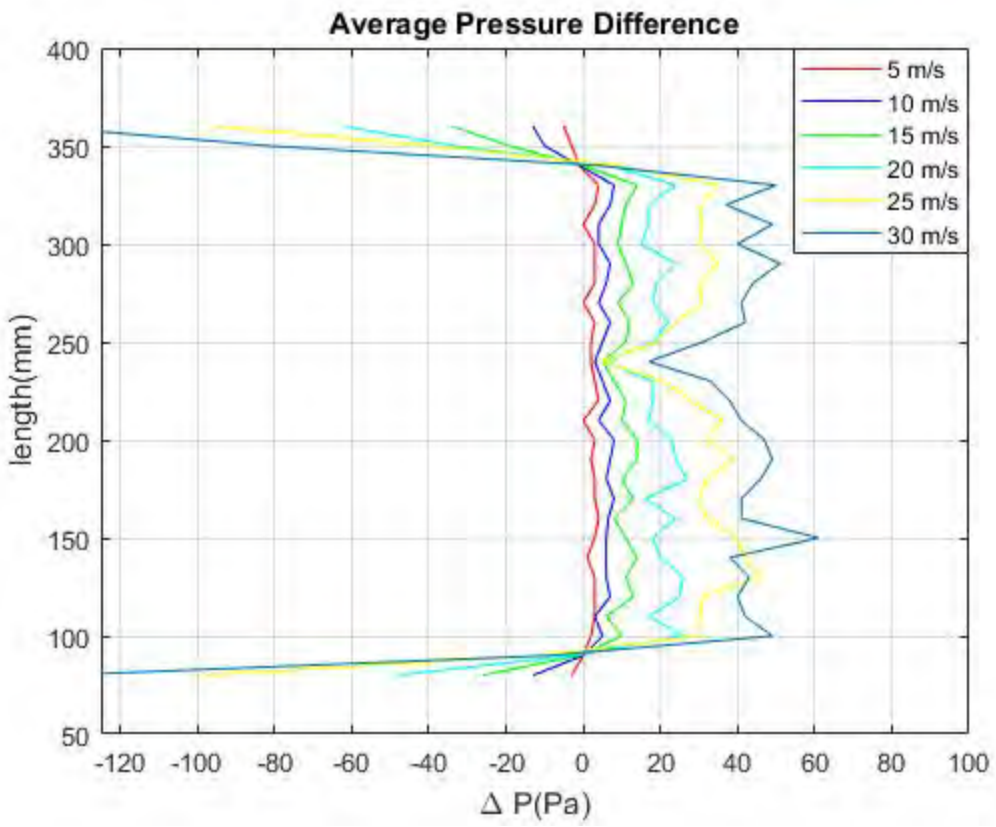

The graphs above show the results of an experiment using the dual pitot tube system set up in the KSWT. Measurements were taken as one pitot tube was lowered. The other pitot tube remained at the same distance from the wall during the experiment.

KSWT is designed with an academic purpose and is spatially optimized. This has made it affordable and small enough to fit into the current lab at Kent State. The negative effect is the wind tunnels flow quality is fair and the testing specimen needs to be rather small. The flow quality is only fair because the flow is sucked through the stagnation chamber which contains one honeycomb screen before being sent through the test section.

Wind Tunnel Research and Development

The KSWT is a fair wind tunnel for the academic purpose at Kent State, but as the aerospace program is expanding we need a more precise instrument. A larger test section would allow for more accurate testing with larger objects. A larger wind tunnel would also allow for better flow quality. The wind tunnel with a larger test section and better flow quality would also allow for private testing and research by local companies around Kent State.

The wind tunnel needs better flow quality so it's decided for a closed-circuit wind tunnel for Kent State. The closed-circuit will allow for better results and though there is a larger cost during construction, the benefits will be overwhelming. The new wind tunnel primary goal is a test section with a cross-sectional area of .8m x .8m and a length of 2m. The length of the test section will increase flow quality while the area will be twice the size of the KSWT. The wind tunnel will use expanding corners with the extended

guide vanes to optimize the space needed for the actual instrument. Using an Excel sheet provided by Miguel Hernandez *et al*'s paper, we were able to get a rough idea of the overall dimensions.

The estimated total dimensions the wind tunnel with a contraction ratio of 6 would be around 11.2- 11.9 meters long, 4.3-4.7 meters wide, and 1.8-1.96 meters height. These dimensions are subject to change with extending the guide vanes and expanding the exit cross-sectional areas. If we were to maximize the contraction ratio to 9, the dimensions would increase with the length, width, and height extending to 13.7, 5.8, and 2.4 meters. This would provide the best flow quality, but is extremely large.

These dimensions will also be simplified into a design in the coming months. The dimensions will be contingent on the area where the wind tunnel will be placed. Current options are the Kent State Airport, and a lab in the new wing of the Aeronautics and Technology building on campus. This would be ideal because the academic use is far more optimal on campus than the off-campus airport. The downside to this is the wind tunnel would need to be more spatially optimized, which would lower the flow quality.

In conclusion, a new wind tunnel at Kent State University would be very beneficial private and academic use. The current wind tunnel provides academic capabilities which provide a basic understanding of airflow but, as the aerospace program advances to the forefront in academics a larger and more precise wind tunnel would benefit this program. This wind tunnel will use expanding corners to decrease its overall geometric footprint, to which is dependent on the final resting place. The satisfaction of the need for a larger wind tunnel will greatly benefit the College of Aeronautics and Engineering at Kent State University.

References

1. Calautit, John Kaiser, et al. "A Validated Design Methodology for a Closed-Loop Subsonic Wind Tunnel." *Journal of Wind Engineering and Industrial Aerodynamics*, 21 Jan. 2014, pp. 180–194.
2. Cattafesta, Louis, et al. "Fundamentals of Wind-Tunnel Design." *Encyclopedia of Aerospace Engineering.*, Dec. 2010, pp. 1–11.
3. Hernandez, Miguel, et al. 'Design Methodology for a quick and Low-cost wind tunnel." *Intech.* 2013. pp. 1-28.
4. Johansson, Arne V. "A Low Speed Wind-Tunnel with Extreme Flow Quality - Design and Tests." *Department of Mechanics, Royal Institute of Technology*, 1992, pp. 1603–1611.
5. Lindgren, Bjorn, and Arne V Johansson. "Design and Evaluation of a Low-Speed Wind-Tunnel with Expanding Corners." Technical Reports from Royal Institute of Technology, Oct. 2002, pp. 1–47.
6. Reinke, Nico. "A Spatially Optimized Wind Tunnel." Institute of Physics, University of Oldenburg, 6 Mar. 2017, pp. 1–18.
7. "Subsonic Wind Tunnel AF1300 | Aerodynamics." *TecQuipment*, www.tecquipment.com/subsonic-wind-tunnel.

Evaluation of Decay Functions for Vector Field Based Obstacle Avoidance

Student Researcher: Yonry R. Zhu

Advisor: Dr. Jay Wilhelm

Ohio University
Department of Mechanical Engineering

Abstract
Obstacle avoidance may be achieved in vector field guidance with the use of repulsive vector fields. The area of influence of these repulsive fields is restricted by scaling their magnitude using a decay function. It is currently unclear how the choice of decay function affects the obstacle avoidance performance of a fixed-wing UAV. The present work investigates the effects of five different decay functions on vehicle performance. For the examined conditions, the best performance is achieved using a hyperbolic tangent decay function when the vehicle velocity to obstacle radius ratio is less than 10. It appears that effective avoidance is achieved when the obstacle field strength rapidly drops to zero once outside of the obstacle radius.

Project Objectives
Vector field (VF) guidance methods for Unmanned Aerial Vehicles (UAVs) incorporate vehicle control, path planning, and trajectory planning within one framework. VF methods generate a field of guidance towards a desired path. VF methods are advantageous for path-centric guidance problems such as circumnavigation of a moving ground target with a fixed-wing UAV.

Repulsive vector fields may be added to the total guidance field to allow for obstacle avoidance. The magnitude of these obstacle vector fields (OVFs) is scaled by a decay function. Currently it is unclear how the choice of decay function affects obstacle avoidance performance. The present work seeks to provide insight into this question by simulating a VF guided, fixed-wing UAV in several obstacle avoidance scenarios.

Methodology
VFs are generated using the Gradient Vector Field method described in [1]. Briefly, this method generates vector fields based on the intersection of two surfaces defined by α_1 and α_2. The total vector field is expressed as the weighted sum of a convergence term, circulation term, and time-varying term. This is given by

$$\vec{V} = G\nabla V + H \wedge_{i=1}^{n-1} \nabla\alpha_i - LM(\alpha)^{-1}\alpha(\alpha)$$

or in component form

$$\vec{V} = G\vec{V}_{conv} + H\vec{V}_{circ} - L\vec{V}_{TV}$$

Example guidance fields generated by this method for circumnavigation and straight-line following are shown in Fig. 1a and 1b respectively. Circumnavigation fields are created by the intersection of a cylinder and plane while straight-line following fields are created by the intersection of two planes. OVFs are generated using the same surfaces as the circumnavigation fields. However, the cylinder radius is set

much smaller than the desired obstacle radius and the weighting coefficient of the convergence term is made negative. The obstacle vector field is then scaled with a decay function. An example OVF is shown in Fig. 1c. There are an unlimited number of possible combinations of VF component weights, VF shapes, and decay functions. To restrict the scope of this paper, all simulations were run with G = -1, H = -1, and H = 0 for the straight VFs and with G = -1, H = $\pm$5 (depending on approach angle), and H = 0 for the OVFs. Five different decay functions, shown in Fig. 2, were selected for examination. For consistency, each decay function was manipulated such that the obstacle field magnitude was scaled to 50% at the desired obstacle radius. This obstacle radius was set to 1 in each simulation.

Three obstacle avoidance scenarios were investigated. Each simulation involved a fixed-wing UAV following a straight line while avoiding obstacles. The UAV was modeled as a Dubins vehicle and was assumed to fly at constant altitude with constant velocity. The vector field provided inputs to control the vehicle heading. The UAV turn rate was limited to a value dictated by vehicle dynamics. The kinematic model of this vehicle is given by the following.

$$\dot{x} = v\cos\theta$$
$$\dot{y} = v\sin\theta$$
$$\dot{\theta} \leq 20 \text{ deg/s}$$

If the vehicle is moving sufficiently fast and the obstacle radius is sufficiently small, it is likely that the vehicle will violate the boundaries of that obstacle. The first scenario investigated this by simulating a head on collision to see how each decay function affected vehicle behavior for different velocity to OVF radius (v/r) ratios. For the remaining, scenarios v/r was set to 10. Vehicles may approach OVFs from a wide variety of initial conditions. The second scenario simulated the UAV approaching the obstacle from several different angles. In a real-world application, the UAV will likely have to avoid multiple objects. The third scenario simulated multi-obstacle avoidance with two parallel and two staggered OVFs.

Results and Discussion

Fig. 3 – 5 show the results of the aforementioned simulations. For v/r $\leq$ 10, the hyperbolic tangent was clearly the superior decay function. In most cases, it was the only decay function that allowed the vehicle to successfully avoid the object and return to the desired path. The inverse square and inverse exponential functions caused the vehicle to completely divert away from the path without returning within the simulated time span. For most cases, the Gaussian and linear functions caused the vehicle to become stuck in a holding pattern, although they allowed for successful object avoidance when the initial approach angle was 90 degrees. At v/r = 100, the obstacle boundary was violated with the linear and hyperbolic tangent functions. The Gaussian function allowed for successful obstacle avoidance, although it took substantially more time to return to the desired path. As before, the inverse square and inverse exponential functions caused the vehicle to completely divert away. At v/r = 1000, the vehicle was moving too quickly to react to the OVF, and the obstacle boundary was violated regardless of the chosen decay function.

Simulations of head-on collision at v/r = 10 were re-run after modifying each decay function to make the OVF magnitude zero at a radius of 1.4. These results are shown in Fig. 4. Each modified decay function allowed for the vehicle to successfully navigate around the obstacle. This suggests that the effectiveness of the hyperbolic tangent is due to its rapid drop-off to zero outside of the OVF radius.

Figures

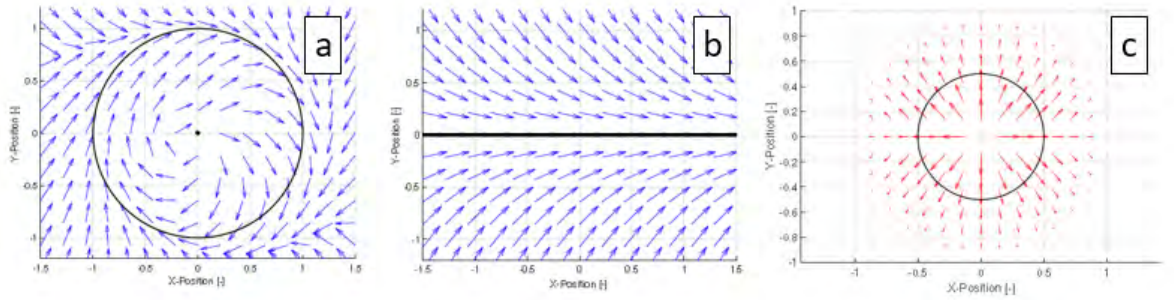

Figure 1. Example vector fields for circumnavigation (a), straight line following (b), and obstacle avoidance (c)

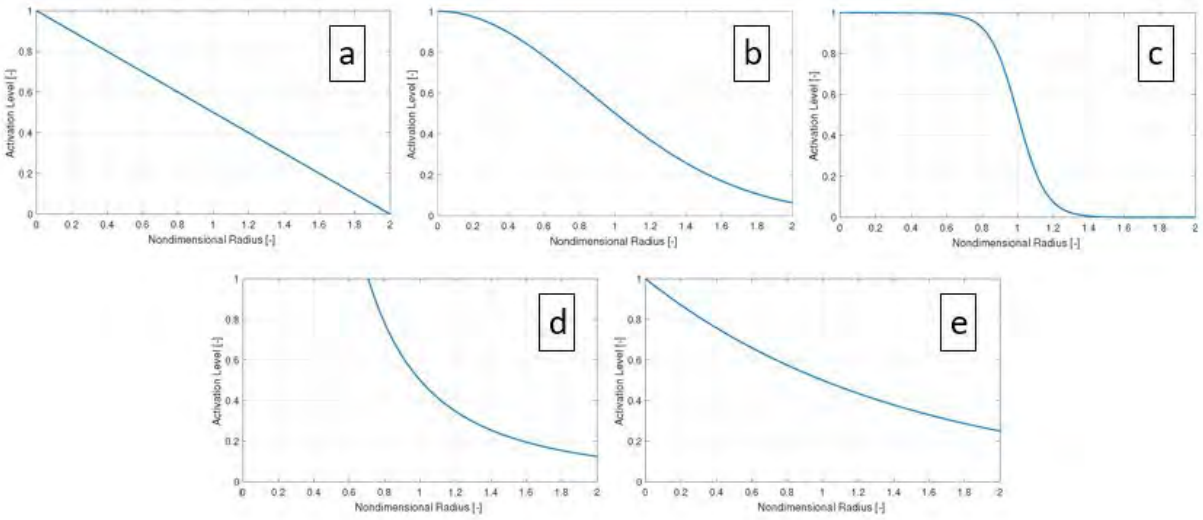

Figure 2. Linear (a), Gaussian (b), hyperbolic tangent (c), inverse square (d), and inverse exponential (e) decay functions.

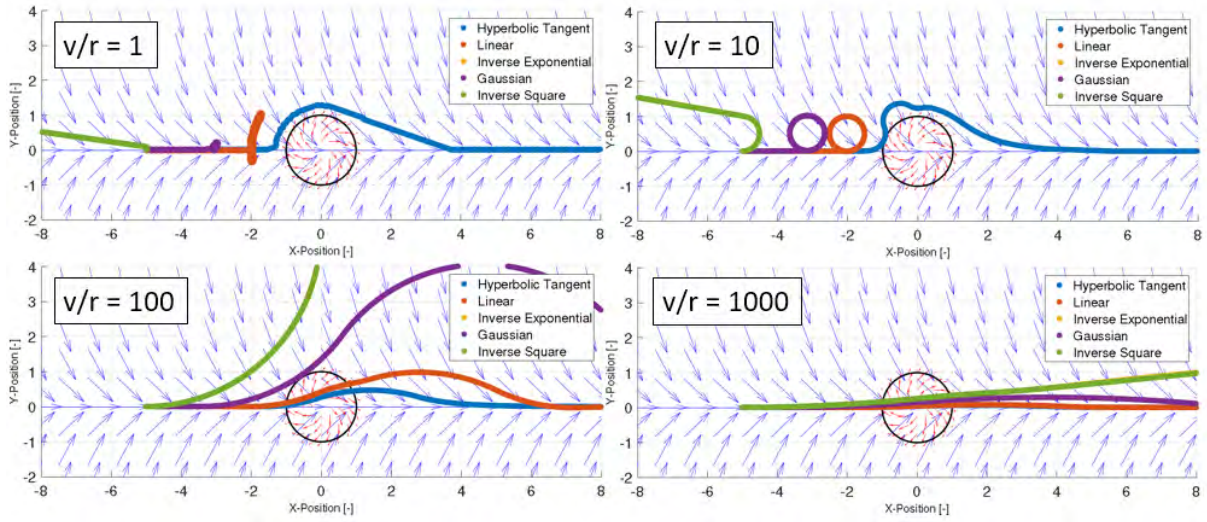

Figure 3. Simulation results for head-on collisions with different v/r ratios. At sufficiently high v/r ratios, the obstacle boundaries are violated.

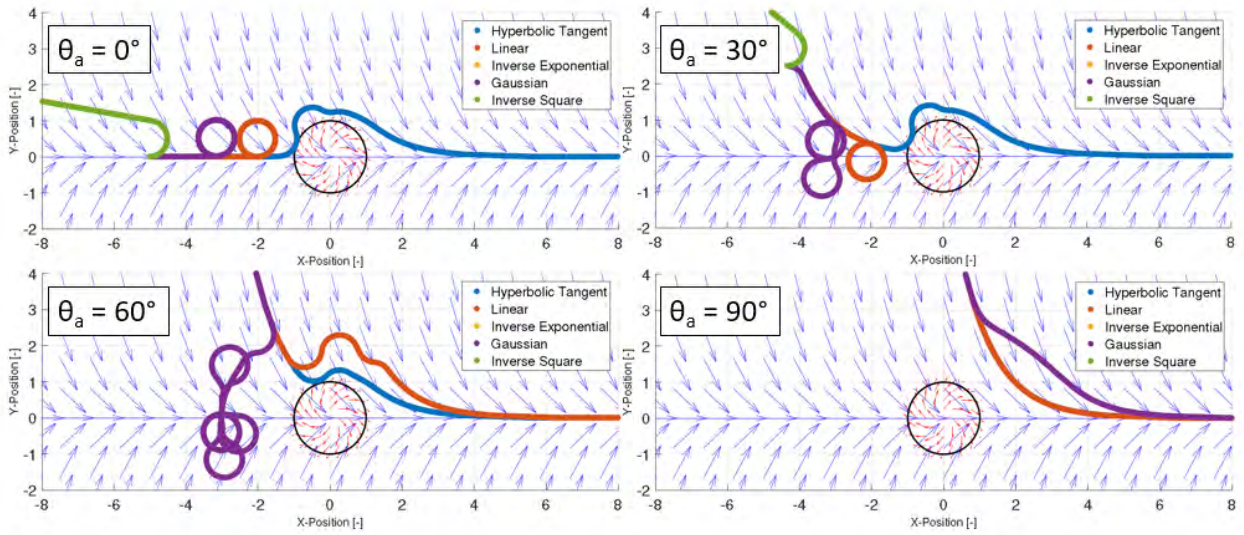

Figure 4. Simulation results with v/r = 10 for different vehicle approach angles.

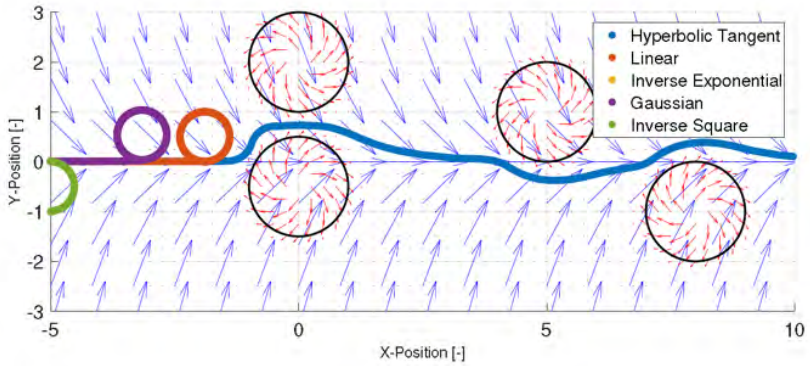

Figure 5. Simulation results with v/r = 10 for multiple obstacle avoidance.

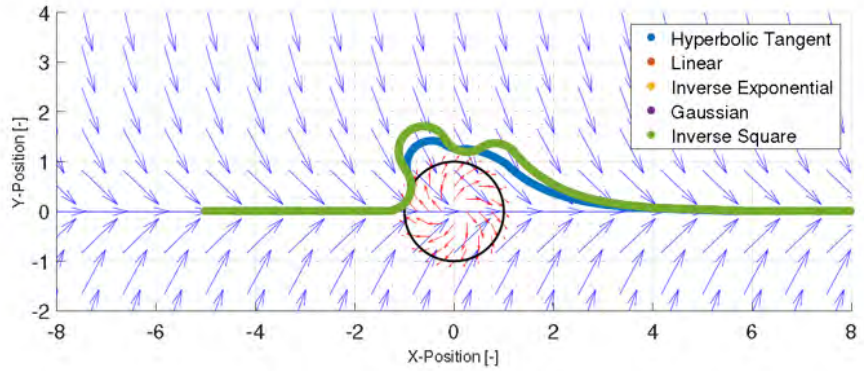

Figure 6. Simulation results with v/r = 10 for head on collision using modified decay functions.

Reference

1. [1] V. M. Goncalves, L.C. A. Pimenta, C. A. Maia, B. C. O. Dutra, and G. A. S. Pereira, Vector Fields for Robot Navigation Along Time-Varying Curves in n-Dimensions, *IEEE Trans. Robot.*, vol. 26, no. 4, pp. 647-659, 2010.